ASSESSING HYDROKINETIC TIDAL ENERGY EXTRACTION FOR ROSE DHU ISLAND, GEORGIA: A CASE STUDY FOR TIDAL RIVERS WITH MARSH ENVIRONS

A Thesis
Presented to
The Academic Faculty

by

Brittany L. Bruder

In Partial Fulfillment
of the Requirements for the Degree
Doctor of Philosophy in the
School of Civil and Environmental Engineering

Georgia Institute of Technology
August 2015

ASSESSING HYDROKINETIC TIDAL ENERGY EXTRACTION FOR ROSE DHU ISLAND, GEORGIA: A CASE STUDY FOR TIDAL RIVERS WITH MARSH ENVIRONS

Advisory Committee Members:

Kevin A. Haas, Committee Chair
School of Civil and Environmental Engineering
Georgia Institute of Technology

Donald Webster
School of Civil and Environmental Engineering
Georgia Institute of Technology

Hermann M. Fritz
School of Civil and Environmental Engineering
Georgia Institute of Technology

Thorsten Stoesser
Institute of Environment and Sustainability
Cardiff University

Annalisa Bracco
School of Earth and Atmospheric Science
Georgia Institute of Technology

Date Submitted: May 15, 2015

To my father:

I hope this makes you proud,

in addition to my ability

... to eat as much as an NFL linebacker.

ACKNOWLEDGEMENTS

This dissertation would not have been possible without the guidance and support of my advisor, Dr. Kevin Haas. Your patience and enthusiasm for teaching and learning has allowed for this truly rewarding experience for which I am extremely grateful. I would like to extend my thanks to my committee members and professors Dr. Hermann Fritz, Dr. Thorsten Stoesser, Dr. Donald Webster, Dr. Paul Work, Dr. Emmanuele DiLorenzo, and Dr. Annalisa Bracco. Far more than professors, you have provided great guidance and support throughout the years. For your time, effort, and faith in my abilities, I thank you.

To my classmates, your friendship and support are immeasurable. To Xiufeng Yang and Brian McFall, Texas forever. To Stephanie Smallegan, our time at Georgia Tech Savannah was just the tip of our friendship. To Courtney DiVittorio, I am sorry for apologizing so much. I wish you all great success and happiness; I look forward to seeing our careers intertwine and the fantastic accomplishments you will achieve.

To the Young family, you have unconditionally adopted Jack and me into your exemplary family, which I aspire emulate one day with your terrific son. And to David Young, you have always made me feel loved and cherished; I can't wait to see our life together unfold.

Finally, I would like to thank my family. To my aunt Lois Cichowski, the cornerstone of our family, throughout the years your kindness and generosity provided for wonderful memories and fostered a true sense of togetherness that I can always rely on. To Candace Bruder, always my biggest champion, even when I broke the vacuum cleaner, I can only aspire to be half the sister you were to me. To my mother Lynn Bruder, your sacrifices and support for my education are the greatest gifts anyone could have ever given me. To all three, I have been completely blessed to have such role models in my life; I can only hope to have a fraction of your intelligence, strength, and compassion. And of course I would like to thank Jack, for there is nothing better in life than running barefoot on the beach with your best friend.

Presented work was supported by the Ray C. Anderson Foundation, Georgia Department of Natural Resources, and a National Science Foundation Graduate Research Fellowship under NSF GRFP Grant No. DGE-0644493. This project is also made possible by the support of the Girl Scouts of America, particularly Nina Smith and Kathleen Cullinan. Thank you for your hard work on Rose Dhu Island and continued passion to inspire young women into the fields of math and science. My studies could also not be completed without the fine research of Dr. Tom Harries and Sandeep Bomminayuni, who graciously lent their time and knowledge. I would also like to thank the staff at the Georgia Tech Hydraulics and Structures labs, particularly Andy Udell, Jeremy Mitchell, and Donnie Otwell, who graciously lent their time and expertise in construction and manufacturing.

TABLE OF CONTENTS

DEDICATION . . . . . **iii**

ACKNOWLEDGEMENTS . . . . . **iv**

TABLE OF CONTENTS . . . . . **vi**

LIST OF TABLES . . . . . **ix**

LIST OF FIGURES . . . . . **x**

SUMMARY . . . . . **xix**

I INTRODUCTION **1**

II LITERATURE REVIEW **9**

2.1 Prediction of Shallow Water Tidal Hydrodynamics 9

2.2 Prediction of Spatial Distributions of Hydrokinetic Energy 12

2.3 Assessing Tidal Hydrokinetic Power 21

2.4 Motivation for Present Study 27

III TIDAL DATA ACQUISITION FOR ROSE DHU ISLAND, GA **28**

3.1 Field Campaigns 28

3.1.1 Field Equipment 29

3.1.2 October 2010 31

3.1.3 November - December 2011 33

3.1.4 June 14-16, 2014 35

3.1.5 June 17-18, 2014 45

3.2 Field Data Processing + Post-Processing 46

3.2.1 GPS Processing 46

3.2.2 ADCP Processing 49

3.2.3 Transect Post-Processing 64

3.2.4 Measurement Uncertainty 67

IV ESTUARINE TIDAL HYDRODYNAMICS **70**

4.1 Numerical Simulations 71

4.1.1 Specifics of Numerical Simulations 71

4.1.2 Simulation Selection 74
4.2 Principles of Estuarine Tidal Distortion 82
4.2.1 Statistical Quantification 83
4.3 Generalized Estuarine Hydrodynamics 85
4.4 Hydrodynamic Effects of Marsh Elevation 87
4.5 Hydrodynamic Effects of Friction 91
4.5.1 Effects of Enhanced Marsh Friction 93
4.6 Summary of Estuarine Hydrodynamics 95
V LOCALIZED TIDAL HYDRODYNAMICS 97
5.1 Measurement Kinematics 97
5.1.1 Current Velocity Characterization + Hotspot Identification 97
5.1.2 Transect Analysis: Hotspot Temporal Evolution 100
5.1.3 Transect Analysis: Along Channel Evolution 111
5.1.4 Kinematic Summary 119
5.2 Measurement Dynamics 119
5.3 Summary of Localized Hydrodynamics 136
VI THEORETICAL AND TECHNICAL RESOURCE ASSESSMENT . 138
6.1 Generalized Effects of Tidal Distortion 138
6.1.1 Synthetic Signal Construction and Normalization 139
6.1.2 Theoretical Power Probability Distributions 141
6.1.3 Technical Power Probability Distributions 146
6.1.4 Effects of Varying Distortion and Constituent Phase 149
6.1.5 Effects of Varying Distortion and Constituent Amplitude 152
6.1.6 Summary for the Generalized Effects of Tidal Distortion 154
6.2 Generalized Effects of Semi-Lunar Variation 155
6.2.1 Synthetic Signal Construction and Normalization 156
6.2.2 Analysis of Combined S_2 and M_2 157
6.2.3 Analysis of Combined S_2, M_2, and M_4 162
6.2.4 Summary of Generalized Effects of Semi-Lunar Variation 169
6.3 Rose Dhu Island Theoretical Resource Assessment 170

6.3.1 Transect Theoretical Power 170
6.3.2 Power Density Calculations 176
6.4 In-Situ Rotor Testing and Efficiency Curve Development 182
6.4.1 Turbine Testing Fundamentals 182
6.4.2 Turbine Data Collection + Processing 185
6.4.3 Turbine Testing Results 188
6.5 Technical Resource Assessment 191
6.6 Resource Assessment Conclusions 194
VII CONCLUSIONS 197
7.1 Dissertation Results 198
7.2 Scientific Merit 203
7.3 Future Considerations 204
7.4 General Remarks 205
APPENDIX A — SIMULATION CONSTITUENT CALCULATIONS 207
REFERENCES 219

LIST OF TABLES

1 Instrumentation specifics for field campaigns. 31

2 Utilized CORS station information. 47

3 CORS stations used for intermediate base station processing and measured distance from rover antenna to water surface, h_η. 48

4 Way-points for charted transects in field campaigns. Coordinates are in UTM Zone 17R and CORS 96 datum. 66

5 Standard Deviation (σ) of GPS measurements provided by GrafNav. 68

6 Simulation descriptions for predicted surface heights and volume fluxes. o_m is representative wetland elevation. f_b and f_m are channel bottom and wetland frictional parameters respectively. 71

7 Skill scores between measurements and simulations aggregating all measurements. 79

8 Skill scores between measurements and simulations for different tidal phases. 80

9 Calculated Skewness and Asymmetry Parameters for Measured Transect . . 85

10 Calculated Skewness and Asymmetry Parameters For Simulation A1 across Estuary. 87

11 Energy production of synthetic diurnal velocity signals 149

12 Energy production of velocity signals with semi-lunar and semi-diurnal variation 165

13 Maximum average power for the local domain, Transect A, using the method of Garrett and Cummins (2005) along with statistical distortion values of volume flux. 171

14 Yearly kinetic energy for the local domain, Transect A, through integration of kinetic energy flux along with statistical distortion values of kinetic energy flux. 172

15 Available energy estimates for points near Rose Dhu Island. Labels refer to points in Figure 92. 178

16 Quadratic fit parameters for dimensional power curves 190

17 Technical energy estimates for points near Rose Dhu Island. Labels refer to points in Figure 92 and Table 15. Turbines refer to efficiency curves in Figure 71. 191

LIST OF FIGURES

1 Relative Growth of US Gross Domestic Product (GDP), Electricity + Energy Production Production, and Carbon Dioxide Emissions. Data Source: (EIA, 2012) 2

2 Existing Hydrokinetic Tidal Energy Projects in the US. *A)* RITE (Verdant-Power, 2007) *B)* Cobscook Bay (ORPC, 2012) 4

3 Bathymetries of hydrokinetic tidal energy sites. *Inset Image*: Map of United States east coast for geographic reference. *A*) Cabscook Bay *B*) RITE *C*) Coastal Georgia. Depths courtesy of *www.tidalstreampower.gatech.edu*. . . . 6

4 Map of Ogeechee Estuary. Orange highlighted area marks Rose Dhu Island. Yellow highlighted area marks the location of strong tidal currents. Inset image: Map of Southeastern US for geographic reference. Satellite image courtesy of Google Earth 2013. 8

5 Examples of complex features surrounding Rose Dhu Island (highlighted in orange). Bathymetry from Bomminayuni et al. (2012). 13

6 Example depiction of helical flow in a channel cross section. Green arrows represent main circulation cell, orange represents secondary cell, and pink represents axial flow. 15

7 Key regions of interest for various confluence geometries identified by Best (1987). Figure inspired by Riley and Rhoads (2012) 16

8 Image of docked field boat. Instrumentation identified. 29

9 Map of Ogeechee Estuary with relevant locations for field campaign operations. Blue area marks Rose Dhu Island. Inset Image: Map of Southeastern United States for geographic reference. 30

10 Predictions of water levels for NOAA Coffee Bluff subordinate station for October field campaign. *A)* Water levels for the month of October highlighting spring tide. *B)* Water levels and field measurement times highlighted in green. 32

11 Spatial surveying strategies. Red dots represent waypoints and blue arrows represent planned measured paths. Rose Dhu Island depicted in orange. *A)* Spatial Reconnaissance for October 2010 Campaign. *B)* Repeated transect measurements for hydrodynamic analysis for November-December 2011 campaigns. Transects are labeled by letters. Blue circles used to determine nominal cross sections of channel curvature. Satellite imagery courtesy of Google Earth 2013 33

12 Predictions of Water Levels for NOAA Coffee Bluff Subordinate Station for November-December 2011 campaign. *A)* Water levels for the months of November and December highlighting spring tide. *B)* Water levels and field measurement times highlighted in green. 34

13 Model predictions of volume fluxes for Transect A. *A)* Predictions for the month of June. *B)* Predictions for chosen field days. Water levels and field measurement times highlighted in green. 36

14 Map of rotor testing locations for June 14-16,2014. Red lines and circles are associated with flood testing; blue lines and circles associated with ebb. Circles are planned testing locations; lines are actual GPS positionings during testing. 37

15 Structural housing for rotor. *A)*: Artistic rendering of structural housing design *B)*: Actual construction of structural rotor housing *C)*: Close up of structural support (small tripod and L-Plate) with spinning rotor 38

16 Image of large tripod and shaft assembly. Yellow highlights large tripod. . . 39

17 Image of small tripod assembly. *A)* Image of small tripod, highlighted in green. Note, top covered in plastic wrap for overnight protection of bearing. *B)* Close up of bearing and small tripod table. Red piece pre-attached to bearing, part of PTO. *C)* Model of Torque arm in yellow. 40

18 Images of L Plate. *A)* Top view of L-Plate highlighted in blue. *B)* Image of L-plate suspended by carabiner 40

19 Images of constructed large tripod, small tripod, L-plate, and rotor at rest. 41

20 Rotor lowering. *A)* Plywood boards removed. Cylindrical sleeves highlighted in orange. *B)* Rotor lowered to full extent with straps attached and L-Plate fitted over sleeves. 42

21 *A)* PTO assembly. *B)* Finished rotor/ADCP assembly prior to measurements commencing 43

22 Proximity of deployed ADCP to rotor shaft. 43

23 Rotor field Measurements. *A)* Tom Harries applying friction to PTO and measuring resultant torque and rotation speed of rotor *B)* Simultaneous deployment of ADCP (attached to wooden board and deployed underwater), PTO (on top of shaft/tripod), and rotor (underwater) 44

24 Charted transects for all field campaigns. 45

25 Schematic of relevant boat dimensions and coordinate systems $\mathbb{I}$, $\mathbb{B}$, and $\mathbb{E}$. Note, in reality $\mathbb{E}$ is vertical and horizontal, but images are exaggerated and rotated for clarity. Image of ADCP courtesy of Teledyne RD Instruments. . 50

26 Example of enhanced dual GPS processing technique for wavy conditions. *A)* Current magnitudes processed with *WinRiver II B)* Current magnitudes processed with Dual GPS technique. Pictured measurement is Transect E measured on June 17, 2014. Time is reference to transect measurement initiation. Currents in [m/s]. 53

27 Decision and flow chart of ADCP processing methods. White boxes represent conditions and solid boxes represent processes. Blue values indicate desired deliverables. Red lines indicate loop. 54

28 Correlation coefficients between depth averaged ${u_z}^{\mathbb{I}}(t'+\tau)$ and ${V_{o\mathbb{B}}}^{\mathbb{E}}(t)$ for various τ. Different lines are different afternoon transects of June 17, 2014 with significant wave motion. 20 transects are presented. A median minima, or optimum τ is found to be 0.79 seconds. 57

29 Summed absolute error between *WinRiver II* and GPS processed transects with varying ${\alpha_{\mathbb{I}}}^{\mathbb{B}}$ [^{o}]. Different lines are different morning transects of June 17, 2014 with little wave motion. 23 transects are presented. 58

30 Power spectral density calculation for o_b for anchored afternoon turbine testing on June 17, 2014. Spectra calculated with a window length of 128 seconds with 50% overlap giving 35 degrees of freedom for a signal approximately 35 minutes long. The null hypothesize is experimental red noise with a 99% confidence interval (CI) for Type I error as explained by Hartmann (2014). 60

31 Example of filtered boat movement with cut off frequency of 0.33 Hz. Red line is movement of GPS 1. Blue line is low pass filtered movement of GPS 1. Black lines represent boat extent. Measurement taken from Transect E on June 17, 2014. 61

32 Examples of the effect of R on the interpretation of high frequency rotational and translational movement for a fixed ${s_{\mathbb{B}}}^{\hat{\mathbb{B}'}}$. Image of ADCP courtesy of Teledyne RD Instruments 62

33 Correlation coefficients between depth averaged ${u_x}^{\hat{\mathbb{I}}}$ and ${V_{xu}}^{\mathbb{I}}$. Different lines are different afternoon transects of June 17, 2014. Red lines indicate morning transects with calm conditions. Blue lines indicate afternoon transects with wavy conditions. 63

34 Example of measurement mapping to charted transect. Measurement locations with regards to charted transect exaggerated 65

35 Probability density functions (PDF) of error velocities for all ADCP bin measurements. Blue bars are empirical distributions and red lines are Gaussian fits. *A)* Measurements from transects and moving measurements. Mean of Gaussian fit: 2x10$^-$4 m/s; standard deviation 0.057 m/s. *B)* Measurements from anchored turbine measurements. Mean of Gaussian fit: 0.01 m/s; standard deviation 0.092 m/s. 69

36 Map of Ogeechee Estuary and model domain. Referenced points and transects in text labeled. Inset image: Map of Southeastern United States for geographic reference. 72

37 Comparison of water level η between model and field measurements in MTL. 77

38 Comparison of volume flux Q between model and field measurements for Transect 12. Positive Q represents flood volume fluxes while negative Q represents ebb. 78

39 Flux/stage diagrams for Simulation A1 at different cross sections defined in Figure 36. *A)* Diagrams for estuary mouth, η_m, and mid-estuary, $\eta_m e$. *B)* Diagram for measured transect, η_t. Horizontal black lines represent marsh elevation o_{mA1}. All surface heights in MTL. Positive Q represents flood volume fluxes while negative Q represents ebb. Period represented: Entire duration of model simulation November 16 -December 29. 2011. 86

40 Hydrodynamic effects of change in marsh elevation: time series for Simulations A1 and B1. *A)* Relative surface heights in MTL. *B)* Relative surface height, or pressure gradient proxy, between the open ocean and transect surface heights. *C)* Transect volume flux. Positive Q represents flood volume fluxes while negative Q represents ebb. Date shown: December 22, 2011. . . 89

41 Hydrodynamic effects of change in marsh elevation: flux/stage diagrams for Simulations A1 and B1. Dashed lines represent marsh elevation for simulation. All surface heights in MTL. Positive Q represents flood volume fluxes while negative Q represents ebb. First tidal cycle of December 22, 2011 represented. 90

42 Hydrodynamic effects of change in domain friction: time series for Simulations A2, C2, and E1. Line colors are darker with increasing friction. *A)* Relative surface heights in MTL. *B)* Relative surface height, or pressure gradient proxy, between the open ocean and transect surface heights. *C)* Transect volume flux. Positive Q represents flood volume fluxes while negative Q represents ebb. Date represented: December 22, 2011. 91

43 Hydrodynamic effects of change in domain friction: flux/stage diagrams for Simulations A2, C2, and E1. Line colors are darker with increasing friction. Positive Q represents flood volume fluxes while negative Q represents ebb. First tidal cycle of December 22, 2011 presented. 92

44 Hydrodynamic effects of change in marsh friction: flux/stage diagrams for Simulations A2, A1, and A3. Line colors are darker with increasing marsh friction. Positive Q represents flood volume fluxes while negative Q represents ebb. First tidal cycle of December 22, 2011 is presented. 94

45 Binary map of differences in surface heights between Simulations A2 and A3 at peak water levels. Dark grey represents areas where water levels are higher for Simulation A2 and light grey represents areas where water levels are higher for Simulation A3 95

46 Depth averaged current magnitudes for the Vernon and Little Ogeechee Rivers for October 19-20, 2010 respectively. Currents in cm/s. Blue arrow indicates area of high currents and interest. 98

47 Depth measurements in NAVD88 coordinate system from 2011 *A)* and 2014 *B)* measurements, with depths in meters and transects labels in red. Location of the topographic bump highlighted with red circle. 99

48 Bathymetric map of numerical model in meters and NAVD88 datum. Depths based on bathymetric surveys (Bomminayuni et al., 2012). 100

49 Axial currents [m/s] measured for Transect A on June 18, 2014, representative of a characteristic flood tide. Negative values represents ebb currents and positive represents flood. Transect distance, D is measured relative to the first waypoint identified in Table 4. 101

50 Cross channel currents [m/s] (depth-averaged detrended) for Transect A on June 18, 2014, representative of a characteristic flood tide. Negative values represents currents in the $-D$ direction and positive represents $+D$. Transect distance, D is measured relative to the first waypoint identified in Table 4. Thick black contours represent zero cross channel velocity. 102

51 Vorticity [s^-1] measured for Transect A on June 18, 2014, representative of a characteristic flood tide. Positive/negative values represent clockwise/counter-clockwise rotation respectively. Transect distance, D is measured relative to the first waypoint identified in Table 4. Thick black contours represent $\omega = 0$. 103

52 Axial currents [m/s] measured for Transect A on December 22, 2011, representative of a characteristic ebb tide. Negative values represents ebb currents and positive represents flood. Transect distance, D is measured relative to the first waypoint identified in Table 4. 106

53 Cross channel currents [m/s] (depth-averaged detrended) for Transect A on December 22, 2011, representative of a characteristic ebb tide. Negative values represents currents in the $-D$ direction and positive represents $+D$. Transect distance, D is measured relative to the first waypoint identified in Table 4. Thick black contours represent zero cross channel velocity. 107

54 Vorticity [s^-1] measured for Transect A on December 22, 2011, representative of a characteristic ebb tide. Positive/negative values represent clockwise and counter-clockwise rotation respectively. Transect distance, D is measured relative to the first waypoint identified in Table 4. Thick black contours represent $\omega = 0$. 108

55 Normalized axial velocity (*A, B*) and vorticity (*C, D*) measurements for flood (*A, C*) and ebb (*B, D*) currents. Axial velocities normalized by the corresponding transect volume flux divided by transect area. Thick black lines represent zero vorticity. Bottom figure (*G*) is corresponding volume flux diagram. Measurements from June 17, 2014. 112

56 Normalized axial velocity (*A, B*) and vorticity (*C, D*) measurements for flood (*A, C*) and ebb (*B, D*) currents. Axial velocities normalized by the corresponding transect volume flux divided by transect area. Thick black lines represent zero vorticity. Bottom figure (*G*) is corresponding volume flux diagram. Measurements from June 18, 2014. 115

57 Ebb axial velocity (*A, B*) and vorticity (*C, D*) measurements for ebb weaker Transect B input (*A, C*) and equal Transect B input (*B, D*). Bottom figure is corresponding volume flux diagram. Thick black lines represent zero vorticity. Bottom figure is corresponding volume flux diagram. Measurements from December 22, 2011. 117

58 Representative curvature for Transect A with $R_1 = 2200$ m and $R_2 = 1500$ m 123

59 Depth integrated cross momentum terms for flood tide. Terms correspond to terms in Equation (48). Rows indicate transect number and point in tidal cycle referenced in the volume flux time series at the bottom. Second to bottom plot is transect depths for reference. X-axes are the D coordinate in $[m]$. 124

60 Flood advective cross channel momentum terms. Columns refer to terms on the left side of Equation (45) except cross velocity. Rows indicate transect number and point in tidal cycle referenced in the volume flux time series at the bottom. Thick black lines represent zero contours and thin black line is measured depth. X- and Y- axes are the D and o coordinates in $[m]$. 126

61 Flood forcing cross channel momentum terms. Columns refer to terms on the right side of Equation (45) except vorticity. Rows indicate transect number and point in tidal cycle referenced in the volume flux time series at the bottom. Thick black lines represent zero contours and thin black line is measured depth. X- and Y- axes are the D and o coordinates in $[m]$. 127

62 Depth integrated axial momentum terms for flood tide. Only the significant terms corresponding to Equation 49 are shown. Rows indicate transect number and point in tidal cycle referenced in the volume flux time series at the bottom. Second to bottom plot is transect depths for reference. X-axes are the D coordinate in $[m]$. 129

63 Flood advective axial channel momentum terms. Columns refer to terms on the left side of Equation (46) except axial velocity. Rows indicate transect number and point in tidal cycle referenced in the volume flux time series at the bottom. Thick black lines represent zero contours and thin black line is measured depth. X- and Y- axes are the D and o coordinates in $[m]$. 131

64 Flood forcing axial channel momentum terms. Columns refer to terms on the right side of Equation (46) except axial velocity. Rows indicate transect number and point in tidal cycle referenced in the volume flux time series at the bottom. Thick black lines represent zero contours and thin black line is measured depth. X- and Y- axes are the D and o coordinates in $[m]$. 132

65 Depth integrated cross momentum terms for ebb tide. Terms correspond to terms in Equation (48). Rows indicate transect number and point in tidal cycle referenced in the volume flux time series at the bottom. Second to bottom plot is transect depths for reference. X-axes are the D coordinate in $[m]$. 134

66 A: Non-dimensional velocity Signals A ($A = S = 0$), B ($A = 0/S = 0.48/\phi = 0°$), and C ($A = 0.48/S = 0/\phi = 90°$). B: $M_2 + M_4$ Signal skewness (solid) and asymmetry (dashed) for varying ϕ. 140

67 Probability Density Function, $f_{V'}$ for non-dimensional velocity, V', for Signals A, B and C 143

68 Probability Density Function, $f_{P'}$ for non-dimensional kinetic power density, P', for Signals A, B and C 144

69 Non-dimensional energy distribution, $P'f_{P'}$ as a function of P' *(A)* and V' *(B)* for Signals A, B and C. 145

70 Exceedence Energy Curves, E'_e for Signals A, B and C. 146

71 Turbine efficiency curves as a function of non-dimensional velocity. 147

72 Non-dimensional energy distribution, $P'f_{P'}$ with (thick lines) and without (shaded area) turbine efficiencies. *(A)*: Turbine 1. *(B)*: Turbine 2 148

73 *A*)Non-dimensional energy distribution, $P'f_{V'}$ for varying ϕ. *B*) Exceedence Energy Curve, E'_e for signals with varying ϕ. 150

74 *A*) Non-dimensional energy distribution, $E_f P'f_{V'}$ for varying ϕ applying Turbine 1 efficiencies. *B*) Non-dimensional energy distribution, $E_f P'f_{V'}$ for varying ϕ applying Turbine 2 efficiencies. 151

75 *A*)Non-dimensional energy distribution, $P'f_{V'}$ for varying skewness. *B*) Exceedence energy curve, $E'_e(V'_c)$ for signals with varying skewness. 152

76 *A*) Non-dimensional energy distribution, $P'f_{V'}$ for varying asymmetry. *B*) Exceedence energy curve, $E'_e(V'_c)$ for signals with varying asymmetry. . . . 153

77 *A*) Available and technical kinetic energy densities for varying ϕ. *B*) Total turbine efficiencies for varying ϕ. 155

78 Non-dimensional velocity signals V'_s with varying r_s and $r = 0$. Entirety of periodic signal not shown. 158

79 Non-dimensional velocity probability distribution functions $f_{V'_s}$ and $f_{|V'_s|}$ for velocity signals with varying r_s. 159

80 *A-B*: Non-dimensional energy distribution functions $P'_s f_{P'_s}$ for varying r_s. *C-D*: Non-dimensional technical energy distribution functions $E_f P'_s f_{P'_s}$ for Turbine 1 and varying r_s. *E-F*: Non-dimensional technical energy distribution functions $E_f P'_s f_{P'_s}$ for Turbine 2 and varying r_s. Left plots are calculations with higher resolution in r_s for $r_s \leq 0.5$. 160

81 *A*) Available and technical kinetic energy densities for varying r_s. *B*) Total turbine efficiencies for varying r_s. 161

82 Non-dimensional velocity signals. All signals constructed with $r_s = 0.2$. V'_{A_s} is constructed with $r = 0$. V'_{B_s} is constructed with $r = 0.25$ and $\phi = 0°$. V'_{C_s} is constructed with $r = 0.25$ and $\phi = 90°$. 163

83 Non-dimensional velocity probability distribution functions $f_{V'_s}$ (A) and $f_{|V'_s|}$ (B) for velocity signals A_s, B_s, C_s. 164

84 Non-dimensional energy distribution $P'_s f_{P'_s}$ as a function of V'_s (A) and $|V'_s|$ (B) for velocity Signals A_s, B_s, C_s. 165

85 Non-dimensional exceedence energy curves E_{es} for A_s, B_s, C_s 166

86 Non-dimensional energy distribution, $P'_s f_{P'_s}$ with (thick lines) and without (shaded area) turbine efficiencies. *A)*: Turbine 1. *B)*: Turbine 2 167

87 Non-dimensional energy distributions with turbine efficiencies, $E_f P_s' f_{P_s'}$. *(A)*: Turbine 1. *(B)*: Turbine 2 168

88 *A*) Available and technical kinetic energy densities for varying ϕ. *B*) Total turbine efficiencies for varying ϕ. 169

89 Histogram for yearly volume flux Q for Transect A for simulations with varying marsh elevation. A1 →B1 represents increasing marsh elevation. *A):* Histogram of yearly volume flux. *B):* Histogram of yearly absolute volume flux. 173

90 Histogram for yearly volume flux Q for Transect A simulations with varying enhanced marsh friction. A2 →A1 →A3 represents increasing marsh friction. *A):* Histogram of yearly volume flux. *B):* Histogram of yearly absolute volume flux. 174

91 Histogram for yearly volume flux Q for Transect A simulations with varying domain friction. E1 →C2 →A2 represents increasing domain friction. *A):* Histogram of yearly volume flux. *B):* Histogram of yearly absolute volume flux. 175

92 Yearly energy density for localized domain utilizing depth averaged currents from Simulation A1. Values in kWhr/m^2. 177

93 Power Density timeseries for points near Rose Dhu Island in Sets 1 (*A*) and 2 (*B*). Labels refer to points in Figure 92 and Table 15. 179

94 Power (*A, C*) and Energy density (*B, D*) histograms for points in Set 1. Corresponding depth averaged velocities are presented in red axis in m/s. In the bottom row the x-axis is normalized by the maximum extent of each curve. Labels refer to points in Figure 92 and Table 15. 180

95 Power (*A, C*) and Energy density (*B,D*) histograms for points in Set 2. In the bottom row the x-axis is normalized by the maximum extent of each curve. Labels refer to points in Figure 92 and Table 15. 181

96 Example Power Curves (*A*) and resultant Efficiency Curve (*B*) for a synthetic Turbine. Color dots in Efficiency Curves refer to C_P maxima in Power Curve. 184

97 Components of mechanical PTO during field testing. Red arrows and text indicate component labels. Orange arrows indicate direction of rotation and torque. Blue and green arrows indicate forces. 185

98 Results of rotor in-situ testing. *A-D:* Dimensional and non-dimensional power versus rotation speed plots from revolution averaged data from all tests except Day 1: Test A. *C-D:* Fitted quadratic curves according to Equation 82 with parameters presented in Table 16 189

99 Energy density histograms for points in Set 1. Shaded area represents available energy; lines represent energy captured by turbine. Red numbers indicate corresponding depth averaged velocities for x-axis. Points refer to locations in Figure 92 and Table 15. 192

100 Energy density histograms for points in Set 2. Shaded area represents available energy; lines represent energy captured by turbine. Red numbers indicate corresponding depth averaged velocities for x-axis. Points refer to locations in Figure 92 and Table 15. 193

SUMMARY

Hydrokinetic tidal power is a novel and emergent technology undergoing continuous advancement with much of the progress focused on large utility scale projects. This resource is potentially underutilized because much of the coastal United States, despite having substantial tidal currents, do not have the deep and wide environments required by most of the developing turbine technology. Wetland estuaries with shallow and narrow tidal rivers have unique hydrodynamics that foster moderately strong currents and are potentially untapped energy resource for the United States. This dissertation includes a detailed characterization of the tidal hydrodynamics for Rose Dhu Island, Georgia used for a tidal energy resource assessment as well as a general feasibility study for tidal estuaries with extensive wetlands.

For predictions and evaluation of the estuarine hydrodynamics, data from an existing numerical model of the estuary encompassing the island is utilized. Field measurements in close proximity to the island are used to calibrate the model as well as characterize local hydrodynamic features. These measurements include water surface elevations, current velocities, and channel volume fluxes obtained using a coupled Global Positioning System (GPS) and Acoustic Doppler Current Profiler (ADCP) assembly.

After the model calibration, the simulation data is used to evaluate the estuarine hydrodynamics. Wetland dominated estuaries commonly have a high degree of non-linear distortion which govern the relative durations and strengths of the tidal stages and thus the overall hydrodynamics and incoming hydrokinetic energy. The Ogeechee Estuary is characterized as ebb dominant with peak ebb and flood volume fluxes near high tide as a result of the increased storage capacity of the wetlands. Lowering the average wetland elevation in the model decreased ebb dominance and quickened the transition from flood to ebb tide. Increased domain friction in the model removed energy from the system and reduced ebb dominance. Enhanced model marsh friction reduced lateral flooding of the wetlands as well as ebb dominance.

Localized measurements surrounding the island are analyzed to determine a location near the southwest coast of the island as a hydrokinetic energy hotspot. A kinematic and dynamic analysis is performed using channel transect measurements to identify key physical processes behind the hotspot formation. The hotspot forms due to sub-critical flow acceleration over a singular bump in the topography. High streamwise momentum is further concentrated at the hotspot due to secondary circulation cells across the channel. Flood tide circulation is characterized by two co-rotating cells induced by channel curvature and delineated by the bump. Ebb circulation consists of two counter-rotating cells from flow confluence of two upstream channels.

Once the hydrodynamics are understood, the theoretical and technical resource assessment of the island is completed. A sensitivity analysis of hydrokinetic energy and tidal distortion is performed on synthetic data. For a principle constituent and its first harmonic, distortion greatly changes as does the distribution of velocities and energy as the relative phase varies. While the theoretical energy remains consistent, the technical energy can greatly vary. This effect is reduced with the addition semi-lunar variation. Using a simplified analytical method, the maximum average channel power is estimated as 8.80 MW. For the hotspot it is estimated that there is 30.3 MWh available to capture yearly with an average power of 3.46 kW for a turbine with an area of 10 m^2. For a generalized turbine with a cut-in and rated speed of 0.8 m/s and 1.5 m/s respectively, a cross sectional area of 10m^2 and a maximum kinetic to electrical efficiency of 41%, the hotspot could provide a yearly technical energy of 10.9 MWh with an average power of 1.25kW for the island. Due to the complex localized hydrodynamics, both the theoretical and technical resource varies greatly across and along the channel.

This dissertation highlights the large spatial and temporal variability of hydrokinetic energy for a wetland environment. In addition it emphasizes the importance of tidal distortion on technical resource assessments. These considerations are more pertinent when performing a hydrokinetic energy resource assessment in a marsh estuary than for large scale bay-ocean exchange environments, the present industry focus.

CHAPTER I

INTRODUCTION

For over 100 years the US has capitalized on the immense productivity of fossil fuels; high energy consumption, corresponding positively with national Gross Domestic Product (GDP), has allowed the United States to be one of the most prosperous countries in the world (Figure 1). However, as the fossil fuel supply is depleted, and the adverse environmental effects of its utilization are becoming more pronounced, the high cost of fossil fuel consumption and the need for clean renewable energy is more apparent today than ever in the US.

Fossil fuels such as petroleum, natural gas, and coal are formed by the decomposition and compounding of organic (carbon) material, a process on the order of hundreds of millions of years. Because of long timescale of replenishment and rapid rate of consumption, fossil fuels are considered a non-renewable resource and may eventually be depleted globally. The US has felt both the economic and political pressures of the depletion of its own reserves. The rise of fossil fuels importation has not only raised the fiscal price, but also costs of national security, providing funds and concessions to countries with questionable US intentions and human rights records. These effects have only been intensified with the increased resource competition from the industrialization of second and third world countries in the past few decades.

The environmental consequences are also adverse and arguably more significant. Combustion of carbon based fossil fuels produce usable heat and energy, however it also produces carbon dioxide as well as other 'greenhouse gases' as a byproduct. Such greenhouse gases are responsible for most notably global warming. The rise in global temperatures has a butterfly effect with the delicate energetic balance of the atmosphere and the ocean, inducing many processes such as climate change and extreme weather events. Since the dawn of the industrial revolution, global carbon dioxide emissions have multiplied over 16 times;

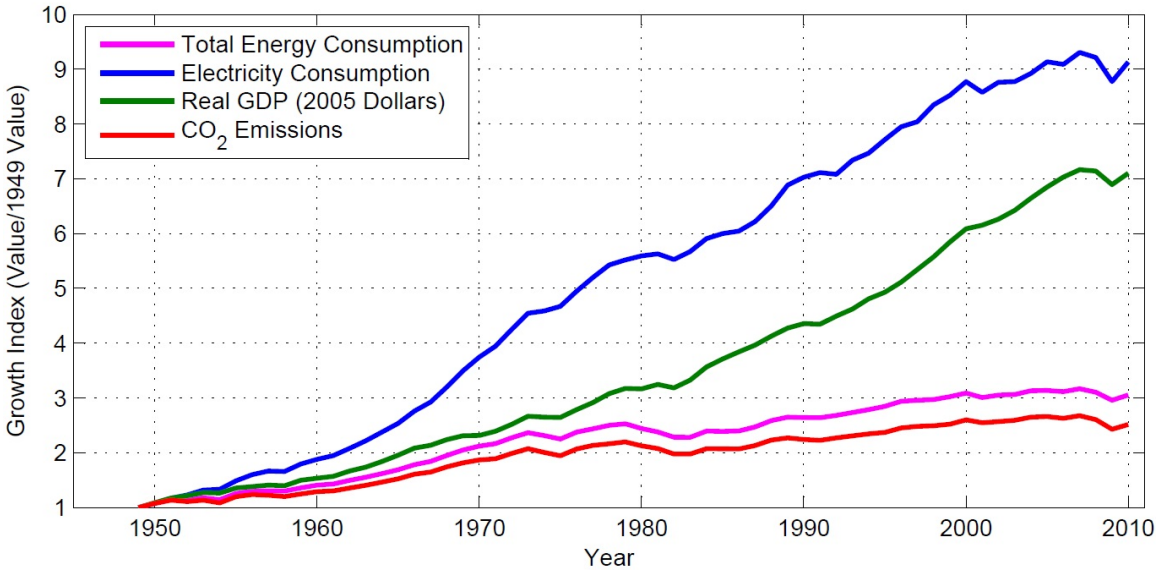

Figure 1: Relative Growth of US Gross Domestic Product (GDP), Electricity + Energy Production Production, and Carbon Dioxide Emissions. Data Source: (EIA, 2012)

half of the total increase occurring since 1970 (Boden et al., 2010). As a result, climatic effects are becoming more evident; according to the Climate Extreme Index (CEI) computed by the US National Ocean and Atmospheric Administration (NOAA), the US weather has been becoming more extreme since the 1970s and 2012 was on record the most climatically extreme year on record for the US (NOAA, 2013).

Such extremes not only are environmentally harmful, but exacerbate the energy crisis by demanding the use of more fossil fuels. Severe droughts have reduced flow rates at hydroelectric dams across the country, reducing hydroelectric output by 45% in some locations (DOE, 2013b). Extreme temperatures lead to the increased use of energy for indoor climate control. High temperatures, severe storms and flooding have forced electrical power plants to curtail production leading to frequent blackouts. Ironically, while the adverse climate effects of fossil fuels have been hindering electrical production, electrical power plants are the leading producer of total fossil fuel pollutant greenhouse gases (EIA, 2012).

In 2011, electrical power plants were the largest energy consumer in the country, responsible for 40% of the total US energy consumption and 67% of that electrical power being drawn from fossil fuels (EIA, 2012). Figure 1 highlights the increase in both carbon dioxide emissions and electricity consumption. Thus supplementing US's electrical needs

with renewable energy will make the most direct and immediate impact on total fossil fuel consumption and emissions. This has already begun with solar, traditional hydropower, and wind technologies. In the past 60 years renewable energy production has nearly doubled in the US, surpassing nuclear power in the 2010. 54% is directed to electric power plants while an additional 33% power residential, commercial, and industrial entities directly (EIA, 2012). However, there are other burgeoning renewable energy sources that have yet to be tapped, one being hydrokinetic tidal power.

Tides are induced by the astronomical forcings between the earth, moon, and sun. At a given point and time on the earth, oceans are acted on by a resultant force comprised of the gravitational pull of all three celestial bodies, and the centrifugal acceleration from their rotation around each other. The magnitude of this tide generating force depends on the relative positions of all three and the specified location on earth. Due to planetary motion, these relative positions constantly change, resulting in a periodic forcing and acceleration of the ocean, varying in time and space. These forcings and accelerations give rise to the upheaval and fall of the water surface at the shoreline known as the tide.

Tidal streams are high velocity sea currents created by the periodic horizontal movement of the tides, often magnified by local topographical features such as headlands, inlets, and straits. To generate electricity from these free stream flows, hydrokinetic turbines are utilized. A marine hydrokinetic turbine consists of two major components: the rotor and power take off (PTO) system. The rotor consists of the blades and shaft that capture the kinetic energy of the tidal stream; and the PTO converts the aforementioned mechanical energy into electrical power. The operation of such turbines is analogous to wind turbines, but underwater, presenting additional engineering challenges.

However, tidal streams have advantages as well, one being the highly deterministic and consistent nature of the tides due to their regular celestial forcing as compared to wind or rainfall. Also, for a given flow velocity the available kinetic energy of tidal streams is over 800 times that of wind due to the density differential between air and water. Compared to traditional hydropower (dams), tidal stream power has a smaller environmental footprint and is relatively invariant of droughts. As compared to fossil fuels, the tides are

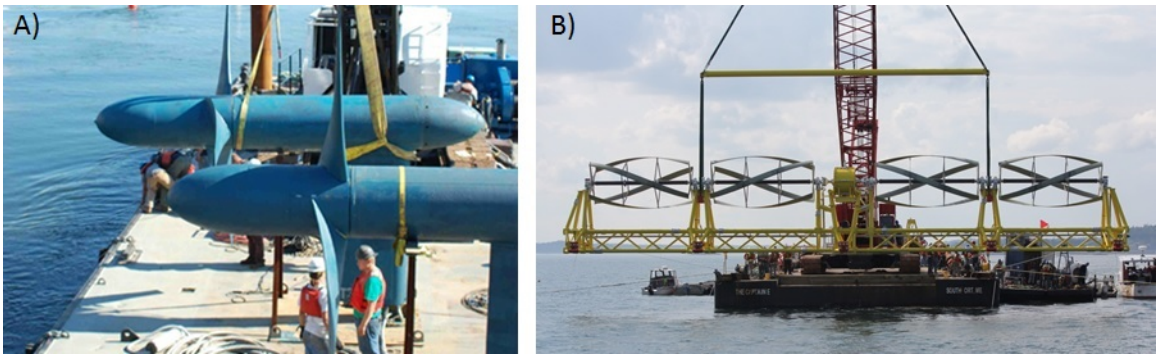

Figure 2: Existing Hydrokinetic Tidal Energy Projects in the US. *A)* RITE (VerdantPower, 2007) *B)* Cobscook Bay (ORPC, 2012)

inexhaustible due to their astronomical forcings and their kinetic energy capture is emissionless. Hydrokinetic tidal power is a promising source of clean and renewable energy.

Hydrokinetic tidal power is a novel and emergent technology undergoing continuous advancement with the majority of the progress focused on large utility scale projects. As of present, only two projects have been successfully demonstrated in the US (Figure 2). The Roosevelt Island Tidal Energy (RITE) project, operated by Verdant Power, deployed six 5m turbines (rated 35 kW) in the East River, NY for 9,000 turbine hours, producing 70 MWh for New York City (DOE, 2013a). Culminating from this, RITE received the first Federal Energy Regulator Commission (FERC) license for a tidal power project in the US for a 1 MW pilot project. In 2012, the Ocean Renewable Power Company (ORPC) deployed the first US commercial grid-connected tidal energy project in Cobscook Bay, Maine near the Bay of Fundy. The FERC licensed project currently consists of 5 TideGen turbines, providing 300 kW and an anticipated yearly output of 1.25 GWh (FERC, 2012). ORPC aims to install additional turbines, each 30 m long, 5 m both wide and tall, moored 5 m above the sea floor, to provide 5 MW over the next several years (State of Maine DOC, 2012).

Although there are only currently two operational tidal energy projects in the US, this number is not indicative of the total available energy resource from US tidal streams. Using numerical ocean modeling, it has been estimated there is upwards of 50 GW of available tidal power along the US coast (Haas, 2011; Defne et al., 2012a). Other than fiscal and

political considerations, this resource is vastly underutilized because much of the coastal US, despite having substantial tidal currents, do not have the deep, wide environments required by the current turbine technology. Using data from the DOE's assessment of tidal stream energy potential, it is calculated that of the area of tidal streams in the continental US with a mean current suitable for tidal energy production ($\geq$ 0.5 m/s and depth $\geq$ 4 m), 49 % has mean currents less than 1.0 m/s and depths $\leq$ 10 m. 71% has mean currents less than 1.0 m/s and depths $\leq$ 15 m. Thus these shallow estuaries, bays and sinuous tidal rivers with moderate velocities are a vast untapped resource for the United States.

The RITE and the Cobscook Bay projects were approximately 12 and 30 m depths respectively and have simpler, more expansive geometries (DOE, 2013a; State of Maine DOC, 2012). Figure 3 highlights both the depth and geometrical differences of different tidal energy sites. In particular, Figure 3C highlights the unique marsh features commonly found in the Southeastern US. Such estuaries are composed of a network of shallow, narrow, and sinuous rivers, as well as expansive wetlands which provide extensive intertidal storage. As a result, a great amount of water is forced through narrow channels, providing tidal flows with substantial velocities. Unfortunately, the existing large scale turbine systems and components cannot be solely scaled down while retaining the same efficiency; thus they require their own unique design.

Another challenge facing tidal power development of shallow, small scale environments, is the prediction of the complex hydrodynamics. In order to obtain licensing such as FERC, numerous environmental studies and impact statements must be produced, requiring extensive measurements and numerical modeling. Changes in hydrodynamics can lead to adverse sediment transport and drying/inundation of wetlands. The project must be able to prove energy extraction will not drastically alter the overall hydrodynamics of the environment. Although the celestial tidal forcing is relatively consistent, the resultant current flows are difficult to analytically predict and model (however once determined for a given location, either by measurements or model, they too can be easily predicted through harmonic analysis techniques). In open water, such modeling and prediction is fairly straightforward.

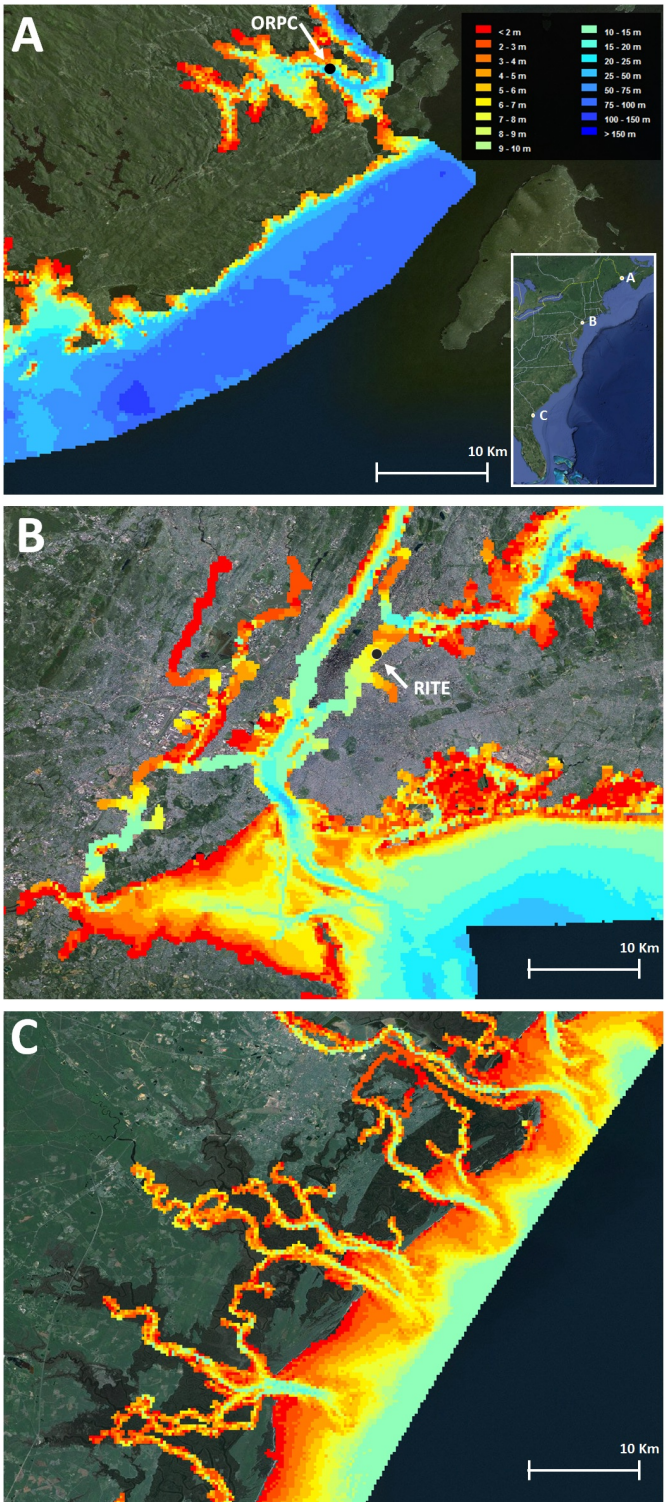

Figure 3: Bathymetries of hydrokinetic tidal energy sites. *Inset Image*: Map of United States east coast for geographic reference. *A*) Cabscook Bay *B*) RITE *C*) Coastal Georgia. Depths courtesy of *www.tidalstreampower.gatech.edu*.

However, for the sinuous tidal rivers networks, some with extensive tidal marshes, the hydrodynamic prediction and assessment can be more complex with many more nonlinear interactions and spatial variation. In addition, marshes not only make for complicated tidal hydrodynamics but also are environmentally sensitive, requiring more scrutiny during the permit process. As a result, little study has been focused on tidal energy applications in US estuaries with tidal marsh environments, despite having widespread energy potential.

A tidal marsh site that is currently being considered for tidal energy production is Rose Dhu Island, Georgia (Figure 4). The island, with only one household of continuous human inhabitants who manage the property, is a virtually undisturbed ecosystem of over 100 acres. The Girl Scouts of Historic Georgia, who own the island, intend to create a sustainable Eco-Village on Rose Dhu Island as well as an adjacent Science Center where environmental science and biology will be taught. The Eco-Village is desired to be powered independently from electrical power plants, by available renewable energy sources, including hydrokinetic tidal energy. The project aims to be a beacon for renewable energy for small coastal communities across the US: a local use of clean renewable energy for electricity, to reduce the consumption and emissions of fossil fuels.

The presented study aims to further establish the precedent for small scale hydrokinetic energy projects in tidal marsh environments through an energy extraction assessment at Rose Dhu Island, Georgia utilizing field measurements and an existing numerical model. In particular, the study: 1) Characterizes the large-scale hydrodynamics of the estuary as pertains to available kinetic energy; 2) Locates hydrokinetic energy hotspots near Rose Dhu Island and identifies the hydrodynamic processes responsible for their formation; and 3) Calculates yearly available and technical energy assessments for hotspots near Rose Dhu Island using data from an in-situ turbine deployment. The developed methodologies can be utilized for permitting and licensing purposes for future construction and implementation of a tidal energy plant on Rose Dhu as well as evaluate the viability of hydrokinetic tidal energy for any tidal marsh environment.

Figure 4: Map of Ogeechee Estuary. Orange highlighted area marks Rose Dhu Island. Yellow highlighted area marks the location of strong tidal currents. Inset image: Map of Southeastern US for geographic reference. Satellite image courtesy of Google Earth 2013.

CHAPTER II

LITERATURE REVIEW

The context of the dissertation is presented through an extensive literature review of hydrokinetic energy extraction in tidal marshes consisting of four sections. The first section introduces known knowledge of tidal hydrodynamics and their prediction for wetland estuaries. The second focuses on more localized features pertaining to open channel hydrodynamics. The third presents existing methods for assessing hydrokinetic energy in tidal systems once the local hydrodynamics are known. Finally, the fourth highlights existing knowledge gaps in the literature and motivation for the proposed study.

2.1 Prediction of Shallow Water Tidal Hydrodynamics

The first to formulate an accurate analytical description of tidal motion was Laplace (1775). Although others had previously acknowledged the gravitational effects of the moon and sun on the Earth's ocean surface, most notably Newton (1687) and his Equilibrium Theory, Laplace was the first to mathematically articulate such motion in the Laplace Tidal Equations (LTE). Although still accurate today with little modification, the three partial differential equations were difficult to solve and thus had little utility for actual tidal prediction. However, their contributions were grossly significant in: 1) proving the representation of tidal motion as a harmonic series; and 2) grandfathering hydrodynamic longwave theory (Cartwright, 1999).

Stemming from LTE, Lord Kelvin Thomson (1868) proposed the oscillatory motion of the tides could be represented through a sum of harmonic expressions with frequencies corresponding to astronomical movements of the earth, moon, and sun. A given tidal parameter, $f(t)$, such as surface height or velocity, could be represented as a function of

time, t, by

$$f(t) = \sum_{n=1}^{N} a_n \cos(\omega_n t + \phi_n) \tag{1}$$

where the amplitude, a_n, phase, ϕ_n, and frequency, ω_n, were solved through spectral analysis of local measurements. Although limited to the measurement locale, this powerful methodology for tidal prediction was highly accurate and is still used today.

Upon spectral decomposition of empirical data, hundreds of different frequencies, later coined tidal constituents were cataloged (Darwin and Adams, 1883; Doodson, 1921). The shear number of constituents, many with no direct correspondence with astronomical movements, highlighted another limitation of harmonic analysis: the absence of physical interpretation for observed/predicted flows. Such knowledge could be used to extrapolate tidal predictions of one area to another without the need for additional measurements. Thus focus returned to LTE and analytical solutions, particularly those for shallow water areas where many unknown constituents were prevalent.

Recognizing the geostrophic scale of the LTE, Airy was first to simplify the equations for local shallow waters through removal of the Coriolis forcing, leading to the classical longwave hydrodynamic equations (Cartwright, 1999). Airy (1842) solved the non-linear equations utilizing perturbation techniques for the simplified case of a single harmonic propagating in a shallow rectangular channel. The formation of a second harmonic with twice the frequency of the original was discovered, leading to new distortion in the tidal signal as seen in empirical observations. Tidal distortion refers to the ebb and flood stages of the tide no longer having equal strength or duration, a deviation from the sinusoidal tides in the deep ocean. It is also commonly referred to as *Tidal Asymmetry*, however in this study this phrase is reserved for its statistical definition which will be discussed in Chapter IV.

Continuing the investigation of Airy, Lamb (1932) formally published analytical solutions for not only the second but additional higher harmonics. Lamb also introduced the concept of compound tides, harmonics produced from the non-linear interaction of other constituents. These compound and higher harmonics constituted many of the unknown tidal constituents and were coined shallow water overtides.

Airy and Lamb were able to prove the generation of shallow water overtides considering solely the non-linear advection terms in the longwave hydrodynamic equations. In the following decades further inclusion of additional nonlinear terms in analytical solutions have shown overtide generation is the result of several other physical mechanisms such as bottom friction, intertidal storage, variable bathymetry, and channel convergence. Thorough reviews of such analytical solutions can be found in Proudman (1953), Dronkers (1964), Le Provost (1991), and Friedrichs and Aubrey (1994). Analytical solutions were and still today remain solely as conceptual or mathematical proofs; due to their numerous simplifications and reduced dimensions they are not typically used as predictions. In addition, with the advent of computational machines in the 1950s and 1960s, the need and presence of novel analytical solutions has dwindled.

With computers, the millions of calculations for solving the full 2D longwave equations across complex estuarine systems could be completed with relatively little time and effort. As a result, tidal predictions could be made estuary-wide without measurements from each of the thousands of grid points. In addition, the relative importance of terms in the governing equations could be tracked from ocean to estuary, essentially documenting the formation of shallow water overtides, tidal distortion, and attributing physical mechanisms. This knowledge is vital today to validate numerical results as well as predict effects of energy extraction in shallow waters for better predictions.

Friedrichs and Aubrey (1988), aggregating the previous works of Dronkers (1986a) and Speer and Aubrey (1985) along with their own numerical model, established tidal distortions in shallow estuaries are due to two principle effects: (1) bottom friction and (2) intertidal storage which are primarily responsible for flood and ebb dominated tides respectively (1988). Non-linear effects of shallow water wave propagation, as proved by Lamb and Airy were found to be negligible in such systems in comparison. The exchange of energy between a principle astronomical constituent and its overtides, most notably the first harmonic, could be used to characterize the degree of distortion along an estuary (Parker, 1991).

Blanton et al. (2002) observed overtide generation and tidal distortion were amplified in tidal marsh systems due to the abrupt changes in channel width presented by the flooding

and drying of tidal flats or wetlands. In particular, it was found the relative height of the tidal flats to high and low tidal stages dictated the tidal morphology and overtide generation throughout the system. It was further reiterated for accurate prediction of velocity currents in tidal marshes, it was found wetting/drying algorithms for the wetlands must be included in numerical models (Huang et al., 2008; Zheng et al., 2003).

2.2 Prediction of Spatial Distributions of Hydrokinetic Energy

While knowledge of tidal forcing is important for determining incoming/outgoing flow conditions and forcings, an understanding and correct representation of open channel hydraulics is required for identifying localized areas of high velocities and currents. For tidal energy applications, most pertinent is the evolution/spatial distribution of axial momentum discussed below. However, as explained afterwards, lateral/vertical momentum have non-trivial implications on the spatial distribution of axial momentum.

In classic open channel flow, such as in a tidal river, when there is a change in cross section there is an associated change in water level and axial velocity depending whether the flow is subcritical or supercritical. The classification of flow is commonly determined by the non-dimensional Froude Number, Fr given by

$$Fr = \frac{U}{\sqrt{gh}} \tag{2}$$

where U is the characteristic velocity, g is gravity, and h is the characteristic nominal depth. Fr is the ratio of the flow velocity and rate of disturbance propagation. For $Fr >= 1$, the flow is deemed supercritical; all disturbances such as change in bathymetry or channel width will be advected downstream and not felt upstream. For $Fr < 1$, the flow is deemed subcritical; all disturbances will propagate both upstream and downstream.

For subcritical flow, A sharp decline in bed elevation or channel expansion, results in higher water levels and lower velocities. A sharp rise in channel wide bed elevation or channel constriction, results in lower water levels and higher velocities, i.e. the formation of localized areas of higher velocities, hotspots. The opposite is true for supercritical flow. Although

the theory above is highly generalized to flows and bathymetry with no cross-channel variation, it can be useful for a first approximation of hotspot locations in an estuarine network. To identify more localized distributions with more complicated bathymetry and planform geometry, such as variation across a curved section, the hydrodynamics need to be resolved not only in more dimensions but also retain higher order processes.

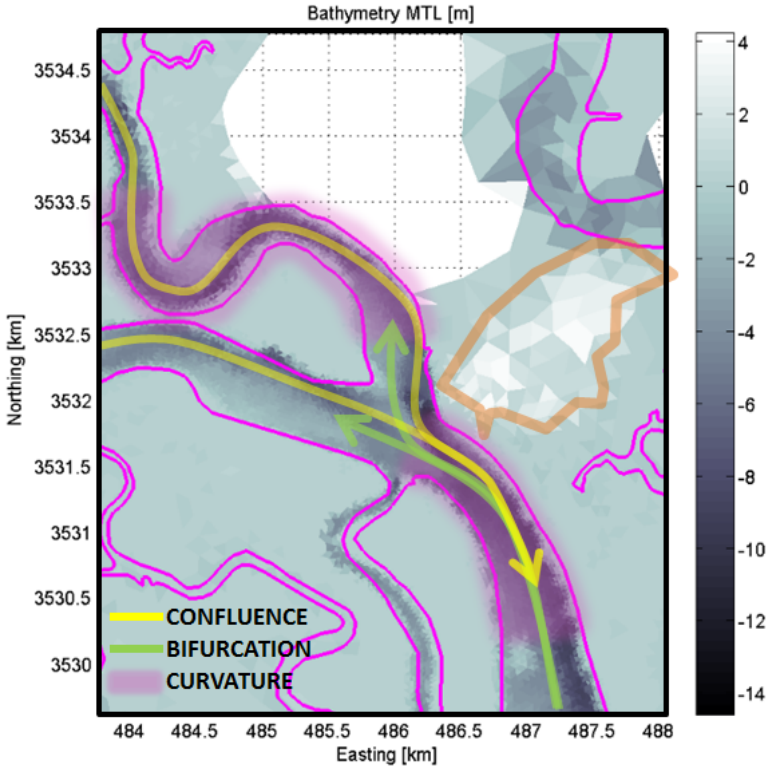

Figure 5: Examples of complex features surrounding Rose Dhu Island (highlighted in orange). Bathymetry from Bomminayuni et al. (2012).

A boon to estuarine tidal hydrodynamics in the last decade was three dimensional numerical models such as the Regional Ocean Modeling System (ROMS) and Finite Volume Community Ocean Model (FVCOM) (Haidvogel et al., 2008; Chen et al., 2003). Such models resolve vertical and lateral momentum transfer that is important for accurately resolving complex open channel hydrodynamics including, but not limited to: curvature; confluences; bifurcations; and irregular bathymetry. As depicted in Figures 3 and 4, such features are common in branching and sinuous marsh networks. They are particular numerous in the

localized domain surrounding Rose Dhu Island (Figure 5). Even though momentum in tidal channels is primarily in the axial direction, lateral and vertical momentum transfer affects the localized distribution of hydrokinetic energy and is thus relevant to tidal energy applications. Much work on these complexities of open channel flow have concerned unidirectional river flow. However, if occurring within the time scale of a tidal phase these open channel river phenomenon may be ascribed to tidal flow.

As outlined by Blanckaert and De Vriend (2004), secondary flow in curved open channels has been observed for nearly 150 years (Thomson, 1876; Boussinesq, 1868). To clarify its formation, Blanckaert and De Vriend (2004) use simplified momentum and vorticity equations defined in a curvilinear coordinate system defined by Batchelor (1967) as

$$0 = \frac{1}{1 + n/R_c} \frac{{u_s}^2}{R_c} - \frac{1}{\rho} \frac{\partial p}{\partial n} - \frac{\partial \overline{u_s' u_n'}}{\partial z} + \nu \bigtriangledown^2 u_n \tag{3}$$

$$0 = -\frac{1}{1 + n/R_c} \frac{\partial}{\partial z} \left(\frac{{u_s}^2}{R_c} \right) - \frac{1}{\rho} \frac{\partial p}{\partial n} - \frac{\partial^2 \overline{u_s' u_n'}}{\partial z^2} + \nu \bigtriangledown^2 \omega_s \tag{4}$$

$$\omega_s = \frac{\partial u_z}{\partial n} - \frac{\partial u_n}{\partial z} \tag{5}$$

where n, z, and s represent the cross-channel, vertical, and streamwise directions respectively, R_c is the radius of curvature of the channel axis, ρ is water density, g is gravitational acceleration, u and u' are the mean and fluctuating (turbulent) velocity components, ω is the vorticity, and ν is the kinematic viscosity.

The classical representation, known as helical flow, consists of a circulation cell in the n-plane (Figure 6). The circulation is formed and perpetuated by a local imbalance between the centrifugal ($\frac{1}{1+n/R_c} \frac{{u_s}^2}{R_c}$) and pressure gradient ($\frac{1}{\rho} \frac{\partial p}{\partial n}$) terms in the lateral momentum equation (Equation (3)). Centrifugal force, proportional to the axial velocity squared, accelerates areas of high axial velocity radially outwards. Because typically $\frac{\partial u_s}{\partial z} > 0$, there is a net acceleration and 'piling' of surface water towards the outer bend. Assuming hydrostatic balance ($\frac{\partial p}{\partial z} = -g\rho$), $-\frac{1}{\rho} \frac{\partial p}{\partial n}$ acts in the opposite direction inwards. At the bed centrifugal force is minimal ($\frac{\partial u_s}{\partial z} > 0$), thus along the bed there is a net acceleration inward, completing

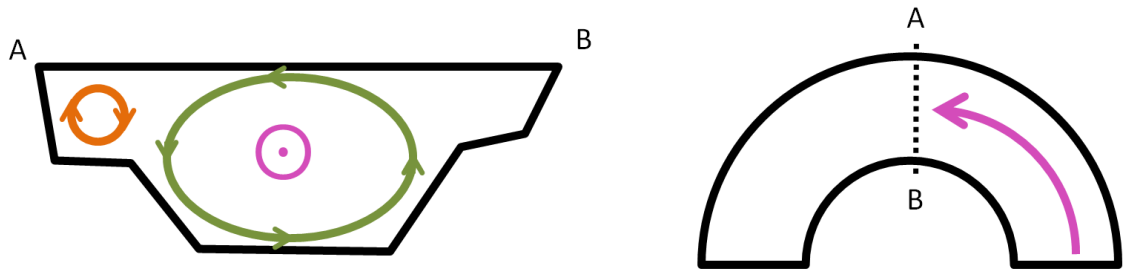

Figure 6: Example depiction of helical flow in a channel cross section. Green arrows represent main circulation cell, orange represents secondary cell, and pink represents axial flow.

the circulation cell, and inducing vorticity in the streamwise direction, ω_s. Conservation of streamwise vorticity, Equation (5), can also used to describe this primary circulation as a balance between centrifugally induced vorticity, $\frac{1}{1+n/R_c}\frac{\partial}{\partial z}\left(\frac{{u_s}^2}{R_c}\right)$, and dissipation from viscous ($\nu \bigtriangledown^2 \omega_s$) and turbulent ($\frac{\partial^2 \overline{u_s' u_n'}}{\partial z^2}$) shear stresses.

Assuming a streamwise velocity profile ($\frac{\partial u_s}{\partial z}$), a dissipative eddy viscosity turbulence model ($\overline{u_s' u_n'} = 0$; $\nu = \nu_t$), and hydrostatic balance ($\frac{\partial p}{\partial z} = -g\rho$), Equations (3), (4), and (5) can be used to solve for the vertical profile of the cross stream velocity, $u_n(z)$ (Blanckaert and De Vriend, 2004). Initial models incorporated this $u_n(z)$ as a first order perturbation to obtain the solution of $u_s(n, z)$ (Rozovskii, 1957; Engelund, 1974). However, as cataloged by Blanckaert and De Vriend (2004), these models only produced good agreement with experimental data for mildly curved bends. Blanckaert and Graf (2004) identified the discrepancy as a result of neglecting the higher order negative feedback of the new u_s profile on the driving centrifugal force. A non-linear model was created by Blanckaert and de Vriend (2003) and improved upon these quasi-3D numerical models for mild to moderately curved flows. However, through a momentum balance of experimental data it was found for strongly curved flows advective transport terms were significant and required the consideration of a fully three dimensional model (Blanckaert and De Vriend, 2004).

These higher order advection terms are also in part responsible for a secondary counter-rotating cell (Figure 6) along the outer bank for curved turbulent flow. Through the same momentum balance of 3D laboratory experiments, Blanckaert and De Vriend (2004) confirms the hypothesis of De Vriend (1977) and Christensen et al. (1999): outer cell vorticity

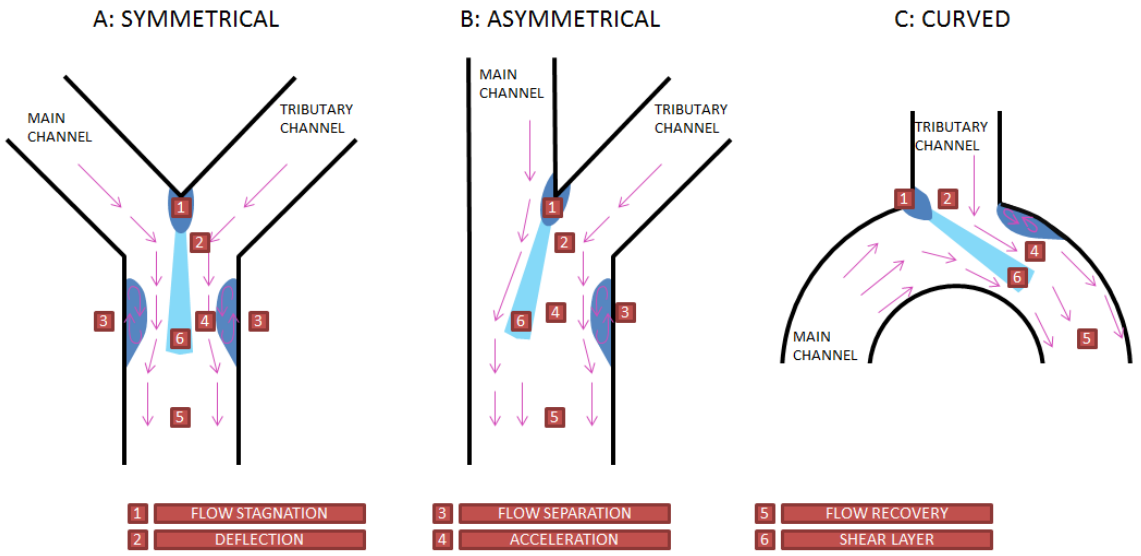

Figure 7: Key regions of interest for various confluence geometries identified by Best (1987). Figure inspired by Riley and Rhoads (2012)

is not generated by the centrifugal term alone but rather along with positive feedback from cross stream turbulent shear stresses in Equation (4). Considering turbulent stresses solely as dissipative of the mean flow like viscous stresses, the outer cell does not form. Thus to accurately model the outer-cell, a non-linear turbulence closure scheme is required to model the two-way exchange of mean flow and turbulent kinetic energy.

Another important consideration for kinetic energy distribution and dissipation is the confluence of two tributary streams (Figures 5 and 7). Confluent flow structures are strongly tied to curvature hydrodynamics since upon collision there is typically a redirection of converging flows. However, a mixing interface between colliding flows and asymmetry in the streamwise direction ($\frac{\partial}{\partial s} \neq 0$) produce additional complexities. As a result, observational studies, i.e. Ashmore et al. (1992); McLelland et al. (1996); Rhoads and Kenworthy (1998), have frequently observed one or two helical cells at flow junctions, yet have had much discord over physical interpretation. This is in part due to the variation of confluent configurations and lack of three dimensional measurements as fully cataloged and discussed by Bradbrook et al. (2000). The analysis of three dimensional models have helped clarify the governing physical processes.

Best (1987) identified six key regions of interest for concordant confluent flows which

have remained relevant for a number of three dimensional model studies with varying channel morphologies (Figure 7) (Bradbrook et al., 2000; Roberts, 2004; Riley and Rhoads, 2012). As flow from the tributary and main channel collide, faster surface flows from both channels converge and create a stagnation zone (1) with higher water elevations and pressure. Coupled with areas of flow separation with low pressure (3), a pressure gradient between the two zones provides the centrifugal acceleration ($\frac{{u_s}^2}{R}$) to deflect flows in zone (2), where s and R retain their curvature definitions but are now oriented along a streamline. Because $\frac{\partial u_s}{dz} < 0$, bed surface flows respond more quickly and cross stream velocities develop parallel to the induced pressure gradient forming secondary helical flow. As the flows converged into a smaller combined cross-section, in part due to the areas of flow separation, surface flows are axially accelerated to their fastest values at zone (4). Such pressure gradients and secondary flow is then diminished to characteristics of the resultant channel in zone (5) due to mixing either by turbulence shear layers (6) or lateral advection.

The resultant location and size of these zones as well as secondary circulation is dependent on confluence planform geometry, junction angle, bed morphology, and momentum flux ratio

$$M_r = \frac{\rho Q_2 U_2}{\rho Q_1 U_1} \tag{6}$$

where Q is flow discharge, U is mean velocity magnitude in a cross channel, and the subscripts 1 and 2 refer to the main and tributary channel (Riley and Rhoads, 2012).

For concordant beds, the resultant helical flow structure is dependent on the ratio of lateral momentum (Rhoads and Sukhodolov, 2008). If lateral momentum is comparable for both streams, i.e. symmetric confluence planforms (Figure 7A) with $M_r = 1$, two counter-rotating helical cells will form. However, if one stream has considerably more lateral momentum, i.e. a symmetric confluence with $M_r \neq 1$ or asymmetric confluences (Figure 7B) with unequal lateral momentum, one helical structure will form in the stronger channel flow and produce a localized area of axial acceleration in the other due to flow constriction (Bradbrook et al., 2000). For curved confluences (Figure 7C), duel cells are observed, however as tributary momentum increases, the helical cell of the curved channel is advected towards the inner bank until only one helical cell with the opposite rotation of

that of the curved channel is formed across the channel (Riley and Rhoads, 2012; Roberts, 2004).

When streamline curvature is returned to that of the main flow, the confluence secondary flow is diminished due to mixing. With increased helical flow, whether from the confluence or existing channel curvature, comes increased lateral advection and thus mixing, shortening the distance between the confluence and zone (5) than if solely by turbulent diffusion. Turbulent eddy structures and velocities ($\omega_z \neq 0$) along the turbulent shear layer, zone (6), are one to two orders of magnitude smaller than that of helical flow (Rhoads and Sukhodolov, 2001). For systems with more symmetric dual rotating helical cells, counter-rotating cells form similarly to a von Karman vortex street; for more asymmetrical flows, co-rotating large scale eddies form driven by a Kelvin-Helmholtz Instability (Constantinescu et al., 2011). These types of structures highlight the need for eddy resolving turbulence models to accurately model the mixing interface (Constantinescu et al., 2012).

In discordant beds, mixing is much stronger and alters helical flow formation (De Serres et al., 1999; Biron et al., 2004; Leite Ribeiro et al., 2012). Discordant beds are where one tributary stream is much shallower than the main channel and is a characteristic of many river junctions (Kennedy, 1984). Upon the river confluence, flow from the deeper channel is entrained towards that of the shallower, inducing a lateral motion of fluid and two layer shear flow. As a result, the turbulent shear zone (6) is widened, mixing greatly enhanced in the near vicinity of the confluence junction, and helical flow is disrupted (Bradbrook et al., 2000). This is especially true for confluences with low flow rates without curvature (Biron et al., 2004).

Helical flow formation is also strongly altered by bed topography. The secondary flow is dependent on the deflection and curvature of the streamlines. Existing topography, often induced by the helical flow itself, can steer flow direction and alter streamline curvature (Bradbrook et al., 2000). The downwelling of helical flow for both confluences and curvauture induces scour holes, however presence of an outer cell can mitigate this (Blanckaert and De Vriend, 2004; Blanckaert and Graf, 2004; Christensen et al., 1999). Thus at the confluence, flow is more inclined to downwell into the scour hole and align with the main

channel, either increasing or decrease flow deflection and helical flow (Bradbrook et al., 2000; Rhoads and Kenworthy, 1998). Similarly, areas of upwelling such as the inner bends, form point bars which also guide flow (Bradbrook et al., 2000; Dietrich, 1987).

Although sediment transport and bed morphology are relevant when speaking of these curved and confluent hydrodynamics, it is important to remember tidal flows are bi-directional and these long term processes may no longer be applicable. In tidal flow, stream confluences are also areas of stream bifurcation in a differing phase. Bifurcations in rivers are rare, inherently unstable, and thus have less consensual research than confluences as reviewed by Kleinhans et al. (2013). Yet recent three dimensional numerical studies have observed numerous similarities between flow planforms and secondary flow between bifurcations, curved flow, and confluences.

As the bifurcation induces flow curvature due to flow stagnation and increased water elevation at the bifurcation point, areas of flow separation form along the inside bends and enhance cross stream pressure gradients and thus counter rotating helical flow for both upstream channels (Bulle, 1926; Neary and Odgaard, 1993; Dargahi, 2004; Thomas et al., 2011; Hardy et al., 2011). However, like confluences, discordant beds limit such helical flow to immediate curvature and essentially dissipate it immediately downstream through mixing (Miori et al., 2012). Flow partitioning is a function of topographic steering, upstream channel curvature, and relative channel slope (Hardy et al., 2011; Miori et al., 2012). Outside of topographic steering, upstream curvature has the greatest effect; flow will be partitioned to the channel in the direction of lateral momentum induced by the centrifugal acceleration of the upstream curvature (Hardy et al., 2011; Thomas et al., 2011). In terms of topograhic steering, flows with larger curvature will have increased scour along the outside bend and deposition on the inside bend (Bulle, 1926; van der Mark and Mosselman, 2013). Like confluences, for tidal flows these long term processes have to be considered with hesitation.

Comparatively to river flow, few studies have been performed on tidal channel confluences and curvature. Some studies consist of inferences from bathymetric measurements or limited current measurements, and are not able to fully resolve secondary circulations (Kjerfve et al., 1979; Dronkers, 1996; Chant and Wilson, 1997; Ginsberg and Perillo, 1999;

Pierini et al., 2005; Ginsberg et al., 2009). Much of the basic flow structures are assumed and draw upon river literature. However with increased three dimensional field measurement and modeling techniques studies have observed helical or secondary circulation in tidal flows with momentum balance calculations (Seim and Gregg, 1997; Lacy and Monismith, 2001; Chant, 2002; Warner et al., 2002; Hench and Luettich Jr, 2003; Basdurak and Valle-Levinson, 2013; Buschman et al., 2013). Such studies consider freshwater river junctions or are mostly located in large scale stratified flow in estuarine entrances. Thus their focus is on the competition/cooperation between lateral convection, Coriolis, and/or baroclinic forcing. Lerczak and Rockwell Geyer (2004) categorize mechanisms driving lateral flows in tidal estuaries: cross channel variations in bathymetry, channel curvature, differential advection of density gradients, coriolis forcing, and stratification. While the first two have been discussed thoroughly, the latter three will not be discussed since it is not anticipated they will be relevant in the well-mixed, small-scale Rose Dhu environment.

Concerning sinuous tidal marsh channels, Seim et al. (2006) has observed energy concentration along the outer bends for both flood and ebb flows as in tidal river bends. These two dimensional field observations of the Satilla River in Coastal Georgia, found a marked difference in tidal constituent amplitudes and phases in bends compared to straight reaches. However, sediment deposition, or point bars on the inside bends are shifted seawards from an ebb-dominant flow as observed in other observations in South Carolina (Barwis, 1977). Most numerical studies have focused on large scale and long term salt marsh network formation and evolution rather than localized hydrodynamics. Such studies, as cataloged by Fagherazzi et al. (2012), are based on empirical topographic features, simplified/depth averaged hydrodynamic equations, or vegetative models which focus on flow of marsh platforms (Temmerman et al., 2003, 2005; D'Alpaos et al., 2007; Vandenbruwaene et al., 2012).

The previous review has highlighted the dependency and sensitivity of the distribution of axial momentum and hydrokinetic energy with regards to secondary circulation and lateral/vertical advection. Such accuracy and knowledge is required for accurate hydrokinetic energy assessments, turbine placement considerations, and predictions of energy extraction effects.

2.3 Assessing Tidal Hydrokinetic Power

The US Department of Energy (DOE) has developed a conceptual framework for assessing potential energy from marine hydrokientic resources (The National Research Council, 2013). The overall assessment process can be considered in three stages: theoretical; technical; and practical. The theoretical resource considers the hydrokinetic energy available for conversion; using measurement or model data the annual power available in the existing flow is determined. Turbine device specifics are not considered, however the general effects of extraction which can alter incoming/outgoing flow and available power may be included. The technical resource refines the theoretical assessment by considering device parameters such as turbine efficiencies. Finally, the practical resource considers real world constraints of turbine operation such as regulatory, environmental, and life cycle concerns. For the assessment of Rose Dhu Island, only the theoretical and a preliminary technical resource assessment is completed. Below, the precedent for tidal stream resource estimation is presented.

The theoretical kinetic energy in a flow field can be predicted for any arbitrary span of time once tidal constituents are obtained from measurements and numerical simulations. The theoretical formulation for the rate of kinetic energy transfer, or power, per unit area is

$$P_\rho = \frac{1}{2}\rho|U^3| \tag{7}$$

where P_ρ is also referred to as the kinetic power density, ρ is the mass fluid density, and U is the predicted velocity magnitude utilizing all available constituents.

It was classically assumed the maximum possible power a turbine could capture was 100% of the available power of the flow passing through; i.e. the integral of the kinetic power density over the swept area of the turbine, A_T. Lanchester (1915), Joukowsky (1920), and Betz (1920) first recognized this was incorrect in what is now known as Linear Momentum Actuator Disk Theory (LMADT). Because fluid flow is treated as a continuum, captured power estimates could not be made in isolation of the up and down stream effects of energy extraction. Using control volume analysis and the Bernoulli principle, it was found that

optimum turbine operation was to extract enough energy so that downstream wake velocity was 1/3 of the upstream flow. This would allow a maximum of 59% of the available power of the undisturbed flow field to be captured, a parameter known as the Betz Limit. Since, it has been commonplace to include a coefficient C_P in Equation (7) and for the Betz formulation $C_P = 0.59$. It is important to note that C_P refers to the maximum *available* power of the flow; it does not consider the efficiency in electrical conversion unique to each turbine design. For the preliminary technical resource assessment, a C_P is utilized according to turbine parameters.

Although the Betz Limit was originally formulated for wind turbines, it was assumed it could be utilized for free stream water turbines. Garrett and Cummins (2004), referred to as GC from now on, first recognized the inaccuracies of this and articulated the significance of induced head differentials by free stream water turbines in a channel. GC argued that if a turbine array across a channel retarded or blocked a proportion of the flow, water 'pile-up' would occur upstream of the turbines, induce a pressure gradient, and change resultant velocities. For wind and open ocean turbines, this 'pile-up' is diffused due to the relatively infinite expanse of the atmosphere and ocean. Re-deriving Betz's solution but within the confines of a channel, GC found the Betz Limit of $C_P = 16/27$ was increased by a factor

$$(1 - A_T/A_C)^{-2} \tag{8}$$

where A_C is the channel cross sectional area and A_T can be the combined area of numerous turbines congruent in a single fence (Garrett and Cummins, 2007). It can be observed if $A_C \to \infty$, C_P returns to the Betz limit for an infinite expanse. However, as $A_T \to A_C$, the solution's assumption of constant volume flux upstream and downstream is violated and the factor goes to infinity.

To quantify the available power for $A_T \to A_C$, GC applied Betz ideology to macro-channel scale in model referred to as GC05, arguing too many turbines or A_T will block or choke the flow in the channel (Garrett and Cummins, 2005). GC05 considered the simplified 1D problem of a tidal turbine array in a short channel connecting two large water bodies with the following assumptions: 1) A_T encompasses the entire channel cross section;

2) A_C does not vary with time, indicating changes in surface height are insignificant to depth; 3) u is uniform across A_C; 4) Tidal forcing is independent of energy extraction assuming basins are large and deep compared to channel; 5) Volume Flux, $Q = A(x)u(x,t)$, is constant in the along channel direction x indicating channel length is small compared to tidal wavelength. GC05 found analytically that the maximum average tidal stream power, P_{GC}, was proportional to both the kinetic energy and peak tidal pressure head in the equation

$$P_{GC} = \gamma \rho g a Q_{max} \tag{9}$$

and to account for additional constituents (a_1, a_2,...) a multiplying factor is employed

$$1 + \frac{9}{16}(r_1^2 + r_2^2 + ...) \tag{10}$$

where

$$r_1 = \frac{a_1}{a}, \quad r_2 = \frac{a_2}{a}, \ ... \tag{11}$$

and a is maximum predicted water level amplitude, Q_{max} is the maximum corresponding volume flux, and γ is a numerically determined parameter mitigating the effects of frictional drag, flow separation, and temporal acceleration.

It was shown by GC05 a γ value of 0.22 can be used for any system with an accuracy within 10%. The validity of Equation (9) was further proved by Sutherland et al. (2007) through numerical modeling of channel-wide energy extraction; GC05 power estimates only differed from numerical results within 10%. However, Sutherland et al. (2007) also found for areas where flow could be diverted, such as split channels, GC05 overestimated up to 50%. Flow was bypassing the sub-channel with the array into another, thus A_T could no longer be considered all encompassing and Assumption #1 was violated.

It was generalized that the extent of cross channel occupancy could have two immediate hydrodynamic effects: 1) If only partially blocked, the 'pile-up' of water upstream of the turbines would divert flow and thus energy to the unblocked section; 2) If fully blocked, upstream would be a uniform flow field with no diverted energy. Thus, GC (2004) argued the most effective placement of turbines was a uniform distribution across a channel .

GC (2007) recognized the impracticality of installing a channel wide tidal turbine array and expanded their previous analysis, referred to as GC07, to include individual turbines and partial arrays in a channel. Analytically it was found the resultant maximum power, P_{max} was a balance between the positive and negative effects of increased pressure head. It was found that as $A_T/A_C \to 1$, only 1/3 of the total channel extraction P_{GC} mentioned in Equation (9) could be extracted due to intense flow diversion and lateral mixing. As $A_T/A_C \to 0$, or singular turbines, such efficiency increased to 2/3, due to the minimal flow disruption and became the Betz limit. It is important to note that as A_T/A_C increases, the actual available power still increases; it is the efficiency that declines. Thus, GC argue there exists an optimal number of individual turbine fences, N, that can be installed with enough space between them to avoid mixing, to provide the same power provided by a uniform fence across the channel, where A_T refers to individual turbine fences.

Vennell (2010) argued the formulations from GC07 were incorrect due to the combination of contrary assumptions from the two theories. GC07 theory was based on assumptions similar to Betz: the optimum tuned turbine provides a downstream wake velocity 1/3 of its original. This was made with the assumption that the free stream velocity bypassing the turbine is unaffected. GC05 theory argues the drag from the turbine array changes the drag coefficient for the entire system and thus free stream flow. Thus Vennell (2010) argued the optimal tuning of 1/3 and resultant power estimates may not be correct.

Through numerical modeling of energy extraction, with turbines tuned to downstream velocities other than 1/3 the upstream, Vennell (2010) was able to show higher energy extraction than that predicted by GC07. In addition, Kim et al. (2012) and Vennell (2013) showed if turbines are optimally tuned, the most efficient partial turbine distribution constitutes most of the channel width, contrary to GC07. Most strikingly, Vennell (2012b,a) also argues, there is no optimum N as suggested by GC07 but rather the most efficient use is densely packing turbines across the maximum extent of the cross section in an optimum number of rows along the channel. From these results, Vennell (2013) has shown for given circumstances tidal turbine arrays can capture power above the Betz Limit of 59%.

Although Vennell's model allows for more extractable energy, its universality is limited

since numerically modeled and tuned for specific locations. In addition, 'turbine tuning' requires variable turbine operation in time, costing additional resources compared to the fixed rotation in GC05 + GC07. As a result, GC05 has become a common method for available tidal power assessment for large inlets (Sutherland et al., 2007; Karsten et al., 2008; Brooks, 2011). It was also utilized used for the tidal energy assessment for the entire US coastline (Haas, 2011; Defne et al., 2012b).

It is important to note however for these energy assessments, GC05 was applied at the mouths of large estuaries and inlets. On an estuary/ocean scale, the assumptions of two bodies connected by a short channel of GC05 are reasonable. However, while the estimate of available power may be correct for the whole estuary, as Sutherland et al. (2007) showed, it is not correct for the local branching sub-channels. In addition, for marshes and shallow channels, intertidal storage invalidates Assumption 2 and lateral momentum transfer in curved channels invalidates Assumption 3. Thus the kinetic power density still is used in lieu of GC05 in some cases , particularly for complex geometries (Blunden and Bahaj, 2006; Chen et al., 2003; Carballo et al., 2009; Iglesias et al., 2012; Polagye and Bedard, 2006).

Recent attempts have been made to expand the work of GC to more complex geometries. Blanchfield et al. (2008), modified Equation (9) to model a closed bay and open ocean, which was successfully verified by Yang et al. (2013) numerically. Atwater and Lawrence (2010) and Polagye and Malte (2011) have numerically solved simplified differential equations similar to GC05, for split channels. Treating tidal networks like electrical circuits, Polagye and Malte (2011) found the most power efficient turbine deployment in networks, was equally across sub-channels or before bifurcation due to flow diversion, and closest to the open ocean if in a serial network of constrictions due to natural energy loss by bottom friction. Similar results were found from numerical models of tidal arrays near theoretical headlands (Draper et al., 2013). However, while such tools are useful for academic purposes, for actual assessments of complex geometries and networks, as acknowledged by Polagye and Malte (2011), numerical modeling is needed to quantify extraction effects.

Few studies have focused on tidal distortion, frequently found in tidal flows in wetlands, on theoretical power output. Using a numerical model, Neill et al. (2014) related distortion

in tidal currents and kinetic power density calculations: a 30% asymmetry in velocity led to a 100 % asymmetry in power. Polagye and Thomson (2013b) has recognized the influence of tidal distortion on turbine operation by coining distortion parameters

$$P_{\rho_{dist}} = \frac{\overline{P_{\rho_{ebb}}}}{\overline{P_{\rho\,flood}}} \tag{12}$$

$$\theta_{dist} = \overline{\theta_{flood}} - \overline{\theta_{ebb}} - 180^{\circ} \tag{13}$$

where $P_{\rho_{dist}}$ is the mean kinetic power asymmetry, $\overline{P_\rho}$ is the mean kinetic energy density over a tidal phase, θ_{dist} is the directional asymmetry between ebb and flood, relative to bidirectional currents, and $\overline{\theta}$ is the mean direction over a tidal phase. Adcock and Draper (2014) modeled the effects of extraction on asymmetry in a channel, and found if a turbine array provides a uniform drag resistance to a channel, even overtides are reduced and the flow becomes more symmetric.

In practice, various methods have been used to predict theoretical power assessments. Most at least have utilized the kinetic power density, P_ρ, as a proxy for theoretical power. P_ρ, calculated from numerical model results, has been used in the following assessments of: Cook Inlet, Alaska; Orkney, United Kingdom; Jiangsu Coast, China; Faro Channel, Portugal; New Jersey, USA; Kennebec River, Maine; Malaysia; Rio de Muros, Spain; and Kinmen Island, Taiwan; (Lanerolle et al., 2012; Neill et al., 2014; Zhang et al., 2013; Pacheco et al., 2014; Tang et al., 2014; Lim and Koh, 2010; Carballo et al., 2009; Chen et al., 2013). Some assessments have also used GC07 such as the assessment of the Kennebec River, Maine and Minas Passage, Canada (Brooks, 2011; Karsten et al., 2008).

The national assessment of the United States estimates power output using P_ρ and GC05, calculated from numerical model results as well (Haas, 2011; Defne et al., 2012b). The RITE site in New York, New York used long term measurements alone and found P_ρ to be an order of magnitude larger than those predicted by the national database (Gunawan et al., 2014). Stevens et al. (2012) and Polagye and Thomson (2013b) also used long term measurements for calculations of p of the Karori Rip, New Zealand and Pugent Sound, Washington. Draper et al. (2010) has utilized GC05 to assess Pentalnd Firth, UK; however, Adcock et al. (2013) has assessed 50% less maximum extractable power using Vennel 2010-13

considering the that the degree of extraction requires rows of turbines.

Other theoretical assessments have directly incorporated energy extraction directly into numerical models as line (turbine arrays) or point (individual turbines) momentum sinks to observe the changes in available power for: The Anglesey Skerries, UK; Bay of Fundy, Canada; Ria de Ribadeo, Spain; Tory Channel, New Zealand; Canoochee River, GA; Pentland Firth, UK; and Bristol Channel, UK. (Serhadlıoğlu et al., 2013; Karsten et al., 2013; Ramos et al., 2014; Plew and Stevens, 2013; Defne et al., 2011; Adcock et al., 2013; Ahmadian and Falconer, 2012). Serhadlıoğlu et al. (2013) and Plew and Stevens (2013) highlight the effect of flow diversion past partial arrays: reduced velocities up and down stream and increased velocities adjacent in the cross stream direction. Furthermore, Ahmadian and Falconer (2012) showed that the best location for array installation was not the locations with high undisturbed P_ρ but in unexpected locations due to flow diversion, highlighting the importance of evaluating near and far field effects of extraction.

2.4 Motivation for Present Study

Tidal energy assessments require accurate predictions of hydrodynamics with and without energy extraction. Most assessments to date have been for broad, deep, and singular tidal channels on the estuarine scale. Such systems lend themselves well to generalized assumptions, and as a result extraction effects and power predictions are better understood. No studies exist for estuaries with extensive tidal marsh environments; the unique features of channel intertidal storage, curvature, and confluence are unknown. This study aims to establish the methodology for tidal stream resource assessments under such conditions.

CHAPTER III

TIDAL DATA ACQUISITION FOR ROSE DHU ISLAND, GA

For the energy assessment, two types of data are utilized: field data acquired from boat based hydrodynamic measurements; and simulation data pulled from a numerical model simulation by Bomminayuni et al. (2012), calibrated with the measurements. This chapter details the acquisition and processing of the field data utilized for the presented analysis. Descriptions of the campaigns that acquired the data are presented first, and processing techniques are outlined second.

3.1 Field Campaigns

Numerous boat-based field campaigns were executed in the immediate vicinity of Rose Dhu Island from 2010-2014. The campaigns are categorized into three types delineated by their objectives: spatial reconnaissance; hydrodynamic analysis; and prototype testing. The spatial reconnaissance campaign in October 2010, was the first field campaign aimed at identifying if and where areas of high hydrokinetic energy exist. Once areas of interest were identified from the first campaigns, hydrodynamic analysis campaigns, held in November-December 2011 and the latter portion of June 2014, consisted of transect measurements of water surface heights, current velocities, and channel volume fluxes to characterize local and estuarine hydrodynamics. These measurements were also utilized to calibrate the numerical model simulations by Bomminayuni et al. (2012). Measurements and model output were then used to identify areas of persistent hydrokinetic energy and a turbine rotor prototype was tested at these locations to obtain mechanical turbine efficiency curves in the June 2014 campaign. The following section outlines the details of the field campaigns by date after a description of the equipment used by all campaigns.

3.1.1 Field Equipment

All measurements were taken aboard a 24 foot pontoon boat with a moon pool near the bow for deploying the rotor and/or instrumentation as shown in Figure 8. The boat, typically dry-docked when not-in use, was launched into the water daily either from the Rodney J. Hall Boat Ramp (2010-2011) or the Bells Landing Boat Ramp (2014) pictured in Figure 9. For the June 2014 deployments, between deployments each day, the boat remained floating and was docked at a nearby residential dock at 83 Rio Road, Savannah, GA also pictured in Figure 9 until the last day of deployment.

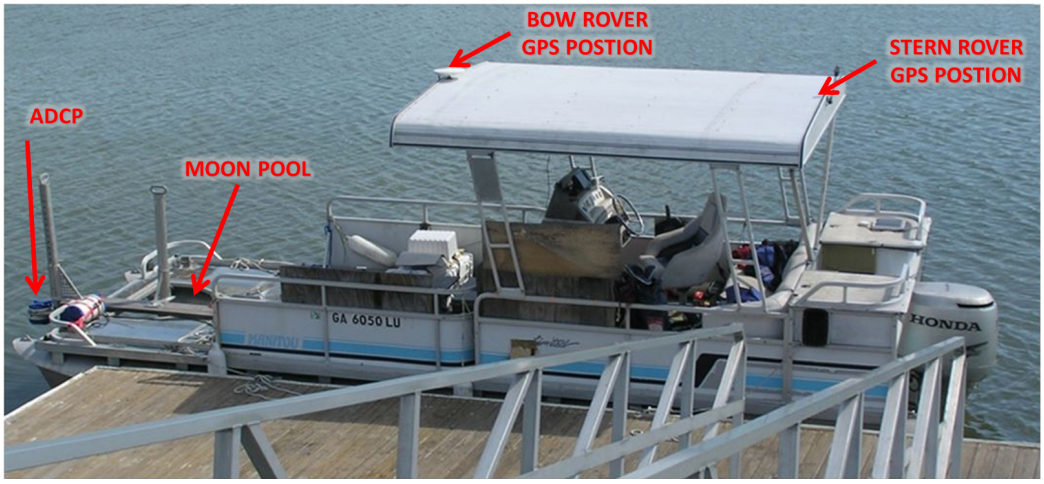

Figure 8: Image of docked field boat. Instrumentation identified.

Current measurements were taken using a downward facing RD Instruments Express Sentinel Self-Contained Acoustic Doppler Current Profiler (ADCP) mounted off the bow of the boat as shown in Figure 8. The ADCP housed a 4-beam convex transducer configuration with a beam angle of 20°, providing a maximum horizontal sample volume footprint of about 4.6 m at the sea bed in a depth of 10 m. Current velocities were measured along the water column with the first cell a blanking distance below the surface and the remaining water column was divided into vertical bins. The instrument measured, averaged, and recorded the current readings between beams within each bin. Exact bin widths, depths, and blanking distances of the ADCP were dependent on the campaign objective and are specified in the specific campaign sections and Table 1. The ADCP recorded directly onto a laptop

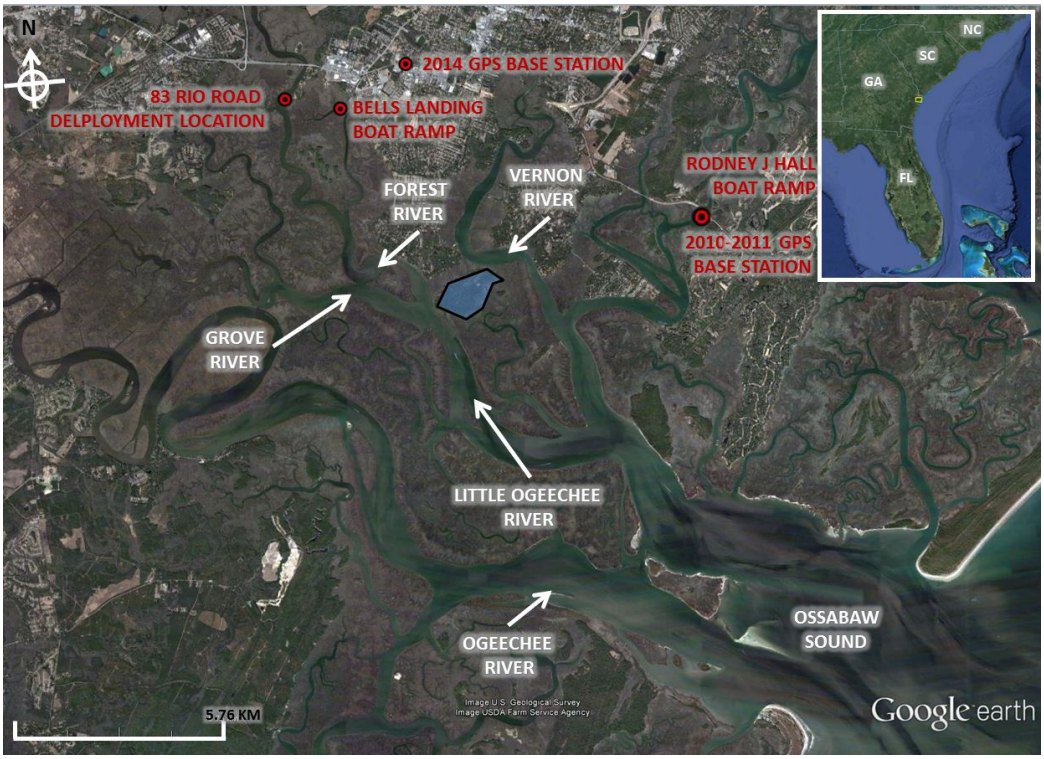

Figure 9: Map of Ogeechee Estuary with relevant locations for field campaign operations. Blue area marks Rose Dhu Island. Inset Image: Map of Southeastern United States for geographic reference.

computer synced to a handheld GPS in local time, using the software *WinRiver II*. ADCP velocity data collected during the boat based surveys were synchronized with the position data provided by a continuous global positioning system (GPS) to provide coordinates of the ADCP measurements.

The GPS system, employed to determine the x-y-z positioning and orientation of the survey vessel as well as water levels consisted of either one or two boat mounted dual frequency receivers along with another receiver on land to act as a fixed base station. Locations of boat-mounted rover receivers are shown in Figure 8. Base stations identified in Figure 9, were used to reduce time dependent position errors from the roving receivers. Ashtech brand GPS receivers used include the Z-12, Z-Surveyor, and Proflex 500 models. The Z-12 receiver recorded internally, the Z-Surveyor recorded either internally or to an on-board computer, and the Proflex models recorded onto a USB stick. Specific GPS base and rover parameters are summarized in Table 1.

Table 1: Instrumentation specifics for field campaigns.

Date	GPS Base Station		GPS Rovers			ADCP		
	Receiver	Sampling Rate [Hz]	Location	Receiver	Sampling Rate [Hz]	Bin Size [m]	Blank Distance [m]	Sampling Rate [Hz]
10/19/2010	Z-12	0.1	Bow	Z-Surveyor	5	0.5	0.91	1.92
10/20/2010	Z-12	0.1	Bow	Z-Surveyor	5	0.5	0.91	1.92
11/27/2011	Proflex	0.1	Bow	Proflex	2	0.5	0.91	1.92
12/22/2011	Proflex	0.1	Bow	Proflex	2	0.5	0.91	1.92
06/14/2014	Proflex	0.1	Bow Stern	Proflex Z-Surveyor	2	0.25	0.81	0.78
06/15/2014	Proflex	0.1	Bow Stern	Proflex Z-Surveyor	2	0.25	0.81	0.78
06/16/2014	Proflex	0.1	Bow Stern	Proflex Z-Surveyor	2	0.25	0.81	0.78
06/17/2014	Proflex	0.1	Bow Stern	Proflex Z-Surveyor	2	0.25	0.59	0.78
06/18/2014	Proflex	0.1	Bow	Proflex	2	0.25	0.59	0.78

3.1.2 October 2010

Two field campaigns were carried out on October 19 and October 20, 2010 to serve as a spatial reconnaissance of current velocities. The main purpose of this surveying was to provide a general picture of the velocities, and thus available hydrokinetic energy in the flow surrounding Rose Dhu to determine if energy extraction is feasible, and if so what areas merit further attention. To measure peak currents, the boat based GPS-ADCP measurements occurred during a peak spring tide.

Until this point, no measurements or model information for the Rose Dhu area were available, thus the timing of peak currents were estimated using NOAA tidal predictions of the nearby Coffee Bluff Station, pictured in Figure 9. Since only water levels were provided, it was estimated peak currents occurred at some point between high and low tide assuming some degree of wave reflection in the estuary. The Coffee Bluff water level predictions for October 19-20, 2010 are pictured in Figure 10.

A portion of the east channel, part of the Little Ogeechee River, was measured on the 19th while the west, part of the Vernon River, was measured on the following day as indicated in Figure 11. Each day included about 8 hr of surveying: 5 hr for observing the peak ebb flow in the morning and 3 hr for observing the peak flood in the afternoon,

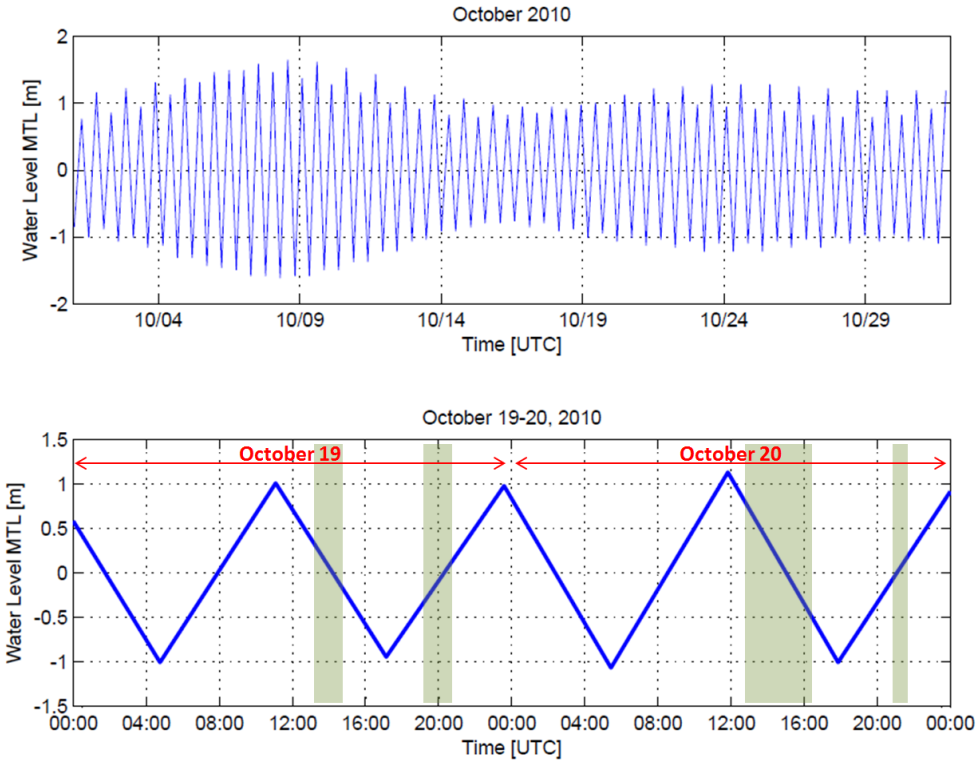

Figure 10: Predictions of water levels for NOAA Coffee Bluff subordinate station for October field campaign. *A)* Water levels for the month of October highlighting spring tide. *B)* Water levels and field measurement times highlighted in green.

limited due to lack of daylight. The surveying strategy, for both flood and ebb tides on each day, consisted of traveling up the channel and zig-zagging between predetermined waypoints on either bank. The waypoints, situated approximately 500m apart, created non-nominal cross-channel transects. Once all predetermined transects were completed, additional smaller zig-zags were made along channel banks for as long as time permitted, resulting in ebb having more measurements than flood. These ancillary measurements focused on the channel banks adjacent to Rose Dhu Island due to the locations logistical importance for a potential tidal turbine installation.

The main purpose of this surveying was to provide a general picture of the available hydrokinetic energy as well as provide water level measurements for numerical model validation as discussed in Chapter IV. This strategy could be used to also validate the spatial distribution of current velocities and hydrokinetic energy within a tidal phase if the distribution is relatively constant within the phase. But because the measurements across the

domain are not taken simultaneously (i.e. the boat cannot be at two places at once), the measurements in total cannot be considered as a snapshot of the spatial distribution at a point in time if the flow is highly variable.

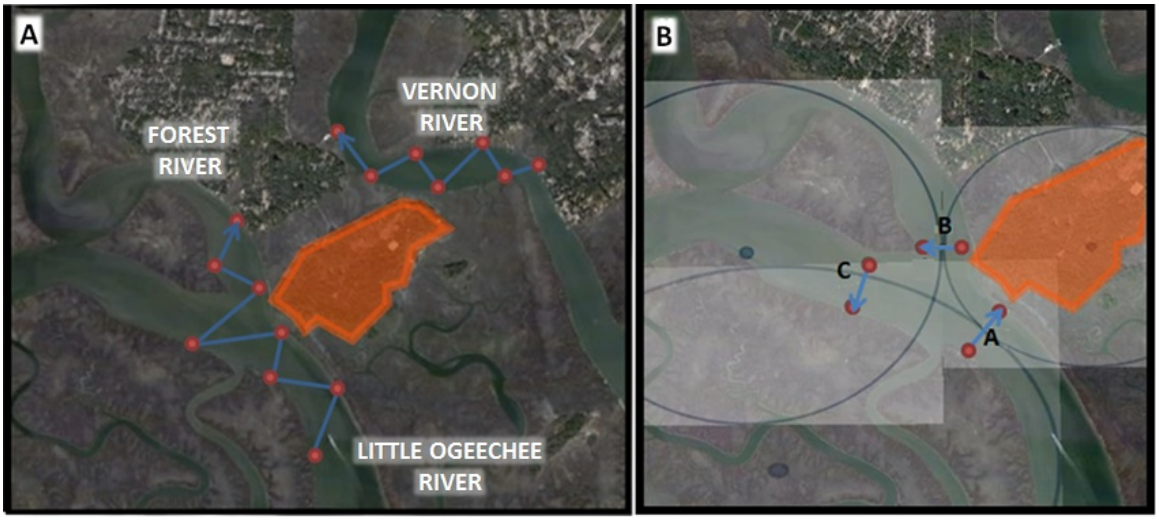

Figure 11: Spatial surveying strategies. Red dots represent waypoints and blue arrows represent planned measured paths. Rose Dhu Island depicted in orange. *A)* Spatial Reconnaissance for October 2010 Campaign. *B)* Repeated transect measurements for hydrodynamic analysis for November-December 2011 campaigns. Transects are labeled by letters. Blue circles used to determine nominal cross sections of channel curvature. Satellite imagery courtesy of Google Earth 2013

3.1.3 November - December 2011

The field campaigns on November 27 and December 22, 2011 were designed to gain further quantitative insight into the temporal evolution of the flow and the hydrodynamic differences between the ebb and flood tidal flows surrounding Rose Dhu. Boat based ADCP measurements, as in the first strategy were taken along three predetermined transects multiple times as shown in Figure 11B. Three transects were selected and positioned to gain further insight into the channel confluence. Transect A was positioned in proximity to an area of high currents observed in the October 2010 campaign as discussed in Chapter V.

The transects are oriented perpendicular to the curvature of the channels to facilitate the decomposition of current velocities into cross channel and axial components for volume flux calculations and analysis of the localized hydrodynamics. Calculation of volume flux

is outlined in Section 3.2.5. However more importantly, in these campaigns as compared to October 2010, fewer transects are charted over a smaller spatial domain, allowing for individual transects to be measured at a higher temporal frequency throughout the tidal cycle to better resolve the evolution of the flow in the channel. Each transect took approximately 5-8 minutes to traverse, all three in 30 minutes. This is a short enough timescale to assume little temporal evolution across a measured transect or set of transects.

As in the October 2010 campaign, Coffee Bluff Station water level predictions were used to identify periods of spring tides and peak tidal currents. Predictions, and measurement times are presented in Figure 12. Again, the number of measurements was limited by daylight and gasoline constraints.

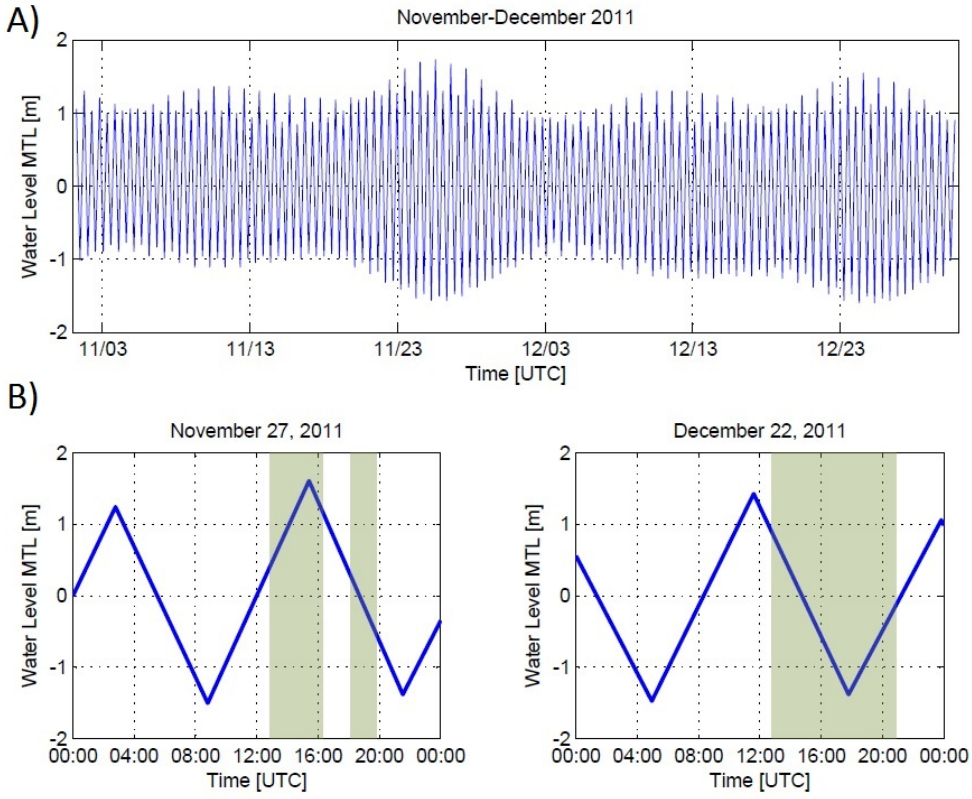

Figure 12: Predictions of Water Levels for NOAA Coffee Bluff Subordinate Station for November-December 2011 campaign. *A)* Water levels for the months of November and December highlighting spring tide. *B)* Water levels and field measurement times highlighted in green.

3.1.4 June 14-16, 2014

The June 2014 field campaigns consisted of two parts: I) Rotor performance in-situ testing from June 14-16 and II) current and water level measurements across pre-determined transects for further analysis of the hydrodynamics on June 17-18. A rotor prototype was tested at hydrokinetic hotspots predicted by the numerical model and measurements prior to 2014. The rotor, sans electrical conversion, was tested through a mechanical brake disk system developed by Dr. Thorsten Stoesser and Tom Harries at Cardiff University. In this section, the logistics of the testing is discussed. Additional information and fundamentals for turbine testing are presented in Chapter VI.

Rotor testing was accomplished through boat based installations, which advantageously allowed assessment at multiple locations with one installation and does not require permitting. To perform these open water tests, the rotor prototype and experimental instrumentation was rigged to the same vessel used for collecting the field measurements. In addition, GPS and ADCP tidal stream velocity measurements of the ambient flow were taken simultaneously to define the inflow characteristics. First, this section will outline the selection of testing timing and locales, then the deployment procedure is discussed.

3.1.4.1 Measurement Timing and Location

The area near Transect A in Figure 11B was deemed to have the highest current velocities and calculated power densities from the previous measurements and model analysis discussed in Chapter VI. Thus, this was the general area of interest for both rotor testing and hydrodynamic analysis. Available numerical model output, calibrated using the previously discussed measurements and further discussed in Chapter IV, from this area was used to predict the timing of peak currents. The timing of the measurements coincide with a spring tidal period. In addition to this criteria, it was necessary for the peak tidal currents to occur during daylight hours with ample time to deploy/set-up and take down instrumentation. The depth averaged velocity predictions at the center of Transect A shown in Figure 11B can be seen in Figure 13.

Analysis in Chapter IV shows the tidal currents near Rose Dhu to be highly asymmetric;

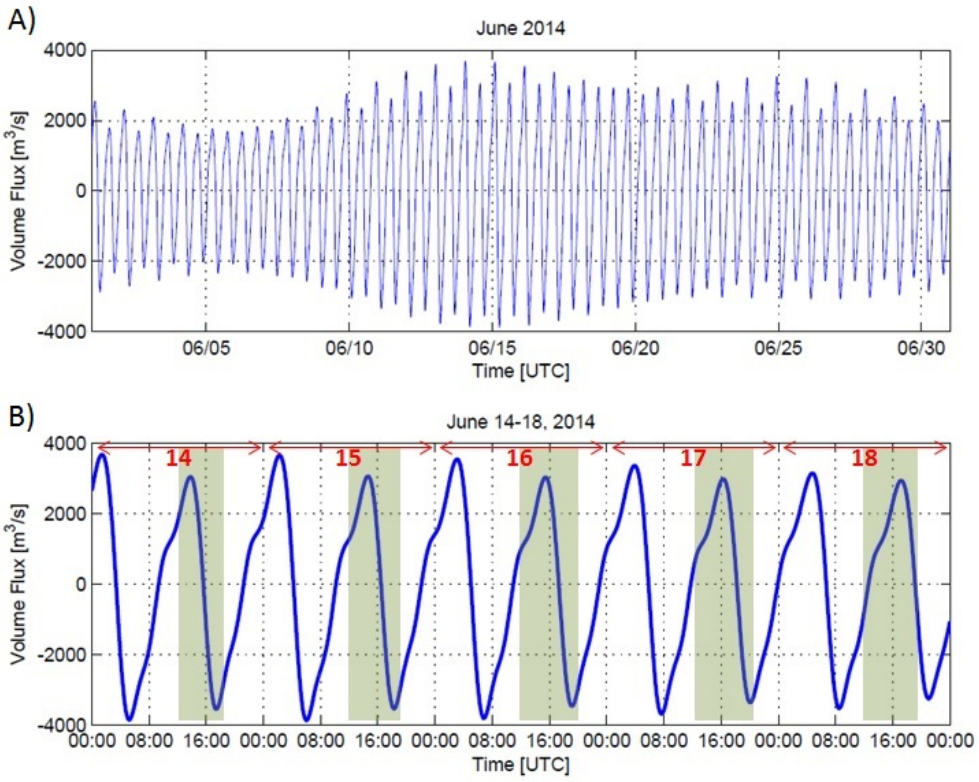

Figure 13: Model predictions of volume fluxes for Transect A. *A)* Predictions for the month of June. *B)* Predictions for chosen field days. Water levels and field measurement times highlighted in green.

the peak ebb current occurs shortly after the peak flood, whereas the peak flood occurs much longer after peak ebb as shown in Figure 13. This was advantageous for testing the turbine rotor; there was little down time between the testing of the rotor between peak flood and ebb and both occurred during daylight hours. Thus it was desired to field test on a day where the flood to ebb transition occurred during the day. Another important feature, perhaps the most crucial, was the current speeds. High current speed were desired. This was done to ensure that the rotor, with a minimum cut-in current speed of operation, would spin and produce data. Ultimately out of the 5 days of experimentation the first three June 14-16, 2014 were chosen because they had the highest peak current velocities.

The location of the turbine rotor testing was identified through previous field measurements. Because it has been observed areas of the highest velocities, or 'hotspots' change location between peak ebb and flood tides, hotspots were identified for each. Velocity

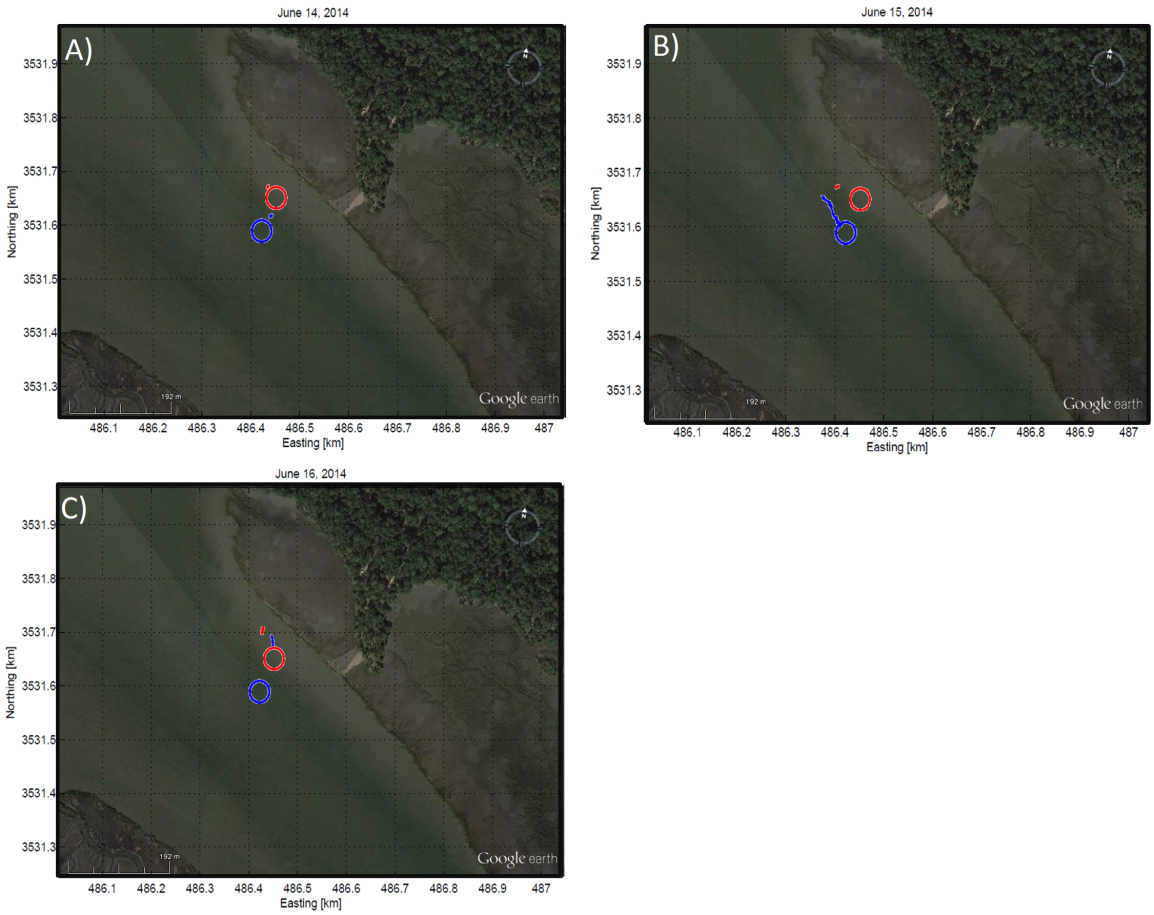

Figure 14: Map of rotor testing locations for June 14-16,2014. Red lines and circles are associated with flood testing; blue lines and circles associated with ebb. Circles are planned testing locations; lines are actual GPS positionings during testing.

current profiles taken across Transect A during peak flood and ebb tides from the 2011 deployments were used. The chosen areas of interest are plotted in Figure 14. Figure 14 also shows where the turbine was deployed for every day. Some deviations are observed from the planned locations due to on-site observations of faster currents. Also, a degree of drift is observed as well. During testing the boat was to remain stationary and anchored. However in some instances, one of the anchors became dislodged and the boat slowly drifted.

3.1.4.2 Rotor Deployment

Construction and assembly of the rotor and its housing occurred aboard the boat. The boat previously housed a 12 foot tall tripod and winch used for vibracoring that was used for raising and lower the rotor and shaft assembly through the moon pool. The testing of

the turbine imposed various design considerations and restrictions considered in developing the unique design of the detachable housing. A conceptual and structurally sound design, pictured in Figure 15A was completed in the 3D modeling program *Solidworks*. The assembly was manufactured in house and completed construction can be seen in Figure 15B-C. In this section, first the initial construction of the rotor and its housing is outlined; steps performed once in the beginning of deployment. Then the deployment procedure, which occurred twice a day, is outlined.

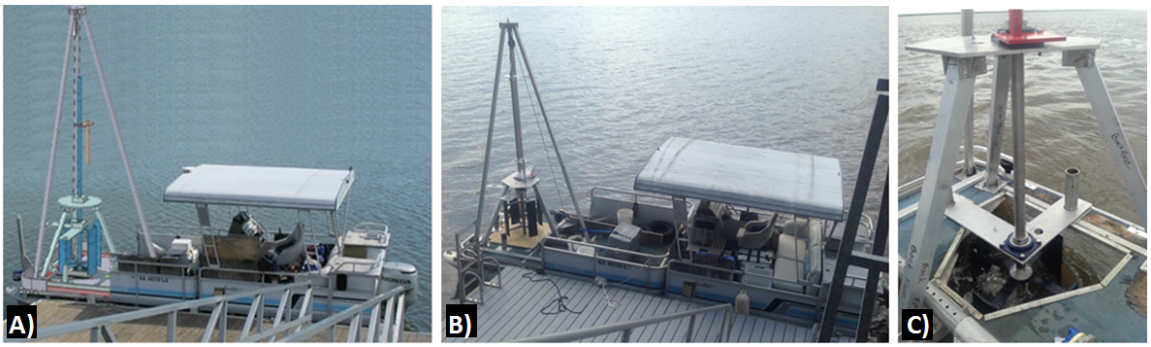

Figure 15: Structural housing for rotor. *A)*: Artistic rendering of structural housing design *B)*: Actual construction of structural rotor housing *C)*: Close up of structural support (small tripod and L-Plate) with spinning rotor

Initial Assembly

Before the boat was launched, a large tripod was erected over the moon pool support the rotor as shown in Figure 16. The large tripod had 1/2 in stainless steel pin supports and an aluminum frame. After the boat was launched and tied to a dock, the shaft and small tripod were erected. The aluminum small tripod was designed to support the weight of rotor and stainless steel shaft, support the power take off (PTO) unit, and resist torque induced by the rotor and PTO. First the disk brake, shown in Figure 16, was placed and locked onto the shaft with the gold key piece. Then the shackle was attached to the same end, with the winch cable looped through the shackle. The winch was then turned on, and the shaft was raised until it was directly under the tripod cap piece and raised approximately 6 inches above the plywood moon pool cover.

The small tripod table, shown in Figure 17, was then slid over the shaft through the

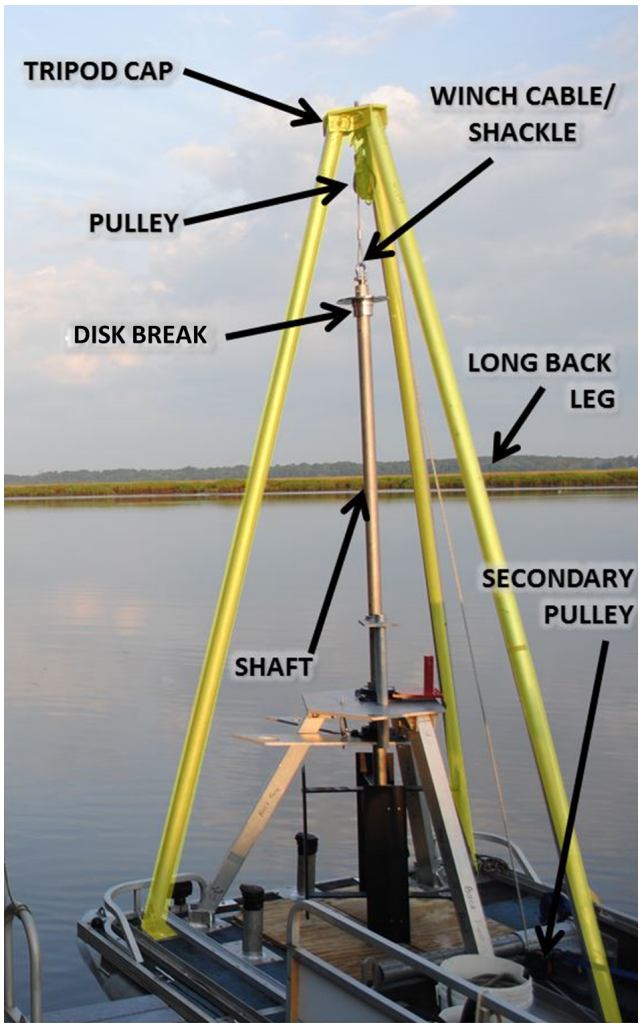

Figure 16: Image of large tripod and shaft assembly. Yellow highlights large tripod.

blue bearings and raised to about 5 ft. The bearings and red PTO piece were pre-attached to the small tripod table. Here the bearings were locked using a hex key so the shaft held the weight of the plate. Once the plate was oriented correctly, the tops of the $\sim$ 4 ft long square channel legs, were pinned into the feet on the table and left dangling using 1/2 in diameter stainless steel pins. The bearing was unlocked and the plate was lowered slowly by hand. The legs were placed in the feet on the deck and pinned. At this point the weight of the small tripod is supporting itself and the shaft is supported by the large tripod and winch cable assembly which is turned off. To keep the shaft from spinning and twisting the winch cable, an aluminum torque arm is slid through the torque arm hole and attached to the shaft using a hex key as shown in Figure 17. The assembly is shown in Figure 17.

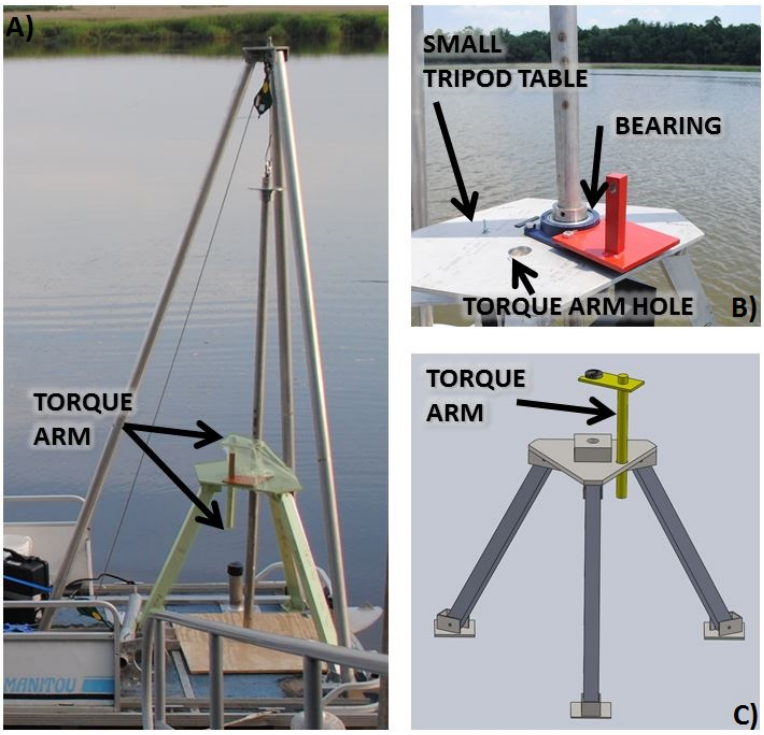

Figure 17: Image of small tripod assembly. *A)* Image of small tripod, highlighted in green. Note, top covered in plastic wrap for overnight protection of bearing. *B)* Close up of bearing and small tripod table. Red piece pre-attached to bearing, part of PTO. *C)* Model of Torque arm in yellow.

An aluminum L shaped Plate is then installed. The L-Plate, shown in Figure 18, is slid over the shaft and raised to the bottom of the small tripod table. The bearings are then locked with a hex key and the plate is attached to the table by carabiner for a fail safe as shown in Figure 18.

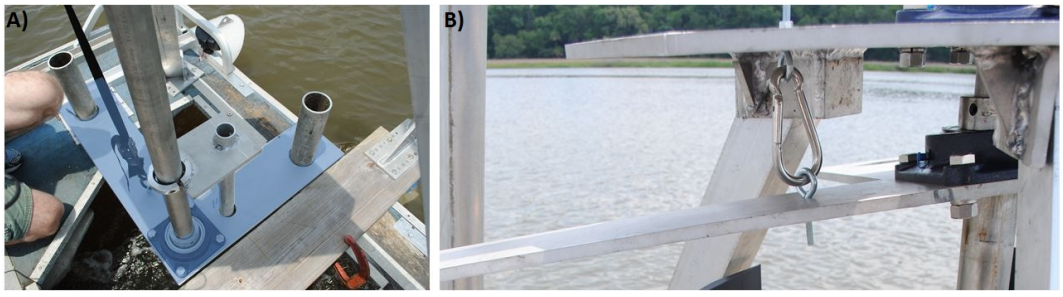

Figure 18: Images of L Plate. *A)* Top view of L-Plate highlighted in blue. *B)* Image of L-plate suspended by carabiner

The rotor is then constructed about the shaft. At the bottom end of the shaft, there are two holes drilled through the shaft. One is approximately 70 cm from the bottom and the other is near the bottom. At each hole, two half circle spoke hubs are attached. First a pin is gently hammered through the center hole and then bolted together with long screws. The rotor spokes are then slid into each hub and bolted to the hub. The blades, flat edge facing the shaft are then screwed in. Once assembly of the rotor is complete, the shaft is lowered so it is resting on the plywood as shown in Figure 19.

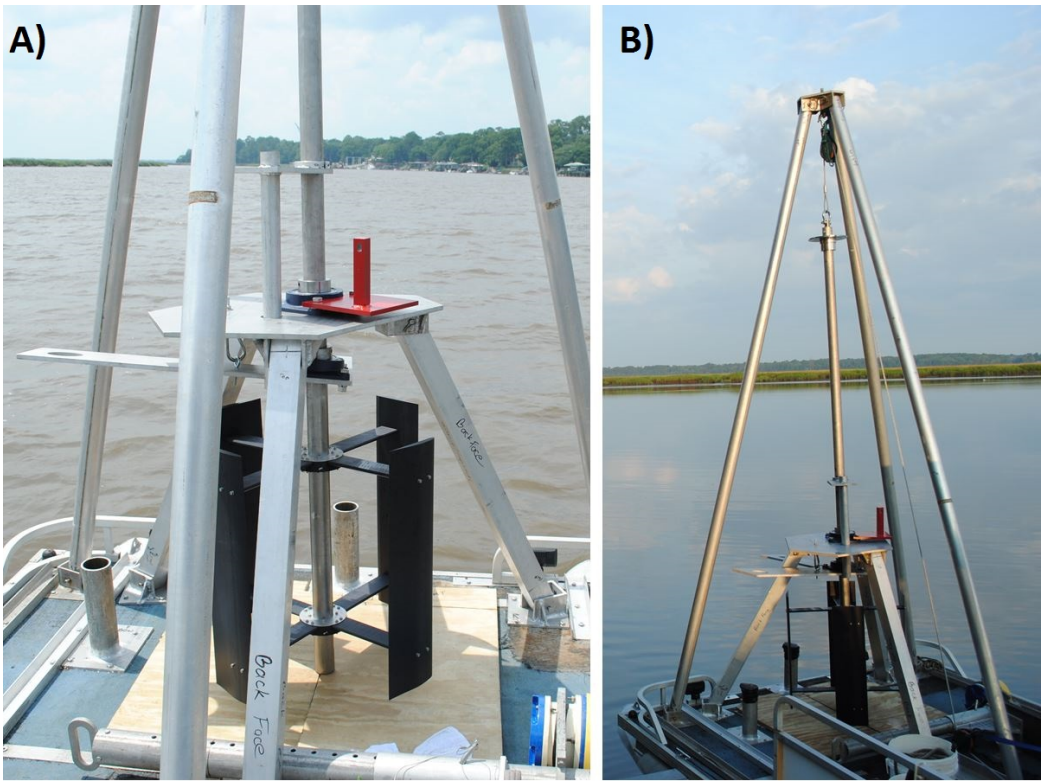

Figure 19: Images of constructed large tripod, small tripod, L-plate, and rotor at rest.

Deployment Assembly

The following steps, outline the boat anchoring, submersion of the turbine as well as the installation of instrumentation. The set of steps were completed twice a day at the hotspot location, once for flood deployment and once for ebb.

Either after leaving the dock or before an afternoon deployment, two GPS were installed on the roof as depicted in Figure 8, turned on, and began recording. Once the boat was

driven to the hotspot, the boat was oriented and anchored so that the bow faced the oncoming current. An anchor was thrown overboard on either the starboard or port side of the boat and tied off. The boat was then repositioned so that the rope did not cross under the bow and still faced the oncoming current. A second anchor was thrown on the opposite side of the boat, and tightened until the boat faced the oncoming current. This step is most easily performed when the current is strong or moderate. However, one needs to plan for enough time to deploy the turbine before peak currents passed.

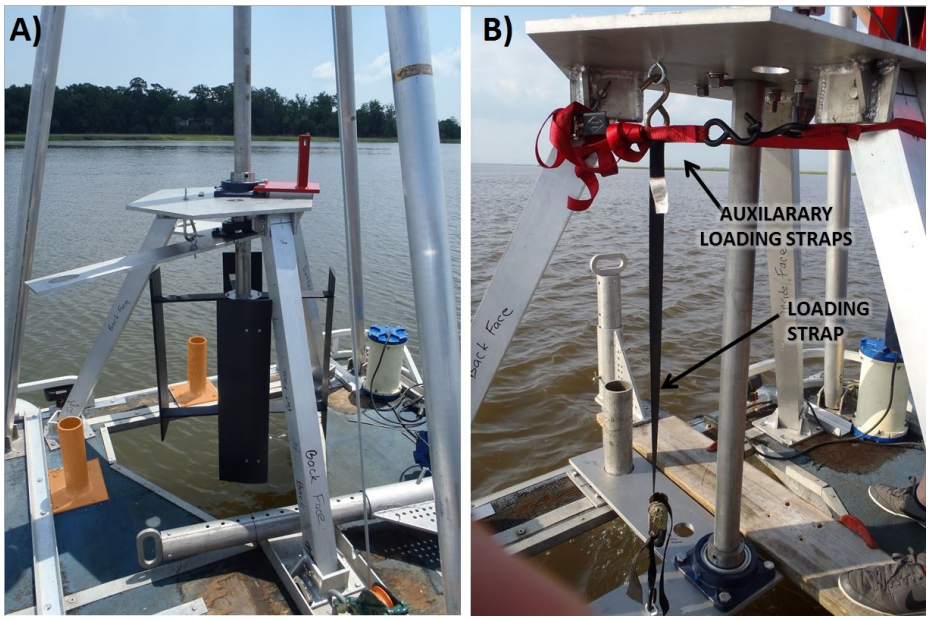

Figure 20: Rotor lowering. *A)* Plywood boards removed. Cylindrical sleeves highlighted in orange. *B)* Rotor lowered to full extent with straps attached and L-Plate fitted over sleeves.

The rotor was then prepared for lowering. The plywood boards are removed from under the rotor as shown in Figure 20. The top bearing on the small tripod plate is loosened with a hex key while the bearing on the L-Plate was tightened. The carabiner is unhooked. While the shaft bears the weight of the L-Plate, someone is spotting it. The rotor is lowered with the winch. Just as the rotor is about to hit the water surface, the winch is stopped. The L-Plate is oriented to fit over the two cylindrical sleeves attached to the deck. In addition the torque arm is repositioned so it has more room to drop. Once the L-Plate is flush against the sleeve footing, the winch is stopped. The bottom bearing is loosened with

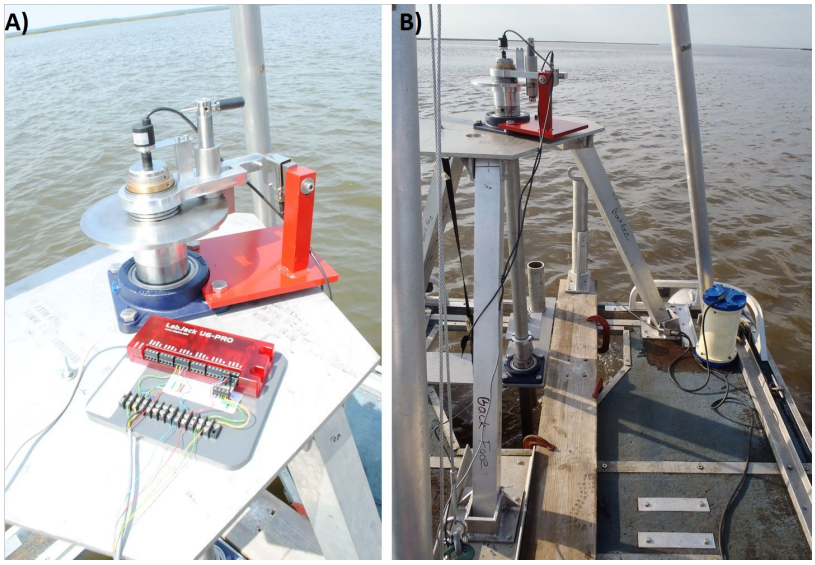

Figure 21: *A)* PTO assembly. *B)* Finished rotor/ADCP assembly prior to measurements commencing

a hex key. Where the carabiner was attached a strap is connected between the L-Plate and the tripod table as shown in Figure 20. Auxiliary straps can be attached also as shown in the figure to reduce vibration.

The winch is lowered until the bottom of the disk brake is flush with the bearing on the small tripod as seen in Figure 21. Both bearings are then tightened. A secondary torque arm is installed on the L-Plate as shown in Figure 18. The winch cable is then removed from the shaft. The bearings are now holding the load of the shaft and rotor.

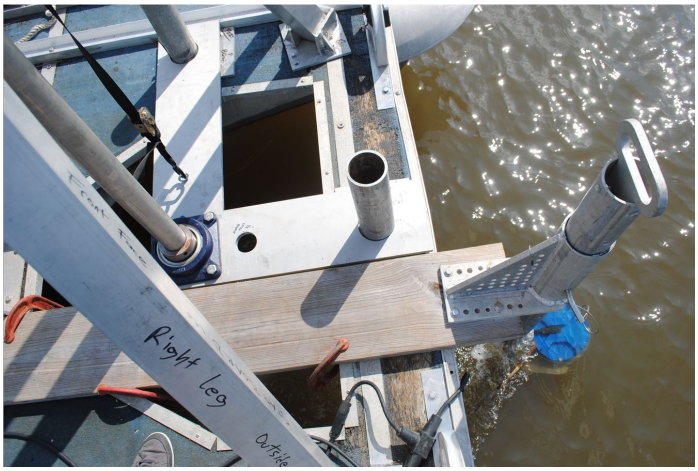

Figure 22: Proximity of deployed ADCP to rotor shaft.

The ADCP is then deployed. The ADCP was secured in its aluminum housing attached to wooden plank as shown in Figures 8, 22, and 23. It was cabled to both the battery pack and the laptop computer. Requiring two people, the ADCP housing was angled under the small tripod and placed flush against the L-plate and deck, clamped to the deck and lowered. Once the ADCP was put in place, the PTO was installed as shown in Figure 22.

After the PTO was installed and the ADCP began pinging, the torque arm was removed and PTO measurements could begin as shown in Figure 23. Throughout periods of currents during the day, the rotation speed and applied torque to the rotor were measured and recorded for various current velocities to develop power curves and to find the maximum power output. Simultaneously, incoming current measurements were recorded using an ADCP to determine the efficiency of the rotor. Over three days, the rotor was evaluated over six tidal cycles, three ebb and three flood, resulting in over 15 hours of testing. The resultant current, rotation speed, and torque measurements are processed and utilized to develop in-situ power curves for the technical resource assessment which is further discussed in Chapter VI.

After measurements, when currents were no longer sustaining rotation, the assembly was

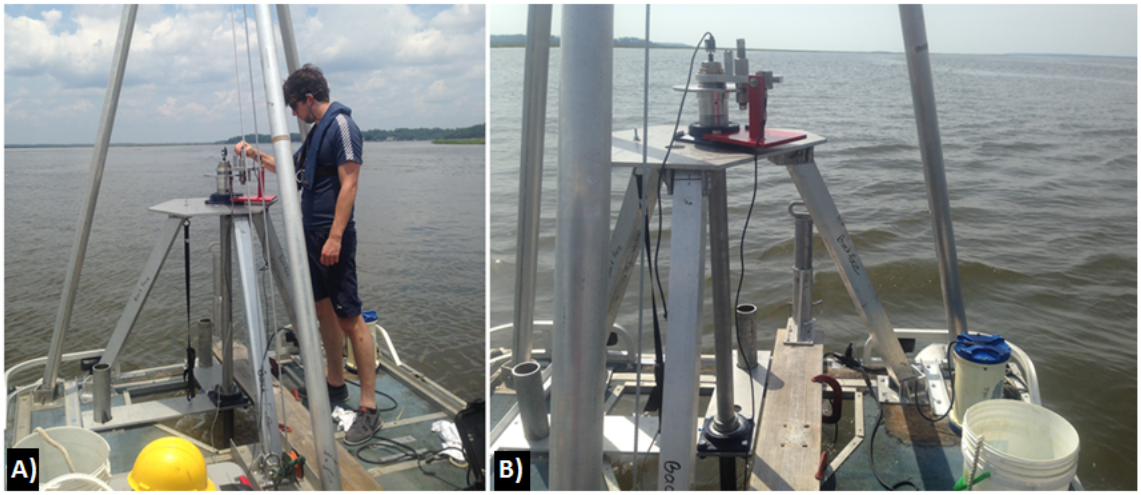

Figure 23: Rotor field Measurements. *A)* Tom Harries applying friction to PTO and measuring resultant torque and rotation speed of rotor *B)* Simultaneous deployment of ADCP (attached to wooden board and deployed underwater), PTO (on top of shaft/tripod), and rotor (underwater)

disassembled to the state shown in the left image of Figure 20 and the anchoring removed. After this, either the boat was moved to another location for more testing, or driven back to the dock.

3.1.5 June 17-18, 2014

Following the rotor testing on June 14-16, 2014, additional transect measurements were conducted for hydrodynamic analysis as in 2010-2011. From results of the 2010-2011 field campaigns, as well as output from a numerical model discussed in Chapter IV, Transect A was considered a point of interest due to its high amounts of hydrokinetic energy and complex confluence hydrodynamics. Thus for June 16-17, 2014, field campaigns were designed to better resolve this area through transect measurements as shown in Figure 24. New transects F and G were charted at the field site on June 18 because it was noticed D and E were not capturing the mixing and converging of the confluent channels at ebb tide.

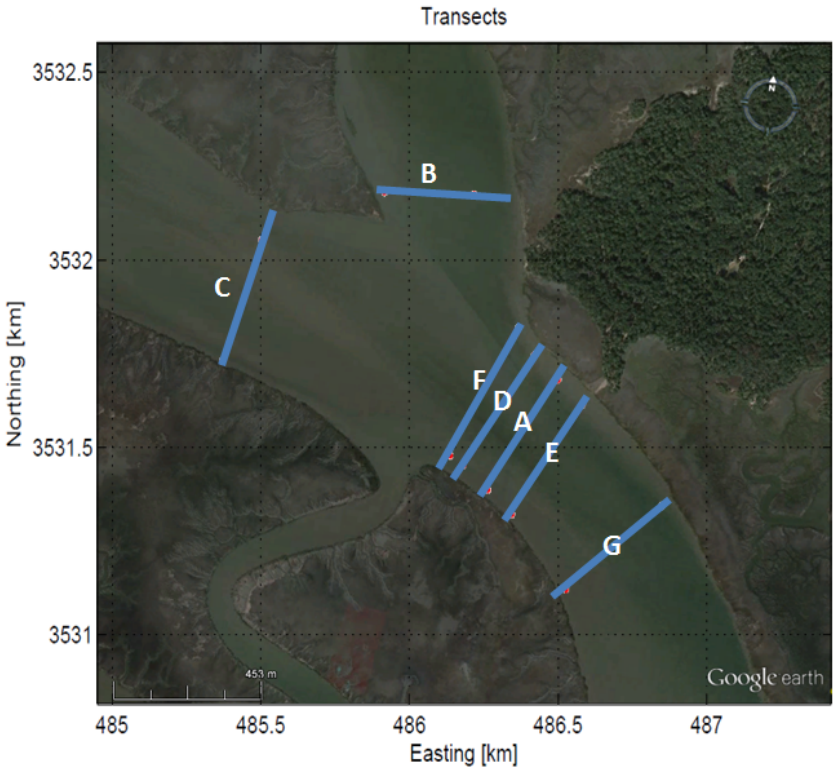

Figure 24: Charted transects for all field campaigns.

The timing of the transect measurements coincided with the spring tide as the rotor experiment; however the magnitude was not as important. The particular tidal phase to be observed was based on needed measurements absent from the previous campaigns, the transition of peak flood to ebb tide. Thus the last two days, June 17-18, 2014 were chosen for transect days since both periods could be observed each day as shown in Figure 13.

3.2 Field Data Processing + Post-Processing

The raw GPS and ADCP data acquired from the field campaigns is processed prior to analysis. The processing methodology includes: correction of rover and base station GPS positions; determination of water level from GPS data; removal of boat motion from ADCP current readings; and decomposition into axial and cross channel velocities for transect measurements. Each step is discussed in detail below.

3.2.1 GPS Processing

GPS coordinates are derived by determining the relative position of the GPS antenna to orbiting satellites; a process known as trilateration. The relative distance is determined by the speed and travel time of radio signals between the GPS antenna and satellite. However, these calculations have errors from satellite orbit deviations, variable light speed in the atmosphere, clock drift, receiver noise, and signal bouncing.

A differential GPS system reduces these errors. The system includes two GPS antenna/receiver pairs. One, the rover, measures the desired positions. The other, the base, is set at a known fixed point and since the position is known, essentially measures the satellite, timing, and atmosphere errors. The US National Geodetic Survey (NGS) has a network of Continuously Operating Reference Stations (CORS) which can serve as the base station.

The closer the receivers/antenna, the more similar the atmosphere, the more similar the error, and the more accurate the correction. Thus, an intermediate base station can be set, in a fixed but unknown position, in closer proximity to the rover. The intermediate station can be corrected against CORS stations, and then the rover can be corrected against

the intermediate station. As discussed in the previous section; in each field campaign an intermediate station was set up near the boat launching location. Further details of GPS operational principles and processing can be found at *http://www.trimble.com/gps_tutorial*.

Thus the GPS processing consists of two steps: correction of the intermediate base station positioning against CORS stations; and correction of the rovers' positionings against the intermediate base station. In this analysis, these errors are calculated and accounted for post-collection because of increased accuracy; however with radio equipment this can be done in real time.

First, receiver data coincidental with field campaign operational times from nearby CORS stations is downloaded from *http://geodesy.noaa.gov/CORS/data.shtml*. Used stations and pertinent information is presented in Table 2. Combinations of CORS station data, dependent on availability, quality, and proximity, is inputed into the processing program *GRAFNET* and used to process intermediate base station files. The particular stations used for each field campaign are presented in Table 3; one CORS station is set as the control point, where its position is considered absolute. The processed intermediate data is then used to correct the rover files in the software *GRAFNAV*.

Table 2: Utilized CORS station information.

Station ID	Station Name	UTM Zone	Position [NAD83]-[m]	Approx. Distance to 2010-11 Int. Base Station [km]	Approx. Distance to 2014 Int. Base Station [km]
GASK	Skidaway Island, GA	17R	[497848.23, 3539050.39]	6	12
SAV5	Savannah Beach, GA	17S	[434346.79, 3555981.23]	63	55
SCWT	Walterboro, SC	17S	[531016.73, 3640619.32]	113	112
SCHA	Charleston Ports, SC	17S	[600647.58, 3627347.66]	142	148
SCCC	College of Charleston, SC	17S	[599473.19, 3627705.39]	141	147
SCEB	Edisto Beach, SC	17S	[562769.15, 3594146.54]	90	95

The resultant GPS data represents the rover antenna position in the NAD83(CORS96) horizontal datum in UTM coordinates (zone 17R), and the NAVD88 vertical datum. To produce water level measurements, η in the mean tidal level [MTL] datum, the following

conversion is

$$\eta = o_1 - h_\eta + \triangle\eta \tag{14}$$

where o_1 is the orthometric height in NAVD88 of the rover at the bow position, h_η is the vertical distance from the bow rover to the water surface measured out in the field, and $\triangle\eta$ is the conversion height between NAVD88 and MTL. $\triangle\eta$ was determined as -0.23 m from the NOAA program $VDATUM$ for the coordinate [487231 m, 3529678 m]; the closest available point to the island approximately 0.75 miles away from Transect A. h_η was measured for every day in the field and is presented in Table 3.

Table 3: CORS stations used for intermediate base station processing and measured distance from rover antenna to water surface, h_η.

Date	Approx. Distance from Int. Base Station to Rose Dhu [km]	CORS Stations	Control Point	h_η [m]
10/19/2010	6.88	GASK SAV5 SCWT	SCWT	2.56
10/20/2010	6.88	GASK SAV5 SCWT	SCWT	2.56
11/27/2011	6.88	GASK SAV5 SCHA SCWT	SCHA	2.56
12/22/2011	6.88	GASK SAV5 SCHA SCWT	SCAH	2.56
06/14/2014	6.34	SCEB SCHA SCWT	SCEB	2.31
06/15/2014	6.34	SAV5 SCWT	SAV5	2.31
06/16/2014	6.34	SAV5 SCWT SCEB	SCEB	2.31
06/17/2014	6.34	SCCC SCEB	SCEB	2.31
06/18/2014	6.34	SCEB SAV5 SCHA SCWT	SCEB	2.31

3.2.2 ADCP Processing

The raw ADCP data consists of four sets of current velocities measured relative coincident with the four beams of the device for each sample, typically referred to as beam coordinates. Thus the currents, u, are measured in a moving and rotating coordinate system which is dependent on the relative orientation and motion of the instrument, which in turn is dependent on the relative orientation and movement of the boat. The purpose of the ADCP processing is to resolve the currents relative to a fixed earth coordinate system, $\mathbb{E}$ corresponding to the UTM horizontal and NAVD88 vertical datums discussed previously.

To accomplish the coordinate transformation, raw beam measurements are transformed to a moving instrument coordinate system, $\mathbb{I}$, then to a moving boat coordinate system, $\mathbb{B}$, and finally to a fixed $\mathbb{E}$ using coupled GPS measurements. The transformation of beam coordinates to $\mathbb{I}$ was always completed instaneously by the acquisition software *WinRiver II*; beam coordinates were never saved. Further transformation methodology depends on the available instrumentation as well as field conditions. This section outlines the coordinate systems, required transformations, and the different methods used to perform them.

3.2.2.1 Coordinate Systems

The notation for discussing the coordinate systems is as follows. Variable subscripts define the coordinate system or value in question and superscripts describe the reference coordinate system. For example, $\overrightarrow{V}_{\mathbb{I}}^{\mathbb{E}}$ is the velocity vector of the instrument coordinate system in the earth coordinate system frame of reference. When the superscript is accented ($\hat{\mathbb{E}}$), only a directional transformation is performed (apparent motion between different axes is not considered). The same applies to position ($\overrightarrow{\Psi}$), orientation ($\overrightarrow{\Theta}$), and angular velocity ($\overrightarrow{\Omega} = \frac{d\overrightarrow{\Theta}}{dt}$) vectors. In referring to the measured current velocities, $\overrightarrow{u}$, the superscript refers to the reference coordinate system as well. The following outlines the general transformation starting from the measured $\overrightarrow{u}^{\mathbb{I}}$. First the position of the current measurements, $\overrightarrow{\Psi_u}$ are mapped to E and then the current measurements themselves.

The instrument coordinate system $\mathbb{I}$ is an orthogonal coordinate system with axial components X, Y, Z, that moves and rotates along with the instrument (Figure 25A). Currents

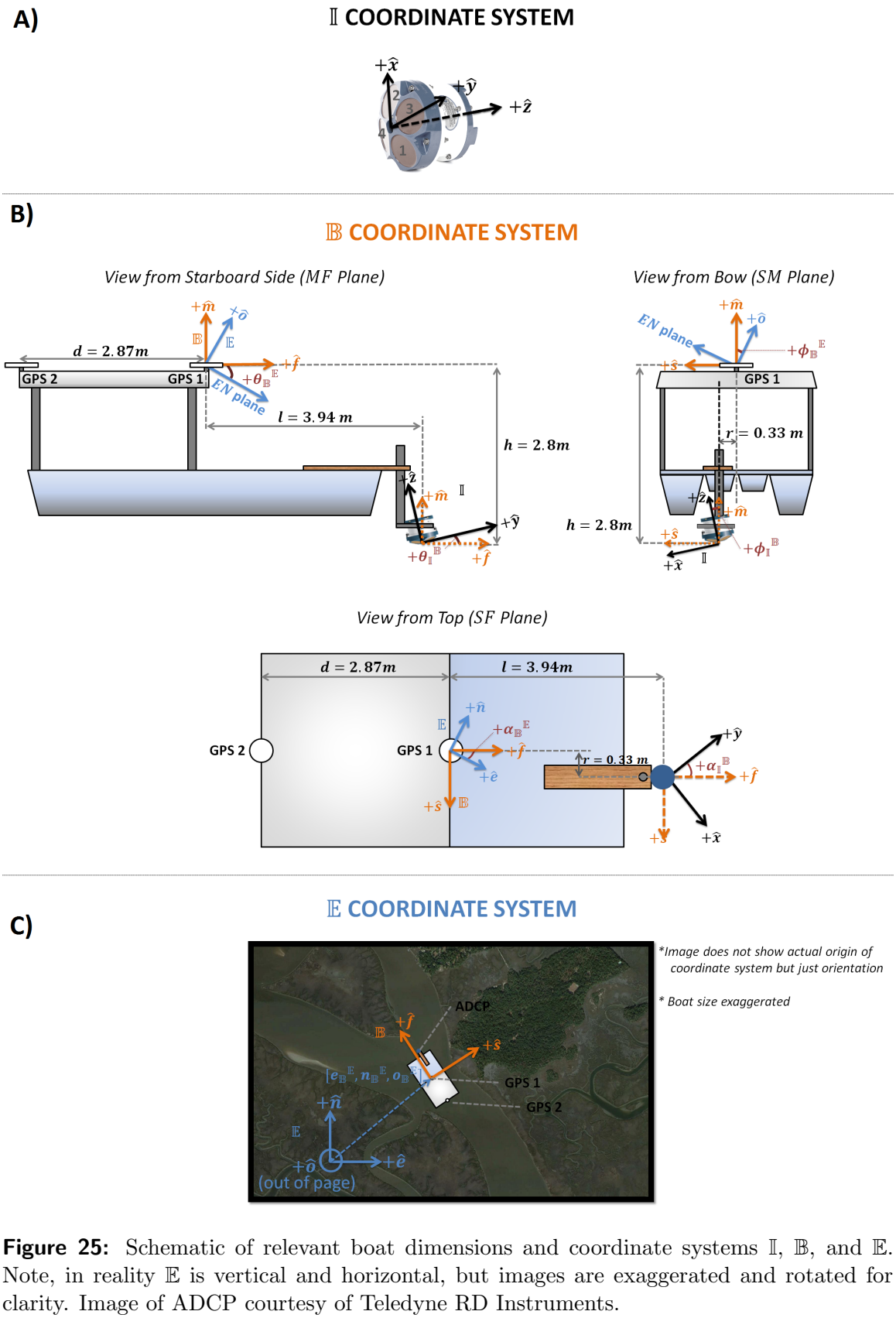

Figure 25: Schematic of relevant boat dimensions and coordinate systems 𝕀, 𝔹, and 𝔼. Note, in reality 𝔼 is vertical and horizontal, but images are exaggerated and rotated for clarity. Image of ADCP courtesy of Teledyne RD Instruments.

are measured relative to the instrument, in the X, Y, Z directions, and bin averaged along the coordinate z in the negative direction. Thus the positional vector of each bin containing a current measurement $\overrightarrow{u}^{\mathbb{I}}$ is $\overrightarrow{\Psi_u}^{\mathbb{I}} = [0, 0, z_{bin}]$. Because the bin width is fixed, z_{bin} and thus the location of the measurement in the instrument coordinate system $\overrightarrow{\Psi_u}^{\mathbb{I}}$ does not change in time. However the position and orientation of $\mathbb{I}$ do change in time since the instrument is aboard a boat that is in motion. The position of the boat is referenced to Earth coordinates E, N, O, (east, north, vertically orthogonal) by the GPS. Thus in order to determine the position and orientation of the instrument axes and thus ADCP measurements in the earth coordinate system, $\mathbb{I}$ must be referenced to the GPS position on the boat.

The boat coordinate system $\mathbb{B}$ is an orthogonal coordinate system with axial components S, F, M, (starboard, forward, mast) that moves and rotates along with the boat. The origin and orientation of $\mathbb{B}$ is aligned with the bow GPS, labeled GPS1, shown in Figure 25B. The relative position and orientation of the ADCP aboard the boat is depicted and described by $\overrightarrow{\Psi_{\mathbb{I}}}^{\mathbb{B}} = [-r, l, -s]$ and $\overrightarrow{\Theta_{\mathbb{I}}}^{\mathbb{B}} = [{\alpha_{\mathbb{I}}}^{\mathbb{B}}, {\theta_{\mathbb{I}}}^{\mathbb{B}}, {\phi_{\mathbb{I}}}^{\mathbb{B}}]$ respectively and are all shown in Figure 25B. α, θ, and ψ represent the heading, pitch, and roll orientation components. Because the ADCP is firmly clamped onto the boat, neither $\overrightarrow{\Psi_{\mathbb{I}}}^{\mathbb{B}}$ or $\overrightarrow{\Theta_{\mathbb{I}}}^{\mathbb{B}}$ change in time and $\overrightarrow{V_{\mathbb{I}}}^{\mathbb{B}} = [0, 0, 0]$.

The position and orientation of the $\mathbb{B}$ coordinate system in earth coordinates $\mathbb{E}$ is described by $\overrightarrow{\Psi_{\mathbb{B}}}^{\mathbb{E}}$ and $\overrightarrow{\Theta_{\mathbb{B}}}^{\mathbb{E}}$. These values vary in time due to the translational motion and rotation of the boat on the water. The specific components are presented in Figure 25B and C as $\overrightarrow{\Psi_{\mathbb{B}}}^{\mathbb{E}} = [{e_{\mathbb{B}}}^{\mathbb{E}}, {n_{\mathbb{B}}}^{\mathbb{E}}, {o_{\mathbb{B}}}^{\mathbb{E}}]$ and $\overrightarrow{\Theta_{\mathbb{B}}}^{\mathbb{E}} = [{\alpha_{\mathbb{B}}}^{\mathbb{E}}, {\theta_{\mathbb{B}}}^{\mathbb{E}}, {\phi_{\mathbb{B}}}^{\mathbb{E}}]$. These values are used to map the position of the instrument axes, $\overrightarrow{\Psi_{\mathbb{I}}}^{\mathbb{E}}$, through the transformation

$$\overrightarrow{\Psi_{\mathbb{I}}}^{\mathbb{E}} = \overrightarrow{\Psi_{\mathbb{B}}}^{\mathbb{E}} + {\mathbf{M}_{\mathbb{B}}}^{\mathbb{E}} \overrightarrow{\Psi_{\mathbb{I}}}^{\mathbb{B}} \tag{15}$$

where ${\mathbf{M}_{\mathbb{B}}}^{\mathbb{E}}$ is a rotation matrix between boat and earth coordinate systems specified by

$${\mathbf{M}_{\mathbb{B}}}^{\mathbb{E}} = \begin{bmatrix} \sin {\alpha_{\mathbb{B}}}^{\mathbb{E}} & \cos {\alpha_{\mathbb{B}}}^{\mathbb{E}} & 0 \\ -\cos {\alpha_{\mathbb{B}}}^{\mathbb{E}} & \sin {\alpha_{\mathbb{B}}}^{\mathbb{E}} & 0 \\ 0 & 0 & 1 \end{bmatrix} \begin{bmatrix} 1 & 0 & 0 \\ 0 & \cos {\theta_{\mathbb{B}}}^{\mathbb{E}} & -\sin {\theta_{\mathbb{B}}}^{\mathbb{E}} \\ 0 & \sin {\theta_{\mathbb{B}}}^{\mathbb{E}} & \cos {\theta_{\mathbb{B}}}^{\mathbb{E}} \end{bmatrix} \begin{bmatrix} \cos {\phi_{\mathbb{B}}}^{\mathbb{E}} & 0 & \sin {\phi_{\mathbb{B}}}^{\mathbb{E}} \\ 0 & 1 & 0 \\ -\sin {\phi_{\mathbb{B}}}^{\mathbb{E}} & 0 & \cos {\phi_{\mathbb{B}}}^{\mathbb{E}} \end{bmatrix} \tag{16}$$

The orientation of the instrument axes, $\overrightarrow{\Theta_{\mathbb{I}}}^{\mathbb{E}}$ can be mapped to earth coordinates by

$$\overrightarrow{\Theta_{\mathbb{I}}}^{\mathbb{E}} = \overrightarrow{\Theta_{\mathbb{B}}}^{\mathbb{E}} + \overrightarrow{\Theta_{\mathbb{I}}}^{\mathbb{B}} \tag{17}$$

The position of the instrument axis is used to map the earth coordinates of the current measurements, $\overrightarrow{\Psi_u}^{\mathbb{E}}$, as

$$\overrightarrow{\Psi_u}^{\mathbb{E}} = \overrightarrow{\Psi_{\mathbb{I}}}^{\mathbb{E}} + \overrightarrow{\Psi_u}^{\mathbb{I}} \tag{18}$$

Although the pitch and roll of the instrument axes do alter the earth coordinates of the bin measurements along the water column, their values were considered small ($< 20°$), their effects considered minimal as specified by the manufacturer, and not included in Equation (18) (Teledyne RD Instruments, 2010).

To map the current velocities $\overrightarrow{u}^{\mathbb{E}}$, first the apparent motion of the instrument axes and thus change in measurement position is removed from the observed current measurements by

$$\overrightarrow{u}^{\hat{\mathbb{I}}} = \overrightarrow{u}^{\mathbb{I}} + \overrightarrow{V_u}^{\hat{\mathbb{I}}} \tag{19}$$

where $\overrightarrow{V_u}^{\hat{\mathbb{I}}}$ is the change in measurement position for a given bin in the instrument XYZ directions. To determine $\overrightarrow{V_u}^{\hat{\mathbb{I}}}$, the motion of the measurement positions in earth coordinates is transformed to instrument directional components by

$$\overrightarrow{V_u}^{\hat{\mathbb{I}}} = \mathbf{M}_{\mathbb{E}}{}^{\mathbb{I}} \frac{d}{dt} \overrightarrow{\Psi_u}^{\mathbb{E}} \tag{20}$$

where $\mathbf{M}_{\mathbb{E}}{}^{\mathbb{I}}$ is a rotation matrix from earth to instrument coordinate system specified as

$$\mathbf{M}_{\mathbb{E}}{}^{\mathbb{I}} = \begin{bmatrix} 1 & 0 & 0 \\ 0 & \cos\theta_{\mathbb{I}}{}^{\mathbb{E}} & \sin\theta_{\mathbb{I}}{}^{\mathbb{E}} \\ 0 & -\sin\theta_{\mathbb{I}}{}^{\mathbb{E}} & \cos\theta_{\mathbb{I}}{}^{\mathbb{E}} \end{bmatrix} \begin{bmatrix} \cos\phi_{\mathbb{I}}{}^{\mathbb{E}} & 0 & -\sin\phi_{\mathbb{I}}{}^{\mathbb{E}} \\ 0 & 1 & 0 \\ \sin\phi_{\mathbb{I}}{}^{\mathbb{E}} & 0 & \cos\phi_{\mathbb{I}}{}^{\mathbb{E}} \end{bmatrix} \begin{bmatrix} \sin\alpha_{\mathbb{I}}{}^{\mathbb{E}} & -\cos\alpha_{\mathbb{I}}{}^{\mathbb{E}} & 0 \\ \cos\alpha_{\mathbb{I}}{}^{\mathbb{E}} & \sin\alpha_{\mathbb{I}}{}^{\mathbb{E}} & 0 \\ 0 & 0 & 1 \end{bmatrix} \tag{21}$$

After apparent motion is removed, the current measurements are mapped to directional components in the earth coordinate system through

$$\overrightarrow{u}^{\mathbb{E}} = \mathbf{M}_{\mathbb{I}}{}^{\mathbb{E}} \overrightarrow{V_u}^{\hat{\mathbb{I}}} \tag{22}$$

where $\mathbf{M}_{\mathbb{I}}{}^{\mathbb{E}}$ is the rotational matrix from $\mathbb{I}$ to $\mathbb{E}$ and specified as

$$\mathbf{M}_{\mathbb{I}}{}^{\mathbb{E}} = \begin{bmatrix} \sin\alpha_{\mathbb{I}}{}^{\mathbb{E}} & \cos\alpha_{\mathbb{I}}{}^{\mathbb{E}} & 0 \\ -\cos\alpha_{\mathbb{I}}{}^{\mathbb{E}} & \sin\alpha_{\mathbb{I}}{}^{\mathbb{E}} & 0 \\ 0 & 0 & 1 \end{bmatrix} \begin{bmatrix} 1 & 0 & 0 \\ 0 & \cos\theta_{\mathbb{I}}{}^{\mathbb{E}} & -\sin\theta_{\mathbb{I}}{}^{\mathbb{E}} \\ 0 & \sin\theta_{\mathbb{I}}{}^{\mathbb{E}} & \cos\theta_{\mathbb{I}}{}^{\mathbb{E}} \end{bmatrix} \begin{bmatrix} \cos\phi_{\mathbb{I}} & 0 & \sin\phi_{\mathbb{I}} \\ 0 & 1 & 0 \\ -\sin\phi_{\mathbb{I}} & 0 & \cos\phi_{\mathbb{I}} \end{bmatrix} \tag{23}$$

Equations (15)-(23) present the generalized method for transforming the boat based ADCP measurements to a fixed earth coordinate system defined by the GPS. Methodology to obtain the various values used for the transformation vary and are presented next.

3.2.2.2 Transformation Methodology

In order to perform the transformations in Equations (15)-(23) to obtain the velocity measurements $\overrightarrow{u}^{\mathbb{E}}$ and their position $\overrightarrow{\Psi_u}^{\hat{\mathbb{E}}}$ in earth coordinates, the movement and orientation of the instrument must be specified. Depending on available field equipment and conditions, methods to obtain these values vary. *WinRiver II* can provide the translational motion and orientation, however for periods of high frequency oscillation (i.e. strong wave impingement and subsequent rocking of the boat) the values are inaccurate and incomplete. The internal sensors fail to accurately resolve the correct instrument orientation. Also, the processing software does not account for the apparent angular velocity induced by the swiftly rotating instrument coordinate system. For high frequency oscillation, this effect is non-negligible.

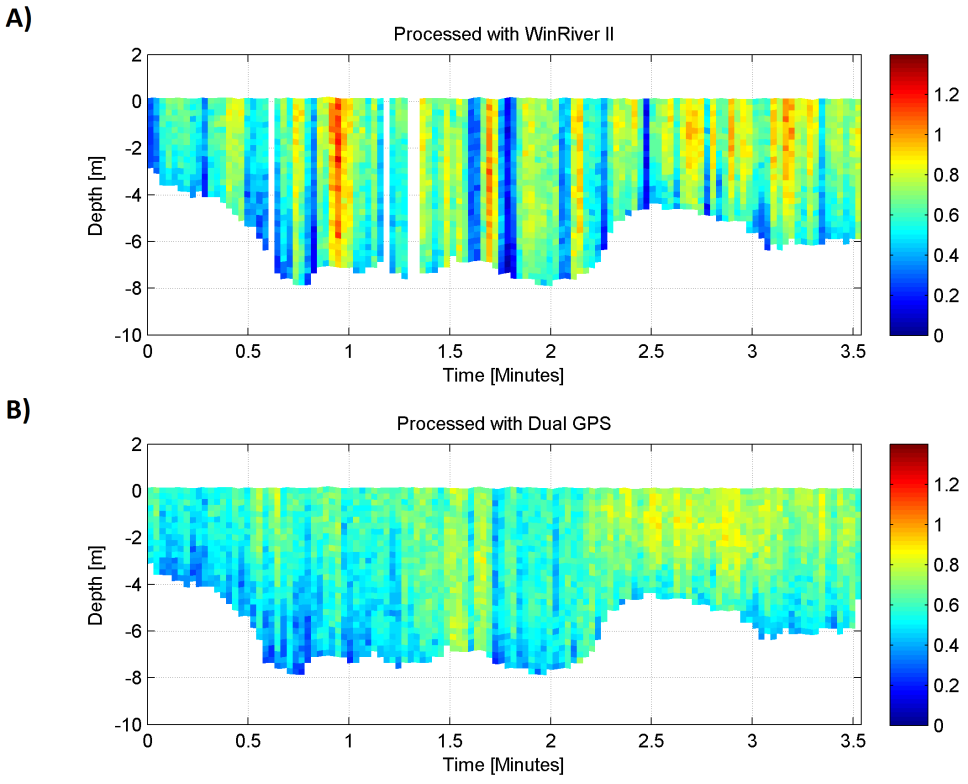

Figure 26: Example of enhanced dual GPS processing technique for wavy conditions. *A)* Current magnitudes processed with *WinRiver II B)* Current magnitudes processed with Dual GPS technique. Pictured measurement is Transect E measured on June 17, 2014. Time is reference to transect measurement initiation. Currents in [m/s].

As a result, final $\overrightarrow{u}^{\mathbb{E}}$ values have severe artificial 'striping' (Figure 26A). The needed information can be inferred from a dual GPS system and the 'striping' removed (Figure 26B). However, corrections cannot be applied from a singular GPS and data with excessive striping are discarded.

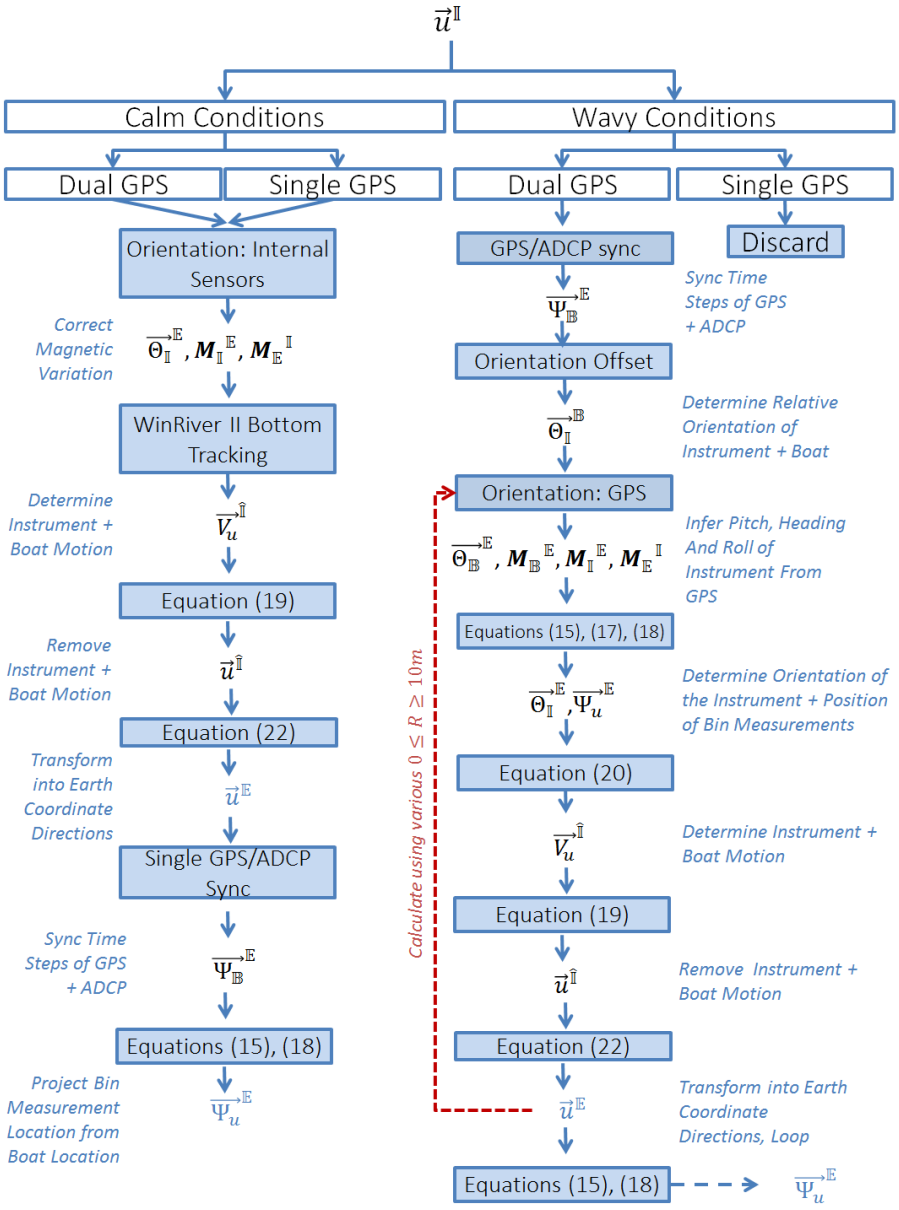

Figure 27: Decision and flow chart of ADCP processing methods. White boxes represent conditions and solid boxes represent processes. Blue values indicate desired deliverables. Red lines indicate loop.

A flow chart is presented in Figure 27 listing the processes required for the coordinate transformation for each condition. For calm conditions, internal sensors of the ADCP and *WinRiver II* are used to determine instrument orientation, remove the apparent velocity induced by instrument motion, and transform the measurements into earth coordinate directions. Manual corrections include syncing ADCP data with the GPS to determine the absolute position of the measurements as well as correcting for magnetic declination in the instrument heading sensor. For wavy conditions, all corrections are completed manually. The ADCP and GPS are first synced to determine measurement position, then the relative orientation of the boat (defined by the GPS) and instrument coordinate systems are determined, orientation of the instrument is then inferred by the GPS measurements, boat motion relative to the instrument is then removed from the measurements, and then the measurements are transformed into earth coordinate components. Individual processes are further described in detail below.

Orientation: Internal Sensors

The internal sensors of the ADCP provide the instantaneous pitch, roll, and magnetic heading of the instrument in a fixed magnetic earth coordinate system, $\mathbb{EM}$. Values are considered accurate for calm conditions. ${\Theta_{\mathbb{I}}}^{\mathbb{EM}}$ is transformed from $\mathbb{EM}$ to $\mathbb{E}$ by

$$ {\Theta_{\mathbb{I}}}^{\mathbb{E}} = {\Theta_{\mathbb{I}}}^{\mathbb{EM}} + {\Theta_{\mathbb{EM}}}^{\mathbb{E}} \tag{24} $$

where ${\Theta_{\mathbb{EM}}}^{\mathbb{E}} = [{\alpha_{\mathbb{EM}}}^{\mathbb{E}}, 0, 0]$. Pitch and roll do not vary between $\mathbb{E}$ and $\mathbb{E}_M$, but heading does and requires a transformation. ${\alpha_{\mathbb{EM}}}^{\mathbb{E}}$ corrects the orientation difference between true north (what is measured by the GPS in earth coordinates), and magnetic north (what is measured by the ADCP compass); a counter clockwise shift is positive. ${\alpha_{\mathbb{EM}}}^{\mathbb{E}}$ is also known as magnetic declination or variation, and is obtained for a point from the International Geomagnetic Reference Field Model from NOAA at *http://www.ngdc.noaa .gov/geomag-web/#declination*. The value for Rose Dhu Island on October 19, 2010 is 6.52^o and increases by a rate of 0.08^o/year. Once ${\Theta_{\mathbb{I}}}^{\mathbb{E}}$ is determined, ${\mathbf{M}_{\mathbb{I}}}^{\mathbb{E}}$ is determined from Equation (23).

WinRiver II Bottom Tracking

WinRiver II removes the apparent motion of the instrument axes from measured currents through the "Bottom Tracking" method as outlined in the technical manual (Teledyne RD Instruments, 2007). $\overrightarrow{V_u}^{\hat{\mathbb{I}}}$ is a depth-averaged velocity that is equal and opposite to the bottom most $\overrightarrow{V_u}^{\mathbb{I}}$ reading. The method assumes a non-moving sea bed, thus the current velocity $\overrightarrow{u}^{\hat{\mathbb{I}}} = 0$ and Equation (19) becomes $\overrightarrow{V_u}^{\hat{\mathbb{I}}} = -\overrightarrow{u}^{\mathbb{I}}|_{seabed}$.

GPS/ADCP Sync

The timestamp of the GPS measurements, t, is continuously synced to satellite UTC time by the GPS rover in-situ. The timestamp of the ADCP, t' is synced to the recording computer, which was synced once to satellite time prior to collection for the day. Without the continuous syncing, the t' can drift throughout the day and the difference, or syncing error, $\tau = t - t'$ grows. Although relatively small, a few seconds, a non-zero τ induces significant error when correcting for high frequency oscillations due to waves with periods on the same order.

To determine τ, a correlation analysis is completed between the depth averaged ${u_z}^{\mathbb{I}}(t' + \tau)$, the measured current velocity in the Z coordinate, and ${V_{o\mathbb{B}}}^{\mathbb{E}}(t)$, the velocity of the boat coordinate system in the O direction for various τ during numerous wave events. Vertical velocities during wake events are advantageous to use due to the relatively large amplitudes and clarity of the signals. Because the motion of the instrument axes leaves an apparent velocity footprint of equal and opposite value in the observed currents, a correlation coefficient between the two are strongly negative. A determined τ with a consistently strong negative correlation throughout the day suggests proper syncing. An example correlation analysis is presented in Figure 28. ${V_{o\mathbb{B}}}^{\mathbb{E}}(t)$ is determined from a central finite difference calculation of the GPS vertical coordinates measured by GPS1, ${o_{\mathbb{B}}}^{\mathbb{E}}$. A coordinate transformation is not needed from B to E because the vertical wave signals have strong effects in the same direction for both coordinate systems. Once an optimal τ is determined, it is added to the ADCP time step to correctly sync the values to GPS time, t. Then GPS values are linearly interpolated onto the new ADCP timesteps to acquire $\overrightarrow{\Psi_{\mathbb{I}}}^{\mathbb{E}}$ for each ADCP measurement.

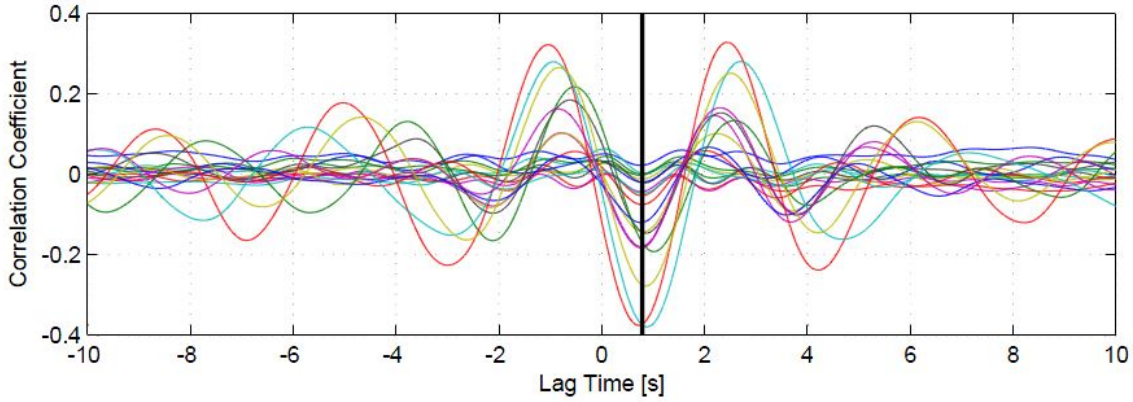

Figure 28: Correlation coefficients between depth averaged ${u_z}^{\mathbb{I}}(t' + \tau)$ and ${V_{o\mathbb{B}}}^{\mathbb{E}}(t)$ for various τ. Different lines are different afternoon transects of June 17, 2014 with significant wave motion. 20 transects are presented. A median minima, or optimum τ is found to be 0.79 seconds.

Orientation Offset

$\overrightarrow{\Theta_{\mathbb{I}}}^{\mathbb{B}}$ represents the constant offset between the boat coordinate axis and the instrument coordinate axes. For pitch and roll these values are considered small and negligible since the ADCP was attached to a board, planar to the boat deck. However, the heading ${\alpha_{\mathbb{I}}}^{\mathbb{B}}$ is difficult to perfectly align with the keel of the boat. When using Bottom Tracking, this value is not needed since the relative motion of the instrument axis is already calculated in the $\mathbb{I}$. However when determining the instrument axes motion from the GPS, and a transformation from earth, to boat and instrument coordinates, this value is very significant.

${\alpha_{\mathbb{I}}}^{\mathbb{B}}$ is determined from an analysis of current measurements of calm conditions from the same day. Because of calm conditions, the effect of change in roll or pitch is assumed very small in both processing methods and the calm condition *WinRiver II* processing is assumed accurate. The Wavy Conditions/Dual GPS flow chart process outlined in Figure 27 is carried out for calm measurements using various ${\alpha_{\mathbb{I}}}^{\mathbb{B}}$ and compared to the *WinRiver II* results for accuracy.

After each $\overrightarrow{u}^{\mathbb{E}}$ is processed using the Wavy Conditions/Dual GPS method and a given ${\alpha_{\mathbb{I}}}^{\mathbb{B}}$, the horizontal current magnitudes $|u^{\mathbb{E}}|$ are calculated and compared to the magnitudes processes using *WinRiver II*. The correct ${\alpha_{\mathbb{I}}}^{\mathbb{B}}$ is assumed to produce magnitudes mimicking

the accurate calculations of *WinRiver II*. Thus the mean-squared difference of the two are calculated and compared; the ${\alpha_{\mathbb{I}}}^{\mathbb{B}}$ producing a consistently small error for a given day is the correct value. Figure 29 shows the summed absolute difference for all the calm transects recorded on June 17, 2014. It is clear the ${\alpha_{\mathbb{I}}}^{\mathbb{B}}$ to produce the smallest error is 7° (clockwise from the F direction). The resultant product is $\overrightarrow{{\Theta_{\mathbb{I}}}^{\mathbb{B}}}$ which can be used for the dual GPS processing method for wavy conditions on the same day. Because the ADCP is never removed from its snug casing during the day; it is assumed this value is constant.

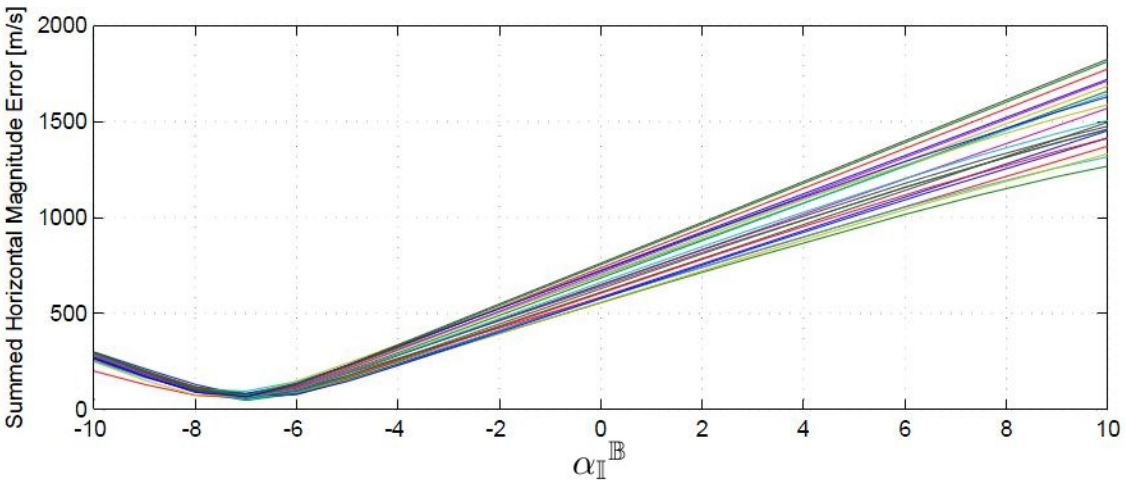

Figure 29: Summed absolute error between *WinRiver II* and GPS processed transects with varying ${\alpha_{\mathbb{I}}}^{\mathbb{B}}$ [^{o}]. Different lines are different morning transects of June 17, 2014 with little wave motion. 23 transects are presented.

Orientation: GPS

Because the internal sensors of the GPS for pitch, roll, and heading are inaccurate for conditions with high frequency orientation oscillation, the dual GPS measurements are used to calculate ${\Theta_{\mathbb{B}}}^{\mathbb{E}}$. The geometry of the dual GPS and ADCP system is fully illustrated in Figure 25. The two GPS antennae are attached to the roof and are in line with the keel or forward (F) axis of the boat. The GPS nearest the bow is referred to as GPS1 whereas the GPS nearest the stern is GPS2; associated variables are subscripted with 1 and 2 respectively.

The relative positions of the two antennae are used to determine the orientation of the

boat coordinate system, assuming the boat is rigid and the roof runs parallel to the deck. The pitch of the boat is found by determining the angle between the two antenna relative to the EN plane through the equation

$$\theta_{\mathbb{B}}{}^{\mathbb{E}} = \arccos \frac{o_{\mathbb{B}}{}^{\mathbb{E}}{}_1 - o_{\mathbb{B}}{}^{\mathbb{E}}{}_2}{d} \tag{25}$$

where $o_{\mathbb{B}}{}^{\mathbb{E}}{}_1$ and $o_{\mathbb{B}}{}^{\mathbb{E}}{}_2$ are the elevation coordinates of the two GPS antenna, and d is the measured physical distance between the two antenna. The heading is found similarly by determining the angle between the two antenna relative to the EO plane by

$$\alpha_{\mathbb{B}}{}^{\mathbb{E}} = \arctan \frac{n_{\mathbb{B}}{}^{\mathbb{E}}{}_1(t) - n_{\mathbb{B}}{}^{\mathbb{E}}{}_2(t)}{e_{\mathbb{B}}{}^{\mathbb{E}}{}_1(t) - e_{\mathbb{B}}{}^{\mathbb{E}}{}_2(t)} \tag{26}$$

where $e_{\mathbb{B}}{}^{\mathbb{E}}$ and $n_{\mathbb{B}}{}^{\mathbb{E}}$ are the easting and northing coordinates of the two antenna respectively.

Assuming that roll motion is purely in the SM plane, an additional GPS unit or point of measurement with separation in the S direction is required for direction calculation of the roll. Thus the two exisiting GPS data are used to provide an estimate of $\phi_{\mathbb{B}}{}^{\mathbb{E}}$. The movement in the SM plane can be determined from the positionings of the GPSs, however difficulty lies in accurately appropriating portions of this movement to boat translation, or rather changes in pitch, heading, and roll.

To try to isolate motion in the SM plane, the coordinates of the midpoint between the two antenna is used and given by

$$\overrightarrow{\Psi_{\mathbb{B}}}{}^{\mathbb{E}}{}_M = \overrightarrow{\Psi_{\mathbb{B}}}{}^{\mathbb{E}}{}_2 + \frac{\overrightarrow{\Psi_{\mathbb{B}}}{}^{\mathbb{E}}{}_2 - \overrightarrow{\Psi_{\mathbb{B}}}{}^{\mathbb{E}}{}_1}{2} \tag{27}$$

To remove translational motion, it is assumed that significant roll motion occurs at a frequency comparable to the incoming waves. Witness accounts on the field campaign estimate this frequency to be 0.33-0.50 Hz, or a wave period of 2-3 seconds. These estimates are further accredited through spectral analysis of $o_{\mathbb{B}}{}^{\mathbb{E}}$ for period of time where the boat is stationary in similar conditions, i.e. during anchored turbine testing shown in Figure 30 where there is a significant power for frequencies over 0.33 Hz.

Thus to remove the low frequency translational motion, $e_{\mathbb{B}}{}^{\mathbb{E}}$ and $n_{\mathbb{B}}{}^{\mathbb{E}}$ undergo a high pass filter with a cut off frequency of 0.33 Hz to produce filtered high frequency signals $e_{\mathbb{B}}{}^{\mathbb{E}'}$ and $n_{\mathbb{B}}{}^{\mathbb{E}'}$. Transformation to S and F coordinates shows the high frequency movement

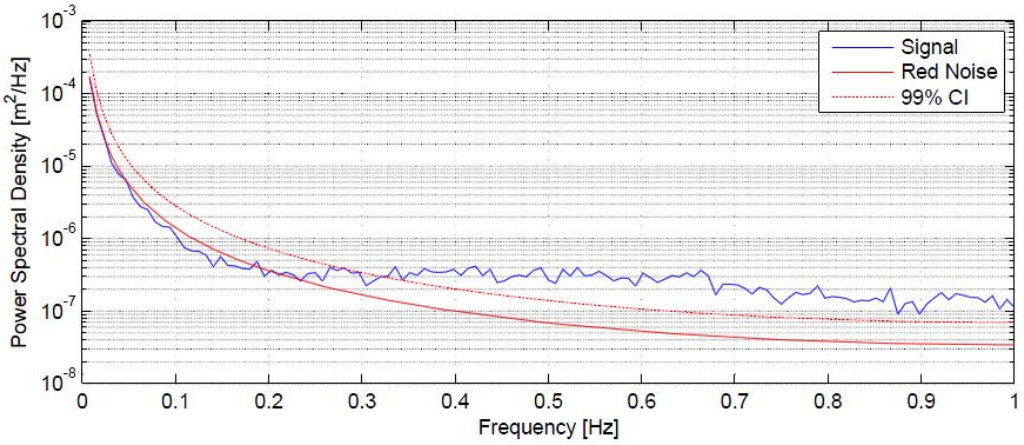

Figure 30: Power spectral density calculation for o_b for anchored afternoon turbine testing on June 17, 2014. Spectra calculated with a window length of 128 seconds with 50% overlap giving 35 degrees of freedom for a signal approximately 35 minutes long. The null hypothesize is experimental red noise with a 99% confidence interval (CI) for Type I error as explained by Hartmann (2014).

is overwhelming in the S direction and negligible in F, supporting it is primarily motion perpendicular to keel of the boat. An example is shown in Figure 31. The red line represents the path of GPS1 where the blue line represents a low pass filtered signal, the differential distance between the two is the high pass filtered signal. In the example, the difference appears oriented almost perpendicular to the boat, along the S direction. The roll motion is assumed to be about the boat's rotational axis, with the absolute radius of rotation, R, unknown. The roll motion cannot be filtered from the O direction since that associated motion occurs at twice the wave frequency, which approaches the Nyquist frequency of the GPS sampling rate. Thus, the radius of rotation R must be estimated in order to determine the roll value after the high frequency motion is mapped to the SM plane.

When mapping the east/north movement to the SM plane, it is assumed the effect of pitch is small. Thus to determine the lateral position of the midpoint, or roof about the boat's M axis, $[{s_{\mathbb{B}}}^{\hat{\mathbb{B}}'}, {f_{\mathbb{B}}}^{\hat{\mathbb{B}}'}]$, a singular coordinate transformation of ${e_{\mathbb{B}}}^{\mathbb{E}'}$ and ${n_{\mathbb{B}}}^{\mathbb{E}'}$ is performed by

$${s_{\mathbb{B}}}^{\hat{\mathbb{B}}'} = {e_{\mathbb{B}}}^{\mathbb{E}'} \sin {\alpha_{\mathbb{B}}}^{\mathbb{E}} - {n_{\mathbb{B}}}^{\mathbb{E}'} \cos {\alpha_{\mathbb{B}}}^{\mathbb{E}}; \tag{28}$$

$${f_{\mathbb{B}}}^{\hat{\mathbb{B}}'} = {e_{\mathbb{B}}}^{\mathbb{E}'} \cos {\alpha_{\mathbb{B}}}^{\mathbb{E}} + {n_{\mathbb{B}}}^{\mathbb{E}'} \sin {\alpha_{\mathbb{B}}}^{\mathbb{E}}; \tag{29}$$

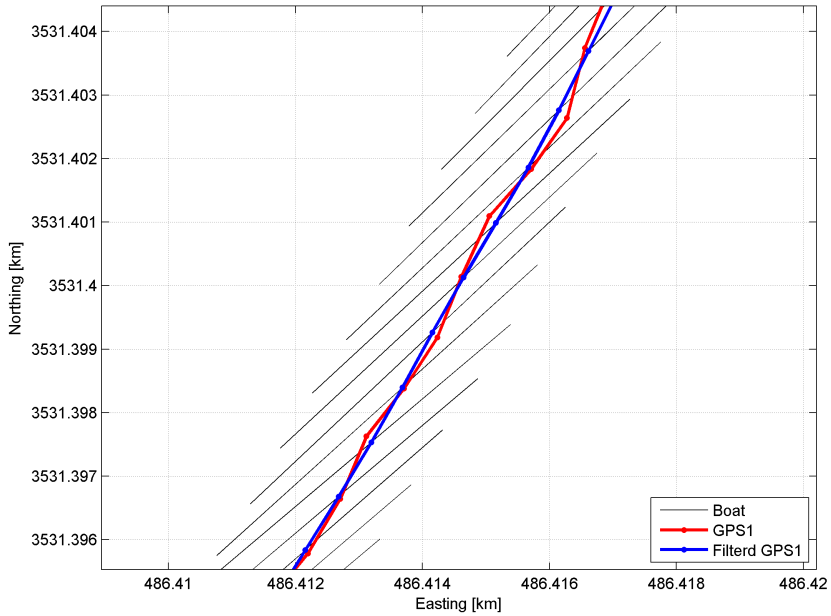

Figure 31: Example of filtered boat movement with cut off frequency of 0.33 Hz. Red line is movement of GPS 1. Blue line is low pass filtered movement of GPS 1. Black lines represent boat extent. Measurement taken from Transect E on June 17, 2014.

As shown in Figure 32, ${s_{\mathbb{B}}}^{\hat{\mathbb{B}'}}$ is used to calculate the roll angle through

$$ {\phi_{\mathbb{B}}}^{\mathbb{E}} = 90^{\circ} - \arccos \frac{{s_{\mathbb{B}}}^{\hat{\mathbb{B}'}}}{R} \tag{30} $$

where R is the distance in the O direction between the midpoint of the GPS antennas and the boats center of rotation.

R is unknown; as shown in Figure 32 it ultimately governs the proportion of ${s_{\mathbb{B}}}^{\hat{\mathbb{B}'}}$ that is associated with rotation ($\triangle {\phi_{\mathbb{B}}}^{\mathbb{E}}$) and solely translation ${s_{\mathbb{B}}}^{\hat{\mathbb{B}'}}$. A distinction is important since the position and apparent velocity of the instrument axis induced by each has the opposite sign. As R increases, ${\phi_{\mathbb{B}}}^{\mathbb{E}}$ decreases in magnitude. Thus, for a given change in position, the instrument undergoes a larger translational motion in the same S direction. As R approaches infinity, ${\phi_{\mathbb{B}}}^{\mathbb{E}}$ goes to zero and the instrument axis purely translates in the same S direction (Case 1). As R decreases, ${\phi_{\mathbb{B}}}^{\mathbb{E}}$ increases as does the degree of rotation (Case 2). When $R = h$, when the center of rotation is at instrument axis, there is no change in position of the instrument axis, only the orientation (Case 3). As R decreases further, ${\phi_{\mathbb{B}}}^{\mathbb{E}}$ increases and induces rotational motion in the opposite direction of ${s_{\mathbb{B}}}^{\hat{\mathbb{B}'}}$ (Case 4). The

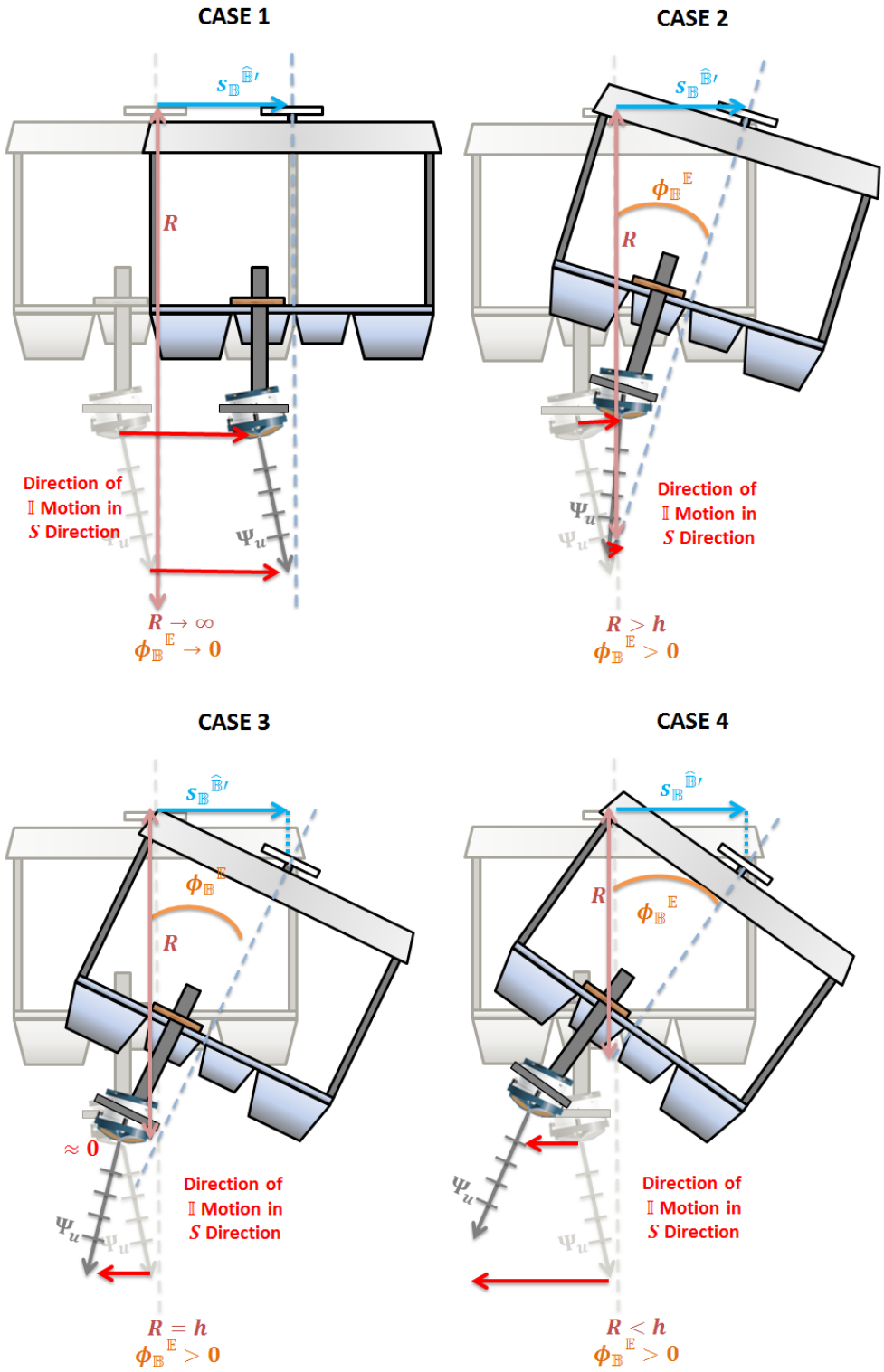

Figure 32: Examples of the effect of R on the interpretation of high frequency rotational and translational movement for a fixed $s_{\mathbb{B}}^{\hat{\mathbb{B}}'}$. Image of ADCP courtesy of Teledyne RD Instruments

effects of R on ${\phi_{\mathbb{B}}}^{\mathbb{E}}$ are significant because they ultimately dictate both the apparent angular and translational velocity for each bin measurement, the former magnified by bin depth values. These discussed effects are buried in Equations (15) and (18), however their individual effects can be separated.

To determine R and thus the roll ${\phi_{\mathbb{B}}}^{\mathbb{E}}$, the Dual GPS process is repeated for various R in an optimization procedure similar to that in the GPS/ADCP sync. Because ${\phi_{\mathbb{B}}}^{\mathbb{E}}$ is relatively small ($\leq 15°$), its coordinate transformation effect is relatively small. However, the apparent angular velocity induced by $\frac{d{\phi_{\mathbb{B}}}^{\mathbb{E}}}{dt}$, buried in the apparent motion of the bin measurement in the X direction ${V_{xu}}^{\mathbb{I}}$, is not and leaves a footprint of equal and opposite direction in the observed current velocity in the X direction ${u_x}^{\mathbb{I}}$. Thus, when added together as in Equation (22), the footprint will diminish, ideally to zero. Thus, a correlation analysis of the depth averaged corrected velocity ${u_x}^{\hat{\mathbb{I}}}$ and ${V_{xu}}^{\mathbb{I}}$ will show the degree of removal. If ${V_{xu}}^{\mathbb{I}}$ is too small, the footprint will still remain and there will be a significant negative correlation. If ${V_{xu}}^{\mathbb{I}}$ is too large, it will over correct and impose a new footprint in the opposite direction and there will be a significant positive correlation.

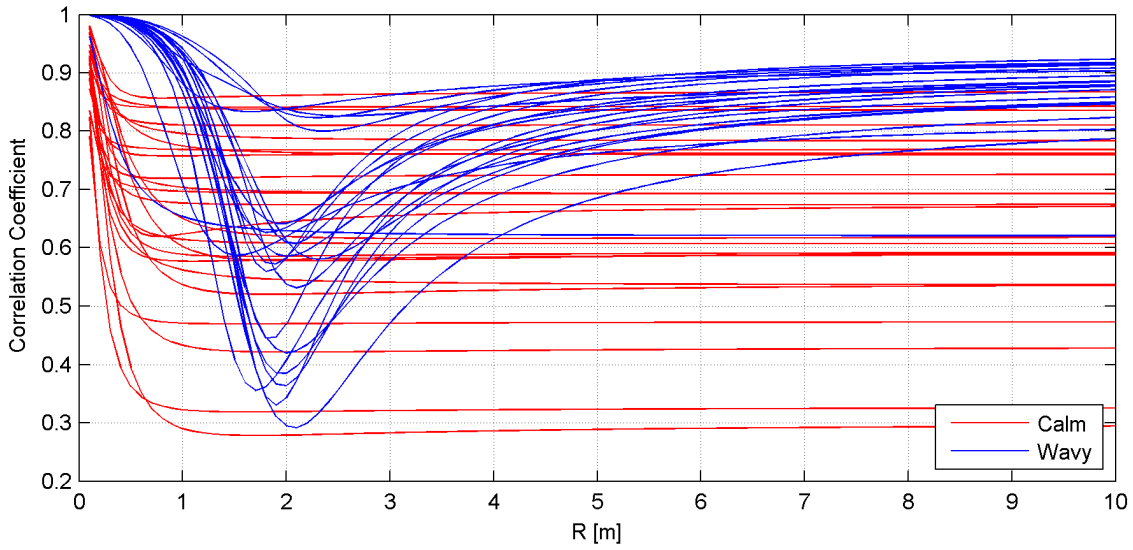

Figure 33: Correlation coefficients between depth averaged ${u_x}^{\hat{\mathbb{I}}}$ and ${V_{xu}}^{\mathbb{I}}$. Different lines are different afternoon transects of June 17, 2014. Red lines indicate morning transects with calm conditions. Blue lines indicate afternoon transects with wavy conditions.

Thus to determine the correct R value, the correlation coefficient is calculated for transects with high frequency motion for various R. The R value with the smallest absolute correlation is assumed to be correct. An example is shown in Figure 33. For wavy conditions there is a clear minima suggesting there is a optimal point between under and over correction. If the process is repeated for calm conditions, the correlation is small and asymptotic for a multitude of large Rs, indicating there is little need for correction and roll is not significant. R is taken as a constant within individual transects or time period on the same scale, assuming similar wave conditions and boat orientation.

Discard

Because a singular GPS cannot resolve the orientation of the boat, for wavy conditions where the sensor is inaccurate, the transects are discarded. Ultimately, this only eliminated 15 transects from June 18, 2014 out of the 198 total transects from all field campaigns.

3.2.3 Transect Post-Processing

By the end of both dual and singular ADCP processing, the resultant measurements consist of current velocity measurements whose direction and bin location are in fixed earth coordinates $\mathbb{E}$ and sample time is synced to GPS UTC. These measurements are presented as $\overrightarrow{u_E} = [u_e(o_{bin}, e, n, t), u_n(o_{bin}, e, n, t), u_o(o_{bin}, e, n, t)]$ where e, n, t are depth uniform and e and n are a function of t. Subscripts and super scripts regarding coordinate systems will be dropped from this point on.

For the spatial reconnaissance and turbine prototype measurements, there is no need for a further coordinate transformation since their objectives are primarily concerned with current velocity magnitudes. However, for the transect measurements, it is desired to transform the measurements into a coordinate system relative to the transect or channel cross section, $\mathbb{T}$, to facilitate volume flux calculations and ebb/flood delineation.

First, each transect measurement at time t is mapped to a coordinate D along its corresponding charted transect as shown in Figure 34. For every transect the origin of D is

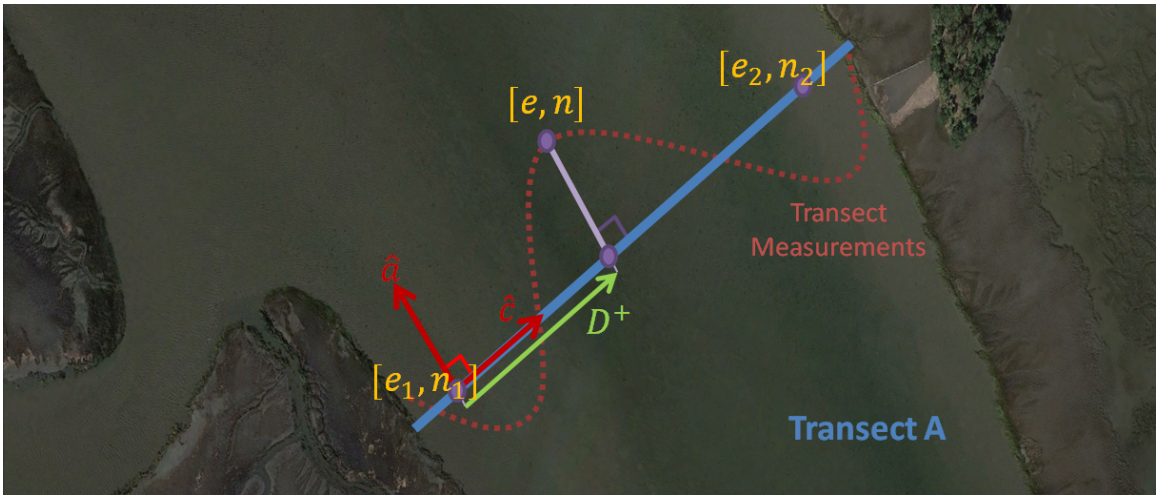

Figure 34: Example of measurement mapping to charted transect. Measurement locations with regards to charted transect exaggerated

taken to be west-most charted way point defining the transect and is positive moving eastward. Because the boat track is not perfectly linear or matching the charted transect, D is calculated as the distance along the transect of the perpendicular intercept formulated as

$$D = \sqrt{(e_D - e_1)^2 + (n_D - n_1)^2} \left(\frac{e_D - e_1}{|e_D - e_1|} \right) \tag{31}$$

where $[e_1, n_1]$ are the east and north coordinate of the most easterly way-point of the charted transect and $[e_D, n_D]$ is the east and north coordinate of the perpendicular intersection of the measured coordinate $[e, n]$ and charted transect. $[e_D, n_D]$ can be solved through the linear system of

$$\begin{bmatrix} e_D \\ n_D \end{bmatrix} = \frac{-m}{m^2 + 1} \begin{bmatrix} 1 & -1 \\ -\frac{1}{m} & m \end{bmatrix} \begin{bmatrix} n_1 - me_1 \\ n + \frac{e}{m} \end{bmatrix} \tag{32}$$

where m is the slope of the charted transect provided by

$$m = \frac{n_2 - n_1}{e_2 = e_1} \tag{33}$$

where $[e_2, n_2]$ are the east and north coordinate of the most westerly way-point of the charted transect. Coordinates of the waypoints for each charted transect are summarized in Table 4. This coordinate transformation reduces the dimensionality of the measurement coordinates so that each bin measurements is located by $[o_{bin}, D, t]$.

Table 4: Way-points for charted transects in field campaigns. Coordinates are in UTM Zone 17R and CORS 96 datum.

Transect	Way-point 1		Way-point 2	
	Easting [m] e_1	Northing [m] n_1	Easting [m] e_2	Northing [m] n_2
A	486264	3531386	486501	3531680
B	485916	3532180	486218	3532174
C	485371	3531730	485503	3532052
D	486345	3531321	486582	3531614
E	486182	3531452	486420	3531746
F	486527	3531120	486850	3531344
G	486138	3531477	486367	3531818

Next, the velocities undergo a directional coordinate transformation from east (E) and north (N) to axial (A) and cross (C). Cross is oriented along the transect, or in other words cross-channel, and is positive for the easterly direction. Axial, perpendicular to cross, is positive in the northernly direction, or in other words, flood flow. Ebb flow, in the southernly direction back out to the open ocean is negative. This directionality and relation to tidal cycle is used for all transects. Because the charted transects were orientated perpendicular to channel curvature, it is designed for the axial component to capture the majority of streamwise flow. The coordinate transformation is carried out through

$$\overrightarrow{u_{\mathbb{T}}} = \mathbf{M}_{\mathbb{E}}^{\mathbb{T}} \overrightarrow{u_{\mathbb{E}}} \tag{34}$$

using the transformation matrix $\mathbf{M}_{\mathbb{E}}^{\mathbb{T}}$ given by

$$\mathbf{M}_{\mathbb{E}}^{\mathbb{T}} = \begin{bmatrix} -\sin {\alpha_{\mathbb{T}}}^{\mathbb{E}} & \cos {\alpha_{\mathbb{T}}}^{\mathbb{E}} & 0 \\ \cos {\alpha_{\mathbb{T}}}^{\mathbb{E}} & \sin {\alpha_{\mathbb{T}}}^{\mathbb{E}} & 0 \\ 0 & 0 & 1 \end{bmatrix} \tag{35}$$

where ${\alpha_{\mathbb{T}}}^{\mathbb{E}}$ is the angle of the charted transect given as

$$\alpha_{\mathbb{T}}^{\mathbb{E}} = \arctan m \tag{36}$$

The final current measurements used for hydrodynamic analysis are $\overrightarrow{u_{\mathbb{T}}}$ in transect coordinates, $\mathbb{T}$. The transect current measurements also undergo a spatial moving average filter with a window of 15 m in D and 1 m in O about each measurement bin.

Measurement in transect coordinates are then used to calculate aggregate quantities of the transects such as volume flux (Q) and kinetic energy flux (Q_{KE}). Volume flux for a given transect at t_t is calculated as

$$Q = \sum_{n=1}^{N} \sum_{k=1}^{K} w_n h_{n,k} u_{an,k} \tag{37}$$

where N represents the total number of data points along the transect, w_n is the D distance along the transect between the midpoints of the two adjacent data points, $h_{n,k}$ is the vertical bin width for the given bin k, K is the total number of vertical bins for a given lateral data point n, $u_{an,k}$ is the axial current velocity for a given bin, and t_t is the timestamp assigned to the transect, the midpoint of the boat traversal. Kinetic energy flux is calculated similarly as

$$Q_{KE} = \sum_{n=1}^{N} \sum_{k=1}^{K} \frac{1}{2} \rho w_n h_{n,k} u_{an,k} |u_{a_{n,k}}^2 + u_{c_{n,k}}^2| \tag{38}$$

For $k = 1$ or K, $h_{n,i}$ is expanded to include the ADCP blanking distance and distance from the last bin to the depth recorded by the ADCP respectively. The extrapolations of the bottom bin to the seabed is expected to have little effect on flux calculations since $u_{an,K}$ is assumed to be boundary layer flow. However, since surface flows are generally faster, the extrapolation of $u_{an,1}$ across the blanking distance increases flux magnitudes as well as the measurement uncertainty slightly.

3.2.4 Measurement Uncertainty

The uncertainty associated with the measurements and calculated values is presented in this section. For GPS position measurements of the base station and rovers, the standard deviation σ, is provided by the programs $GRAFNAV$ and $GRAFNET$ as a time series and the daily average is presented in Table 5. Overall the combined errors are small and less than 5cm. This is excellent resolution for horizontal position, good resolution for water level tidal stage measurements, and inadequate for measuring water level gradients across the domain.

Uncertainty for the current measurements provided by $WinRiverII$ through a measure known as the *error velocity*, ϵ_v (Teledyne RD Instruments, 2007). The four beam measure

Table 5: Standard Deviation (σ) of GPS measurements provided by GrafNav.

October 2010				
	σ_E (Easting [m])	σ_N (Northing [m])	σ_H (Horizontal [m])	σ_O (Vertical [m])
Base Station	-	-	0.007	0.005
Bow Rover	0.013	0.013	-	0.031
November 2011				
	σ_E (Easting [m])	σ_N (Northing [m])	σ_H (Horizontal [m])	σ_O (Vertical [m])
Base Station	-	-	0.007	0.005
Bow Rover	0.011	0.014	-	0.026
December 2011				
	σ_E (Easting [m])	σ_N (Northing [m])	σ_H (Horizontal [m])	σ_O (Vertical [m])
Base Station	-	-	0.007	0.005
Bow Rover	0.012	0.012	-	0.025
June 14, 2014				
	σ_E (Easting [m])	σ_N (Northing [m])	σ_H (Horizontal [m])	σ_O (Vertical [m])
Base Station	-	-	0.008	0.005
Bow Rover	0.014	0.014	-	0.029
Stern Rover	0.017	0.015	-	0.042
June 15, 2014				
	σ_E (Easting [m])	σ_N (Northing [m])	σ_H (Horizontal [m])	σ_O (Vertical [m])
Base Station	-	-	0.007	0.005
Bow Rover	0.013	0.013	-	0.040
Stern Rover	0.014	0.013	-	0.027
June 16, 2014				
	σ_E (Easting [m])	σ_N (Northing [m])	σ_H (Horizontal [m])	σ_O (Vertical [m])
Base Station	-	-	0.007	0.005
Bow Rover	0.015	0.013	-	0.029
Stern Rover	0.012	0.016	-	0.035
June 17, 2014				
	σ_E (Easting [m])	σ_N (Northing [m])	σ_H (Horizontal [m])	σ_O (Vertical [m])
Base Station	-	-	0.008	0.005
Bow Rover	0.012	0.013	-	0.027
Stern Rover	0.014	0.019	-	0.053
June 18, 2014				
	σ_E (Easting [m])	σ_N (Northing [m])	σ_H (Horizontal [m])	σ_O (Vertical [m])
Base Station	-	-	0.008	0.005
Bow Rover	0.012	0.015	-	0.039

of velocity of the ADCP instrument is redundant, only three beams is needed for a fully defined measurement. The fourth beam however is used to decrease variance in the data, check that all four beams are measuring the same flow field, and provide a measure of the ϵ_v. ϵ_v is the difference between the two vertical velocity measurements of the two three beam solutions. The measure helps aggregate the resultant effects of different broadband ADCP parameters such as bin size and sampling rate that can affect resolution and accuracy. The standard deviation of the error velocity is considered a good estimate of the random error (Teledyne RD Instruments, 1996).

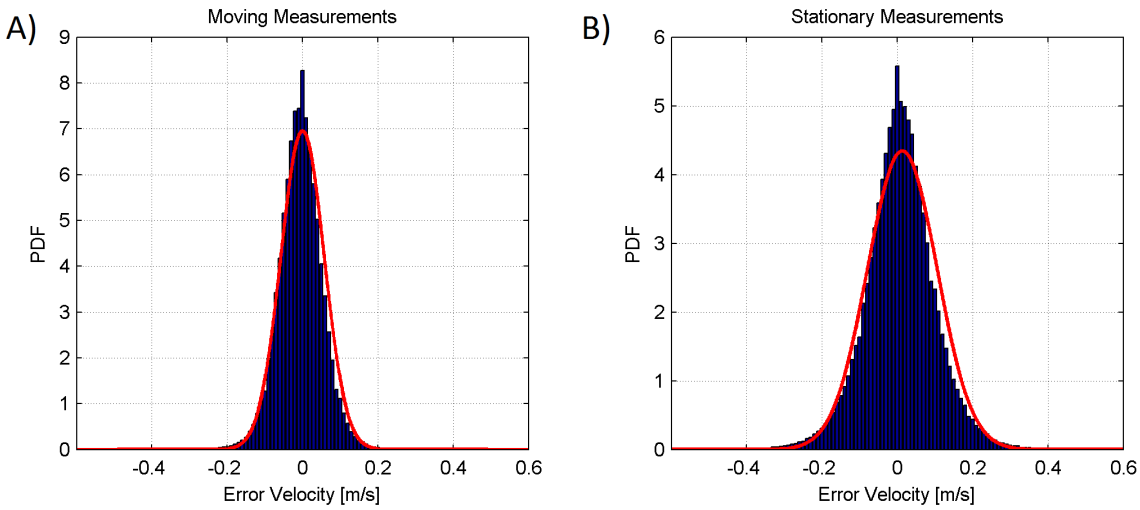

Figure 35: Probability density functions (PDF) of error velocities for all ADCP bin measurements. Blue bars are empirical distributions and red lines are Gaussian fits. *A)* Measurements from transects and moving measurements. Mean of Gaussian fit: 2x10^{-}4 m/s; standard deviation 0.057 m/s. *B)* Measurements from anchored turbine measurements. Mean of Gaussian fit: 0.01 m/s; standard deviation 0.092 m/s.

The error velocities are output as a single value, scaled for horizontal velocity magnitudes, in instrument coordinates (with no apparent motion removed) for each bin in a ping, or measurement. This value is sensitive to the pitch and roll, larger for rapidly changing conditions, and can be thought of a maximum error that is reduced with processing (Teledyne RD Instruments, 2007). Probability density functions of the error velocities for all the bin measurements is shown in Figure 35. Overall the error is smaller for moving measurements (Figure 35A) than the anchored turbine measurements (Figure 35B). This is due to the smaller bin widths and thus sample size within a bin for the anchored tests. Fitting a Gaussian curve to the velocity errors, the mean and standard deviation for the moving measurements are 2 x 10^{-4} m/s and 0.057 m/s and for the stationary measurements are 0.013 m/s and 0.092 m/s.

Bias error is present in the ADCP uncertainty as well; it is dependent on various factors: beam geometry, signal/noise ratio, mean current velocity, and temperature. Bias is typically less than 0.01 m/s (Teledyne RD Instruments, 1996).

CHAPTER IV

ESTUARINE TIDAL HYDRODYNAMICS

For the resource assessment, numerical model data is utilized to provide water level and current velocity information extending beyond the time and length scales of available field data. Data from an existing 3D FVCOM numerical model application of the Ogeechee Estuary are utilized for constituent calculations and hydrodynamic predictions of water levels and volume fluxes of measured transects. The field measurements however are used to validate and understand model output.

First it is important to accurately represent and understand the incoming kinetic energy flux to the localized domain. This is governed by the large scale hydrodynamics of the encompassing estuary. Previous studies have characterized the Ogeechee, as well as other wetland estuaries in the US Southeast as heavily distorted or asymmetric (Blanton et al., 2002; Huang et al., 2008; Zheng et al., 2003). For these estuarine systems, with extensive and shallow intertidal wetlands, the distortion is an effect of significant bottom friction and intertidal storage.

This chapter contains the characterization of the distortion and large scale hydrodynamics in the in the Ogeechee Estuary and immediate flow to Rose Dhu Island. First, the numerical simulation is described and its large scale hydrodynamics validated using the field data presented in Chapter III. Next, the physical mechanisms of wetland tidal distortion is explained as well as a novel statistical method to quantify it. This methodology is then used on data from simulations ran with varying friction and storage parameters to quantify their relative importance on distortion and the estuarine tidal hydrodynamics. This knowledge is important for accurately assessing the incoming theoretical kinetic energy and foreseeing estuarine scale effects of energy extraction.

4.1 Numerical Simulations

A 3D FVCOM numerical model application of the Ogeechee Estuary has been developed by Bomminayuni et al. (2012). A brief description of the model, base simulation, and varying parameters relating to tidal distortion is provided first. A summary of the specified model parameters for all the simulations is shown in Table 6. Second, the accuracy of the simulations are compared using field measurements from Chapter III and a simulation is chosen for the resource assessment.

Table 6: Simulation descriptions for predicted surface heights and volume fluxes. o_m is representative wetland elevation. f_b and f_m are channel bottom and wetland frictional parameters respectively.

	Simulation Name	Model Parameters			
		o_m [m] [MTL]	f_b	f_m	$\frac{f_m}{f_b}$
Increasing Marsh Elevation ↓	A1	0.3	0.0025	0.025	10
	B1	1.0	0.0025	0.025	10
Decreasing Marsh Friction ↓	A3	0.3	0.0025	0.05	20
	A2	0.3	0.0025	0.0025	1
Increasing Domain Friction ↓	C2	0.3	0.01	0.01	1
	E1	0.3	0.02	0.02	1

4.1.1 Specifics of Numerical Simulations

FVCOM is a three-dimensional, free-surface primitive equations model originally developed by Chen et al. (2003). The model uses unstructured triangular grids in the horizontal and σ-coordinate transformation in the vertical for a better representation of the irregular bottom topography. The governing equations of the model are the momentum and continuity equations which are closed using the Mellor and Yamada level 2.5 turbulence scheme for vertical mixing and the Smagorinsky turbulence closure scheme for horizontal (Mellor and Yamada, 1982; Smagorinsky, 1963). The governing equations are solved in the integral form by computing fluxes between non-overlapping horizontal triangular control volumes.

A more detailed description of the modeling approach is available in the user manual (Chen et al., 2006).

The computational domain includes the main channel and intertidal marsh zones of the entire Ogeechee Estuary as shown in Figures 4 and 36. Specifying marsh zones as any location with elevation above mean tidal level, 49.3% of the inland wetted surface area is classified as wetland. The horizontal grid spacing is 300 m at the open boundary (located in the ocean) and varies between 20 to 100 m in the tidal channels of the estuary. The model utilizes 10 layers in the vertical direction; for the deepest channel in the estuary with water depth of 10 m, this corresponds to a vertical resolution of 1 m. The mean water depth at each of the numerical grid points is calculated through an interpolation of bathymetric data consisting of field measurements and survey data from the NOAA database.

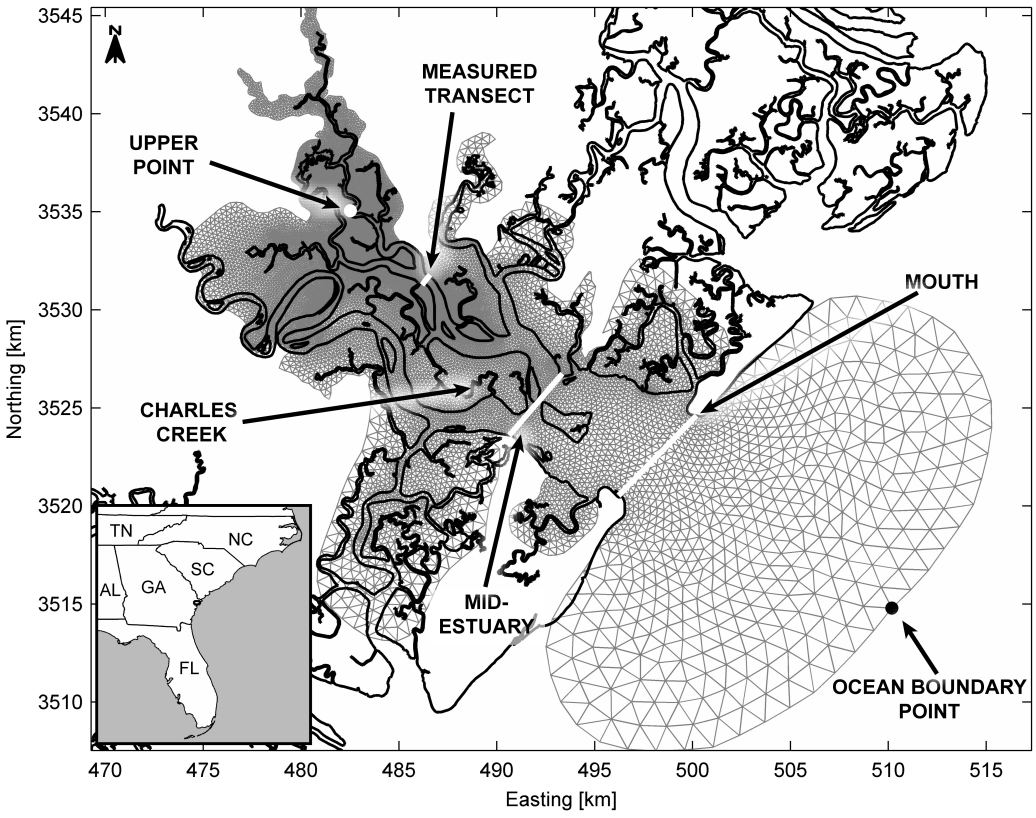

Figure 36: Map of Ogeechee Estuary and model domain. Referenced points and transects in text labeled. Inset image: Map of Southeastern United States for geographic reference.

The model is driven by 6 major tidal constituents (S2, M2, N2, K2, K1, and O1) specified at the open boundary; the amplitudes and phases are computed from the ADCIRC tidal database (*http://www.unc.edu/ ims/ccats/tides/tides.html*). The water levels and current magnitudes within the domain are zero initially and the tidal forcing at the open boundary is ramped up to its actual value over two days to avoid any numerical instability. In total, the simulation is run over a 45 day period (November 16 to December 29, 2011) with a time step of 1.25 seconds in baroclinic mode to encompass the 2011 field campaigns. Stream water input is not included in the model because this estuary is primarily tidally driven with a small watershed and minimal freshwater flow (Dame et al., 2000).

4.1.1.1 Intertidal Storage

FVCOM includes a wet/dry point treatment technique to simulate the flooding and draining processes over the intertidal zones in the estuary. Wet and dry points in the computational domain are distinguished through the local total water depth (H) calculated as the sum of mean water depth and water surface elevation. If H is greater than the thickness of the viscous layer specified at the bottom, H_{min}, the grid cells are treated as wet and vice-versa. A dry grid cell is assigned zero velocity with no flux entering through the boundaries to facilitate total mass conservation. All simulations are performed with a $H_{min} = 5$ cm.

Simulation B1 uses a different data source than the others for its representation. Simulation B1 is modeled using data from the National Wetlands Inventory (NWI) consisting of sparse measured data from the 1980s. The other simulations are modeled using high resolution 2009 LIDAR elevation data of Chatham and Bryan County published from NOAA and Savannah Area Geographic Information System in 2012. When discussing wetland elevation o_m, the average value for the upper estuary near the measured transect is used. Although marsh elevations are variable, the parameter o_m effectively highlights the net effect of the intertidal storage on the hydrodynamic forcing between the upper estuary and open ocean. o_m is 0.3 m and 0.9 m for the LIDAR and NWI data respectively.

4.1.1.2 Domain and Marsh Bottom Friction

Bottom friction in FVCOM is calculated using a drag coefficient (C_D) formulation

$$\tau_x, \tau_y = \rho * C_D * \sqrt{u.^2 + v.^2} * (u, v) \tag{39}$$

where ρ is the density of water, τ_x, τ_y are the bed shear stresses and u, v are the velocities in x, y orthogonal directions of the grid cell respectively. The drag coefficient C_D is determined by matching a logarithmic bottom layer at a height z_{ab} above the bottom

$$C_D = max\left(\frac{k^2}{\ln\left(\frac{z_{ab}}{z_o}\right)^2}, f\right) \tag{40}$$

where $k = 0.4$ is the von Karman constant, $z_0 = 0.001$ is the bottom roughness parameter, and f is the input friction coefficient that can be varied.

Simulations A2, C2, and E1 are run with different values of this parameter (f_b) applied uniformly across the domain. In addition f is enhanced to various degrees for grid cells with mean water depth greater than zero, i.e., the intertidal zones (f_m), to investigate the effect of increased marsh vegetation on flow characteristics in Simulations A1, A2, and A3. The values of f_b and f_m are presented in Table 1 for each simulation. A base value of 0.0025 is used for f_b as suggested by Chen et al. (2003), used by others (Huang et al., 2008; Weisberg and Zheng, 2008; Zheng et al., 2003), and shown in measurements from a nearby Georgia estuary (Seim et al., 2002). This value is increased and decreased by various orders of magnitude for both f_b and f_m to observe the relative influences.

To choose the best simulation for the resource assessment, the simulations are compared to the field measurements using various skill scores. The model simulations are then compared with each other and measurements along the estuary to accurately describe the tidal distortion of the system and its susceptibility to these parameters; highlighting the importance of their accuracy.

4.1.2 Simulation Selection

In order to evaluate the efficacy of the model to simulate the large scale hydrodynamics of the estuary, volume fluxes, Q, and water surface heights relative to the mean tidal level (MTL), η, are compared between measurements (subscript f) and simulation output (subscript m).

The transect utilized for volume flux comparison is Transect A since it has the most available transect measurements spanning over numerous campaigns as well as swift currents. To calculate Q_m from the model output, raw simulation data from the unstructured grid are interpolated onto a grid with the same vertical grid resolution along the predetermined transect. Velocities are transformed to obtain the axial and cross channel velocities using Equation (34). Volume fluxes are calculated using Equation (37). Constituents of the volume flux are calculated using the MATLAB program TTIDE created by Pawlowicz et al. (2002) and used to predict a model Q_m value for each measurement timestamp t_f as explained in Equation (1). The timestamp assigned to a Q_f measurement is midway through each transect, which took on average 5 minutes to transverse.

Similarly, for η_f, the average water level is taken along a measurement transect and assigned to the timestamp of the midpoint t_f. For η_m, a representative water level timeseries is pulled from the midpoint of the model transect and used to calculate constituents and to predict $\eta_m(t_f)$ values for all measurement days. For days without measured transects such as October 20, 2010 and June 14-16, 2014; model water levels are predicted at uniform 15 minute timesteps (t_m) as in the original simulation, for the particular day. Water levels measurements are averaged in 15 minute windows centered about the model timestamp time (t_m) to provide an $\eta_f(t_m)$ for each model timestamp.

To quantitatively compare each simulation and measurements, two skill scores with different emphases are used: the CSS score and the Murphy Score. For reference, in these equations x can be Q or η, $\bar{x}$ is the average, k is the particular observation/simulation pair, and K is the total number of pairs. A description of each score is provided below.

The CSS score, as used by Timko et al. (2012) and defined by Von Storch and Zwiers (2001); is insensitive to the differences in amplitude and evaluates the accuracy of the phase. The score for a quantity, x, is calculated as

$$CSS = \frac{\sum_{k=1}^{K}(x_m(k) - \bar{x}_m)(x_f(k) - \bar{x}_f)}{\sqrt{\sum_{k=1}^{K}(x_m(k) - \bar{x}_m)^2 \sum_{k=1}^{K}(x_f(k) - \bar{x}_f)^2}} \tag{41}$$

A value of $CSS = 1$ signifies model is related to the measurement by an increasing monotonic function while $CSS = 0$ signifies complete disagreement, and $CSS = -1$ signifies the

model is related to the measurement by a decreasing monotonic function. In this study the CSS score is representative of the signal shape and tidal distortion accuracy.

The Murphy Score, as defined by Murphy (1988), is given by

$$MS = 1 - \frac{\sum_{k=1}^{K}(x_m(k) - x_f(k))^2}{\sum_{k=1}^{K}(x_f(k) - \bar{x}_f)^2} \tag{42}$$

where a MS is a scaled representation of the mean squared error (MSE) of the model with regards to the measurements. An MS value of 1 represents zero error or discrepancy between model and measurements. $MS = 0$ indicates the MSE of the model and measurements is the same as the variance of the measurements where $MS < 0$ indicates the MSE of the model and measurements is greater than that of the measurements themselves. The Murphy Score is used to evaluate a simulation's ability to capture the correct amplitude of the measurement. Using the amplitude centric MS score in tandem with the signal shape concerning CSS score, the study uses a holistic methodology to assess the accuracy of each simulation.

The measurements are presented in Figures 37 and 38 along with the two model Simulations A1 and B1, representing an envelope for all the simulation results. Skill scores between the measurements and all simulations are shown in Tables 7 and 8A-D. First, the skill scores are calculated by summing all measurement/model comparisons across all the field campaigns to gather an aggregate description of the simulation accuracy (Table 7). However, realizing the accuracy of a simulation varied between different phases of the tidal cycle (as is clear in Figures 37 and 38), and some phases were more heavily measured than others, skill scores are computed for specific tidal stages (Tables 8A-D). The results of both methods of comparison are discussed below.

Considering all field campaigns, all simulations show good agreement with the water level measurements for both distortion (CSS) and amplitude (MS) with average values of 0.97 and 0.86 respectively. The simulations with the LIDAR wetland elevations (A1, A2, A3, C2, E1) perform markedly better than that of the NWRI (B1) for both MS and CSS scores. Distortion slightly improved with increased domain friction (Simulations A2→C2→E1).

The skill scores for the volume fluxes from all the campaigns have similar magnitudes

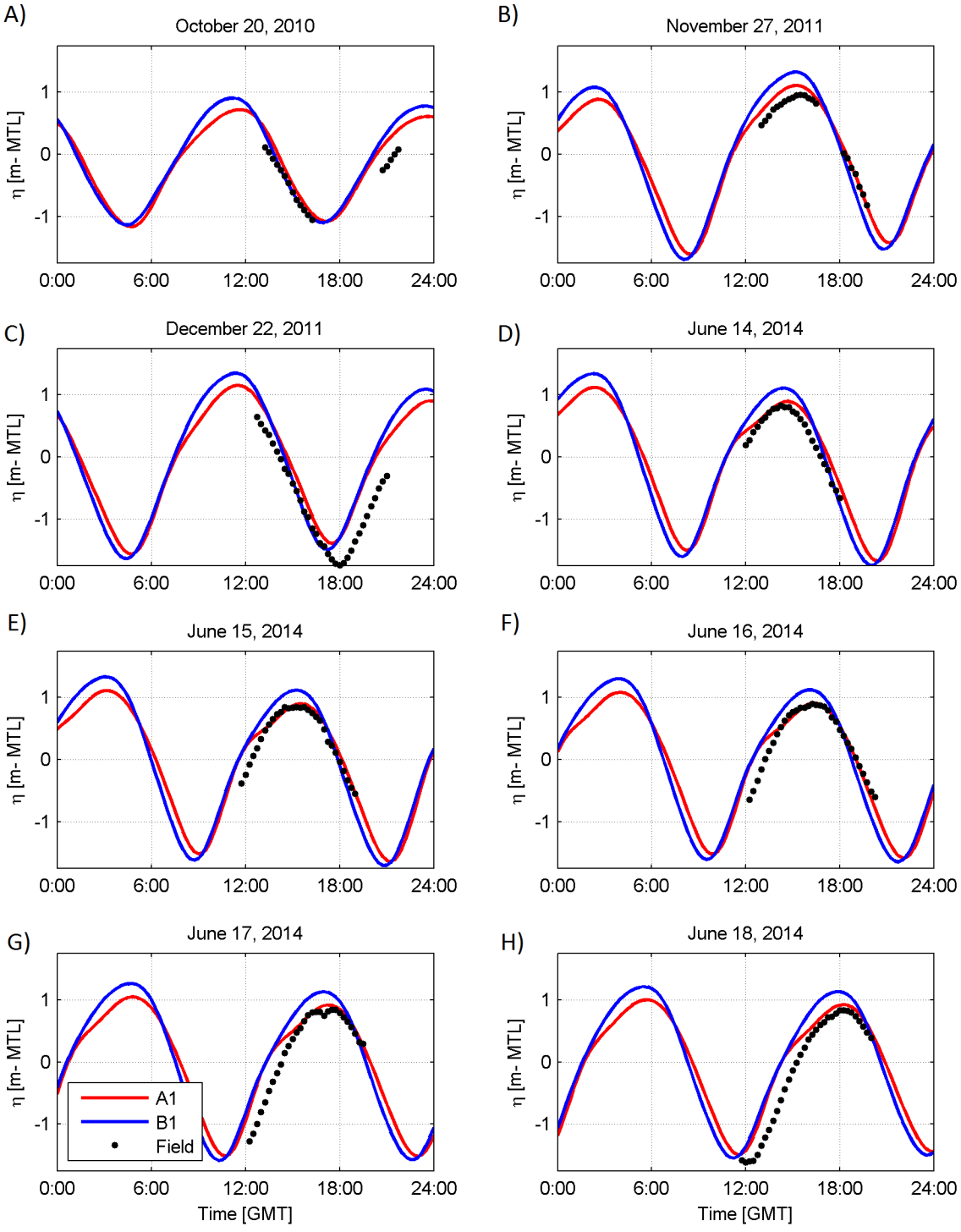

Figure 37: Comparison of water level η between model and field measurements in MTL.

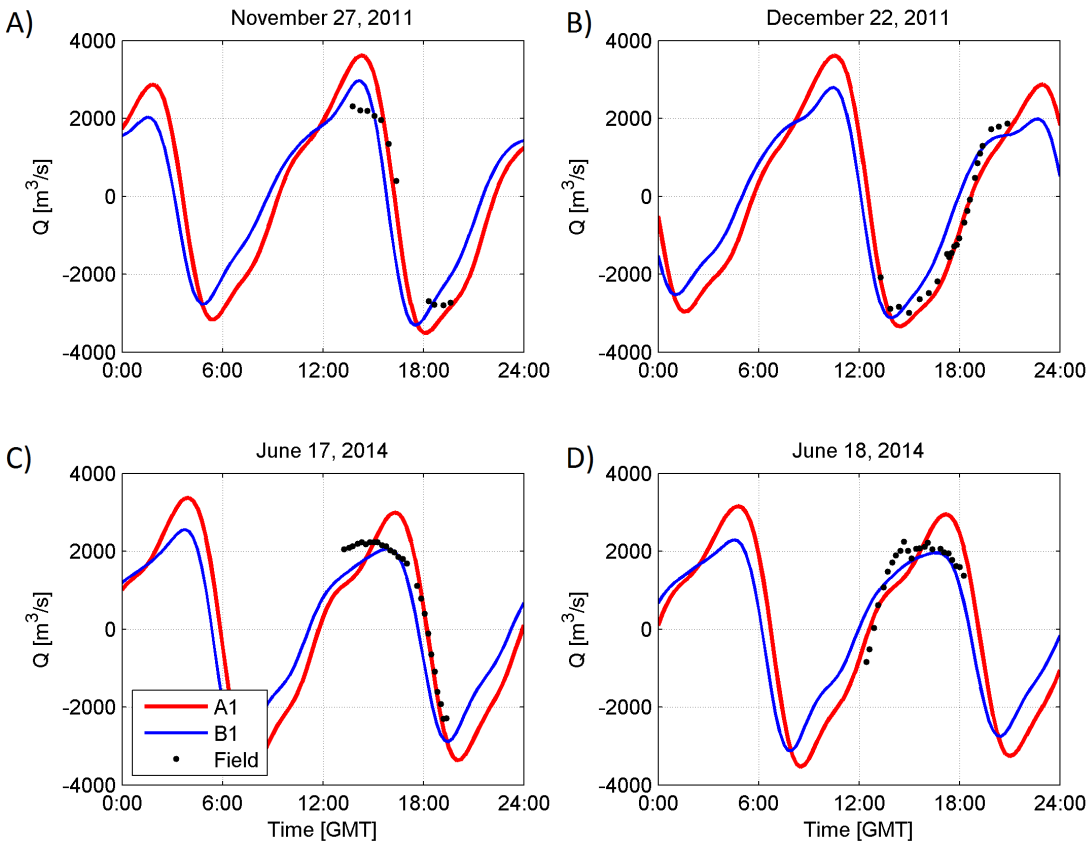

Figure 38: Comparison of volume flux Q between model and field measurements for Transect 12. Positive Q represents flood volume fluxes while negative Q represents ebb.

and show good agreement as in the water level scores. Again, the LIDAR simulations mostly perform better, however Simulation B1 has a markedly higher MS score for Q then it did for water levels, even surpassing the one LIDAR Simulation A2. Q skill scores for simulations varying in domain friction are less conclusive than for water levels.

To gain further insight into the performance of the simulations, skill scores are calculated for particular tidal phases. The tidal cycle is delineated into four phases: peak flood; flood to ebb transition; peak ebb; and ebb to flood transition. Peak periods are delineated by a cut-off value for the fluxes: above 75% of the absolute peak measurement volume flux for that day. Thus, only days with volume flux measurements are considered, November 27 and December 22, 2011 and June 17-18, 2014; the skill scores are presented in Tables 8A-D.

For the peak flood phase, the simulations in Table 8A clearly show a discrepancy between model and measurements for all simulations. Such discrepancy is clearly shown in Figures

Table 7: Skill scores between measurements and simulations aggregating all measurements.

ALL MEASUREMENTS	Simulation Name	Surface Height		Volume Flux	
		CSS	MS	CSS	MS
Increasing Marsh Elevation ↓	A1	0.97	0.86	0.96	0.89
	B1	0.95	0.76	0.93	0.85
Decreasing Marsh Friction ↓	A3	0.97	0.86	0.96	0.90
	A2	0.97	0.86	0.95	0.84
Increasing Domain Friction ↓	C2	0.98	0.87	0.95	0.89
	E1	0.98	0.86	0.94	0.87

37, 38 and 39 as well. All simulations have good and consistent agreement with water level distortion around 0.97; however amplitude skill scores drop drastically with the NWRI Simulation B1 having the worst at 0.21. MS scores increase with domain friction, most likely due to dampening of the system to reduce the model tidal range.

The volume fluxes for peak flood phases show the poorest skill scores for all of the phases with a minimum MS of -31 and CSS of 0.01. Simulation B1, with the old elevation data, has markedly the best congruence in distortion and amplitude; although both still relatively poor compared to those of other phases. Although showing a small increase in amplitude skill, increased domain friction reduces distortion skill significantly, except when there is enhanced marsh friction as in Simulations A1 and A3.

For the transition between flood and ebb, the simulations in Table 8B show much improvement in volume flux scores however a slight reduction in surface height agreement. Agreement for surface height distortion is relatively consistent between simulations, however decreases with increased domain friction. The MS value shows a clear decrease in amplitude agreement, with the NWRI simulation having the worst.

The volume fluxes have improved distortion and amplitude agreement for the ebb-flood transition. Distortion skill scores are consistently high, with Simulation B1 having the lowest around 0.94. However there is a greater variation in MS with Simulation B1 having the worst at 0.22 and those with enhanced marsh friction, Simulations A1 and A3, having the best at 0.8 and 0.81.

Table 8: Skill scores between measurements and simulations for different tidal phases.

A) PEAK FLOOD	Simulation Name	Surface Height		Volume Flux	
		CSS	MS	CSS	MS
Increasing Marsh Elevation ↓	A1	0.98	0.59	0.10	-25.26
	B1	0.99	0.21	0.48	-5.00
Decreasing Marsh Friction ↓	A3	0.98	0.56	0.12	-22.57
	A2	0.97	0.67	0.05	-31.56
Increasing Domain Friction ↓	C2	0.98	0.75	0.02	-20.48
	E1	0.98	0.80	0.01	-20.10

B) FLOOD → EBB	Simulation Name	Surface Height		Volume Flux	
		CSS	MS	CSS	MS
Increasing Marsh Elevation ↓	A1	0.89	0.27	0.97	0.80
	B1	0.89	-2.46	0.94	0.22
Decreasing Marsh Friction ↓	A3	0.89	0.20	0.97	0.81
	A2	0.84	0.44	0.97	0.66
Increasing Domain Friction ↓	C2	0.81	0.63	0.98	0.75
	E1	0.78	0.28	0.99	0.75

C) PEAK EBB	Simulation Name	Surface Height		Volume Flux	
		CSS	MS	CSS	MS
Increasing Marsh Elevation ↓	A1	0.97	0.86	0.82	-0.85
	B1	0.96	0.88	0.02	-1.40
Decreasing Marsh Friction ↓	A3	0.97	0.90	0.78	-0.39
	A2	0.97	0.67	0.87	-3.86
Increasing Domain Friction ↓	C2	0.96	0.45	0.86	0.16
	E1	0.96	0.33	0.80	-3.19

D) EBB → FLOOD	Simulation Name	Surface Height		Volume Flux	
		CSS	MS	CSS	MS
Increasing Marsh Elevation ↓	A1	0.97	-0.85	0.96	0.91
	B1	0.94	-1.21	0.95	0.63
Decreasing Marsh Friction ↓	A3	0.97	-0.91	0.97	0.91
	A2	0.97	-0.62	0.95	0.90
Increasing Domain Friction ↓	C2	0.99	-0.52	0.97	0.86
	E1	0.97	-0.66	0.98	0.78

For the peak ebb phase, the simulations in Table 8C again show good distortion agreement around 0.97 in water levels and varying agreement in amplitude. Increased domain friction reduces amplitude agreement again most likely due to reduction in tidal range. Since the opposite effect is shown in MS scores for the peak flood stage, this highlights that the simulations are over predicting high tide and under predicting low tide; a uniform scaling will not improve results or distortion in water levels.

For the peak ebb volume fluxes, simulations with the LIDAR data have good distortion agreement with an average of 0.85. Simulation B1 has a drastically different MS score of 0.02. This difference between the LIDAR and NWRI simulation CSS scores is much greater than the improvement of Simulation B1 for the peak flood stage, and could be considered more significant. The MS scores varied, with Simulations B1 and the domain frictional extremes A2 and E1 having the worst with scores less than -1.

For the transition from ebb to flood, the simulations in Table 8D show good distortion agreement around 0.97 in water levels and poor agreement in amplitude. Again, Simulation B1 performs the worst for both distortion and amplitude at 0.94 and -1.21 respectively. For volume fluxes all simulations have good distortion agreement above 0.95. Good amplitude agreement was present as well but with greater variation; simulations with enhanced friction have higher values of 0.9, simulations with increased domain friction have lower values, and Simulation B1 had the lowest with 0.62.

Ultimately, for choosing a simulation, more emphasis is placed upon the distortion, or CSS score. This is because discrepancies in amplitude could be more or less accounted for by a scaling factor whereas distortion error is not uniform. Also distortion governs the duration of peak flow, which will be shown to be significant for energy calculations in Chapter VI. More emphasis is placed upon volume flux skill scores as well since it is more directly relevant for a hydrokientic energy assessment. With all of this in consideration, the Simulation A1 is chosen for the energy assessment since it consistently is among the top performers for all phases.

While the skill scores provide a measure of congruence with the measurements, they do not provide a physical interpretation of the variation in hydrodynamics. This knowledge is

useful for troubleshooting numerical models for other wetland estuaries that could be used for resource assessments. Since the presented study is to act as a primer for other assessments in wetland estuaries, this information is discussed and explored further. A physical interpretation of the estuarine hydrodynamics is provided below with an emphasis on the unique tidal distortion that accompanies wetland estuaries.

4.2 Principles of Estuarine Tidal Distortion

Tidal distortion refers to the condition where tidal stages have unequal strength or duration. For both surface heights and tidal currents it can refer to the relative magnitude and breadth of peaks and troughs, or the relative slopes of periods of increase and decrease. Generally an inference is made that shorter rising tides equate stronger flood currents or a flood dominated system and shorter falling tides equate an ebb dominated system. The distortion itself arises from the superposition of principle astronomical constituents and higher harmonics formed from non-linear processes. Although numerous non-linear processes exist, tidal distortion within shallow estuaries is thought to be caused by two principle processes: 1) bottom friction and 2) intertidal storage (Friedrichs and Aubrey, 1988; Parker, 1991; Speer and Aubrey, 1985).

Significant bottom friction is classically identified as a mechanism to induce flood dominated tides (Speer and Aubrey, 1985). Bottom friction opposes the direction of flow and dissipates kinetic energy. However with more momentum loss per unit volume at lower water levels, the effect is stronger at low tide. As a result wave propagation at low tide slows, inducing a steepening of the wave form between the estuary and ocean. This increases the floodward pressure gradient and resultant currents, hastening the rising tide (Dronkers, 1986b). Conversely, at high tide friction is less influential and there is no enhancement for ebb currents. Thus flood tide is shorter and stronger than ebb, resulting in a flood dominated system.

Intertidal storage refers to the variable width of channel cross-sectional area with surface height, most notably with intertidal wetlands. Previous studies have associated intertidal

storage with a mechanism to induce ebb dominated tides (Blanton et al., 2002; Dronkers, 1986b; Friedrichs and Aubrey, 1988; Speer and Aubrey, 1985; Friedrichs and Perry, 2001; Lawrence et al., 2004). When surface heights rise and inundate the banks of flat and expansive wetlands, the surface area of the channels increase dramatically. By continuity the rate of surface level rise decreases, increasing the floodward pressure gradient between the estuary and ocean, leading to a surge in flood currents. During ebb tide, the rate of water level decrease above the wetland banks is reduced as well and enhances the ebb gradient and currents. Thus the storage itself does not induce distortion between ebb and flood current magnitudes, but rather it alters the relative timing of peak ebb and flood tides.

Depending on whether the wetland elevation is lower or higher than the mean tidal level (MTL), peak flood and ebb tides either occur closer to low water and the flood to ebb transition is longer, or vice versa (Blanton et al., 2002; Dronkers, 1986b). The distortion in magnitude lies in the increased role of friction and shallow water advection in the wetlands. Wave propagation at high tide is slowed in the marshes due to the shallow depths (Speer and Aubrey, 1985). As a result, water level decreases at a slower rate in the wetlands than the main channel. This water level differential induces an additional pressure gradient and inclination to drain the marshes, leading to stronger and shorter ebb tides (Boon and Byrne, 1981; Dronkers, 1986b).

4.2.1 Statistical Quantification

Typically, the distortion of an estuarine system is characterized by the relative amplitude and phase of a principle constituent and its first harmonic (Friedrichs and Aubrey, 1988). For much of the global coasts, including the US east coast, this is the M_2 constituent and M_4 overtide. A single constituent comparison is accurate if the M_4 overtide is the dominant higher harmonic. However, if others are significant, such as shown for the Ogeechee in Appendix A and other studies, the analysis needs to be repeated and compared for each additional overtide (Blanton et al., 2002). Because the analysis of this study extends across the estuarine domain with varying and multiple overtide amplitudes, this study uses

statistical calculations on full time series in lieu of constituents to succinctly quantify the aggregate distortion.

To quantify and compare the degree of tidal distortion across the domain and between simulations, the statistical asymmetry and skewness are calculated for surface height and volume flux time series from the simulation output. Previously used for applications such as nearshore wave analysis, skewness , S_x, and asymmetry, A_x, of a signal x, are given by Elgar and Guza (1985) as

$$S_x = \frac{\frac{1}{T}\sum_{t=1}^{T}(x(t)-\bar{x})^3}{\left(\frac{1}{T}\sum_{t=1}^{T}(x(t)-\bar{x})^2\right)^{\frac{3}{2}}} \tag{43}$$

and

$$A_x = S_{imag(\mathcal{H}(x))} \tag{44}$$

respectively where $x(t)$ is the quantity at time indice t, $\bar{x}$ is the mean of $x(t)$, and $\mathcal{H}(x)$ represents the Hilbert Transform of x. Essentially, the asymmetry A_x, is the skewness calculation of the imaginary portion of the Hilbert transform of x.

Asymmetry, A_x, represents the degree of symmetry about the vertical axis. For a time series of surface heights or fluxes, this represents the relative duration of periods of increase and decrease. For positive values of A_x, the rising period is longer than the falling, i.e. troughs appear soon after crests, but crests appear relatively later after troughs. For negative values of A_x the reverse is true; the falling period is longer than the rising and crests appear soon after troughs.

Skewness, S_x, refers to the degree of asymmetry about the horizontal axis, taking into account the relative broadness and magnitudes of the peaks and troughs. For surface height and volume flux time series, this represents the relative duration and magnitude of high/low tide and ebb/flood durations respectively. For positive S_x, the crests have larger magnitude than the troughs and are narrower (less temporal duration above the mean). For negative values, the troughs have larger magnitudes and are narrower.

Table 9 shows the asymmetry and skewness calculations for Transect A volume fluxes and water levels for every simulation. Q and η were derived from interpolated model data, as described in Section 4.2, for the entirety of the original model output for November 16

to December 29, 2011 (i.e. no constituent calculations or predictions). These statistical values are referenced throughout the rest of the chapter in discussing the distortion of the estuarine hydrodynamics.

Table 9: Calculated Skewness and Asymmetry Parameters for Measured Transect

	Simulation Name	Surface Height		Volume Flux	
		Asymmetry	Skewness	Asymmetry	Skewness
Increasing Marsh Elevation ↓	A1	0.022	-0.31	0.67	-0.13
	B1	0.070	-0.20	0.73	-0.34
Decreasing Marsh Friction ↓	A3	0.019	-0.29	0.68	-0.12
	A2	0.044	-0.38	0.67	-0.18
Increasing Domain Friction ↓	C2	-0.021	-0.39	0.58	-0.13
	E1	-0.072	-0.38	0.50	-0.084

4.3 Generalized Estuarine Hydrodynamics

Flux/stage plots from Simulation A1 for the three transects identified in Figure 36 are shown in Figures 39A-B and highlight the general distortion features characteristic to the estuary and common to all the simulations. For correct chronological order, the diagrams should be read counter-clockwise. In Quadrants I-II for Figures 39A, the effect of intertidal storage is clear. As η rises above the wetland tidal flat elevation (o_{mA1}), there is a drastic change in slope signifying a decrease in the rate of water level rise relative to the increase in flood volume fluxes. Similar to Blanton et al. (2002) and Lawrence et al. (2004), this is a result of the increased pressure gradient between the swiftly rising ocean and slowly rising estuarine waters. After peak high tide in Quadrant II, the volume flux changes rapidly from a flood to ebb current while the water level falls slowly due to the same differential in pressure gradient. Once the water level falls below o_{mA1}, the enhanced pressure gradient is reduced and the slope is steeper in Quadrant IV (signifying a faster/slower change in η/Q respectively). It is shown in Figure 39B extensive intertidal storage with an elevation above the MTL produces peak ebb and flood fluxes near high tide (Blanton et al., 2002; Dronkers, 1986b).

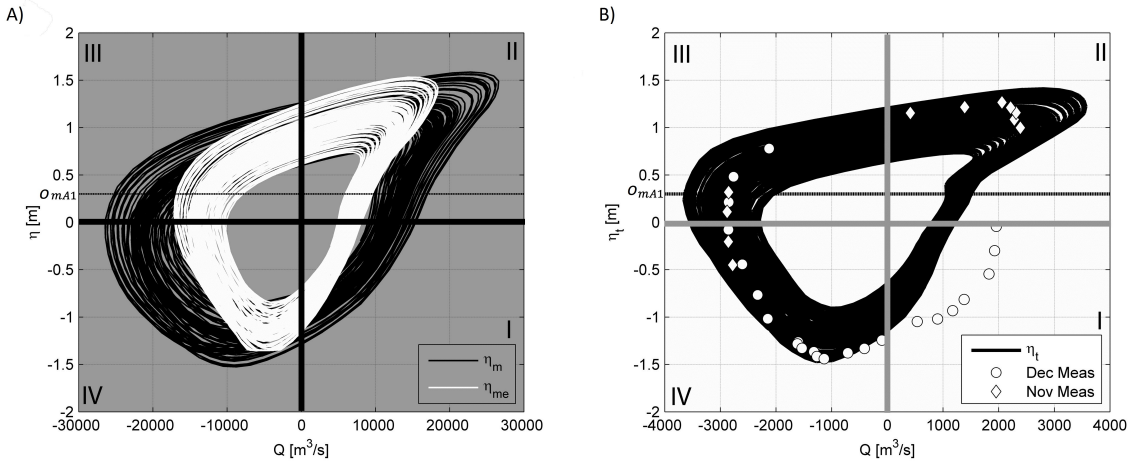

Figure 39: Flux/stage diagrams for Simulation A1 at different cross sections defined in Figure 36. *A)* Diagrams for estuary mouth, η_m, and mid-estuary, $\eta_m e$. *B)* Diagram for measured transect, η_t. Horizontal black lines represent marsh elevation o_{mA1}. All surface heights in MTL. Positive Q represents flood volume fluxes while negative Q represents ebb. Period represented: Entire duration of model simulation November 16 -December 29. 2011.

This qualitative description of the tidal distortion is supported by calculations of skewness and asymmetry for the η and Q time series for the three transects from Simulation A1 in Table 10. For all transects, $A_Q > 0$, signifying peak ebb currents follow shortly after peak flood. Negative values of S_η indicate a longer high tide with less magnitude. Further up the estuary, S_η increases in magnitude, demonstrating the presence of the increased pressure gradient between the lower and upper estuary. A slight ebb dominance in the estuary is indicated with $S_Q < 0$ for all transects; this is not clearly apparent in Figures 39A-B. This suggests the differential of wave celerity between the main channel and the intertidal storage induces an additional inclination and ebb dominance Boon and Byrne (1981); Dronkers (1986b). This increased inclination for the measured transect well inside the estuary, is indicated by a positive A_η, a shorter falling tide.

Interestingly, $A_\eta < 0$ for the mouth and mid-estuary due to the absence of significant intertidal storage. The deep, broad channels with minimal wetland coverage near the estuary mouth do not have extensive flooding and drainage to induce an additional ebb inclination. In the absence of extensive intertidal storage, the growth of the compound constituents from

Table 10: Calculated Skewness and Asymmetry Parameters For Simulation A1 across Estuary.

Distance Along Estuary ↓	Surface Height		Volume Flux	
	Asymmetry	Skewness	Asymmetry	Skewness
Mouth	-0.011	-0.016	0.52	-0.014
Mid-Estuary	-0.067	-0.080	0.62	-0.025
Transect	0.022	-0.31	0.67	-0.13

the nonlinear continuity, friction, and inertial terms dominate, and produce negative asymmetry (Parker, 1991). The volume flux from the mouth to the mid estuary transect has a 30% decrease, clearly highlighting the storage capacity of the preceding wetlands, although not enough to make $A_\eta > 0$. However further up the estuary, wetland coverage expands, the channel cross sections bifurcate, and the volume flux for the measured transect is reduced by a full order of magnitude. Therefore the impact of the intertidal storage dominates and the skewness and asymmetry are largest in magnitude at the measured transect, which is furthest up the estuary.

Ultimately for the Ogeechee Estuary, the relative timing of peak ebb and flood currents, or A_Q, is an estuary scale feature and governed by the pressure gradient between the upland wetlands and open ocean influenced by the spatial gradient of S_η. However flood or ebb dominance, governed by S_Q and A_η, appear to be more localized with increased ebb distortion further up the estuary as wetland coverage increases.

4.4 Hydrodynamic Effects of Marsh Elevation

It is clear from Section 4.3 that the intertidal storage provided by the wetlands has significant influence on the tidal distortion of the Ogeechee Estuary. It is known that the distortion effects of intertidal storage is heavily dependent on the height of the tidal flats in relation to MTL (Blanton et al., 2002; Dronkers, 1986b). Thus the accuracy of the estuary model clearly hinges on the correct representation of the intertidal storage, particularly the wetland elevation. The LIDAR data used for the wetland elevation for Simulation A1 is generally

accepted to be more accurate than the NWI data used for Simulation B1 (Brock and Purkis, 2009; Hladik and Alber, 2012).

This is reflected in the skill scores shown in Table 6. The skill scores for both η_t and Q are much higher for Simulation A1, an improvement for η_t and Q of 3 and 7%. As shown in Figure 37, the water level for Simulation A1 appears more accurate as evident by the higher skill score for η_t. However, for the volume flux it is less clear because the CSS is insensitive to amplitude errors and is only an indicator of phase errors. Thus the discrepancy in time series magnitude is misleading; the shape and distortion of Simulation A1 is in better agreement with the measurements, particularly for the December measurements. The improved skill scores of the water level and fluxes for Simulation A1 indicates the better quality elevations supplied by the LIDAR data improves model distortion accuracy.

To analyze the influence of wetland elevation on the tidal distortion, plots of time series from a representative spring tidal cycle from Simulations A1 and B1 are shown in Figure 40. These plots include the water surface heights at the open ocean boundary and measured transect, the relative surface height difference or pressure gradient proxy between the open ocean and transect, and the corresponding volume fluxes. It is important to note both simulations share the same ocean boundary surface height since they both undergo the same tidal forcing. The corresponding tidal stage diagram is presented as well in Figure 41.

The estuary scale effects of the intertidal storage is seen for the rising tide in Figures 40 and 41. For both Simulations A1 and B1, when the water level surpasses the wetland elevations, (o_{mA1}, o_{mB1}), the rise in η_t decreases (Figure 40A), the ocean/estuary pressure gradient increases (Figure 40B), and there is a resultant surge in Q (Figure 40C). However for Simulation B1 with the higher marsh elevation, the decrease in water level rise rate occurs later with a minimal increase in pressure gradient. This results in a smaller proportion of the tidal cycle spent flooding the intertidal storage. Thus the effects of intertidal storage are not as prevalent in Simulation B1 and are particularly noticeable in Figure 41; the decrease in the rate of η_t rise and surge in Q is not as apparent.

Thus the higher wetland elevation ultimately reduces the distortion effects associated with intertidal storage: a flattening high tide and surges in volume fluxes. However, the

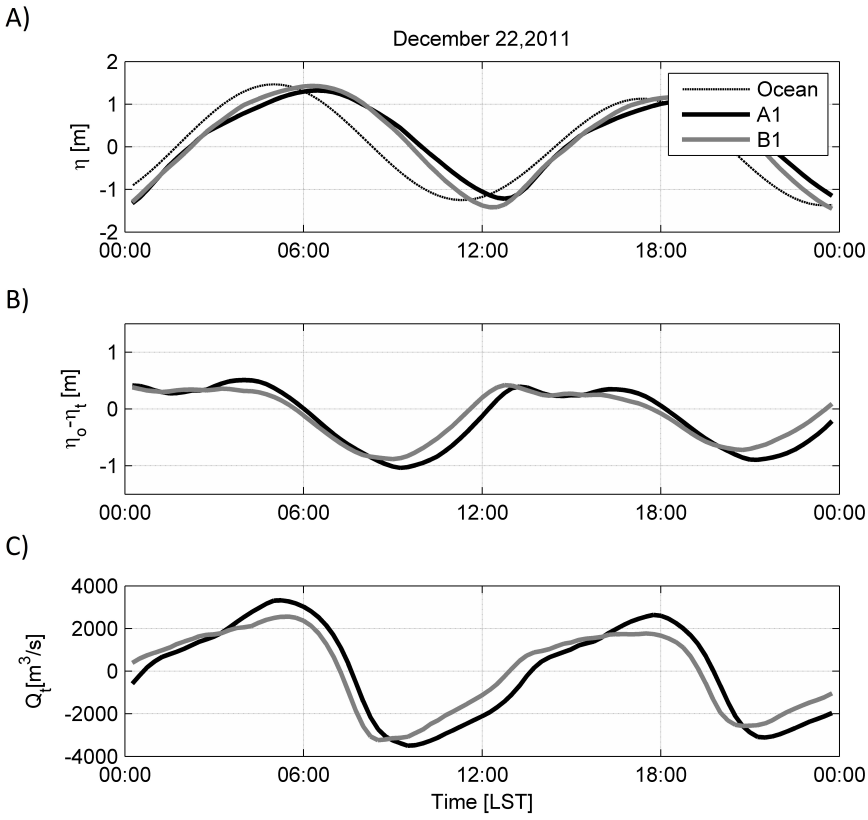

Figure 40: Hydrodynamic effects of change in marsh elevation: time series for Simulations A1 and B1. *A)* Relative surface heights in MTL. *B)* Relative surface height, or pressure gradient proxy, between the open ocean and transect surface heights. *C)* Transect volume flux. Positive Q represents flood volume fluxes while negative Q represents ebb. Date shown: December 22, 2011.

ebb dominance resulting from the intertidal storage is not decreased for the simulation with higher marsh elevation. While Simulation B1 has smaller peak ebb Q than Simulation A1, the relative magnitude compared to the peak flood Q is larger. In addition, the timing between the two peaks in Simulation B1 is shorter, providing a more asymmetric curve.

This is a result of the additional ebb inclination provided by the wetlands. Simulation A1 floods the wetlands earlier and longer. The water depth in the flooded wetlands is more comparable to the channel depth, leading to a smaller differential in wave propagation. Thus the additional ebb inclination is not as large, the wetlands do not drain as fast, and the water level does not drop as fast. Therefore Simulation A1 is less ebb dominant despite having an increased intertidal storage volume.

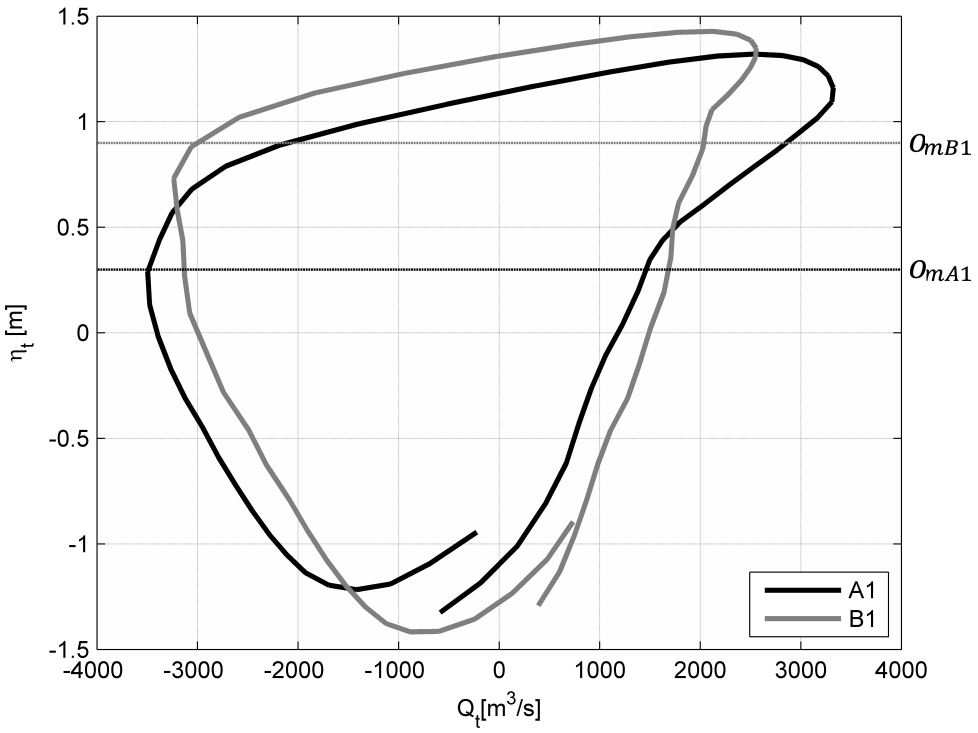

Figure 41: Hydrodynamic effects of change in marsh elevation: flux/stage diagrams for Simulations A1 and B1. Dashed lines represent marsh elevation for simulation. All surface heights in MTL. Positive Q represents flood volume fluxes while negative Q represents ebb. First tidal cycle of December 22, 2011 represented.

The qualitative description of the distortion is supported by statistical calculations presented in Table 9. The flattening of high tide due to the prolonged wetland flooding leads to a more negative S_η for Simulation A1. The shorter falling tide and ebb dominance for Simulation B1 leads to a more positive A_η and negative S_Q. The more positive A_Q highlights that peak ebb and subsequent flood fluxes occur closer together for Simulation B1.

The general response of the Ogeechee Estuary to wetland storage above mean tidal level is for the flow to be ebb dominant. However, increasing the intertidal storage by lowering wetland elevation enhances the effects on high tide and increases volume flux magnitudes, yet decreases the relative ebb-dominance and volume flux asymmetry typically associated with intertidal storage above the mean water level. Therefore, the elevation of the wetlands and not the total storage determines the level of volume flux asymmetry for the Ogeechee Estuary.

4.5 Hydrodynamic Effects of Friction

To evaluate the effect of bottom friction on the distortion, three simulations with different domain friction factors are compared: Simulations A2, C2 and E1 as listed in Table 6. The resultant skill scores for these simulations show little variation which agrees with the findings from Section 4.1.2; the Ogeechee estuarine distortion hydrodynamics has characteristics of a system chiefly governed by intertidal storage. However, the variation in the skewness and asymmetry coefficients for the simulations (Table 9) indicates that there is an effect of bottom friction on the tidal distortion. Therefore it is worthwhile to examine the specific influence of bottom friction on tidal distortion.

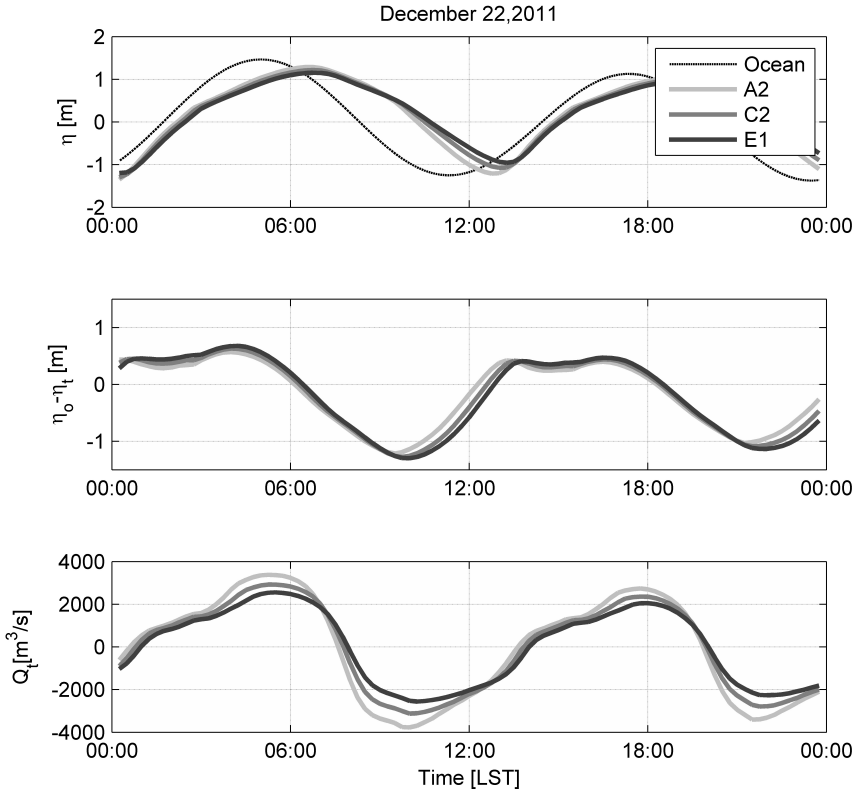

Figure 42: Hydrodynamic effects of change in domain friction: time series for Simulations A2, C2, and E1. Line colors are darker with increasing friction. *A)* Relative surface heights in MTL. *B)* Relative surface height, or pressure gradient proxy, between the open ocean and transect surface heights. *C)* Transect volume flux. Positive Q represents flood volume fluxes while negative Q represents ebb. Date represented: December 22, 2011.

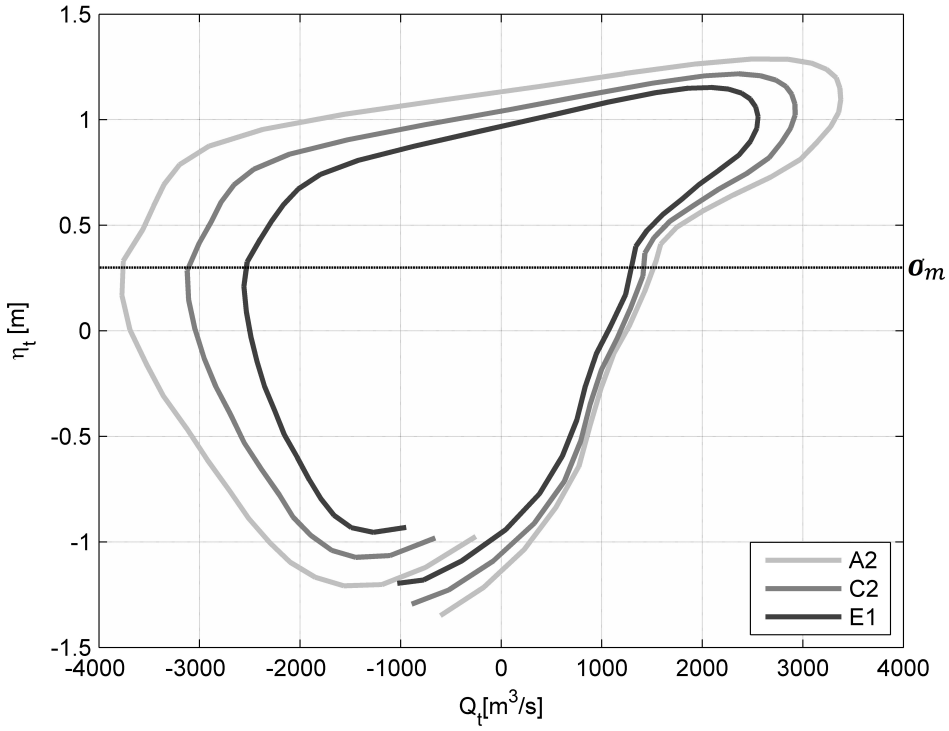

Figure 43: Hydrodynamic effects of change in domain friction: flux/stage diagrams for Simulations A2, C2, and E1. Line colors are darker with increasing friction. Positive Q represents flood volume fluxes while negative Q represents ebb. First tidal cycle of December 22, 2011 presented.

The time series of the water level, pressure gradient, and volume fluxes are shown in Figure 42 and the flux/stage diagram is shown in Figure 43 for the three simulations. Not surprisingly as shown in Figures 42 and 43, the increased friction coefficient leads to reduced velocities, resulting in smaller volume fluxes for both flood and ebb tide. Conservation of mass dictates that the reduced volume flux leads to a smaller total tidal range. This is evident from the reduced water level excursion shown in the flux/stage diagram for Simulation E1 in Figure 43. The effect of the bottom stress is more pronounced for lower water levels. Therefore the reduction of the ebb flux is slightly more significant than the flood flux as shown in Figure 42C. This directly causes the volume flux skewness to be less negative (Table 9).

The increased friction also slows down the speed of the wave propagation, again more so for smaller water depths closer to low tide. Therefore the low tide occurs later for the

higher friction case whereas the lag in the high tide is less significant as seen in Figure 42. As evident in Table 9, the lag in low tide creates much more negative asymmetry in the water levels for higher friction. This is also weakly observed in lags of the peak flood and ebb volume flux leading to a small reduction in positive asymmetry for the volume flux.

Thus increased channel friction in the Ogeechee model simulation does have the expected effects on distortion; the flow is less ebb dominant with increased friction. However, rather than enhancing only the flood pressure gradient, as seen in Figure 42, the pressure gradient for the latter half of the ebb tide is enhanced and extends the duration of the ebb tide making the volume flux skewness more positive.

4.5.1 Effects of Enhanced Marsh Friction

Because the influence of intertidal storage on the model distortion is so dominant, changes in bottom friction have less impact on distortion. However within the intertidal storage itself, friction is enhanced due to the presence of vegetation relative to the channels (Huang et al., 2008; Nepf, 1999). To evaluate the effects of higher bottom friction in the marsh, simulations with various $\frac{f_m}{f_b}$ ratios are compared. Simulations A2, A1 and A3 have a marsh to channel friction ratio of 1, 10 and 20, respectively as shown in Table 6. While the skill scores remain consistently high for these three simulations, the skewness and asymmetry shown in Table 9 do show variability, particularly for the skewness in both water level and volume flux.

The flux/stage diagrams for the three simulations are shown in Figure 44. For the rising tide, upon wetland inundation, simulations with higher marsh friction have a swifter and higher rise of η_t and a slightly smaller floodward surge in Q. Similarly, the tide falls faster and has a smaller surge in Q for ebb tide. This results in a larger and narrower water level crest, i.e. an increase in positive skewness (Table 9). This is because the higher marsh friction reduces the rate of flow into the marsh, thereby causing the water level to remain slightly higher in the channel.

This phenomenon is depicted in Figure 45; the water level height differential represents the lateral extent of the surface heights for the two simulations at high tide. The water

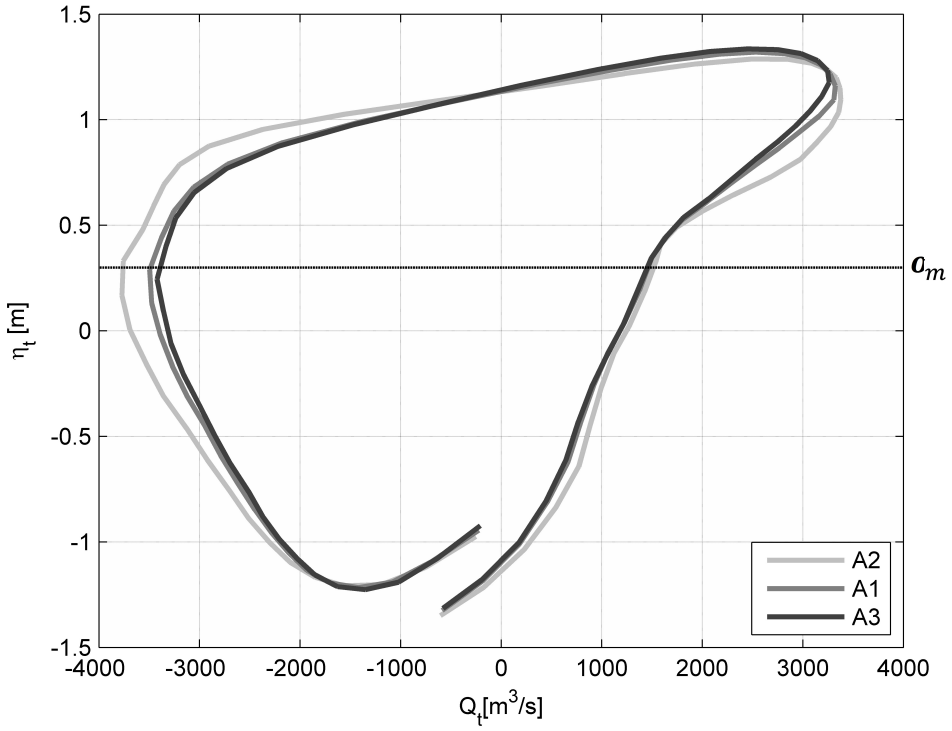

Figure 44: Hydrodynamic effects of change in marsh friction: flux/stage diagrams for Simulations A2, A1, and A3. Line colors are darker with increasing marsh friction. Positive Q represents flood volume fluxes while negative Q represents ebb. First tidal cycle of December 22, 2011 is presented.

surfaces of Simulation A3 with higher friction, do not extend as far into the wetlands but are higher in the channels and adjacent wetlands. Thus increased marsh friction laterally impedes flow and inundation into the wetlands and reduces the effects of intertidal storage. This is further demonstrated by calculations of intertidal marsh volumes. The intertidal volume for each grid cell is calculated as the surface area times the maximum tidal range on December 22, 2011. The ratio of marsh intertidal volume to total volume for Simulations A2, A1, and A3 are 32.7, 30.6 and 29.7% respectively, thereby showing a clear reduction in intertidal storage.

Another impact of the higher water levels in the channels and marshes adjacent to the banks is the depth discrepancy between the channels and the wetlands is not as large, reducing the differential in wave celerity. Thus, the ebb inclination is not as strong and results in a longer falling tide and weaker ebb volume flux. This is further highlighted in

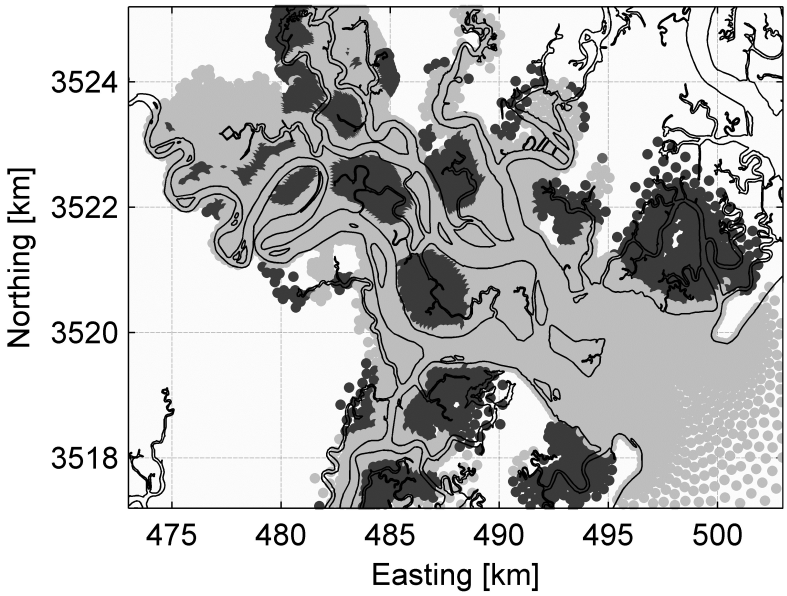

Figure 45: Binary map of differences in surface heights between Simulations A2 and A3 at peak water levels. Dark grey represents areas where water levels are higher for Simulation A2 and light grey represents areas where water levels are higher for Simulation A3

Table 9; water level asymmetry is less positive and volume flux skewness is more positive for simulations with higher marsh friction.

Increased marsh friction reduces lateral spreading and increases flooding depths in wetlands in immediate proximity to the channel banks. This decreases the celerity differential and ebb dominance. As a result, water level skewness and volume flux are more positive whereas water level asymmetry is less positive. Ultimately, it is shown in the Ogeechee model simulations that enhanced marsh friction reduces the effect of wetland intertidal storage on tidal distortion.

4.6 Summary of Estuarine Hydrodynamics

In this chapter, data from various numerical simulations of the Ogeechee Estuary are evaluated against field measurements. Wetland estuaries commonly have a high degree of nonlinear distortion which govern the relative durations and strengths of the tidal stages and thus the overall hydrodynamics and incoming hydrokinetic energy. This type of distortion

is known to be caused primarily by intertidal tidal storage and bottom friction. Parameters relating to these processes are varied between simulations to observe their implications on tidal distortion and improve model accuracy. Field measurements congruence is measured by a skill score and relative distortion is quantified by the statistical parameters asymmetry and skewness. A summary of the results is presented below.

Skill scores assessing the congruence between model and measurements for distortion and amplitude are calculated and compared for tidal phases. Simulation A1, with the more resolute LIDAR elevation, typical domain friction coefficient, and 10x enhanced marsh friction, is chosen because it consistently had reasonable distortion skill scores for all phases. Distortion accuracy is given precedence since it could not be corrected by a simple scaling factor and governs not only the strength but duration of strong volume fluxes and currents.

The distortion of the Ogeechee estuary is primarily governed by intertidal storage. The full estuary system has positive volume flux asymmetry with peak ebb and flood volume fluxes near high tide. However, the degree of ebb dominance illustrated by the surface height asymmetry and the volume skewness calculations across the estuary varies considerably, making the degree of ebb dominance a more localized effect.

Increased channel friction in the Ogeechee Estuary affects tidal distortion; the flow is less ebb dominant with increased friction. Instead of shortening the rising tide, it extends the duration of the falling tide making the volume flux skewness less negative. Increased wetland friction reduces the influence of wetland intertidal storage on tidal distortion. The model suggests an increase in wetland friction does little to dampen wave propagation at high tide but rather impedes the lateral flooding of wetlands, reducing ebb dominance.

CHAPTER V

LOCALIZED TIDAL HYDRODYNAMICS

In this chapter details of the localized hydrodynamics are analyzed to isolate areas of persistently high current velocities suitable for tidal energy extraction. Measurements are used to describe the kinematics, including the axial flow as well as cross channel secondary circulation. Areas of concentrated high kinetic energy, or hotspots, for possible energy extraction are identified. Terms from the momentum balance are then calculated from the measurements and evaluated to determine their relevance to the dynamics of the system.

5.1 Measurement Kinematics

In this section, the kinematics, or current velocity distributions surrounding Rose Dhu Island are discussed. First, the spatial distribution of depth averaged currents are analyzed to isolate an area of high current velocities, known as a hotspot. Secondly, velocity distributions in a transect charted through the hotspot are presented to observe the cross channel and vertical variation. Lastly, transects before, coincident, and past the hotspot are presented to observe the formation and dissolution of the hotspot velocities along the channel.

5.1.1 Current Velocity Characterization + Hotspot Identification

The goals of the 2010 field campaign were to identify hotspots and observe if current velocities were indeed large enough to support tidal energy applications. Each day, currents were measured for both spring flood and ebb tidal cycles on the Vernon and the Little Ogeechee rivers (north and south of Rose Dhu respectively). Depth averaged current magnitudes from the October 19-20, 2010 measurements are presented in Figure 46. The measurements show the Little Ogeechee river boasts much higher currents than the Vernon river with depth average velocities reaching over 1.0 m/s, which is sustainable for turbine rotor rotation and

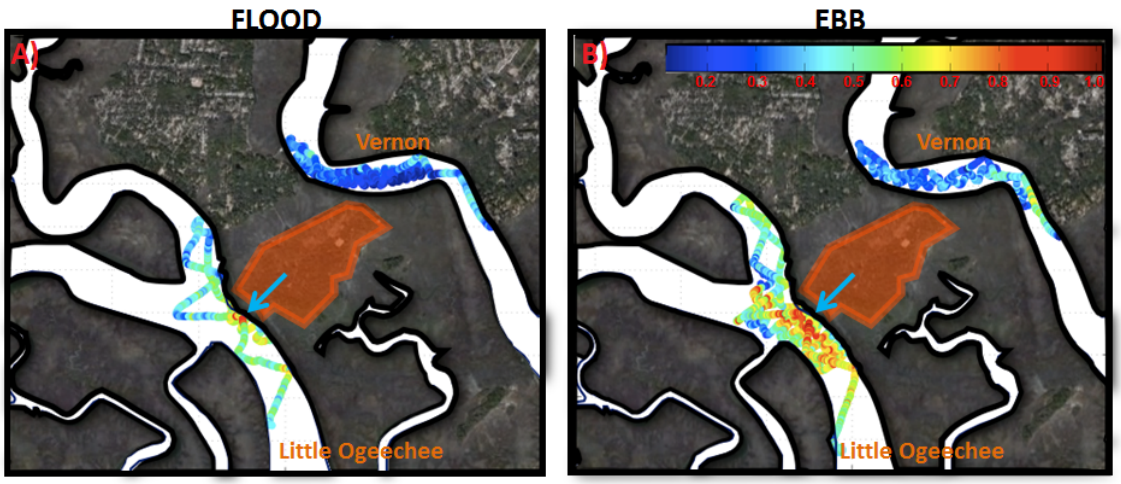

Figure 46: Depth averaged current magnitudes for the Vernon and Little Ogeechee Rivers for October 19-20, 2010 respectively. Currents in cm/s. Blue arrow indicates area of high currents and interest.

thus tidal energy. An area near the bank of Rose Dhu Island highlighted in Figure 46, with high observed currents for both phases, was identified as a potential hotspot for further analysis.

To facilitate a more systematic analysis of the flow in the region around the hotspot, additional measurements along specific transects were completed in 2011 and 2014 as shown in Figure 47. Transect A was charted through the hotspot and repeatedly measured in all subsequent field campaigns in 2011 and 2014. In 2011, Transects B and C were charted to measure the relative distribution of flow between the two channels split from Transect A (Figure 47A). In 2014 additional transects were charted in the nearby vicinity of Transect A to gain further insight into the evolution of flow near the hotspot (Figure 47B). On June 17 Transects D and E were charted to observe the flow in the immediate vicinity of the hotspot. On June 18 Transects F and G were charted to observe the evolution of flow along the channel containing the hotspot.

In addition to spatial resolution, the field campaigns were timed to collectively capture the entirety of the tidal cycle. Because observations are used from all the campaigns to provide a narrative of the tidal cycle, it is important to note there was a slight change in

bathymetry between 2011 and 2014 as shown in Figure 47. An area of particular importance is the topographic bump found in Transect A highlighted by a red circle. In 2014 this feature is more pronounced. While the effects of this feature are somewhat amplified in 2014 as a result, it is shown that the 2011 and 2014 measurements share the same general hydrodynamic processes.

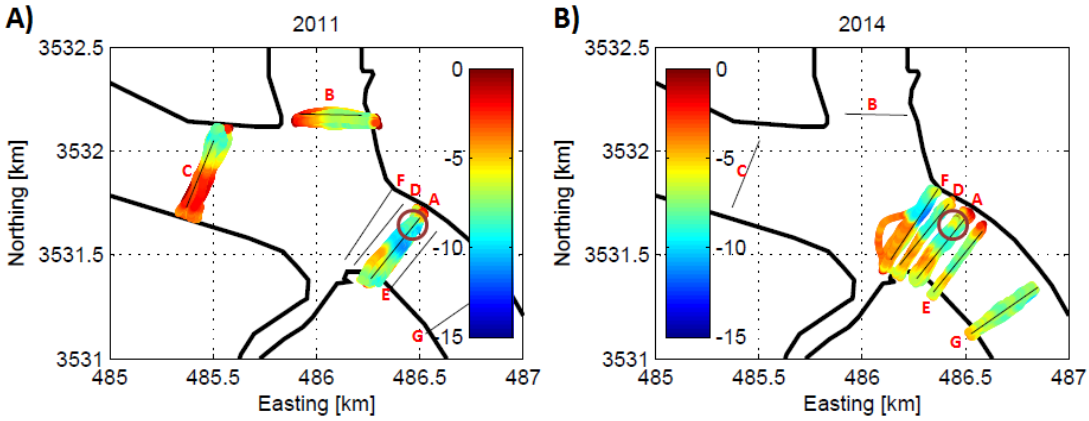

Figure 47: Depth measurements in NAVD88 coordinate system from 2011 *A)* and 2014 *B)* measurements, with depths in meters and transects labels in red. Location of the topographic bump highlighted with red circle.

In addition to the depths collected during the transect measurements, multiple bathymetric surveys were completed in 2010 to provide depth measurements across the localized domain for the numerical model (Bomminayuni et al., 2012). For clarity and further insight into the along channel measurements, the interpolated bathymetric grid used for the numerical model is presented in Figure 48 for reference. A point for consideration is the overall magnitudes of the depths. Areas of interest have at least 2 m of depth. Thus, according to the Froude Number the minimum value to reach super critical flow is 4.42 m/s. Because the field campaigns showed no currents close to this value, in the transect analysis inferences are made based on subcritical behavior throughout the tidal cycle: channel constrictions and a rise in bed elevation lead to increased current velocities, and disturbances can be felt both up and downstream.

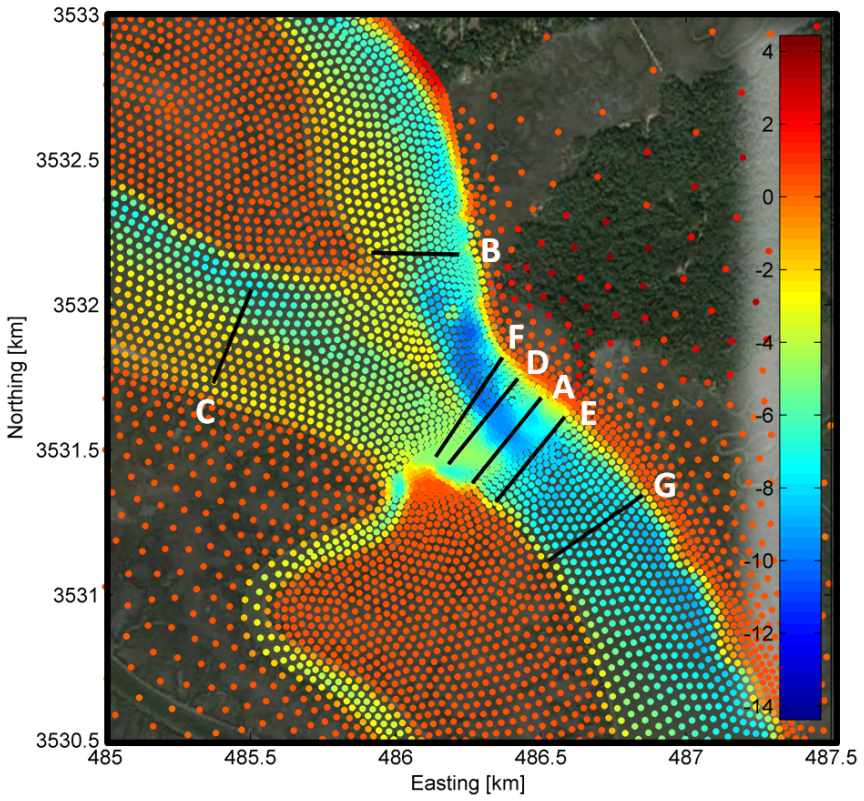

Figure 48: Bathymetric map of numerical model in meters and NAVD88 datum. Depths based on bathymetric surveys (Bomminayuni et al., 2012).

5.1.2 Transect Analysis: Hotspot Temporal Evolution

The temporal evolution throughout the tidal cycle of Transect A and the hotspot is presented in Figures 49-54. Here the transect measurements are mapped and plotted in a coordinate system relative to the most westward waypoint as discussed in Chapter III. The coordinate D represents the distance from the waypoint, reading west to east along the transect; the hotspot is located approximately at $D = 280$ m over the small bump. Axial velocities are contoured (Figures 49, 52) to identify the hotspot as well as cross channel velocities (depth-averaged detrended) (Figures 50, 53) and vorticity (Figures 51, 54) to depict the secondary circulation. Transects representing key distributions are shown; their corresponding volume fluxes are depicted and labeled in the same figure to reference timing in the tidal cycle.

Figures 49-51 highlight the beginning, peak, and diminishing of flood tide as defined by positive volume fluxes. Interestingly, axial flood currents first develop along the seabed

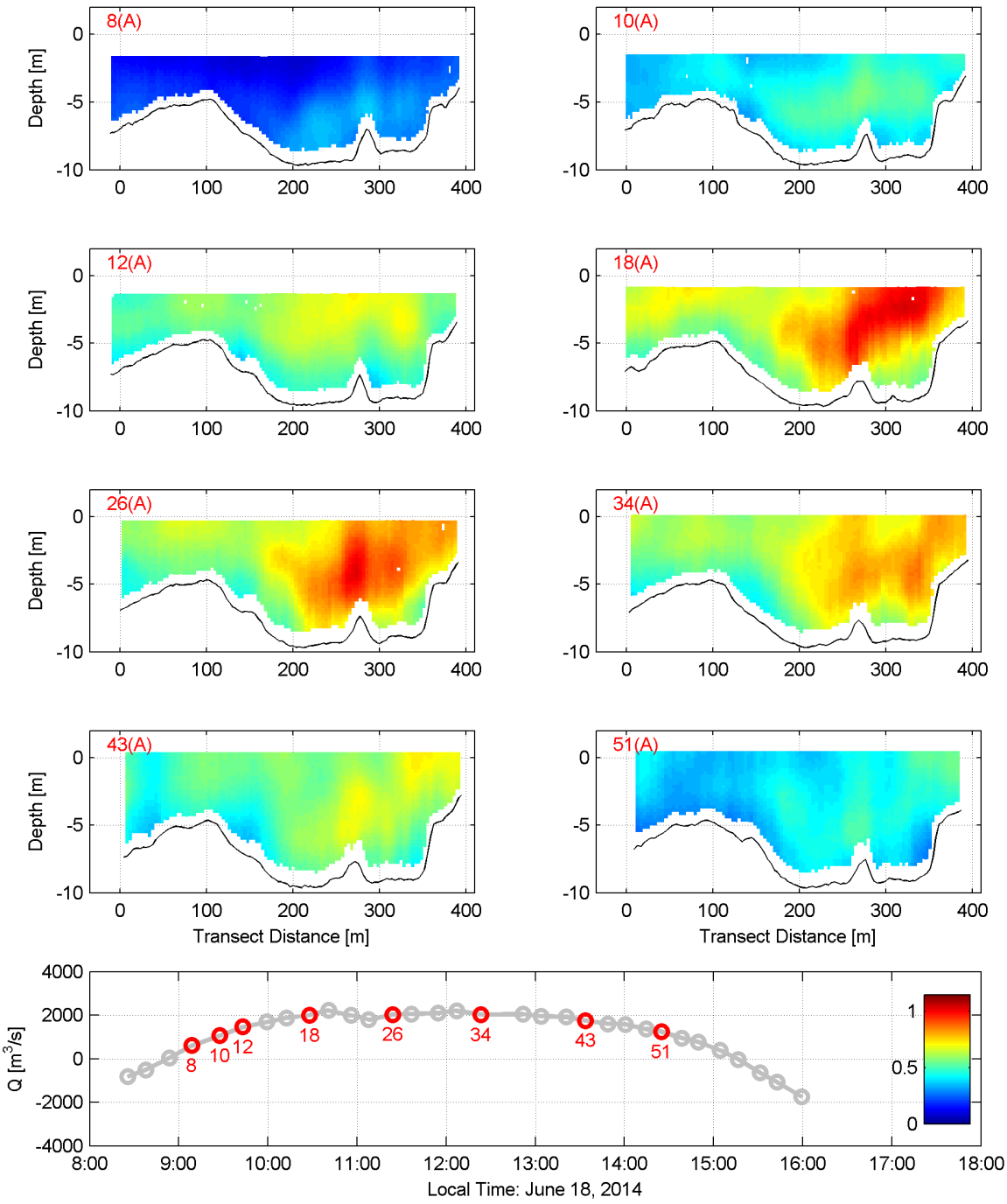

Figure 49: Axial currents [m/s] measured for Transect A on June 18, 2014, representative of a characteristic flood tide. Negative values represents ebb currents and positive represents flood. Transect distance, D is measured relative to the first waypoint identified in Table 4.

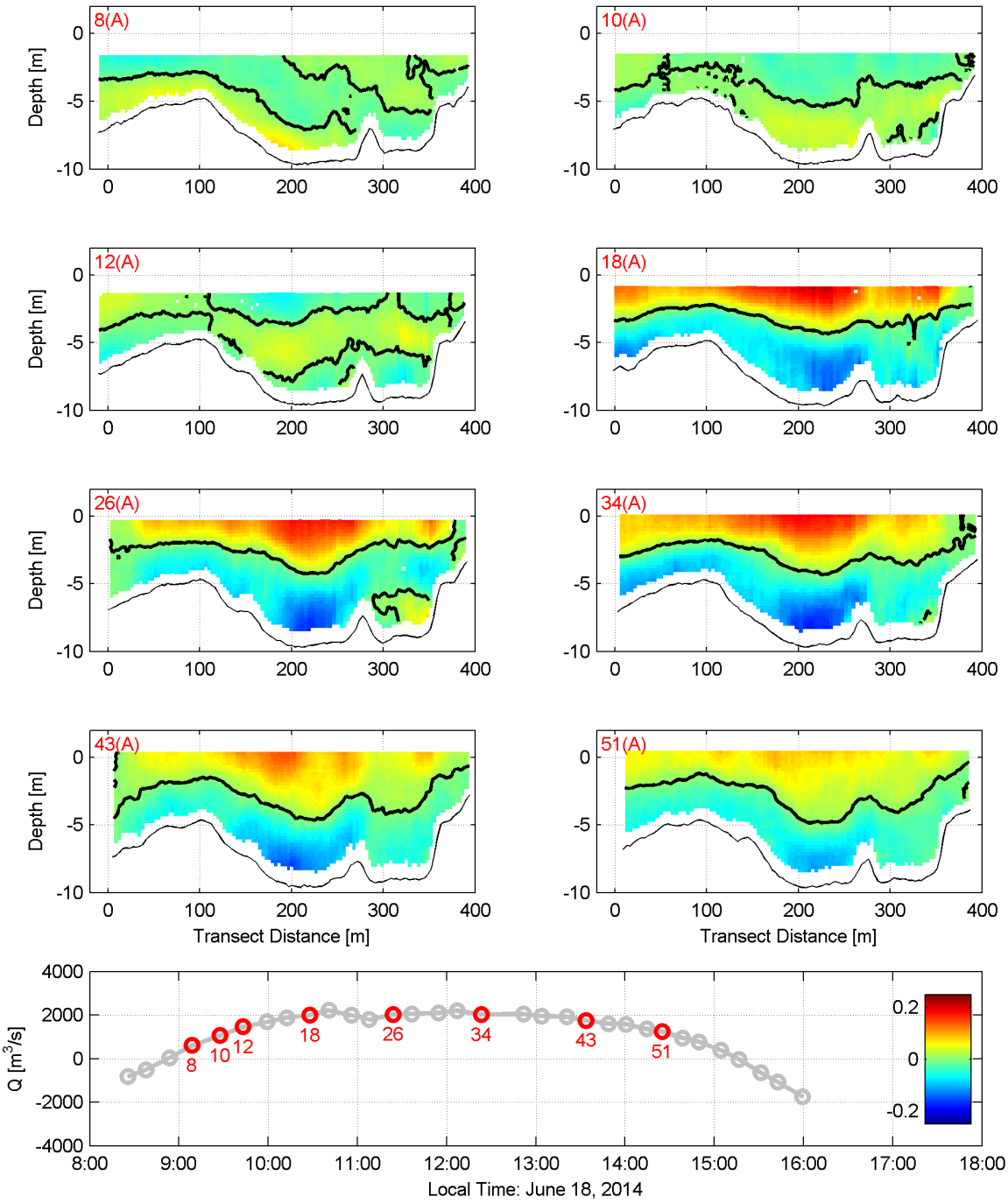

Figure 50: Cross channel currents [m/s] (depth-averaged detrended) for Transect A on June 18, 2014, representative of a characteristic flood tide. Negative values represents currents in the $-D$ direction and positive represents $+D$. Transect distance, D is measured relative to the first waypoint identified in Table 4. Thick black contours represent zero cross channel velocity.

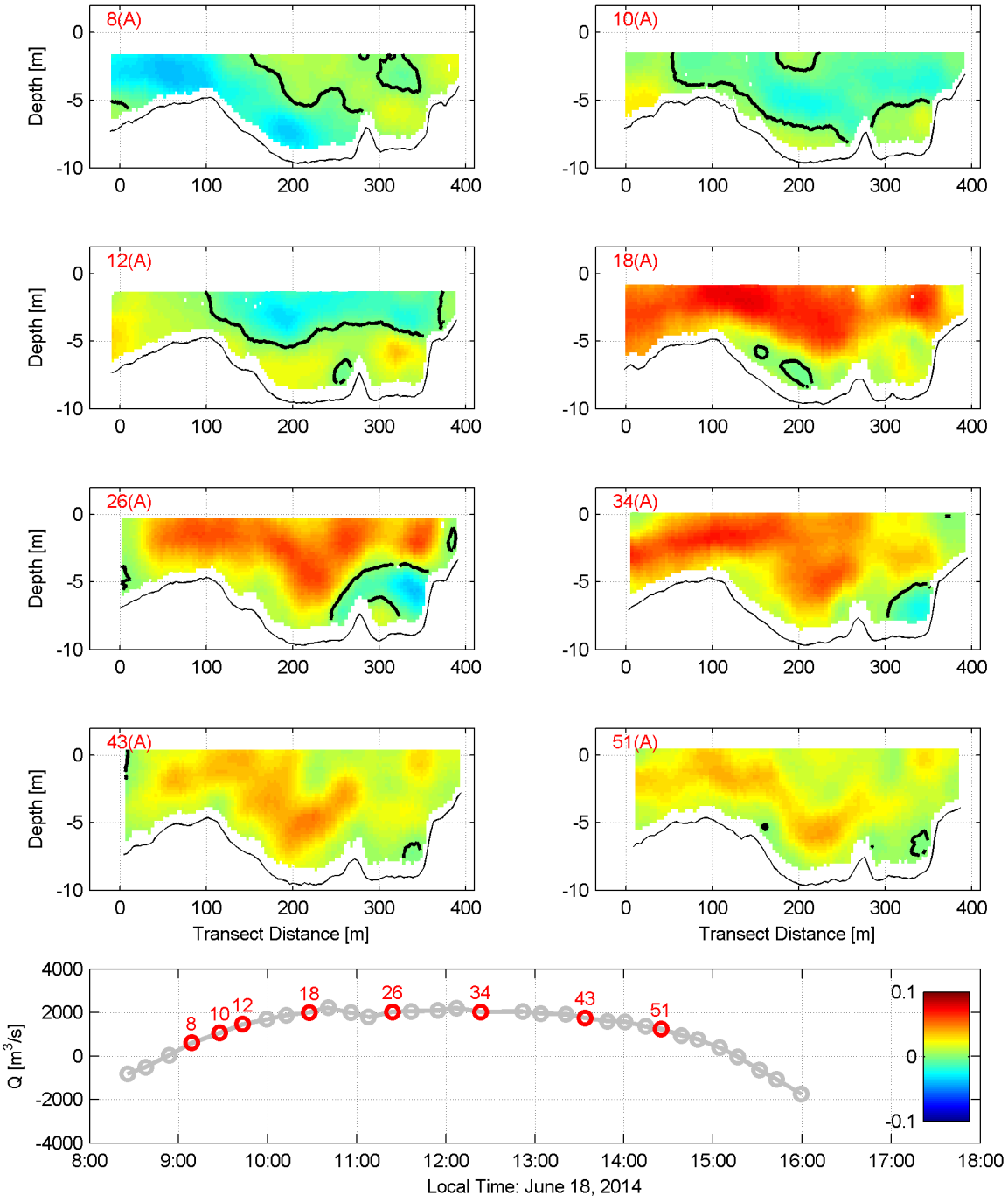

Figure 51: Vorticity $[s^{-}1]$ measured for Transect A on June 18, 2014, representative of a characteristic flood tide. Positive/negative values represent clockwise/counter-clockwise rotation respectively. Transect distance, D is measured relative to the first waypoint identified in Table 4. Thick black contours represent $\omega = 0$.

in Figure 49: Transect 8(A). The slightly stronger axial currents along the seabed are accompanied by positive cross channel velocities except to the right of the bump, $D > 290m$, where they are negative (Figure 50: Transect 8(A)). The resultant vorticity shows two distinct circulation cells, negative (counter-clockwise) on the left-hand side and positive (clockwise) on the right-hand side of the channel (Figure 51: Transect 8(A)). As the flood tide strengthens in Transects 10(A)-12(A), the moderate axial current concentration migrates toward the surface (Figure 49), as does the positive cross channel velocities (Figure 50). The negative vorticity in the left-hand side of the channel is pushed to the right and upwards being replaced by a larger positive circulation cell.

As flood tide nears peak strength negative vorticity is essentially eliminated from the transect (Figure 51: Transect 18(A)) and positive cross channel velocities are solely concentrated along the surface along the entirety of the channel (Figure 50: Transect 18(A)). The magnitudes of cross channel velocity and vorticity markedly increase, as does the axial velocity as expected with the strengthening flood tide (Figure 49: Transect 18(A)). In Transect 18(A) the strongest axial currents are concentrated at the surface and the outer bend of the channel to the right of the bump ($D > 280$ m). To the left of the bump, ($D < 280$ m) currents are slightly weaker and concentrated in the middle of the water column. At the bump ($D = 280$ m), axial currents are strong and depth uniform, an isolated feature in the transect. Unique distributions of cross channel velocities and vorticity are found over the bump as well (Figures 50-51: Transect 18(A)). Over the bump at $D = 280$ m, the positive cross channel velocity concentration is pinched at the surface and the negative vorticity is cleaved on either side. The vertical velocities, not shown, are split about the bump as well with upward velocities to the right and downward velocities to the left, indicating two co-rotating circulation cells centered about the bump.

As peak flood tide continues, the two co-rotating circulation cells remain (Figure 50: Transect 26(A)). However, a third counter-rotating cell forms in the pocket to the right of the bump along the seabed ($D > 280$ m and $o < -5$ m) (Figure 51: Transect 26(A)). All three cells converge at and slightly to the right of the bump in the middle of the water column ($D = 300$ m and $o = -5$ m). The strongest axial currents are still concentrated

mostly on the outer bend of the channel but are no longer solely concentrated at the surface. The strong axial velocities are centered in the water column at the convergence of the three circulation cells.

As the tide rises further, the volume flux stays the same although the axial velocities are decreased and the distribution of the axial velocities is further distorted (Figure 49: Transect 34(A)). Aside from the axial velocities being markedly weaker overall, the axial concentration over the pocket (300 m$< D <$ 350 m) has migrated further downward but axial velocities over the bump and outermost shelf on the bank ($D >$ 350 m) have remained spatially consistent; as a result a 'W' shape across the channel of high axial velocity concentration is formed. While the axial velocity diminishes, the cross channel velocities and the positive vorticity decrease very little (Figure 50-51: Transect 34(A)). However the third counter-rotating positive circulation cell is significantly diminished in strength and size.

As the flood volume flux weakens and the water level reaches peak high tide, the axial velocities continue to diminish in strength and spread rapidly as compared to the secondary circulation (Figure 49: Transect 43(A)). The small areas of the most persistent axial velocities are in the middle of the water column over the bump ($D =$ 280 m) and at the surface above the outer shelf ($D >$ 350 m). The cross channel velocities are reduced and positive co-rotating vorticity cells are weakened (Figures 50-51: Transects 43(A)). The positive circulation cells is completely diminished and the others are weakening. At the end of the flood cycle in Transect 51(A), the secondary circulation continues to weaken (Figures 50-51) and the axial current distribution weakens and homogenizes across the transect (Figure 49) as the system approaches slack and thus ebb tide.

Figures 52-54 highlight the beginning, peak, and diminishing of ebb tide from December 22, 2011 as defined by negative volume fluxes. Unlike flood tide, ebb tide develops along the surface rather than the bed (Figure 52: Transect 1(A)). On the left-hand side of the channel ($D <$ 200 m) axial velocities are concentrated in a thin layer along the surface. On the right-hand side ($D >$ 200 m) stronger axial velocities are found more uniformly throughout the water column. The demarcation of these distributions is clear and striking along the entire water column at the deepest part of the channel. This division may be due

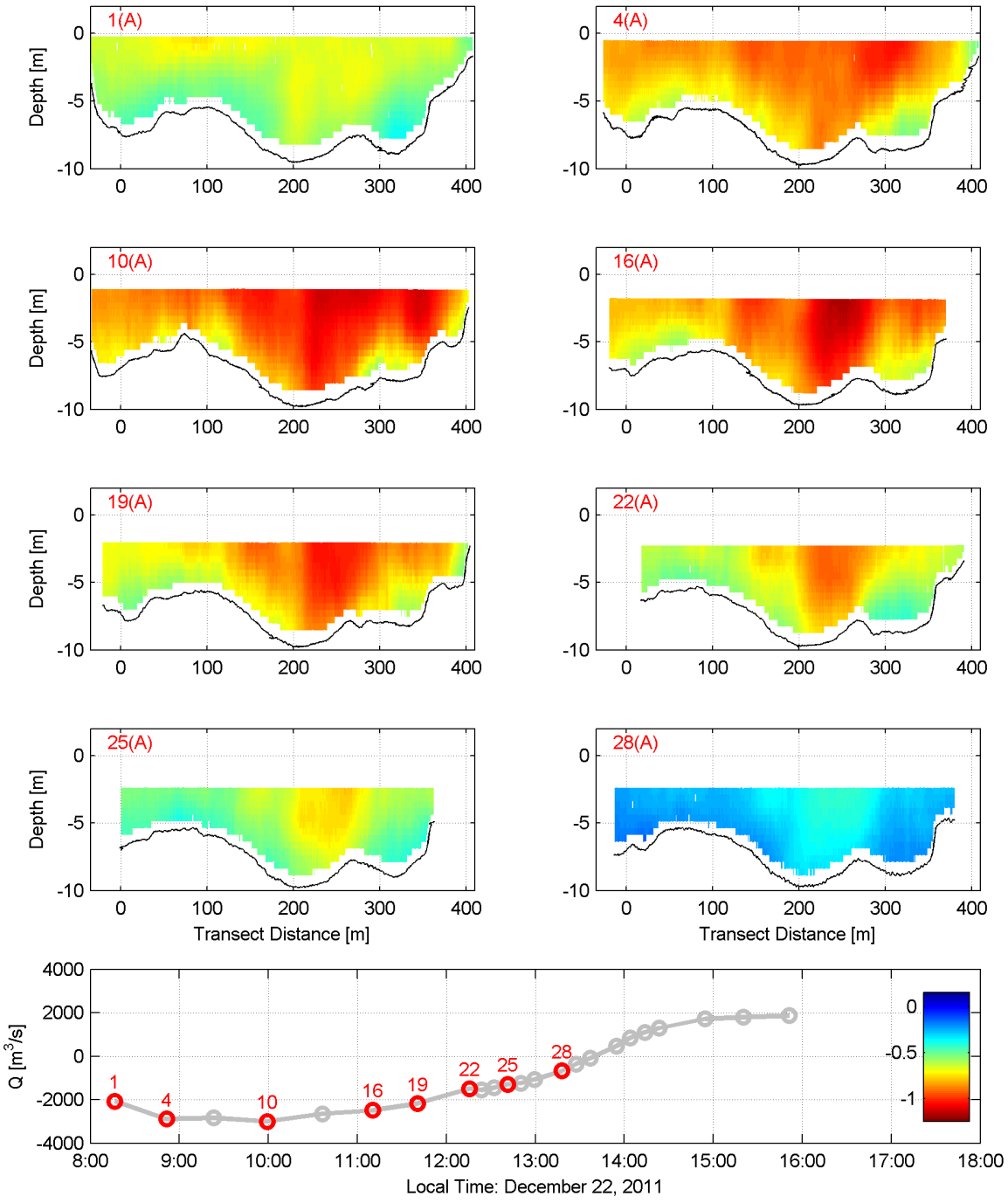

Figure 52: Axial currents [m/s] measured for Transect A on December 22, 2011, representative of a characteristic ebb tide. Negative values represents ebb currents and positive represents flood. Transect distance, D is measured relative to the first waypoint identified in Table 4.

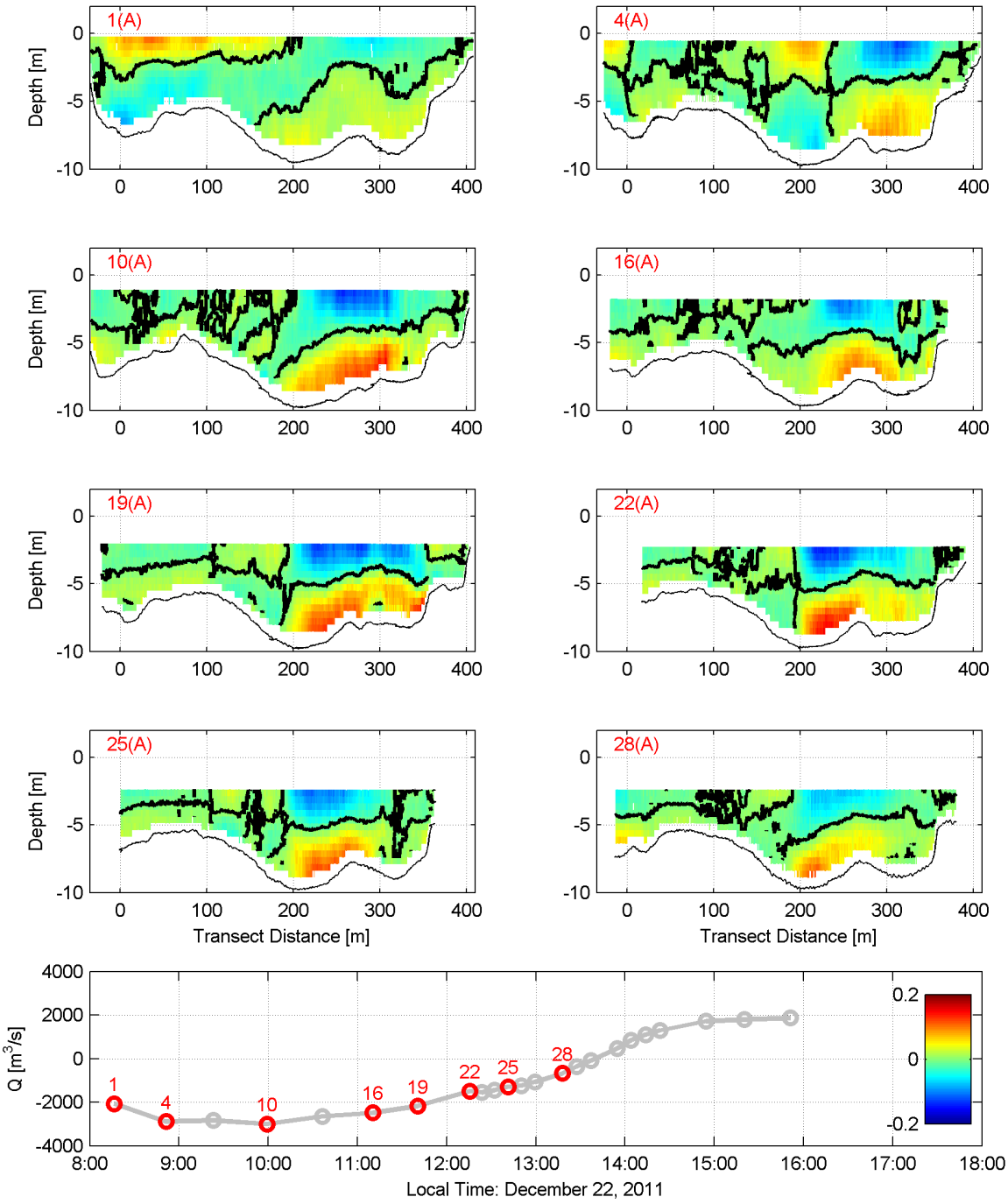

Figure 53: Cross channel currents [m/s] (depth-averaged detrended) for Transect A on December 22, 2011, representative of a characteristic ebb tide. Negative values represents currents in the $-D$ direction and positive represents $+D$. Transect distance, D is measured relative to the first waypoint identified in Table 4. Thick black contours represent zero cross channel velocity.

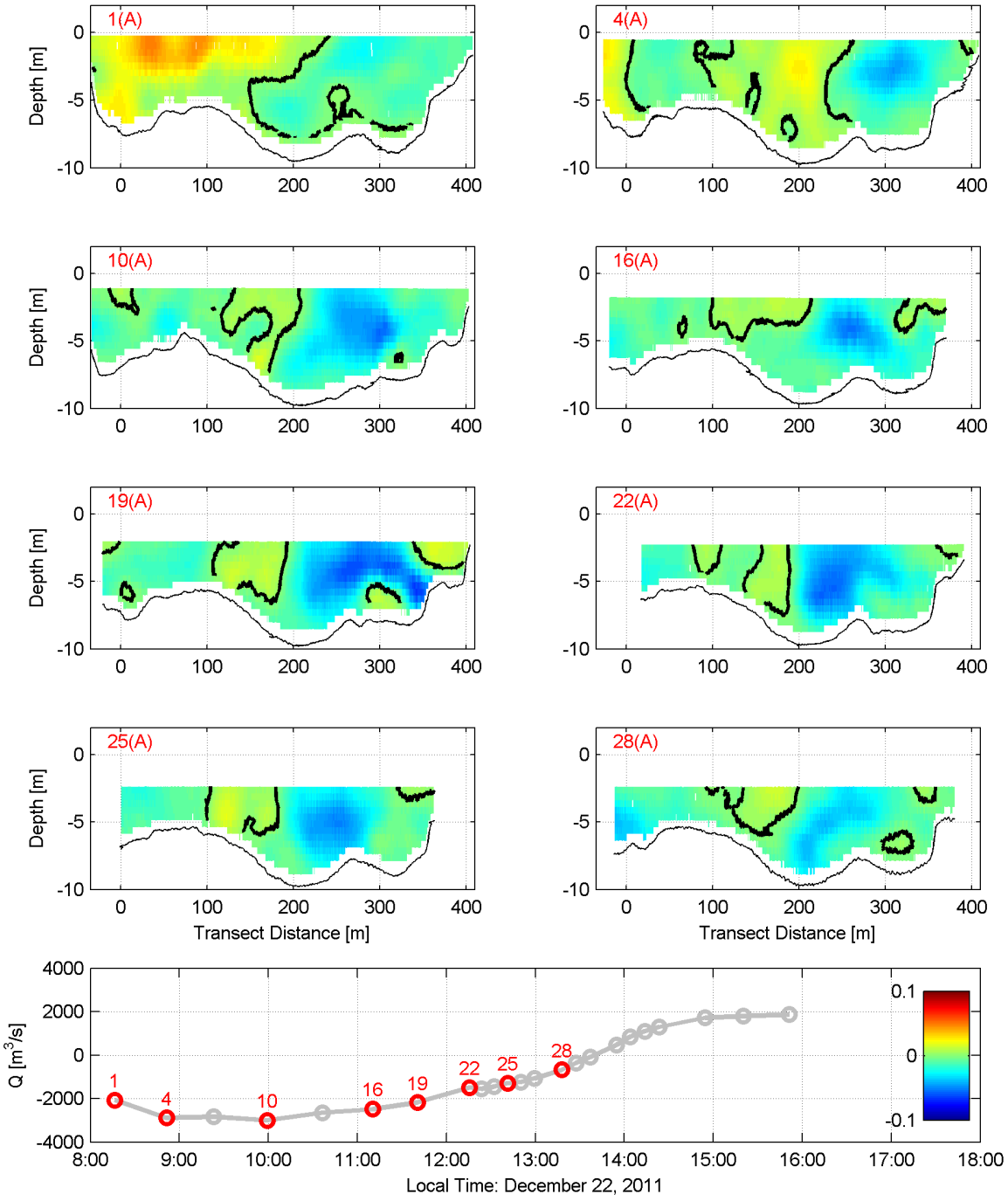

Figure 54: Vorticity [$s^{-}1$] measured for Transect A on December 22, 2011, representative of a characteristic ebb tide. Positive/negative values represent clockwise and counter-clockwise rotation respectively. Transect distance, D is measured relative to the first waypoint identified in Table 4. Thick black contours represent $\omega = 0$.

to the confluence of the flows from the two upstream channels; $D = 200$ m is the location of the shear layer between the two.

Evidence of this is further seen in the cross channel velocity distribution (Figure 53: Transect 1(A)). On the left- and right-hand side of Transect A, the surface cross channel flows are in opposite directions, pointing towards the center of the channel. Accompanying the cross channel surface flows are bed flows in the opposite direction, forming secondary circulation cells which are indicative of the flow curvature and centrifugal acceleration due to the confluence of Transects B and C. The cells are opposing, producing two large areas of opposite vorticity: a clockwise cell on the left-hand side and a counter-clockwise cell on the right-hand side (Figure 54: Transect 1(A)).

As the ebb tide strengthens, the cell on the right-hand side of the channel gains strength and definition (Figure 54: Transect 4(A)). Its spatial extent is restricted, confined to the right of the bump. The counter-rotating cell on the left-hand side, with positive vorticity, has migrated towards the right-hand side where it extends throughout the water column on the left-hand side of the bump. The demarcation of these cells is further evident in the cross channel velocity distribution where zero cross channel velocity extends throughout the water column slightly to the left of the bump ($D = 280$ m)(Figure 53: Transect 4(A)). Two weak and ill-defined secondary circulation cells remain on the left-hand side of the channel. Although the axial currents are more depth uniform on the left-hand side, the demarcation in the center of the transect between the two flows is still discernible at $D = 220$ m; particularly near the bed where strong axial flow to the right penetrates deeper.

As the tide strengthens the demarcation is more clearly seen at the surface; the strongest axial currents are concentrated just to the right of $D = 220$ m (Figure 52: Transect 10(A)). Another small area of axial current concentration is to the right of the bump ($D = 350$ m). The counter clockwise circulation cell has now migrated towards the center of the channel [Figure 53: Transect 10(A)]. The corresponding cross channel velocities are also extended past the center of the channel at the surface (Figure 54: Transect 10(A)). Correspondingly, the clockwise cell with negative vorticity has shifted to the left, weakened, and are less coherent. The far left-hand side ($D < 100$ m) appears more uniform in axial velocity with

weaker cross channel velocities/vorticities and smaller cells appearing almost as eddies.

The two main circulation cells remain as the water level and volume flux drop swiftly (Figure 54: Transect 16(A)). The clockwise cell with positive vorticity weakens and is primarily at the surface. The counter clockwise cell with negative vorticity is saddled over the bump ($D = 280$ m). On the far right-hand side ($D > 350$ m) a small circulation cell forms at the surface with negative vorticity, counter rotating with the cell over the bump (Figure 54: Transect 16(A)). Interestingly, the locations of the negative circulation cells correspond with areas of decreased axial velocity (Figure 52: Transect 16(A)). In both areas the axial currents are weaker and less depth uniform. The opposite is true for the counter clockwise cell with positive vorticity; its axial currents became stronger, more depth uniform, and more centered over the bump.

As the ebb tide continues to recede, axial currents on the left-hand side of Transect A continue to weaken quicker than those on the right-hand side and the demarcation at the center is shifted slightly towards the left ($D = 200$ m)(Figure 52: Transect 19(A)). However like the flood tide, the secondary circulation and vorticity remain relatively consistent in magnitude (Figure 53: Transect 19(A)); various small counter rotating eddies form on either side of the channel. Upon further ebb weakening, the circulation cells (Figure 54: Transect 22(A)) remain where there is a semblance of relatively strong ebb axial velocities (Figure 52: Transect 22(A)). The strongest concentration of axial currents is still over and slightly left of the bump and the second strongest is slightly to the left of this.

As ebb tide approaches slack, the circulation cells continue to lose strength and definition (Figures 53-54: Transects 25(A)-28(A)). However the decline of secondary circulation is not as swift as the decline in axial currents (Figure 52: Transects 25(A)-28(A)). Again, the concentrated axial currents are slightly to left of the bump on the right-hand side of the channel and become more limited to the surface. These vestiges of ebb flow remain persistent as the tide transitions to flood, leading to the flood tide developing first along the seabed.

The temporal analysis of velocity distributions across Transect A demonstrates that strongest axial currents are persistently focused near or adjacent to the bump on the right-hand side of the transect ($D = 270$ m) throughout the tidal cycle. It is hypothesized the

precise location, extent, and coherence of the hotspot is dependent on three factors: the various secondary circulation patterns that form; the along stream change in topography induced by the bump; and the confluence of the two streams into Transect A.

The first factor is non-trivial since the circulation cells are highly non-linear. Their formation is dependent on pressure gradients across the channel. These pressure gradients can be formed by variable subcritical flow constriction across the channel such as that formed over the bump or from centrifugal acceleration due to flow curvature. Both are dependent on the strength of the axial current, which in turn is dependent on the circulation. The centrifugal acceleration is also dependent on the flow curvature, which can be dictated by along channel bathymetry as well as the variable curvature induced by the confluence and bifurcation of the two streams. Thus, in order to understand the secondary circulation and its effect on the concentration of axial velocity, the along stream factors: the bump and the confluence of the two streams are evaluated next.

5.1.3 Transect Analysis: Along Channel Evolution

In order to understand the along channel evolution of the flow, measurements from Transect A are compared to measurements from up and downstream transects (Transects B, C, D, E, and F). Transects immediately precedent and subsequent in time are compared to Transect A with the assumption of instantaneous comparisons. For periods of rapid change, such as the development of ebb tide, this assumption loses some validity. To rectify this, current velocities are normalized by the transect volume flux divided by the measured transect area, essentially a channel averaged velocity. The corrections are not made for vorticity measurements since they are not dependent on the overall velocity magnitude but rather spatial gradients. The corrections are not made for comparisons of Transects A, B, and C either since volume fluxes varied greatly between the three and their relative overall magnitudes are significant for analysis of bifurcation and confluence. It is important to note this normalization only corrects the overall magnitudes of the transect volume flux and analysis of spatial distributions may still be biased.

It is important to understand the hydrodynamic effects of the bump in Transect A on

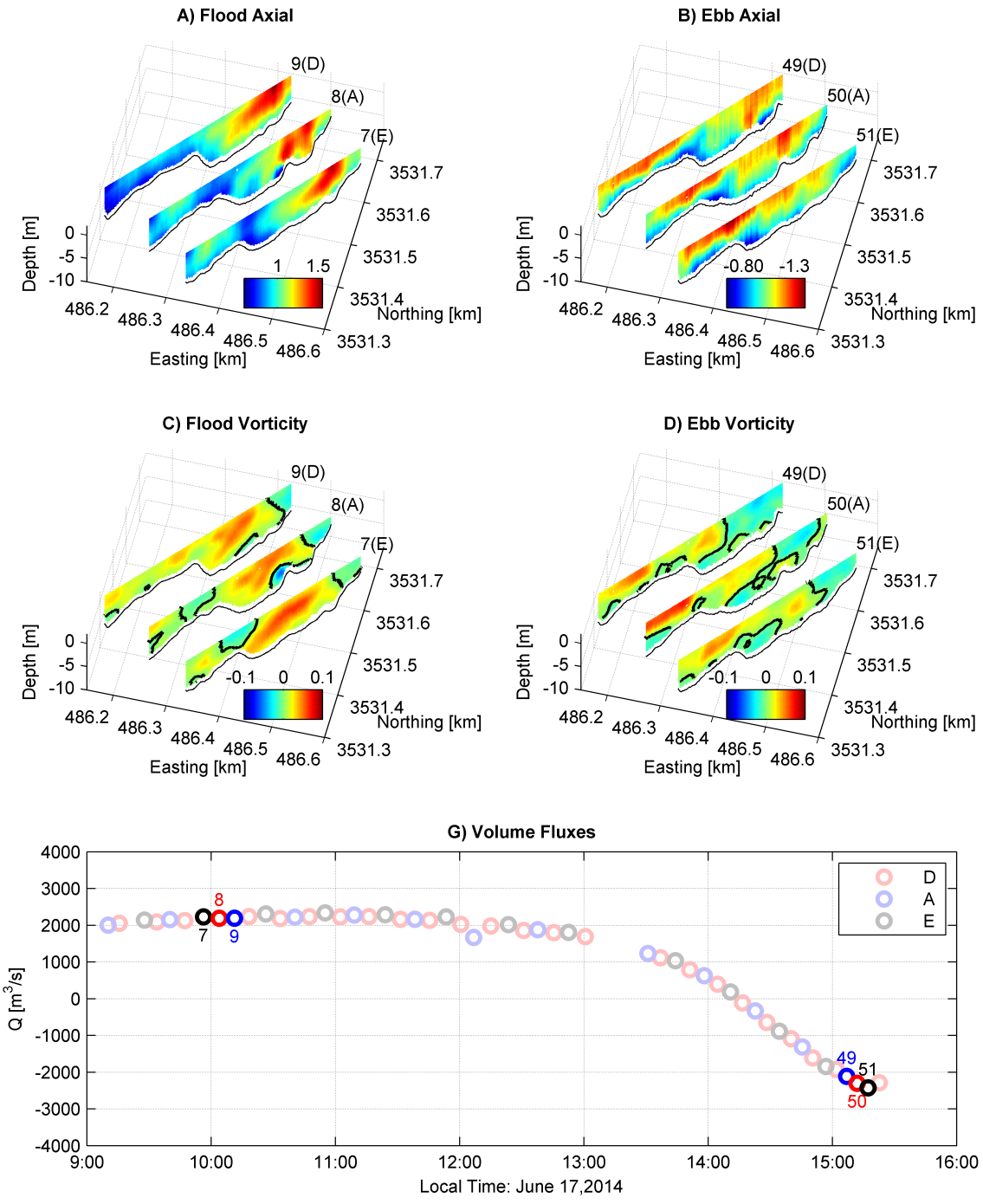

Figure 55: Normalized axial velocity (A, B) and vorticity (C, D) measurements for flood (A, C) and ebb (B, D) currents. Axial velocities normalized by the corresponding transect volume flux divided by transect area. Thick black lines represent zero vorticity. Bottom figure (G) is corresponding volume flux diagram. Measurements from June 17, 2014.

axial velocities and secondary circulation and how far the effects are felt up and downstream. Transects D and E are utilized in this analysis due to their proximity to Transect A and their relatively flat bathymetry. A comparison of the transects are made for representative flood and ebb tides in Figure 55.

Transects 7(E), 8(A), and 9(D) are used to evaluate the evolution of bump effects for flood tide in Figures 55A, C. As the flood flow travels up the channel, it first passes through Transect 7(E) and continues in a northwesterly direction. In Transect 7(E) a singular clockwise circulation cell extends across the channel and a small counter-clockwise cell rests on the shelf on the far northeast corner. As discussed in the literature review, this a signature of classic secondary circulation for centrifugal acceleration in response to channel curvature. The axial velocity distribution shows further evidence of this; the strong axial currents are concentrated at the surface along the outer bend (Figure 55(A): Transect 7(E)).

This spatial distribution is disrupted upon the flow reaching Transect 8(A); the clockwise circulation cell is pinched over the bump forming an additional co-rotating clockwise cell to the right of the bump (Figure 55C). A negative cell forms to the left of the bump near the seabed as previously observed for strong flood flow in Figure 51: Transect 26(A). The axial distribution is also disrupted; over the bump the concentration of axial currents is distorted with depth uniform velocities directly over the bump (Figure 55(A): Transect 8(A)). Upon reaching Transect 9(D), the distortion and circulation from the bump is highly diminished (Figure 55(C)). The seabed positive circulation cell has weakened and flattened, allowing for a singular negative cell at the surface reminiscent of Transect 7(E) and classic secondary circulation for centrifugal acceleration. The axial distribution downstream of the bump also has regained a spatial distribution similar to the distribution upstream of the bump.

Both Transects D and E do not have as pronounced of a bump as in Transect A and do not show the same axial distributions and secondary circulation patterns studied for Transect A in Figures 52 and 54. Thus it is clear the split co-rotating cells, counter rotating seabed cell, and depth uniform axial velocity concentration over the bump are highly localized features.

Transects 47(E), 48(A), and 49(D) show the evolution of bump effects for ebb tide in

Figure 55B, D. For ebb tide, the flow travels southeasterly from Transect 49(D) to 47(E). There is a clear demarcation of strong currents again near the center of the deeper part of the channel that is depth uniform (Figure 55B: Transect 49(D)). The two counter circulating cells are also present in all three transects (Figure 55D). The concentration of strong axial velocity on the right-hand side is shifting towards the left-hand side of the channel. However the strong depth uniform velocities, as in flood, are highly localized.

The effect of the bump for ebb tide is less important because its effects appear secondary to those of the confluence of the two streams. The concentrated high axial flow on the left-hand side is restricted, while the strong currents on the right-hand side move towards the center, mimicking the bathymetry. The two incoming streams are not fully mixed or recovered by Transect 47(E).

To better resolve the confluence of the two streams, Transects F and G are compared to Transect A. Transects F and G are are further up and downstream respectively of Transect A and were charted to better resolve the bifurcation point of flood tide and the confluence flow recovery of ebb tide. Normalized axial currents and vorticity are plotted for representative transects for flood and ebb tide in Figures 56A-E.

Flood tide is resolved for Transects 25(G), 26(A), and 27(F), as shown in Figures 56A, C. As the flow enters the domain at Transect 25(G) there is a concentration of strong currents along the outside bank as expected due to the channel curvature (Figure 56A). Correspondingly, there is a singular clockwise circulation cell also representative of flow curvature (Figure 56C). Like the transition between Transects 7(E) and 26(A) in Figures 55A, C, as the flow passes over the bump in Transect 26(A) in Figures 56A, C, the circulation cell is pinched, additional cells form, and axial currents are concentrated over the bump. The axial currents are further distorted further upstream (Figure 56A: Transect 27(F)) and the vorticity and circulation is highly reduced (Figure 56A: Transect 27(F)). There does not seem to be any evidence of the effects from the downstream flow splitting at the measured transects.

Unfortunately for ebb tide, the only measurements available for Transects G, A, and F were near the diminishing end. Transects 3(F), 2(A), and 1(G) show the evolution of the

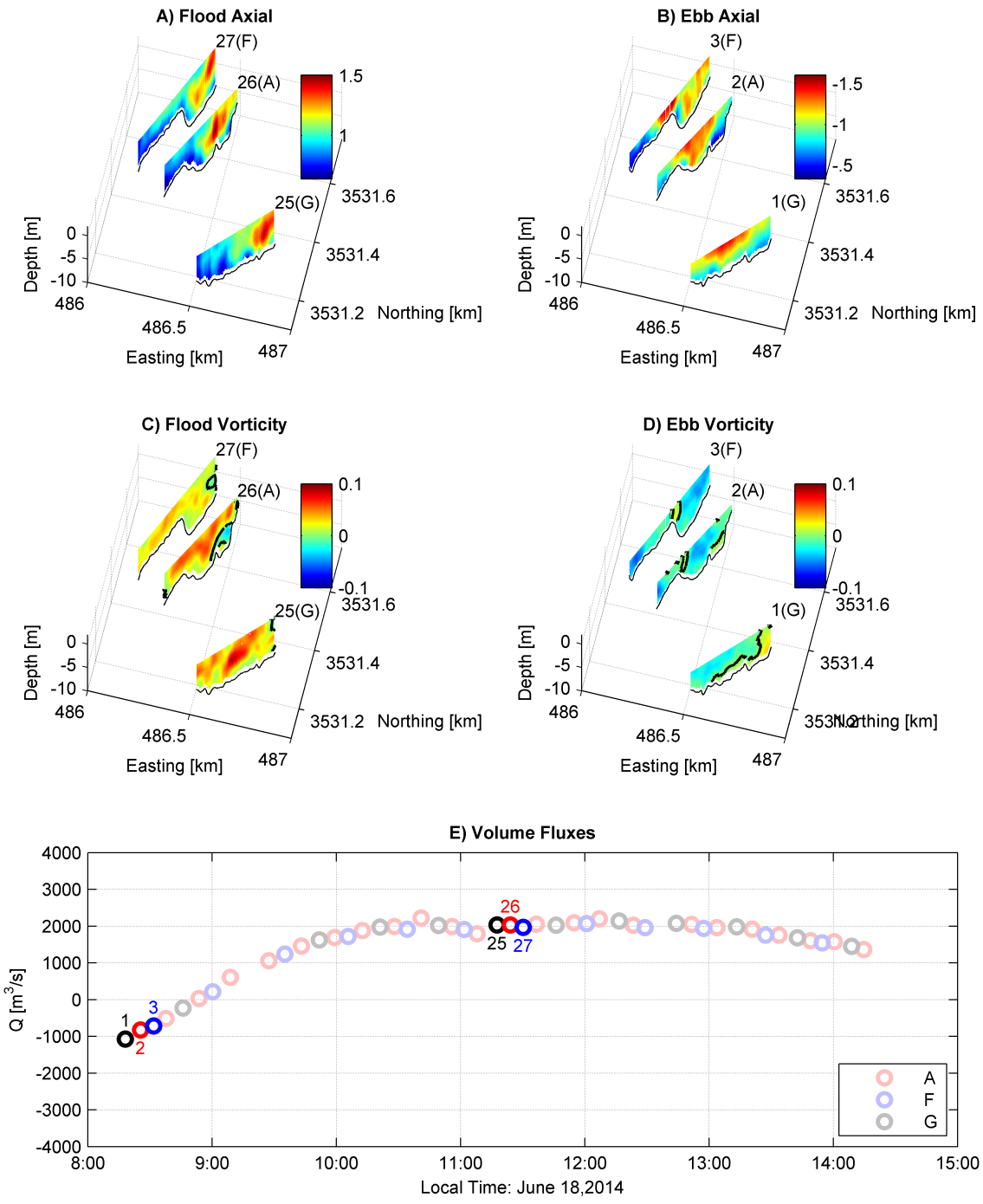

Figure 56: Normalized axial velocity (A, B) and vorticity (C, D) measurements for flood (A, C) and ebb (B, D) currents. Axial velocities normalized by the corresponding transect volume flux divided by transect area. Thick black lines represent zero vorticity. Bottom figure (G) is corresponding volume flux diagram. Measurements from June 18, 2014.

southeasterly flow in Figures 56B, D. Since the tide is relatively weak, overall the measurement magnitudes and spatial distributions are weaker and less defined. Upstream of Transect 2(A), Transect 3(F) shows the two counter-rotating circulation cells as discussed previously. However, the positive circulation cell on the left-hand side is considerably weaker, apparent in Transect 2(A) as well. This is due to the weakened state of the tidal cycle the measurements were obtained. The weakening of the left-hand side of the channel, flow from Transect C, was previously shown in Figure 52. Whereas the left-hand side of the channel is stronger than the right hand-side in the beginning of ebb tide, at the end of ebb tide it is far weaker for similar volume fluxes.

The negative circulation cell, representing flow from Transect B, continues to push towards the shallow left-hand side of the transect in Transect 2(A) (Figure 56D), as shown previously in Figure 55D. This push continues downstream until it spans the entirety of the channel (Figure 56D: Transect 1(G)). The axial velocities show more cross channel uniformity as well as a surface concentration more centered on the left-hand side of the transect (Figure 56B: Transect 1(G)). Thus it appears by Transect G that the flow has recovered. However, although the flow appears fully mixed, it does not mimic the flow distribution of flood in Figure 56A: Transect 25(G), particularly the location of the axial velocity concentration across the channel. For simplified flow around a curve, the resultant secondary circulation should be the same regardless of stream-wise direction; surface flow is directed towards the outer bend and flow along the seabed is directed inward. Despite having the same channel geometry, in Transect 25(G), the vorticity is reversed between flood and ebb tide. Thus the curvature of the channel geometry has not redirected the confluent flows; the curvature and associated circulation of the confluent flow from Transect B is still dictating circulation downstream. This is a result of Transect B retaining strength and Transect C drastically rescinding near the end of ebb tide. As discussed in Chapter II, the flow curvature of confluences is dependent on not only the fixed channel geometry but also the relative strengths of the upstream channels.

The relative strengths of flow through Transects B and C throughout the tidal cycle are shown in Figure 57 from the December 2011 measurements. The volume fluxes in Figure

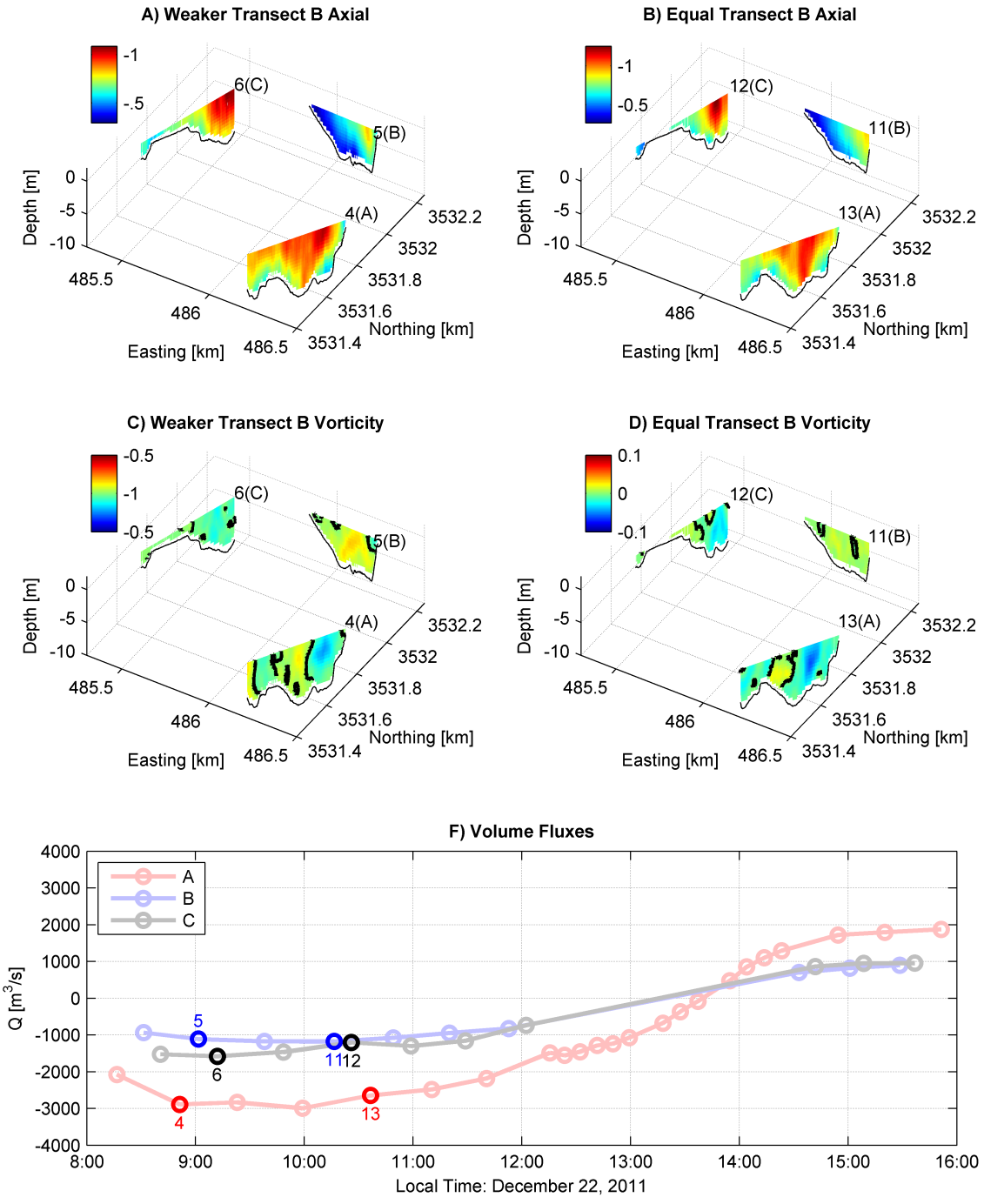

Figure 57: Ebb axial velocity (*A, B*) and vorticity (*C, D*) measurements for ebb weaker Transect B input (*A, C*) and equal Transect B input (*B, D*). Bottom figure is corresponding volume flux diagram. Thick black lines represent zero vorticity. Bottom figure is corresponding volume flux diagram. Measurements from December 22, 2011.

57F show the confluence Transect A is split from Transects B and C approximately equally. Since the previous analysis showed that for flood the point of flow splitting is further downstream of Transect A, transects are only provided for ebb tide where the relative strengths of Transects C and B do have an effect on the flow distribution in Transect A. Figures 57A, C and Transects 4(A), 5(B), and 6(C) depict the strengthening ebb tide where Transect C is markedly stronger than Transect B. Figures 57B, D and Transects 11(A), 12(B), and 13(C) depict the weakening ebb tide where Transect B and Transect C have comparable strength.

When Transect 6(C) has a larger volume flux than Transect 5(B) the larger axial velocity for both transects are concentrated on the right-hand side of their respected channels. In transect 4(A) the stronger axial currents span the full channel, although larger on the right-hand side. As ebb tide weakens, volume flux from Transect C recedes quicker than Transect B (Figure 57F). As a result the axial currents on the left-hand side of Transect 13(A) are weaker and do not extend as far towards the seabed (Figure 57C). Transect 12(C) still has relatively stronger velocities than Transect 11(B) despite having an equivalent volume flux. Transect B, has a comparable volume flux despite its weaker currents due to its larger cross channel area (10% larger than Transect 12(C)). Due to the drop in water level, flow on the left-hand side of Transect 12(C) is almost eliminated, explaining the reduction of axial currents on the left-hand side of Transect 13(A).

For both instances, the secondary circulation of the upstream transects is weak with slight negative vorticity in Transect C and positive vorticity in Transect B (Figures 57B, D). However strong secondary circulation does form in Transect A. Thus as Transect B merges obliquely into Transect A, a counter clockwise circulation is formed on the right-hand side. Similarly, as Transect C flows obliquely into Transect A, a clockwise cell is formed on the left-hand side. What little secondary circulation is contained in the upstream transect is lost when Transects B and C merge, change direction, and form the counter rotating circulation cells associated with flow confluence.

5.1.4 Kinematic Summary

Domain wide measurements are analyzed to isolate areas of persistently high current velocities suitable for tidal energy extraction near the island. A localized point near the southwest coast of the island is identified as a hydrokinetic energy hotspot over a topographic bump along the outer bank of Transect A. Vorticity, cross, and axial current measurements across Transect A are used to further analyze the depth varying current distribution as well as secondary circulation throughout the tidal cycle.

During flood tide the topographic serves as a physical boundary and location of the interface of two co-rotating clockwise cells. Strong axial currents persistently exist throughout the water column at this point. These features are highly localized at Transect A; up and downstream the topographic bump, axial velocity concentration, and split cells become more homogenized. Axial velocity magnitudes and secondary circulation grow and weaken with the tidal stage, secondary circulation is somewhat more persistent.

At peak ebb tide, two clear inflows are delineated at the center of Transect A by their cross channel velocities and corresponding counter rotating circulation cells. The interface of the flows migrates slightly about the center depending on the relative strength of ebb tide. For a strengthening tide, Transect C has stronger inflow and thus the interface is slightly to the right of center. As the tide strengthens and sequentially weakens, Transect B gains relative strength to Transect C and the interface migrates slightly to the left. The relative strengths of the co-rotating cells and axial current distributions associated with each cell vary throughout the ebb cycle accordingly.

This section qualitatively describes the velocity distributions about the hotspot throughout the tidal cycle. Next, the underlying physical processes are quantified by calculating terms from the momentum balance.

5.2 Measurement Dynamics

For further insight into the physical mechanisms behind the secondary circulation and concentration of high kinetic energy, terms from the governing momentum equations are

calculated from the measurements. Terms are calculated and presented for the flood and ebb snapshots for Transect A to observe their relative contribution and evolution through the tidal cycle. A complete momentum balance is not possible due to limitations of the measurement resolution; most notably turbulence and gradients in the axial direction cannot be calculated with confidence due to the lack of resolution in time and axial direction (Transects E, A, and D are 100 meters apart) respectively.

The full governing equations are presented in Equations (45)-(47) for curving flow with a large radius of curvature R_c. Except for the inclusion of vertical and axial advection, they are similar to the equations derived by Kalkwijk and Booij (1986) frequently referred to as the KB equations (Alaee et al., 2004). The coordinate system is analogous to the transect coordinate system $\mathbb{T}$, in the cross, axial, and vertical directions (C, A, O). The only difference is the inclusion of the corresponding radius of curvature R_c. Major physical assumptions for the momentum balance include hydrostatic pressure, incompressible flow, small viscous dissipation, and steady flow. Although the flow is not steady with the changing tide, it is assumed change occurring within the five minutes to measure a transect is small. Terms in black are those that can be fully resolved by the measurements. Red terms are those that cannot be resolved by measurements and blue terms can be approximated or inferred by the measurements. The equations are:

Cross Channel Momentum

$$u_c \frac{\partial u_c}{\partial c} + u_a \frac{\partial u_c}{\partial a} + u_o \frac{\partial u_c}{\partial o} = -g\frac{\partial \eta}{\partial c} + \frac{{u_a}^2}{R_c} - T_c \tag{45}$$

Axial Momentum

$$u_c \frac{\partial u_a}{\partial c} + u_a \frac{\partial u_a}{\partial a} + u_o \frac{\partial u_a}{\partial o} = -g\frac{\partial \eta}{\partial a} - \frac{u_a\, u_c}{R_c} - T_a \tag{46}$$

Continuity

$$\frac{\partial u_c}{\partial c} + \frac{\partial u_o}{\partial o} + \frac{\partial u_a}{\partial a} = 0 \tag{47}$$

where g is gravity, T represents the combined Reynolds stresses for the given direction and could not be resolved or approximated accurately. c is analogous to the transect coordinate D as shown in Figure 34.

The partial derivatives are calculated using a first order central finite difference scheme from the measured transects mapped to the transect coordinate systems. The derivatives are smoothed using a moving spatial filter as are the original velocity measurements: 15 m in the C direction and 1 m in the O direction about each measurement bin. To calculate the axial gradient of the axial velocity ($\frac{\partial u_a}{\partial a}$), the continuity equation is used with the resolvable terms. The resultant ($\frac{\partial u_a}{\partial a}$) is then used to calculate the $u_a \frac{\partial u_a}{\partial a}$ term in the axial momentum equation.

To approximate the pressure gradient terms, the advective accelerations in Equations (45) and (46) are rewritten using continuity and the equations are depth integrated using the kinematic boundary conditions at the surface and seabed. The depth uniform hydrostatic pressure gradients are solved as

Depth Integrated Cross Channel Momentum

$$g\frac{\partial \eta}{\partial c}H = \int_{-h_o}^{\eta} \frac{{u_a}^2}{R_c} do - \int_{-h_o}^{\eta} \frac{\partial {u_c}^2}{\partial c} do \tag{48}$$

Depth Integrated Axial Momentum

$$g\frac{\partial \eta}{\partial a}H = \frac{\tau_B}{\rho} - \int_{-h_o}^{\eta} \frac{u_a\ u_c}{R_c} do - \int_{-h_o}^{\eta} \frac{\partial u_c u_a}{\partial c} do - \int_{-h_o}^{\eta} \frac{\partial {u_a}^2}{\partial a} do \tag{49}$$

where h_o is the water depth, and H is the total length of the water column $\eta + h_o$, ρ is the water density, and τ_b is the bottom axial shear stress and is approximated by the quadratic stress formula

$$\tau_b = \rho C_D |u_a|\ u_a \tag{50}$$

where $u_a(D, o_{bot})$ represents the axial velocity of the bottom bin for a point along the transect, C_D is the bottom drag coefficient. A typical value C_D value of 2.5x10^{-3} is used, as in Simulation A1 of the numerical model. The resultant momentum terms $\frac{\tau_b}{\rho}$ are small compared to the others in Equation (49) by an order of magnitude. Larger values up to $C_D = 10^{-2}$ have been observed and used for environments with surface waves and secondary circulation (Bricker et al., 2005; Vennell and Old, 2007), however even applying $C_D = 10^{-2}$ here, the associated momentum terms are still considerably smaller at [10^{-3} m/s^2] as compared to [10^{-2} m/s^2]. The temporal acceleration associated with the estuarine

tidal forcing is approximated by the change in transect averaged axial velocity between subsequent Transect A measurements and found to be on the same order. Neglecting these terms will overestimate the magnitude of pressure gradient over the entirety of the transect, however this analysis is focused on the localized features and not greatly affected.

Surface stresses are assumed negligible in both equations and the cross channel bottom stress is also assumed negligible. It is unknown whether the depth averaged axial advection of the cross channel momentum term is significant($\frac{\partial u_c u_a}{\partial a}$); it is not included here because it cannot be resolved. $\frac{\partial {u_a}^2}{\partial a}$ is solved for as $2u_a\frac{\partial u_a}{\partial a}$ using the chain rule and the $\frac{\partial u_a}{\partial a}$ term found from continuity. The integrals are solved numerically using trapezodial integration over the bin depths o_{bin} and transect distances D. $-h_o$ and η are approximated as the elevation of the bottom and top bins.

To determine the centrifugal terms, $\frac{u_a\ u_c}{R_c}$ and $\frac{{u_a}^2}{R_c}$, R_c needs to be correctly determined. The size and value of R_c is important because it governs the strength and direction of the centrifugal terms. The associated sign is the directionality of R_c in the C coordinate direction. Centrifugal acceleration points outwards so it is in the direction of R_c. To correctly map the R_c value, the flow curvature must be specified for every point. For flood tide, R_c is approximated as the depth uniform R_{cf} given by

$$R_{cf} = R_1 + (D - D_{mp}) \tag{51}$$

where $D_{mp} = 189$ m is the distance from the first waypoint of Transect A to the midpoint of the transect and R_1 is the radius of curvature for the channel midpoint as depicted in Figure 58. The value of $R_1 = 2200$ m is chosen to represent the channel curvature; at the transect midpoint the arc is perpendicular with the transect and thus parallel to the axial flow direction. This is analogous to the representation by Batchelor (1967) in Equations (3)-(5) in Chapter II for a channel with constant curvature in the stream wise direction. The kinematic analysis does not show signs of flow bifurcation at Transect A; thus it is assumed the sign of flow curvature is constant across the transect.

For ebb tide, the kinematic analysis shows flows with opposing curvature from Transects B and C. Thus R_c for ebb tide is approximated by the piecewise function R_{ce} given by

$$R_{ce} = \begin{cases} R_1 + (D - D_{mp}) & D < D_i \\ -R_2 + (D - D_{mp}) & D \geq D_i \end{cases} \tag{52}$$

where D_i is the approximated interface of the confluent flows taken to be 220 m based on the distribution of the cross channel velocity u_c as well as associated signatures in the cross channel momentum balance discussed in detail later. The value of $R_2 = 1500$ m is chosen and is illustrated in Figure 58. As for flood tide, the associated arc is perpendicular to the transect at the midpoint of the channel. Note that R_{ce} is discontinuous at D_i however the piecewise function serves as a good first order approximation for evaluating the qualitative contribution of the centrifugal terms in the momentum balance.

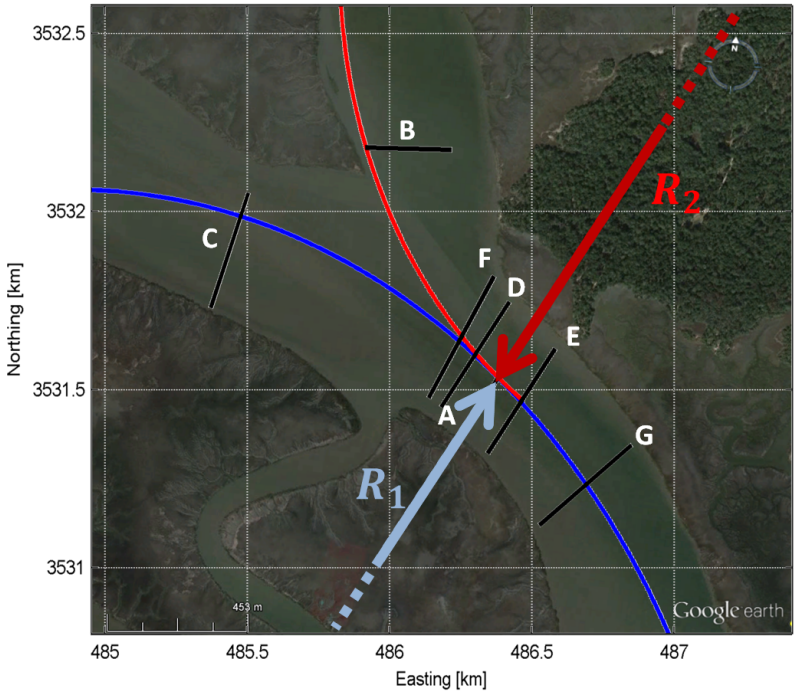

Figure 58: Representative curvature for Transect A with $R_1 = 2200$ m and $R_2 = 1500$ m

The resolvable momentum terms are calculated for the same transects in the kinematic temporal analysis section. Both the depth integrated and vertical varying momentum equations are evaluated for the cross and axial directions. As in the kinematic analysis, first the flood tide will be analyzed followed by ebb.

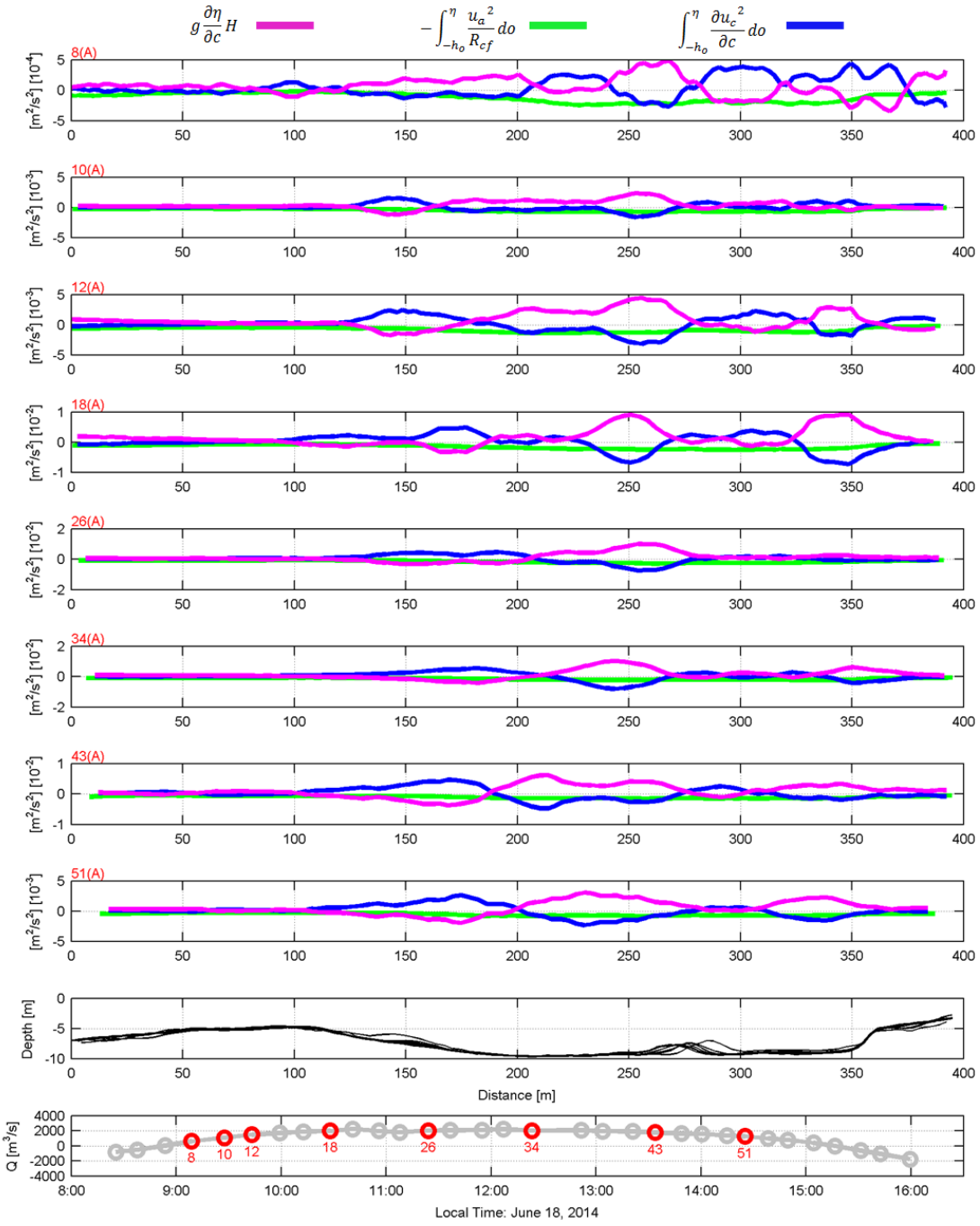

Figure 59: Depth integrated cross momentum terms for flood tide. Terms correspond to terms in Equation (48). Rows indicate transect number and point in tidal cycle referenced in the volume flux time series at the bottom. Second to bottom plot is transect depths for reference. X-axes are the D coordinate in $[m]$.

Terms from the depth integrated cross momentum equation (Equation (48)) are presented in Figure 59. In general the pressure gradient is positive, initially induced by the centrifugal force piling water on the outside of the bend. This water surface profile is a signature of secondary circulation for a curving flow: water along the surface is advected towards the outer bend due to centrifugal acceleration; at a physical boundary water piles up; it induces a pressure gradient directed towards the inner bend ($-C$ direction); and drives a return flow inward along the seabed completing the clockwise cell as seen in the kinematic analysis. However the cross channel advection plays an increasingly important role inducing more variability into the pressure gradient. Comparing transect plots, it is clear the features and magnitudes of the terms grow and shrink along with the tidal stage; Transects 18(A)-34(A) have the most pronounced features and are discussed in more detail. At $D = 250m$ the pressure gradient term, $g\frac{\partial \eta}{\partial c}H$, has a large, positive peak indicating the water surface is rising with an apex at the subsequent zero-crossing near $D = 270$ m, to the left of the bump in the seabed. The same signature is present at $D = 350$ m for the second co-rotating clockwise cell.

The cross channel advective term $\int_{-h_o}^{\eta} \frac{\partial {u_c}^2}{\partial c} do$ is clearly responsible for the peaks in the cross channel pressure gradient The term shows cross velocity acceleration and deceleration to the left of the bump, indicating a change in flow direction which is in congruence with the secondary circulation. The centrifugal term, $-\int_{-h_o}^{\eta} \frac{{u_a}^2}{R_c} do$, is slightly negative, although initially the driving force for the secondary circulation, it becomes much smaller than the cross-channel accelerations. Because both these terms are depth varying, their exact contribution to momentum balance will be better resolved in the vertically varying momentum analysis.

The resolvable terms from the depth varying cross channel momentum equation (Equation (45)) are plotted in Figures 60 and 61 along with the cross channel velocity and the vorticity respectively. In Figure 60, the cross channel advection of the cross momentum, $-u_c \frac{\partial u_c}{\partial c}$, is plotted in the first column. For peak flood, Transects 18(A)-34(A), it is clear the accelerating cross channel flow is advecting momentum away from the inner bend towards the center as indicated by the negative values ($D < 200$ m). To the left of the bump the

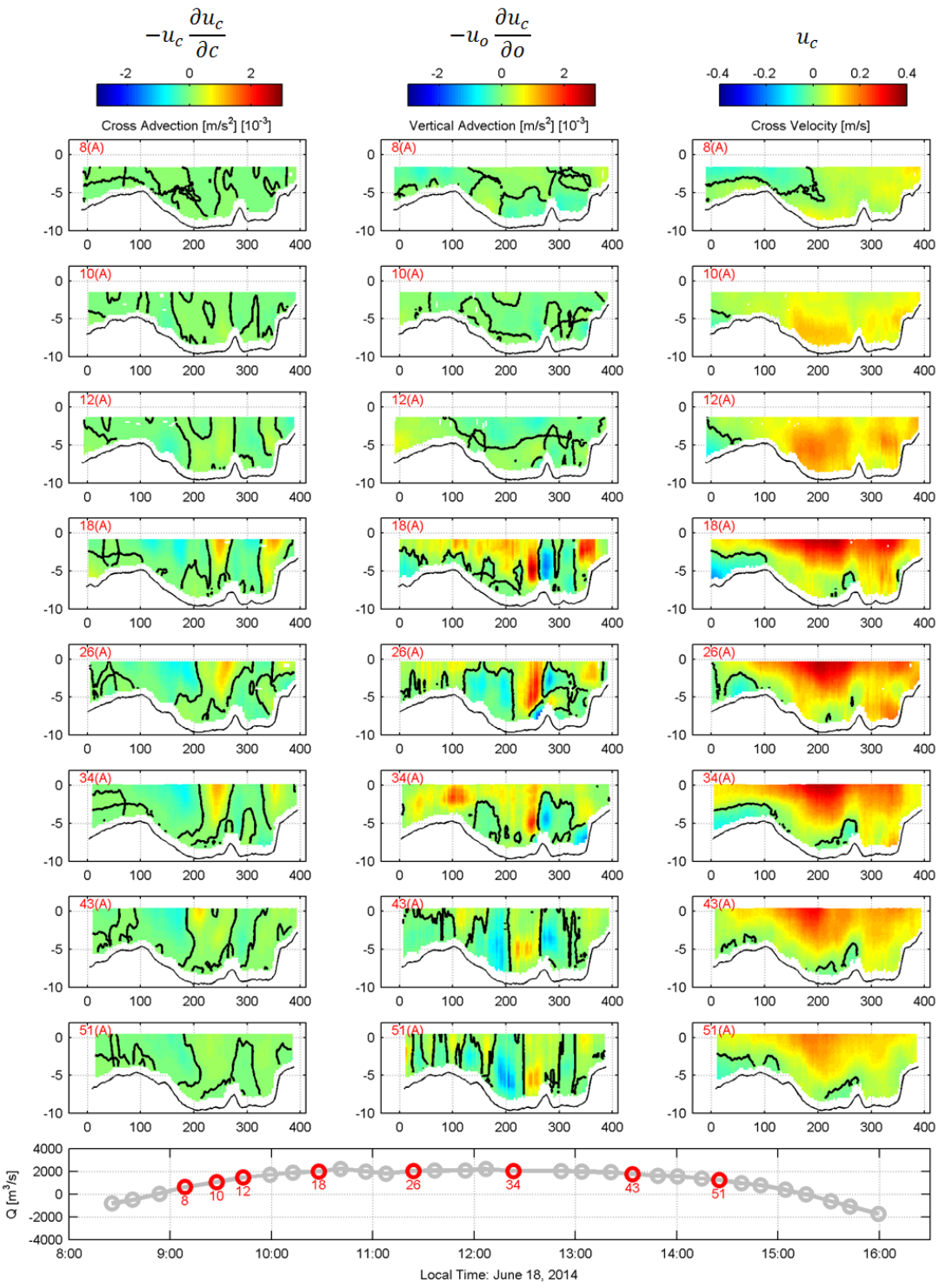

Figure 60: Flood advective cross channel momentum terms. Columns refer to terms on the left side of Equation (45) except cross velocity. Rows indicate transect number and point in tidal cycle referenced in the volume flux time series at the bottom. Thick black lines represent zero contours and thin black line is measured depth. X- and Y- axes are the D and o coordinates in $[m]$.

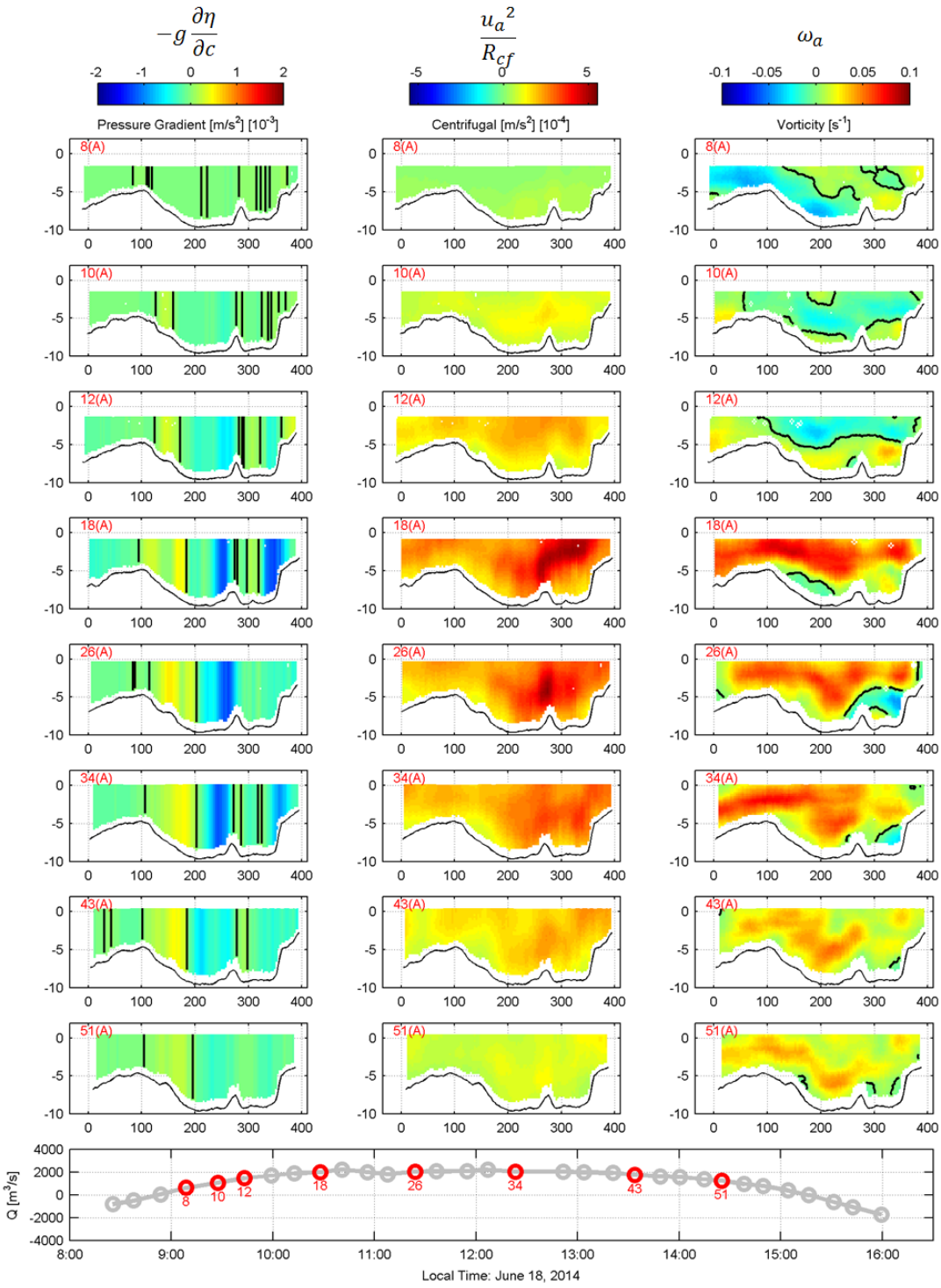

Figure 61: Flood forcing cross channel momentum terms. Columns refer to terms on the right side of Equation (45) except vorticity. Rows indicate transect number and point in tidal cycle referenced in the volume flux time series at the bottom. Thick black lines represent zero contours and thin black line is measured depth. X- and Y- axes are the D and o coordinates in $[m]$.

deceleration causes positive advection; cross channel momentum is becoming concentrated (200 m$<$ D $<$ 250 m). This is indicative of the secondary circulation cell and is further reinforced by the vertical advection term, $-u_o \frac{\partial u_c}{\partial o}$, shown in the second column of Figure 60. To the left of the bump, the downwelling of the cell is carrying the stronger cross-channel momentum toward the seabed (positive vertical advection) leading to stronger cross-channel velocities throughout the water column. On the left-hand side of the cell, there is vertical advection of weaker cross channel momentum towards the surface, indicative of upwelling and reducing the cross-channel velocity. The same signature can be seen to the right of the bump ($D >$ 270 m) for the second co-rotating cell. The effects on the kinematics is evident in the cross channel velocity distribution u_c in the third column of Figure 60. The strongest cross channel currents are concentrated over the full water column on the right hand side of each individual circulation cell and are reduced on the left-hand side.

The associated forcing terms from the right hand side of the cross channel momentum balance (Equation (45)) are shown in Figure 61. The pressure gradient term in the first column further highlights the driving force for the flow reversal associated with the secondary circulation, in particular: the positive forcing accelerating the flow on the left-hand side and a negative forcing decelerating the flow on the right hand side of each cell. Although the forcing associated with centrifugal acceleration is small compared to the other terms, its spatial distributions in the second column of Figure 61 show striking similarities with the resultant kinematics exemplified by the vorticity in the third column. In the peak flow Transects 18(A)-34(A), contours of strong centrifugal acceleration mimic contours of vorticity. This is striking because the calculations of the terms from the measurements are completely independent. Thus the centrifugal acceleration is the driver of the vorticity and circulation; the pressure gradient and advection terms are resultant and feedback to further distort the circulation.

The cross channel momentum analysis illuminates why the secondary circulation exists and evolves, however it does not explain the existence of two co-rotating cells. The significant terms from the depth integrated axial momentum equation, Equation (49), for each transect is plotted in Figure 62. Similar to the terms in the depth averaged cross momen-

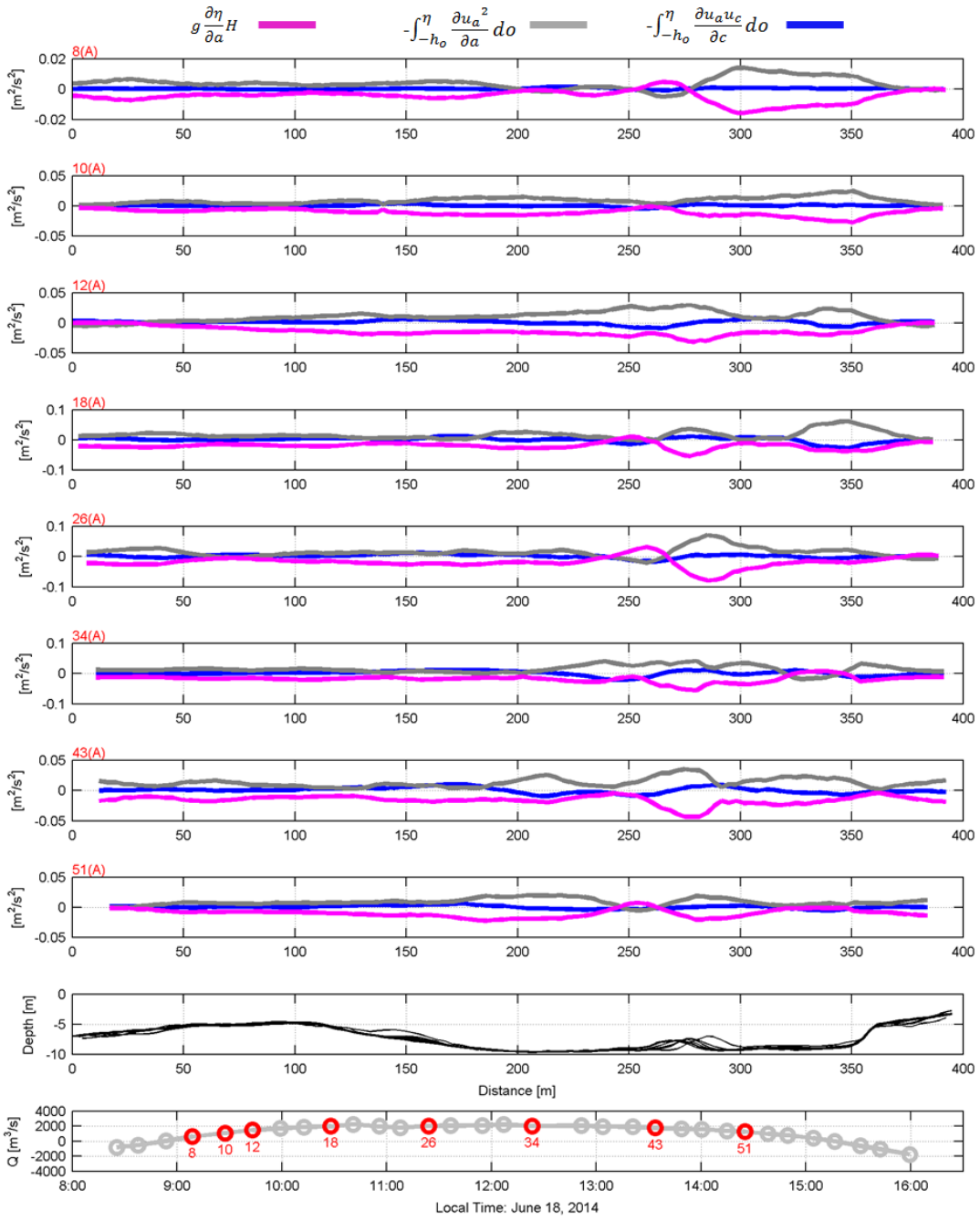

Figure 62: Depth integrated axial momentum terms for flood tide. Only the significant terms corresponding to Equation 49 are shown. Rows indicate transect number and point in tidal cycle referenced in the volume flux time series at the bottom. Second to bottom plot is transect depths for reference. X-axes are the D coordinate in $[m]$.

tum equation, features and magnitudes grow and shrink with the tidal stage. The pressure gradient is generally negative, driving the flood volume flux except in the vicinity of the topographic bump. In the absence of any topographic features or channel curvature, the primary balance would be between the pressure gradient and the bottom stress. A persistent feature clear for the stronger flow in Transects (18(A)-34(A)), is the small positive peak and subsequent larger negative dip in the pressure gradient at $D = 250$ m and $D = 280$ m respectively. This positive peak is indicative of a slight rise in the water surface in the positive axial direction and the negative dip is indicative of a more drastic drop. The zero crossings of each, the locations of the apexes, are to the left and centered over the bump respectively.

The lowered water surface over the bump is in accordance with subcritical flow behavior for flow over a raised bed. As axial flow approaches the bump, it is redirected and loses axial momentum near the surface. This disturbance is felt upstream, water piles up behind, inducing an enhanced pressure gradient in the direction of flow, and accelerates the rest of the water column. This is further supported by the fact this large dip in the pressure gradient term is balanced by the axial advection term, $\int_{-h_o}^{\eta} \frac{\partial {u_a}^2}{\partial a} do$.

The raised water surface to the left of the bump is induced by the secondary circulation discussed in the cross channel momentum analysis. As shown in the kinematic analysis, the circulation features associated with the bump and Transect A are highly localized to that transect. Thus, the water surface elevations associated with the secondary circulation are as well. Thus the piling of the water due to the secondary circulation on the outer bends of the cells are represented as positive water surface gradients and retardant pressure gradients in the axial direction as shown by the small peak to the left of the bump in Figure 62. This is further supported by the fact that the cross advection term associated with the secondary circulation, $\int_{-h_o}^{\eta} \frac{\partial u_a u_c}{\partial c} do$, has a larger contribution at this location.

To further observe the effect of the secondary circulation on the axial momentum, contour plots of terms in Equation (46) are shown in Figures 63 and 64. The cross channel advection term in the first column, $-u_c \ \frac{\partial u_a}{\partial c}$, shows the loss of axial momentum at the surface to the left of the bump but shows a gain to the right in Transects 18(A)-26(A). This

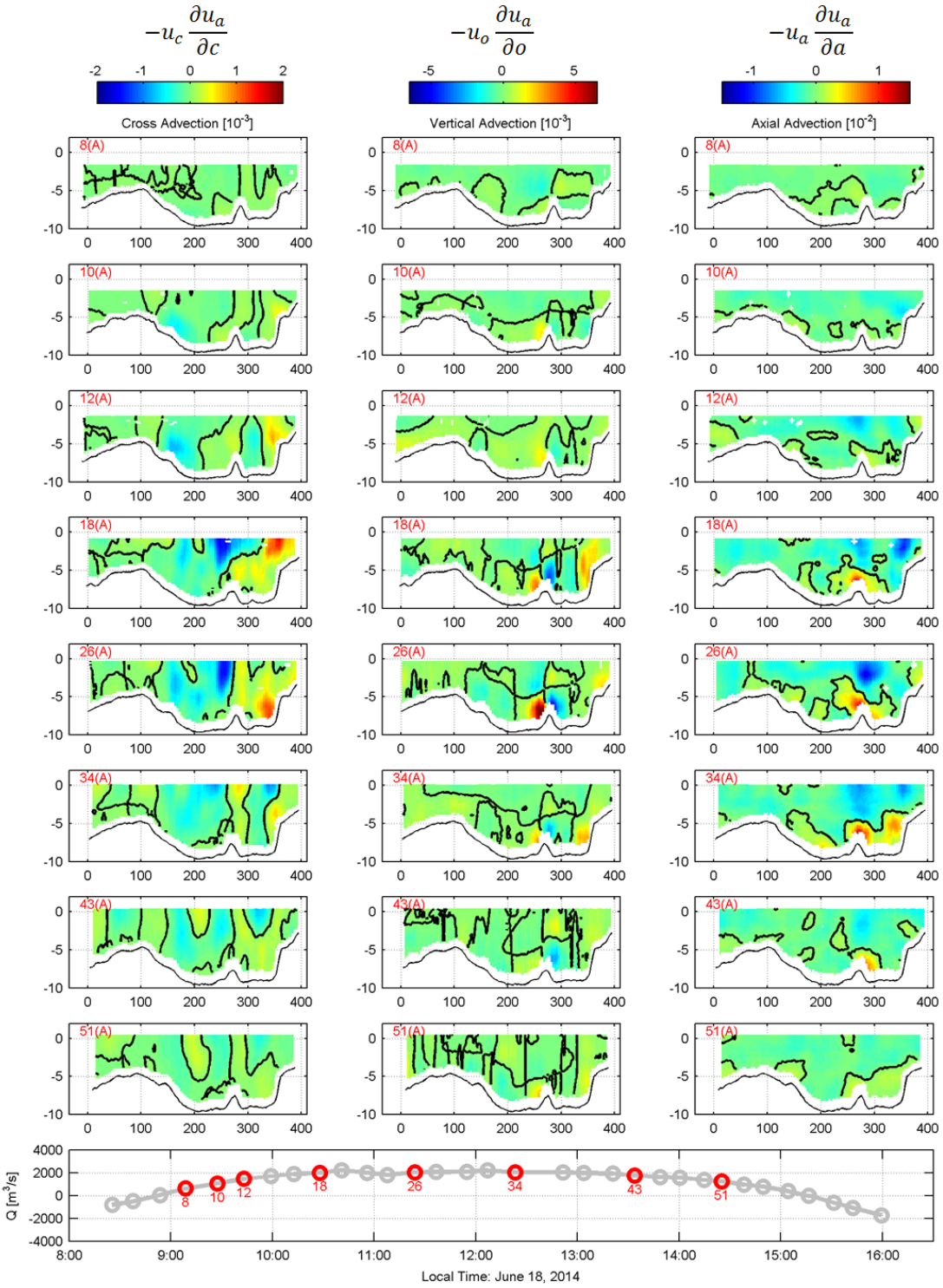

Figure 63: Flood advective axial channel momentum terms. Columns refer to terms on the left side of Equation (46) except axial velocity. Rows indicate transect number and point in tidal cycle referenced in the volume flux time series at the bottom. Thick black lines represent zero contours and thin black line is measured depth. X- and Y- axes are the D and o coordinates in $[m]$.

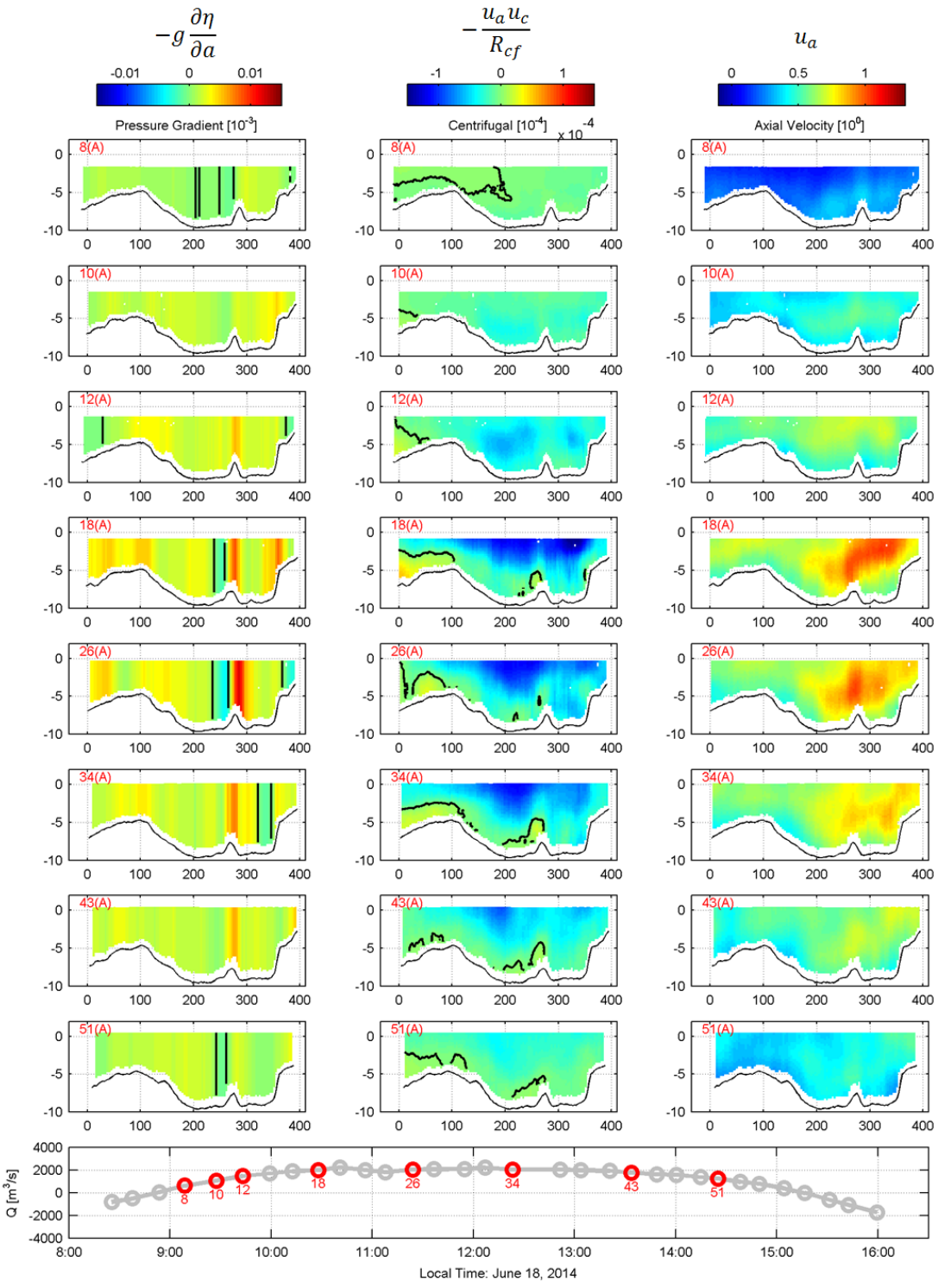

Figure 64: Flood forcing axial channel momentum terms. Columns refer to terms on the right side of Equation (46) except axial velocity. Rows indicate transect number and point in tidal cycle referenced in the volume flux time series at the bottom. Thick black lines represent zero contours and thin black line is measured depth. X- and Y- axes are the D and o coordinates in $[m]$.

is due to the circulation cell to the left of the bump advecting weaker axial momentum from the far left-hand side of the channel, and the cell to the right of the bump advecting the stronger axial momentum to the outer bend.

The second column in Figure 63 shows the checkerboard pattern of the vertical advection term, $-u_o \frac{\partial u_a}{\partial o}$. The downwelling on the right hand side of the left cell is transporting higher axial momentum downwards indicated by the reduction of the surface and increase near the bed. Similarly the upwelling on the left-hand side of the right cell shows the opposite pattern. The overall effects of the acceleration on the axial velocity distribution is shown in the last column of Figure 64, where strong axial currents are concentrated above the bump and smeared along the surface to the right.

The axial advection term in the last column of Figure 63, $-u_a \frac{\partial u_a}{\partial a}$ supports sub-critical flow behavior over the bump with the reduction in axial momentum at the surface along with an increase near the sea bed, resulting in nearly depth uniform axial flow over the bump. Subcritical flow behavior is also again shown by the pressure gradient in the first column of Figure 64 along with the negative pressure gradients induced by the piled water on the outside bends of the circulation cells.

As in the cross channel momentum balance, the centrifugal term $\frac{u_c u_a}{R_{cf}}$ is small relative to the other terms. In general, the centrifugal term is reducing the axial momentum as some of the axial momentum is transformed to cross momentum. However, there is a clear reduction in negative values near the seabed over the bump. This has a similar effect as the vertical momentum over the bump, leading to more depth uniform axial velocity. This could be a result of the enhanced subcritical flow advecting the associated cross channel momentum downstream; unfortunately, the relevant term, $-u_a \frac{\partial u_c}{\partial a}$ in the cross channel momentum equation (Equation (45)), cannot be resolved.

For ebb tide, many of the signatures associated with secondary circulation seen previously in flood tide are also present. However, because of the opposing curvature of the confluent streams and resultant counter-rotating cells, the directionality of some of these terms differ. The depth averaged cross momentum equation is plotted for each ebb transect in Figure 65. The signals have more noise than the flood measurements due to the increa-

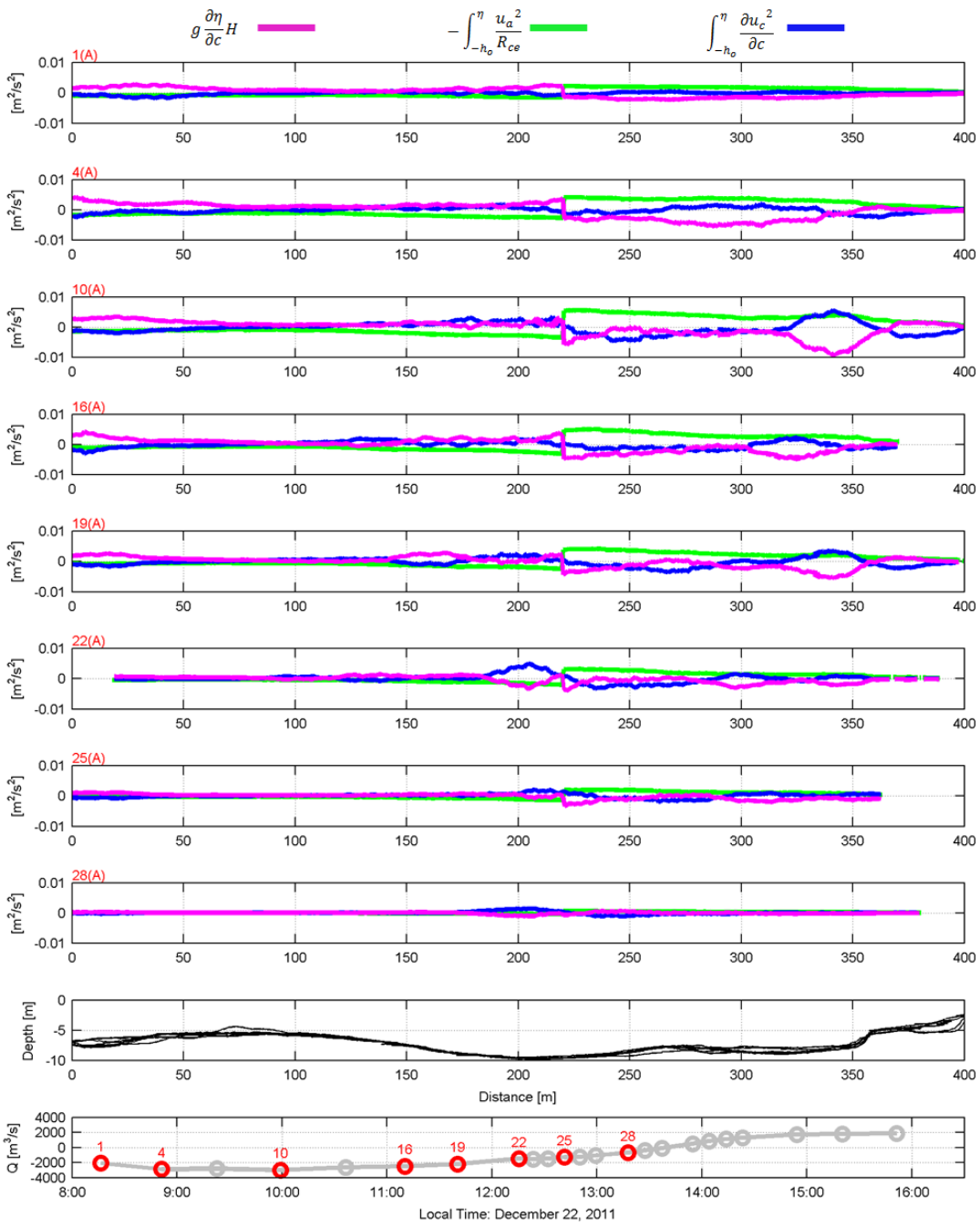

Figure 65: Depth integrated cross momentum terms for ebb tide. Terms correspond to terms in Equation (48). Rows indicate transect number and point in tidal cycle referenced in the volume flux time series at the bottom. Second to bottom plot is transect depths for reference. X-axes are the D coordinate in $[m]$.

sed sampling rate of the December measurements and amplified effects in the resultant gradient calculations. As in flood, the magnitudes and features of the terms increase and decrease with the tidal stage. Another interesting temporal feature is the relative magnitudes of the left-hand side of the channel and the right. As discussed previously in the kinematic analysis, flow from Transect C rescinds quicker than from Transect B. This is evident in the depth averaged cross momentum equations as well, explaining the reduction in circulation on the left-hand side.

The centrifugal term $\int_{-h_o}^{\eta} \frac{{u_a}^2}{R_c} do$, shown in Figure 65 is more significant for the ebb tide than in the flood; its contribution is of the same magnitude of the convective acceleration. The centrifugal term represents a negative pressure gradient to the right of the interface at $D = D_i = 220$ m and a positive pressure gradient to the left. These opposing terms represent the convergence and rise of the water at the center of the channel from the two counter-rotating cells. The zero crossing of the advective term $\int_{-h_o}^{\eta} \frac{\partial {u_c}^2}{\partial c} do$, represents the peak of the water surface: where down-welling occurs. Knowing this, D_i was chosen as approximately this location to best represent the interface of the two cells and the change in sign of R_{ce}.

The pressure gradient terms also shows a gradient in the water surface on the far right side of the transect $D > 300$ m. This pattern is indicative of the co-rotating cells seen in the flood tide in Figure 59 however of opposite sign. It suggests the counter clockwise cell on the right-hand side is split into two as well.

Contour analysis of the vertically varying momentum terms for the ebb tide is not shown. For the cross channel momentum, the advective terms and forcing terms reiterate the processes evaluated using Figure 65. The axial momentum analysis for ebb tide is also not shown because as witnessed in the field, large scale eddies with vertical vorticity frequently spun through Transect A during ebb tide. As a result, consistent steady features in the axial momentum terms were difficult to ascertain from the data. As described in the kinematics section literature review, flow confluences with discordant beds can be very turbulent and volatile; this transect analysis is not appropriate to pull out consistent features. A series of stationary ADCPs could better resolve the mean state of the transect for ebb tide.

5.3 Summary of Localized Hydrodynamics

In this chapter the localized hydrodynamics are analyzed to isolate areas of persistently high current velocities suitable for tidal energy extraction. The outer bend of Transect A near the island has persistently high current velocities for both flood and ebb tide. To identify the physical processes behind this hotspot location the kinematics and dynamics surrounding the spot are studied through the use of measurements from specific transects across the channel.

For flood tide, the concentration of strong axial velocity is a result of the topographic bump in Transect A. The bump induces an acceleration of flow throughout the water column above it due to sub-critical flow behavior. Axial momentum is further restricted to this area due to the two clockwise, co-rotating secondary circulation cells associated with flow in a curved channel. There are dual co-rotating cells rather than one cell because the bump not only serves as a physical boundary but also locally accelerates axial flow, advects cross channel momentum away at the surface, and splits the cells. Ultimately, the sub-critical flow and secondary circulation grows and weakens with the tide and overall axial velocity. However, the secondary circulation takes longer to dissipate and continues to distort axial momentum distributions well after peak flood tide.

For the ebb tide, the cross channel momentum distribution is governed primarily by the centrifugal acceleration terms of the confluent streams which is an order of magnitude larger than the centrifugal acceleration associated with the channel curvature in flood tide. Upstream of the hotspot, flows from two confluent streams are funneled and redirected into a singular channel. Redirection of each inflow requires opposite curvature and thus opposing centrifugal acceleration. The resultant circulation is two counter-rotating secondary circulation cells, with surface flow directed towards the interface of the two confluent streams, forming peaked water surface near the center of the channel. Circulation along the seabed is guided by the bathymetry: the bump on the right hand side of the transect splits the counter clockwise cell on the right hand side of the channel into two co-rotating counter clockwise cells. As in flood tide, the strength of these cells and associated pressure gradients grow and weaken with the tidal stage. Axial momentum is consistently concentrated depth

uniformly slightly to the right and above of the bump due to the secondary circulation. The concentration is restrained to the middle of the channel due to the opposing cross channel velocities from the other incoming channel flow. The cross channel momentum is relatively consistent as compared to the axial throughout ebb tide. The axial momentum is highly volatile and turbulent as expected for confluent channels with discordant beds.

Some terms of the momentum balance could not be resolved, most notably the advection of cross channel momentum in the axial direction as well as turbulence terms. The axial advection term is suspected important for areas with great variability in the streamwise direction. This includes the localized topographic bump, or hotspot. It is hypothesized this term is responsible for advecting cross channel momentum downstream from the hotspot, interrupting secondary circulation.

The turbulence terms are highly important in both the axial and cross momentum balances. As remarked by Blanckaert and De Vriend (2004), additional circulation cells form from the positive feedback of the cross channel turbulent shear stresses; they are not solely dissipative terms. In the axial momentum, turbulent shear stresses are particularity important for ebb tide, particularly at the shear interface of the two confluent flows as well as the discordant beds where there is entrainment and strong mixing (De Serres et al., 1999; Biron et al., 2004; Leite Ribeiro et al., 2012). The turbulence through the vertical shear also governs the final vertical structure of the currents.

The consistent mechanisms behind hotspot formation that can be resolved include subcritical flow over a topographic bump, secondary circulation due to flow curvature, both by channel curvature and flow confluence, and concentration of axial momentum along circulation cell vertical interfaces and boundaries. It is important to note the topographic bump is a function of sediment transport and may be variable over longer timescales than measured (>weeks). This will be an important consideration if an actual turbine assembly is installed; the disturbed hydrodynamics due to energy extraction may change the topography and alter the hydrodynamics. Thus it will be important to resolve variability of the feature through bathymetric surveys spanning months or modeling energy extraction and sediment transport.

CHAPTER VI

THEORETICAL AND TECHNICAL RESOURCE ASSESSMENT

The previous chapters analyzed the tidal hydrodynamics surrounding Rose Dhu Island; model results were compared against measurements and the tidal distortion was characterized. These results are used to perform theoretical and technical tidal current energy resource assessments and to explore the effects of tidal distortion on the resource.

To accomplish this, first the generalized effects of tidal distortion on theoretical and technical hydrokinetic energy are explored through the analysis of simplified synthetic signals. Next, the yearly theoretical resource estimates of Rose Dhu is performed and the effects of localized and estuarine distortion is explored. Turbine efficiency curves are developed in part from an in situ turbine rotor testing at localized hotspots. These curves are utilized to complete the technical resource assessment for Rose Dhu and explore the effects of tidal distortion. Exploring the effects of tidal distortion on the theoretical and technical hydrokinetic resources is beneficial not only for Rose Dhu Island, but assessments for other wetland locations as well since it is such a dominant characteristic of wetland estuaries.

6.1 Generalized Effects of Tidal Distortion

Tidal distortion can lead to amplifications of tidal current velocities for a given stage, increasing viability for hydrokinetic energy utilization. However, current enhancement in a given tidal stage implies weaker currents in the opposite stage. Hydrokinetic turbines have limited windows of operation defined by the minimum cut-in speed and maximum rated speeds and have different turbine efficiency curves as a function of velocity.

Spatial variations of constituent phasing were analyzed to identify optimum turbine installation locations and reduce intermittency in total power production for both regional (Polagye and Thomson, 2013a) and national (Iyer et al., 2013) scales. However, both studies concentrated on areas with relatively deep channels, small overtide amplitudes, and little

distortion. The effect of the phasing between constituents and distortion of the velocity signal itself as pertains to power production was not detailed.

To further hydrokinetic energy extraction in shallow environments, presented within this section is the sensitivity of turbine selection and operation as a function of non-linear current velocity distributions quantified by the statistical parameters of skewness and asymmetry. Synthetic velocity signals are constructed with varying values of tidal distortion. Distribution functions of velocities, available power, and energy density contribution are defined, calculated and presented for each. Turbine efficiency curves are implemented to observe the effect of the varying velocity distributions on technical energy density.

6.1.1 Synthetic Signal Construction and Normalization

Tidal distortion arises from the cascade of energy from the principle astronomical tidal constituents to higher and compound harmonics known as overtides. Typically, the distortion of an estuarine system is characterized by the relative amplitude and phase of a principle constituent and its first harmonic (Friedrichs and Aubrey, 1988). For much of the global coasts, including the US east coast, this is the M_2 constituent and M_4 overtide, however such analysis and characterization has utilized higher harmonics as well (Blanton et al., 2002). For velocity timeseries, a larger M_4/M_2 ratio signifies a more distorted tide. The relative phasing, $\phi = 2M_2 - M_4$, indicates a longer ebb-to-flood transition ($90°\pm 90°$) or longer flood-to-ebb transition ($270°\pm 90°$), or indicates a longer flood tide ($180°\pm 90°$) or ebb tide ($0°\pm 90°$).

Although calculated constituents are an accurate characterization of tidal distortion and useful tool for model/measurement validation, they provide incomplete insight into the physical causes of the distortion. Most notably, this method can only compare two constituents at a time, disregarding other non-tidal forcing and overtide constituents. Thus, this study quantifies distortion through calculating the statistical asymmetry (A_x) and skewness (S_x) of the signals as defined in Equations (43) and (44).

Both A_x and S_x, when used to describe tidal signal distortion from a principle constituent and dominant overtide such as M_2 and M_4, can be related back to the relative

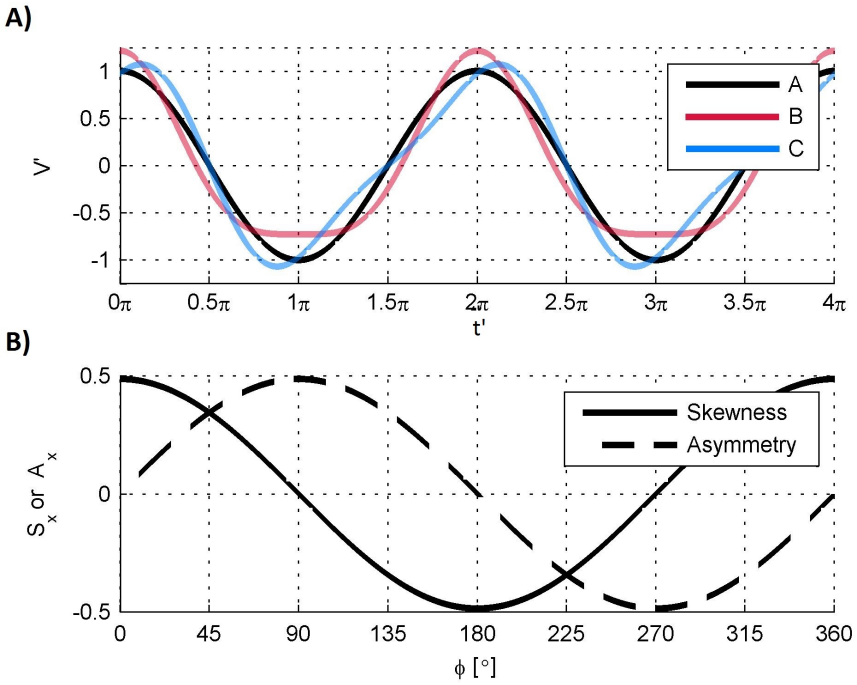

Figure 66: A: Non-dimensional velocity Signals A ($A = S = 0$), B ($A = 0/S = 0.48/\phi = 0°$), and C ($A = 0.48/S = 0/\phi = 90°$). B: $M_2 + M_4$ Signal skewness (solid) and asymmetry (dashed) for varying ϕ.

phasing. Theoretically, velocity signals with a positive A have a longer flood-to-ebb transition and corresponds to a $2M_2 - M_4$ phase difference of $90° \pm 90°$ with more positive values being closer to $90°$ as shown in Figure 66. Positive S corresponds to a longer ebb tide and a phase difference of $(180° \pm 90°)$ with larger skewness values will be closer to $180°$ and so on.

The effects of skewness and asymmetry on tidal energy are studied through the use of two synthetic velocity signals of the form

$$V(t) = A_{M_2} cos(\omega_{M_2} t) + A_{M_4} cos(\omega_{M_4} t - \phi) \tag{53}$$

where t is time, A and ω are respectively the amplitudes and frequencies of the M_2 and M_4 constituents, and ϕ is the relative phasing of the two constituent signal contributions.

To accurately compare the aggregate effects of distortion to non-distortion, Signal A is created as

$$V_A(t) = A_{M_2} \sqrt{1 + r^2} cos(\omega_{M_2} t) \tag{54}$$

where r is the ratio of the M_4 and M_2 amplitudes, A_{M_4}/A_{M_2}. Signal A represents a non-distorted M_2 signal with the same *spectral* energy as a distorted signal. The amplitude of Signal A is used to produce the non-dimensional velocity magnitude

$$V'(t') = \frac{|cos(t') + rcos(2t' - \phi)|}{\sqrt{1 + r^2}} \tag{55}$$

where $t' = \omega_{M_2} t$ is the non-dimensional form of time. Signal B with $\phi = 0°$, as shown in Figure 66, corresponds to maximum skewness and zero asymmetry while Signal C with $\phi = 90$ has zero skewness and maximum asymmetry. Both signals, have an A_{M_4}/A_{M_2} amplitude ratio, $r = 0.25$, a possible, albeit large ratio that has been observed in highly non-linear estuaries (Bomminayuni et al., 2012).

Time series of the non-dimensional kinetic power density, $P'(t')$, are created from the velocity signals as

$$P'(t') = V'(t')^3 \tag{56}$$

Equation 56 is analogous to Equation (7) in Chapter II but non-dimensional. For a time varying kinetic power density such as in Signals A, B and C, P' can be integrated over a tidal period of time to provide the kinetic energy density E' defined as

$$E' = \frac{3}{8} \int_0^{2\pi} P'(t') dt' \tag{57}$$

such that E' of the undistorted Signal A is 1.0.

6.1.2 Theoretical Power Probability Distributions

A probability density function (PDF) of V' or P' over a given tidal cycle is calculated numerically from each signal as $f_{V'}(V')$ and $f_{P'}(P')$ respectively. The mean power over the tidal cycle is then calculated as

$$\bar{P'} = \int_0^{P'_{max}} P' f_{P'} dP' \tag{58}$$

The integrand $P' f_{P'}$ can be thought of as the relative contribution to the average power output or energy for each value of P' or its respective V'.

The non-dimensional total kinetic energy density over a tidal cycle is found as

$$E' = \frac{3}{8} 2\pi \bar{P'} \tag{59}$$

where once again the non-dimensional total kinetic energy density of Signal A is 1.0. Exceedence energy as a function of the cut-in power P'_c is calculated as

$$E'_e(P'_c) = \frac{3}{8} 2\pi \int_{P'_c}^{P'_{max}} P' f_{P'} dP' \tag{60}$$

The exceedance energy $E'_e(P'_c)$ represents the total kinetic energy density in the signal produced by kinetic power densities above the cut-in power, i.e. technical kinetic energy density without the considerations of turbine efficiencies. A value of E'_e equal to one represents the full technical kinetic energy density computed from the full range of the signal.

As compared to a pure velocity and power PDF, plots of $f_{P'}P'$ and E'_e, help compare not only the relative distribution of powers and velocities, but also their relative *contribution* to the total energy taking into account both duration and magnitude. This assists in comparing important velocity operating ranges between signals.

PDFs of velocity magnitude V' are plotted in Figure 67 for Signals A, B and C which have zero distortion, pure skewness, and pure asymmetry respectively. For all the signals, there are peaks at the corresponding velocity crest and trough magnitudes because these areas are broader than the transitional velocities at the zero-crossing. Because the trough and crest are symmetric about the x-axis for both A and C, there is only one peak in the PDF. However the higher harmonic in Signal C increases both crest and trough, resulting in a peak in the PDF with a slightly larger magnitude despite being symmetric about the x-axis.

Most striking are the double peaks for Signal B, which have maximum skewness. The first peak at a lower velocity corresponds to the weaker but broader trough velocity. Therefore the peak corresponding to the trough velocity signal is weaker at approximately 0.7 the magnitude of the undistorted signal, however has the highest peak in the PDF. Similarly, the crest magnitude, corresponds to a velocity approximately 1.2 the magnitude of the undistorted signal and is much narrower, therefore has a smaller peak in the PDF.

Figure 67 highlights important considerations for turbine operation and selection for distorted tides. Signals A and C have fairly large single PDF peaks for their maximum velocities whereas Signal B has the smallest pdf peak for its maximum velocity. Such

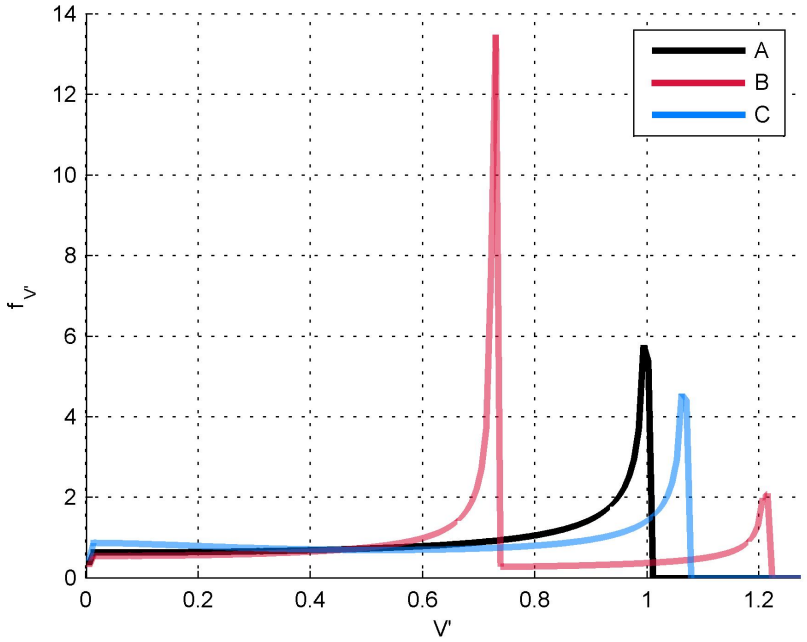

Figure 67: Probability Density Function, $f_{V'}$ for non-dimensional velocity, V', for Signals A, B and C

discrepancies in distributions for signals with the same signal energy and relative constituent amplitudes highlights the importance of accurate phase information in resource assessments. Signal B highlights a key consideration of turbine operation and selection for skewed tides: weighing the relative contribution of the lower velocities occurring over a longer time period or the stronger currents occurring for shorter periods. To further assess this, power density distributions and energy density plots are constructed.

Figure 68 depicts a PDF for the nondimensional power density P'. Through the cube of the velocity, weak velocity signals near transitional periods are aggregated producing a large peak in the PDF near zero. This further emphasizes the additional power arisen from the increase in velocity of the distorted tides; while Signal B had 1.2 times the peak velocity of A, its peak power is now more than 1.6 that of A. Although informative on power magnitudes, Figure 68 still does not tell much about the relative contribution to energy. Although there is great representation at low P', because the actual value of P' is so small, its relative contribution to the energy is negligible. Thus inferring energy production from Figure 68 can be misleading.

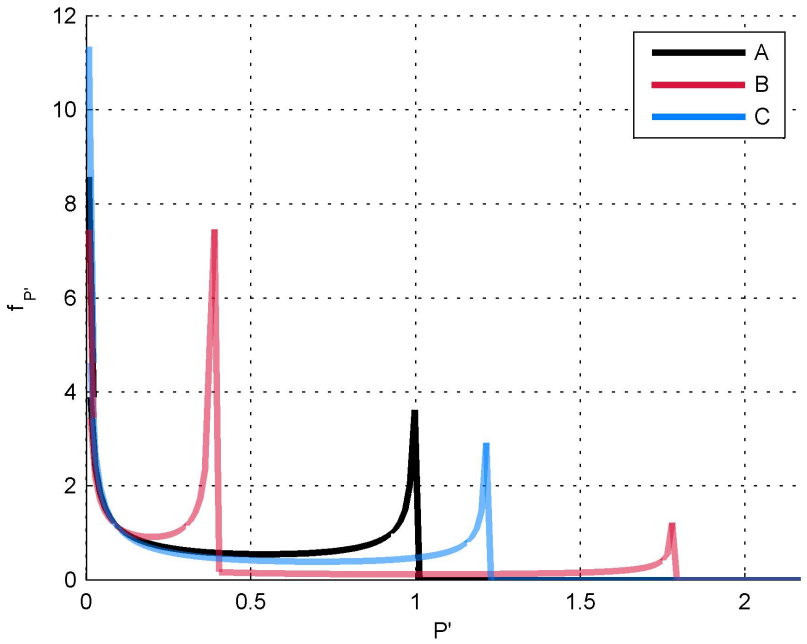

Figure 68: Probability Density Function, $f_{P'}$ for non-dimensional kinetic power density, P', for Signals A, B and C

As Equation (58) indicates, the mean power is formed from the integral of $P'f_{P'}$. Therefore the area under plots of $P'f_{P'}$ is an indicator of the relative contribution for each P' to the mean power and hence energy as seen from Equation (59). As seen in Figure 69A, the large peaks at minimal velocities are diminished due to the weighing of the respective P' value as compared to the PDF in Figure 68. As expected, most of the energy is contributed by the peak velocities since peaks in the PDF corresponded to maximum power magnitudes for Signals A and C. The weighing factor of P' also reduces the difference in proportional peaks between the trough and crest magnitudes. However, as seen in Figure 69, the smaller trough magnitude provides the largest energy due to its extended duration.

To facilitate assessing the implications of cut-in velocities, plots of $P'f_{P'}$ and Equation 60 are mapped back from P' to its respective V' in Figure 69B. Thus, for a turbine with a velocity cut-in speed above 70% of the non distorted magnitude, for Signal B, a large portion of the available energy would be negated even though it has the largest crest magnitudes of the three signals. Interestingly, this would not occur for Signals A and C, despite having similar spectral energy and overall smaller crest magnitudes. At face value, a signal with

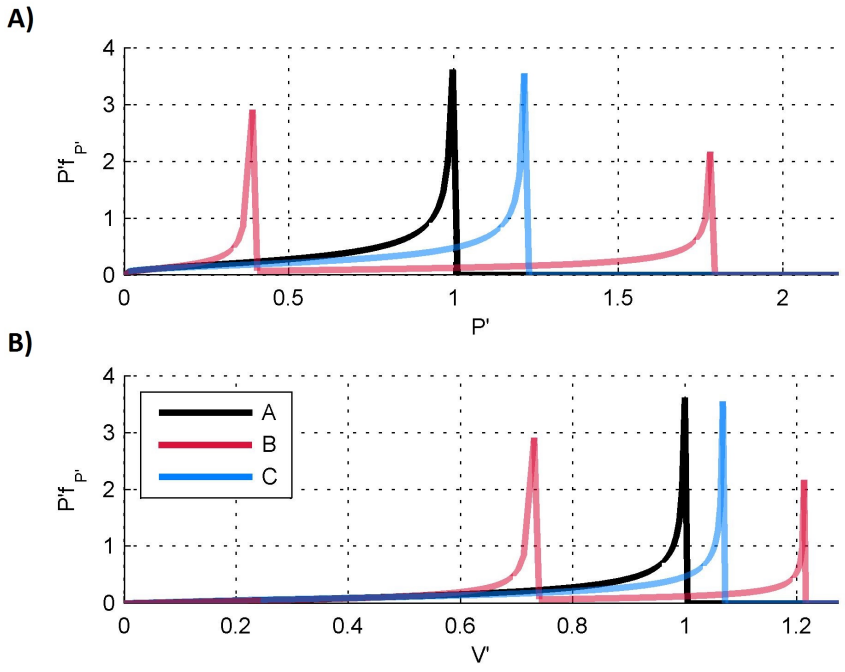

Figure 69: Non-dimensional energy distribution, $P'f_{P'}$ as a function of P' *(A)* and V' *(B)* for Signals A, B and C.

a large peak velocities would seem to fair better for turbines with higher cut in speeds, however, for a skewed signal this may not be the case.

This concept is further explored using the exceedance energy curves defined by Equation (60) and shown in Figure 70. The exceedance energy density is normalized by the energy density of the undistorted signal. Thus the relative difference in E'_e for all signals can be treated as a direct comparison of captured energy, not relative to their own total available energy. The exceedance energy density is fairly consistent for all signals with only a small decrease until $V'_c = 0.6$. E'_e remains relatively high above 0.95, signifying approximately 5% of the total energy of the undistorted signal is contained in those velocity ranges.

However, for $V'_c = 0.6 - 0.75$ there is a drastic deviation in Signal B, corresponding to the first peak seen in Figure 69. Here, E'_e drops to approximately 0.65, signifying a (0.95-.65) 30% loss of energy. Thus, it can be ascertained that the first peak for Signal B, or the trough velocities, provide approximately 30% of total energy of the signal. If a cut in speed is applied at $V'_c = 0.75$ with 100% efficiency Signals A and C still provides over 90% of the total available energy of the undistorted signal while Signal B, with the larger

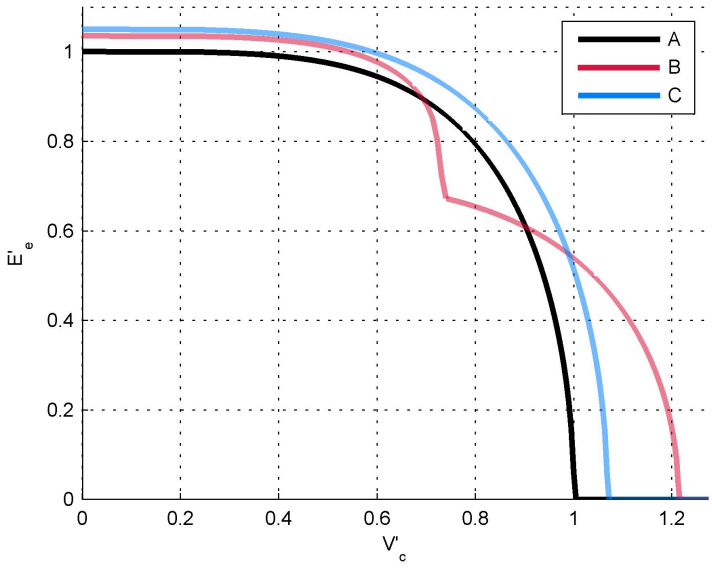

Figure 70: Exceedence Energy Curves, E'_e for Signals A, B and C.

peak velocity magnitude would only provide 65%. It is not until approximately $V'_c = 0.9$ and $V'_c = 1$ where the energy captured in Signal B is greater than A and C respectively.

Although the E'_e curves clearly show the available energy incorporating cut-in speeds, it cannot highlight the effects of variable efficiencies. To accomplish this, efficiency curves are implemented and the analysis is repeated.

6.1.3 Technical Power Probability Distributions

The efficiency curves used here are designed as

$$E_f(V') = \begin{cases} 0 & V' \leq V'_c \\ C_D & V'_C \leq V' < V'_R \\ \frac{C_D|V'_R|^3}{|V'|^3} & V' \geq V'_R \end{cases} \tag{61}$$

where C_D is a constant efficiency or percent of the power extracted, although arbitrary in this study since constant, it is set at 0.59 or the Betz Limit. V'_c and V'_R are the cut in and rated speeds respectively. Essentially below the cut in speed, efficiency is zero, no power is extracted. Between the V'_c and V'_R, the efficiency is constant and thus power production is consistently proportional to the increase in available energy. For velocities greater than V'_R, the turbine produces power at the rated speed, thus E_f decreases.

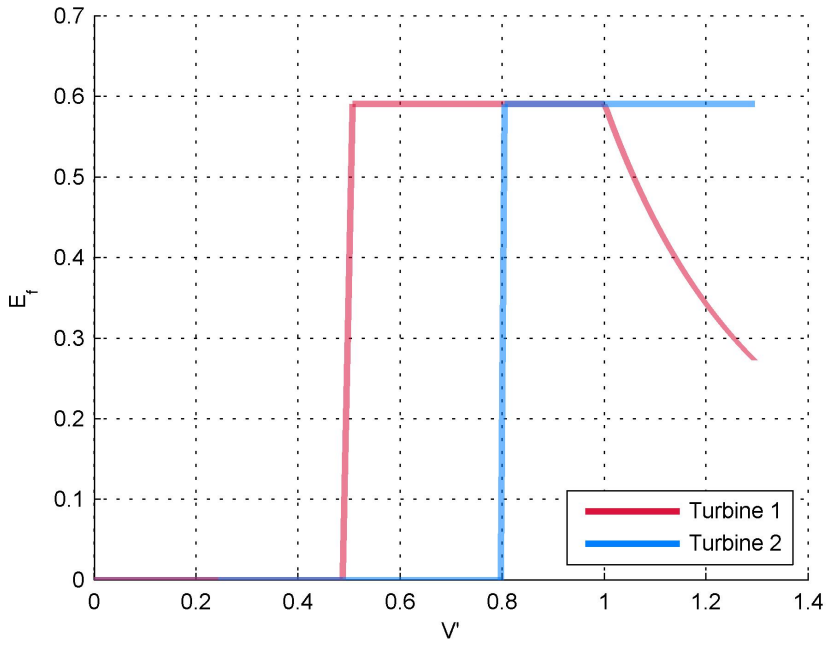

Figure 71: Turbine efficiency curves as a function of non-dimensional velocity.

Two efficiency curves are constructed and plotted as a function of V' in Figure 71. Turbine 2 represents a turbine with a high cut in speed and rated speed whereas Turbine 1 represents a device with a low cut-in and rated speeds, designed for moderate currents. It is important to remember V' is not the actual cut-in speed but the ratio of the undistorted velocity magnitude; thus although a rated speed of 0.8 appears low, it can be scaled to larger values.

To implement the efficiency curves into the energy production distributions, $E_f(V')$ is mapped to $E_f(P')$ and is inserted into Equation (58) providing the mean technical power

$$\bar{P}'_t = \int_0^{P'_{max}} E_f(P') P' f_{P'} dP' \tag{62}$$

Similarly, the non-dimensional techncial kinetic energy density over a tidal cycle is found as

$$E'_T = \frac{3}{8} 2\pi \bar{P}'_t \tag{63}$$

E'_T quantifies the captured technical energy as compared to the available energy in Signal A. To describe the turbine efficiency for a particular signal, the total turbine efficiency, E_{fT}

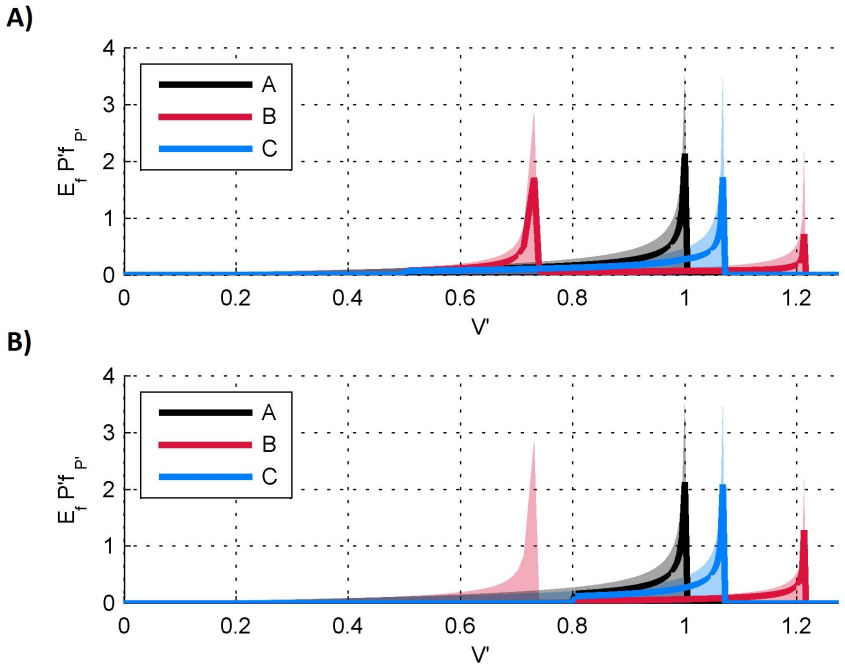

Figure 72: Non-dimensional energy distribution, $P'f_{P'}$ with (thick lines) and without (shaded area) turbine efficiencies. *(A)*: Turbine 1. *(B)*: Turbine 2

is defined as

$$E_{fT} = \frac{\bar{P}'_t}{\bar{P}'} \tag{64}$$

The implications of the efficiency curves can be seen from the plots of $E_f P' f_{P'}$ in Figure 72. Turbine 1, designed to capture the middle of the velocity distribution, captures the large peak at moderate velocities for the skewed Signal B, but has relatively low energy production at the higher velocities compared to the available energy. The technical energy density for A, B, and C, is shown in Table 11 as 0.58, 0.49, and 0.57 respectively. Turbine 2, designed to capture the upper reaches of the velocity distribution, has technical energy densities for A, B, and C of 0.47, 0.39, and 0.51 respectively. The total turbine efficiencies E_{fT} mimic technical energy densities for both turbines.

For Signals A and C, with singular peaks above the rated speed in Turbine 1 still has a decrease in technical energy for Turbine 2. However Signal B, which has large power production potential in the moderate range of the distribution, captures much less energy when focusing efficiency on the high velocities. Taken collectively, this is somewhat counter

intuitive when tidal resource assessments are focused on peak velocity magnitudes: turbines with higher rated and cut-in speeds may not perform best for sites with large peak velocities. It also signifies the importance of accurate assessment of phase; differing values of skewness and asymmetry for for M_2/M_4 signals provided different technical resource assessments with variations up to 15% when considering the particular turbine configurations.

Table 11: Energy production of synthetic diurnal velocity signals

	Signal A	Signal B	Signal C
r	0	0.25	0.25
ϕ[°]	-	0	90
Skewness	0	0.48	0
Asymmetry	0	0	0.48
E'	1	1.03	1.05
Turbine 1 E'_T	0.58	0.49	0.57
Turbine 2 E'_T	0.47	0.39	0.51
Turbine 1 E'_{fT}	0.58	0.48	0.54
Turbine 2 E'_{fT}	0.47	0.38	0.49

6.1.4 Effects of Varying Distortion and Constituent Phase

The comparisons of Signals B and C demonstrate the extremes of asymmetry and skewness, signals separated by 90° phase difference. It was clear in the previous analysis each signal produced clearly different velocity distributions and technical power density, particularly when turbine cut in speeds are applied. Thus, it is important to accurately predict the phasing and thus asymmetry and skewness of the velocity signals. However, it is anticipated most phase errors will not be on the order of 90° and the signals themselves a combination of asymmetry and skewness. Thus it is useful to analyze the power distributions for the full range of phases and asymmetry/skewness combinations to show the sensitivity of the velocity distributions to distortion parameters.

6.1.4.1 Available Energy

Figure 73A displays the relative energy contribution of the velocities for varying phase ϕ. The contour plot of Signal B and C can be seen at $\phi = 0°$ and $\phi = 90°$. Signals of opposite skewness and asymmetry, negative values, can be seen at $\phi = 180°$ and $\phi = 270°$. However,

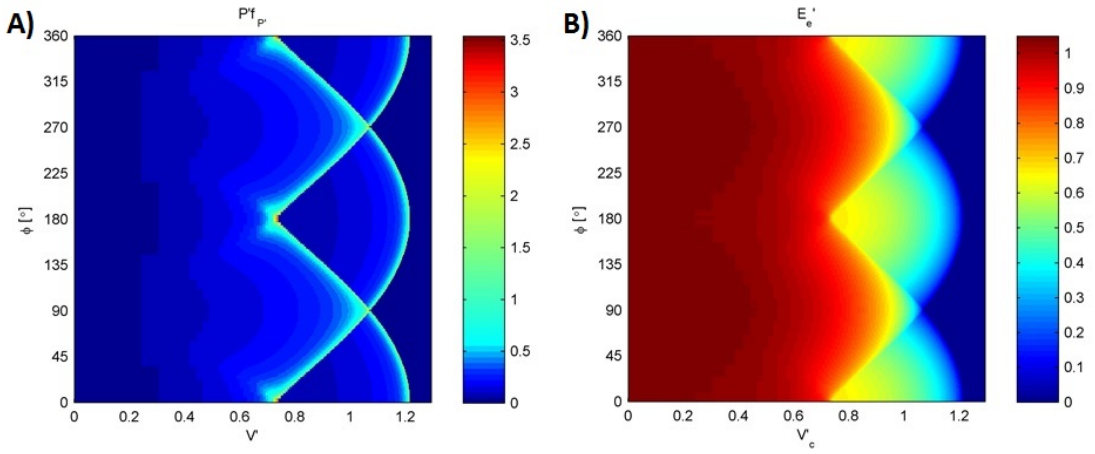

Figure 73: *A*)Non-dimensional energy distribution, $P'f_{V'}$ for varying ϕ. *B*) Exceedence Energy Curve, E_e' for signals with varying ϕ.

because power density is a function of the absolute value of the velocity, thus disregarding sign conventions of ebb and flood, the values are the same as those at $\phi = 0°$ and $\phi = 90°$.

As ϕ ranges from maximum skewness to maximum asymmetry, the two peaks seen in Signal B appear to converge into a singular peak as seen in Signal C. Thus signals with combined asymmetry and skewness still have a bi-modal distribution, however as skewness decreases, such peaks collapse together into one. This is further highlighted in the exceedance energy curve seen in Figure 73B. At maximum skewness ($\phi = 0°, 180°, 360°$) there is a sharp gradient in energy at approximately $V_c' = 0.7$. The decrease in energy with V_c' becomes more gradual with decreasing values of skewness. From Figure 73B it is clear that signals with increasing skewness are more susceptible to decreases in energy density from different turbine cut-in speeds.

6.1.4.2 Technical Power

The contour analysis is repeated for $E_f P' f_{P'}$ curves for both turbines and is shown in Figures 74A-B. For Turbine 1, it is clear that the low cut in speed does little to reduce energy production below that velocity. There is very little change between those areas in Figures 73 and 74 . Visibly, only a small portion of available energy is neglected between V'=0.35m/s and 0.5 m/s. Being on the low end of the $P'f_{P'}$ distribution , this represents a small degree of energy.

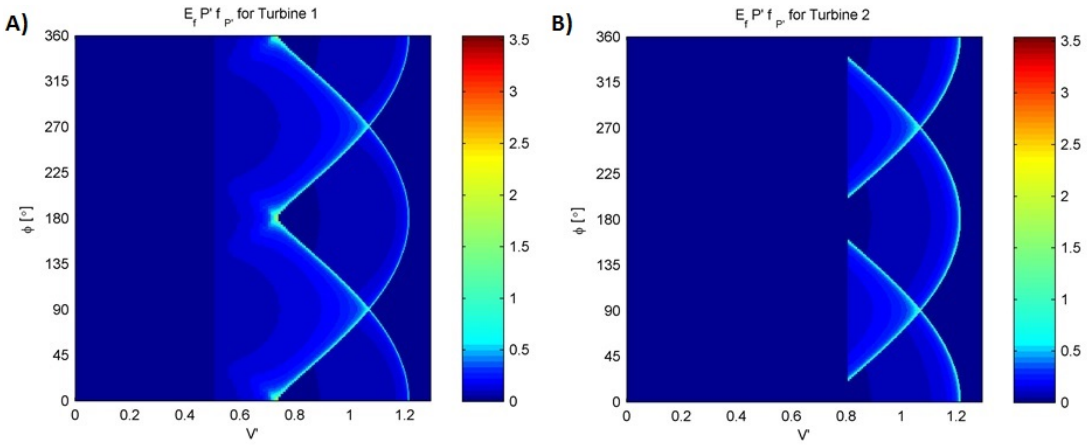

Figure 74: *A*) Non-dimensional energy distribution, $E_f P' f_{V'}$ for varying ϕ applying Turbine 1 efficiencies. *B*) Non-dimensional energy distribution, $E_f P' f_{V'}$ for varying ϕ applying Turbine 2 efficiencies.

However, there is significant change in the distribution of energy for the higher velocities above the rated speed $V' = 1$. In Figure 74A the breadth of the peaks is much narrower than for the available energy in Figure 73. This effect is amplified as V' increases and is a result of the rated speed capping the technical power density. Thus from Figure 74A, it is clear that technical power density from high velocity signals is reduced further. As skewness grows from 0, the singular distribution of energy splits, with a small portion migrating towards higher velocities with lower efficiencies. As skewness grows, and the peak migrates towards higher velocities, efficiencies continue to drop and the energy peaks become narrower and of lesser magnitude. The larger portion of the singular peak migrates towards lower velocities with higher efficiencies and thus the breadth and intensity of these peaks remain less reduced as compared to Figure 74B.

Figure 74B shows $E_f P' f_{P'}$ for Turbine 2. Here, there is little change in the distribution of energy for the larger velocities and great change in the lower as compared to Figure 73B. With a relatively high cut-in speed, much of the moderate and lower velocity energy is removed. However, with a high rated speed, the distribution of energy for the higher velocities is retained. It is clear as skewness grows from 0, the distance between the splitting peaks grows. Thus, the benefit of a lower cut in speed, or larger operating range, grows as well.

For signals with small skewness and large asymmetry, approximately 6% less of the available energy is extracted with Turbine 2 relative to Turbine 1. However, for values with large skewness, the lower peak is clearly neglected. Thus, even though the peak at higher velocities is retained, Turbine 2 captures almost 10% less of the available energy than Turbine 1. This highlights the significance of the capturing the lower portion of the velocity distribution due to its extensive persistence in the tidal signal.

6.1.5 Effects of Varying Distortion and Constituent Amplitude

The previous section analyzed the effect of the relative phase of the M_2 and M_4 constituent on signal skewness and asymmetry and the resultant available and technical kinetic energy density. However, the degree of distortion, the M_4/M_2 ratio r was kept fixed. Thus velocity signals are created with varying r and the non-dimensional analysis repeated. Two sets of velocity signals are created: one with a constant $\phi = 0°$ to observe the effect of increasing skewness alone; and one with a constant $\phi = 90°$ to observe the effect of increasing asymmetry alone.

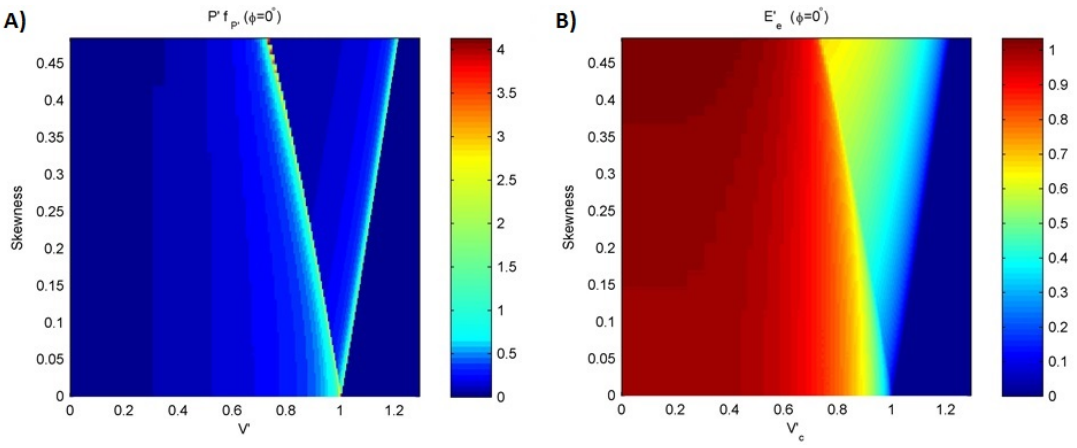

Figure 75: *A*)Non-dimensional energy distribution, $P'f_{V'}$ for varying skewness. *B*) Exceedence energy curve, $E'_e(V'_c)$ for signals with varying skewness.

For both values of ϕ, r is varied from 0 to a maximum feasible value of 0.25. It is important to note that all signals are uniquely normalized for each value of r using Equation (55). Thus, values of V' and E' refer to fraction of the undistorted value, analogous to Signal

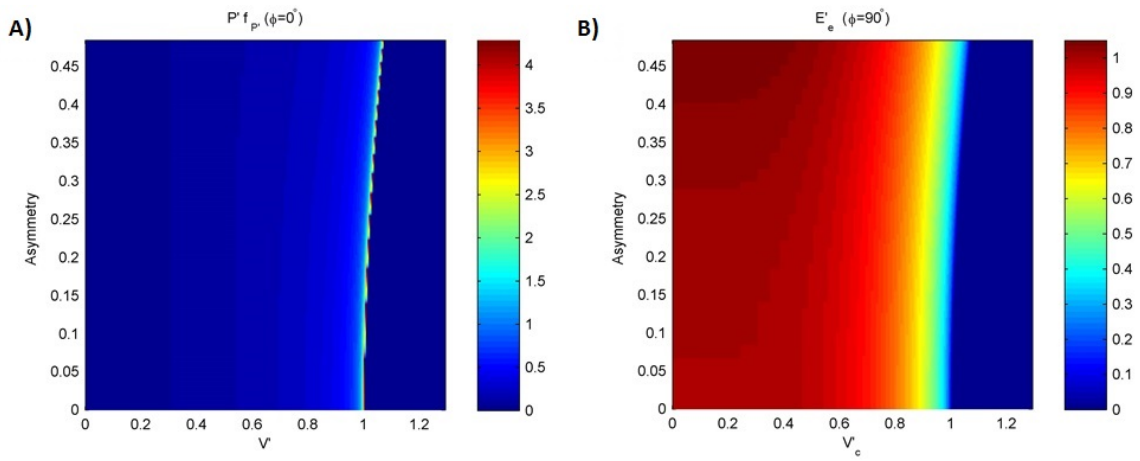

Figure 76: *A*) Non-dimensional energy distribution, $P'f_{V'}$ for varying asymmetry. *B*) Exceedence energy curve, $E'_e(V'_c)$ for signals with varying asymmetry.

A, for each value of r. Skewness and asymmetry are calculated for each value of r for each signal. Skewness for signals with $\phi = 0°$ and asymmetry for signals with $\phi = 90°$, both increase with increasing r identically from a value of 0 to a maximum of 0.48.

Figure 75 shows $f_{P'}P'$ and E_e plotted for signals with $\phi = 0°$. In Figure 75A it is clear that as r grows and thus the skewness, the distribution peaks split over an increasing range of velocities. In addition, the upper velocity peak becomes fainter, as the lower velocity peak becomes slightly larger in intensity. This is a result of the broadening of the trough versus the narrowing of the crest. Figure 75B shows the effect of the distribution splitting on the energy exceedance curve. As in Figure 70, for in Signal B there exists two distinct lobes of energy concentration. As skewness decreases, the extent of the second lobe over the velocity distribution shrinks while the first expands until collapsed into one. This signifies as skewness increases more energy is concentrated in the lower end of the velocity distribution.

Figure 76 shows $f_{P'}P'$ and E_e plotted for signals with $\phi = 90°$. Figure 76A highlights the expansion of the velocity distribution as asymmetry increases; the single peak increases in velocity. Figure 76B shows the increased concentration of energy for a given V'_c as asymmetry grows; more energy becomes concentrated near the velocity crests and troughs.

Figures 75A and 75B show similar characteristics to Figures 73A and 73B with varying M_4/M_2 phase with varying combinations of asymmetry and skewness. In particular, both images show the divergence of the energy distribution. Figures 75 and 76 corresponds to

sections of Figures 73A and 73B, from $\phi = 90°$ to $\phi = 0°$. However, one major difference is while the divergence in Figures 75A and 75B are relatively linear, the divergence in the corresponding sections of Figures 73A and 73B are not. This is a result of the increasing asymmetry along with the change in M_4/M_2 phase.

Figures 76A and 76B show that as Asymmetry increases, the velocity distribution extends and concentrates in slightly higher velocities. Clearly the effect of asymmetry is much less than the effect of skewness on the available energy density. Hence the technical energy density from signals A and C are very similar. Thus the combined effects of the skewness and asymmetry induced by the M_4/M_2 phasing focus energy into a singular peak for signals of high asymmetry and focus energy into a secondary peak of lower velocity for signals with high skewness. This reiterates the implications of capturing the secondary peak of lower velocity in tidal energy applications.

6.1.6 Summary for the Generalized Effects of Tidal Distortion

Tidal currents with large magnitudes of skewness, have an increase in peak velocity but decrease in duration for one portion of the tidal cycle along with a decrease in peak velocity and increase in duration for the other. Tidal currents with large magnitudes of asymmetry have broader velocity distribution with more energy near peak magnitudes. Although altered in velocity magnitudes, such changes are compensated for by changes in duration; available energy of a skewed or asymmetric signal varies minimally to one with the same signal energy and no distortion.

Because signals with skewness and asymmetry have significantly different distributions of velocities, the technical energy for these signals may be vastly different. Depending on the turbine characteristics, technical energy assessments for a specified turbine can vary up to 10% between signals of varying skewness and asymmetry. Figure 77 highlights the effects of the M_2/M_4 phase variation, a proxy for skewness and asymmetry, on turbine efficiency.

For highly skewed tidal signals ($\phi = 0, 180°$), it is imperative to capture the first peak of the bimodal velocity distribution despite having lower velocities and thus power. Because of its large duration during the tidal cycle, it provides a significant percentage of the total

energy. For Turbines tuned for upper range velocities (Turbine 2), efficiency drops 15% for these signals (Figure 77B). For a turbine tuned for median velocities (Turbine 1), efficiency drops by a smaller degree. For both turbines, the captured technical energy varies greatly between phase shifts and skewness values, despite having a relatively consistent available kinetic energy density (Figure 77A). Such discrepancies in energy outputs highlight the importance of phase, asymmetry and skewness for technical resource assessments.

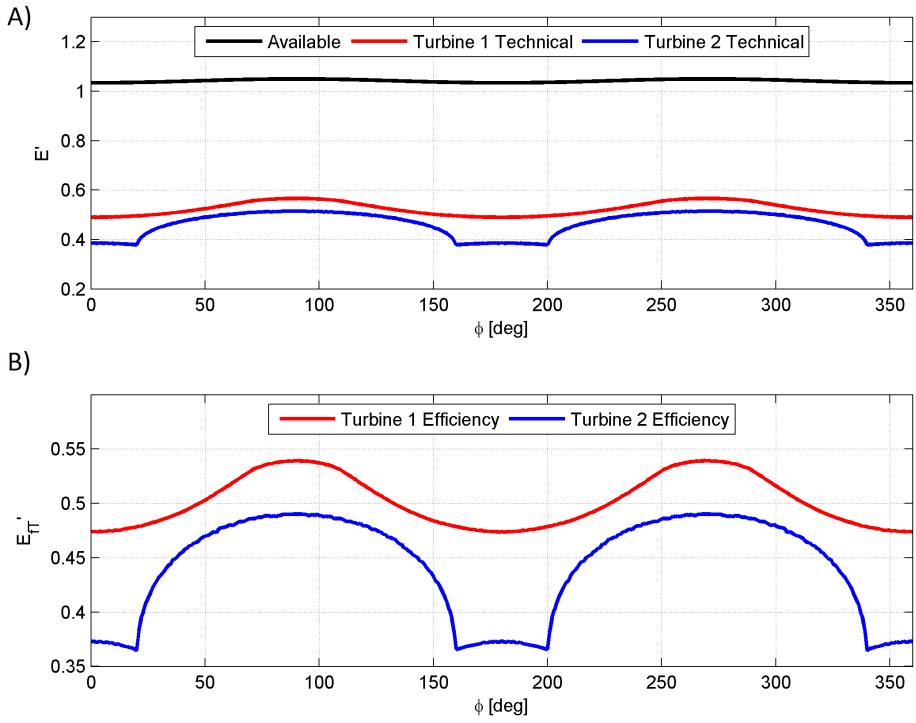

Figure 77: *A*) Available and technical kinetic energy densities for varying ϕ. *B*) Total turbine efficiencies for varying ϕ.

6.2 Generalized Effects of Semi-Lunar Variation

While the M_2 and M_4 constituents are the primary contributors to tidal distortion in this study, they are not the only constituents that contribute a significant amount of energy. Another significant constituent is the semi-diurnal solar, S_2, with a period of 12 hours. Because ω_{S_2} - ω_{w_2} is very small; their superposition induces a 'wave envelope' as shown in

Figure 78 with a frequency $\omega_{S_2M_2}$ of

$$\omega_{S_2M_2} = \frac{1}{2}\frac{1}{\omega_{S_2} - \omega_{M_2}} \tag{65}$$

as explained by Dean and Dalrymple (1984).

The effect of the M_2/S_2 superposition on velocity, power, and energy distributions is presented in this section. First, the combined effects of S_2 and M_2 are studied, and then the combination of S_2, M_2, and M_4 are analyzed. For each case, normalized signals are created and their velocity distributions are calculated along with skewness/asymmetry calculations.

6.2.1 Synthetic Signal Construction and Normalization

To analyze the effects of the S_2 constituent on a non-distorted tide, a synthetic velocity signal, V_{A_s} is created of the form

$$V_{As}(t) = A_{M_2}\sqrt{1 + r^2 + {r_s}^2}cos(\omega_{M_2}t) \tag{66}$$

where $r_s = \frac{A_{S_2}}{A_{M_2}}$ is the amplitude ratio of the S_2 and M_2 constituents. Similar to the previous section, Signal A_s represents a non-distorted M_2 signal with the same spectral energy as a distorted signal with semi-lunar variation. If the S_2 component is removed, $A_{S_2}, r_s \to 0$, signal $V_{As}(t) \to V_A(t)$ from the previous section. It is important to note, distortion refers to the addition of the M_4 signal; the addition of S_2 does not change skewness, asymmetry, or thus distortion.

The amplitude of Signal A_s is used to create non-dimensional distorted signals which incorporate S_2 as

$${V'}_s(t') = \frac{cos(t') + rcos(2t' - \phi) + r_s cos(\frac{\omega_{S_2}}{\omega_{M_2}}t' - \phi_s)}{A_{M_2}\sqrt{1 + r^2 + {r_s}^2}} \tag{67}$$

where $t' = \omega_{M_2}$ is the non-dimensional time as defined in the previous section and ϕ_s is the $\frac{\omega_{S_2}}{\omega_{M_2}}M2 - S_2$ phase difference. However, because ϕ_s only introduces a phase shift to the envelope and does not affect the distributions, a value of $\phi_s = 0$ is used herein. Thus, the signals are normalized by the amplitude of the undistorted M_2 signal. To ensure correct statistical calculations, the signal length includes complete periods of $\omega_{M_2}, \omega_{S_2}$ and $\omega_{M_2S_2}$, which is at minimum 2484 hours or $t' = 400\pi$.

As in Equations (56) and (57), the non-dimensional kinetic power and energy densities P'_s and E'_s are calculated by

$$P'_s(t') = |V'_s(t')^3| \tag{68}$$

and

$$E'_s = \frac{3}{1600}\int_0^{400\pi} P'_s(t')dt' \tag{69}$$

such that $E'_s = 1$ for the undistorted signal V_{A_S}. Similarly, the mean technical power $\bar{P'}_{T_S}$, exceedence energy E'_{e_S}, and technical energy density E'_{T_S} are provided by

$$\bar{P'_{T_S}} = \int_0^{P'_{max_S}} E_f(P'_S)P'_S f_{P'_S} dP'_S \tag{70}$$

and

$$E'_{e_S}(P'_c) = \frac{3}{1600}2\pi \int_{P'_c}^{P'_{max_S}} P'_S f_{P'_S} dP'_S \tag{71}$$

and

$$E'_{T_S} = \frac{3}{1600}2\pi \bar{P'_{T_S}} \tag{72}$$

and the total turbine efficiency E'_{fT_S} is calculated similarly to Equation (64).

6.2.2 Analysis of Combined S_2 and M_2

Signals with varying r_s are constructed and presented in Figure 78 for a constant $r = 0$. The five signals represent a signal where the S_2 constituent: is non-existent, $r_s = 0$ (Signal A_s); has half the amplitude of M_2, $r_s = 0.5$; the same amplitude of M_2, $r_s = 1$; double the amplitude than M_2, $r_s = 2$; and a much greater amplitude than M_2, $r_s = 10$.

For all the signals in Figure 78 there is no clear differentiation between ebb and flood velocities. The statistical calculations support this, with skewness and asymmetry calculations equaling zero for any value of r_s. Thus, the S_2 constituent does not induce any distortion for any amplitude or relative phase with the M_2. However, Figure 78 does show a varying range in velocities within the spring/neap cycle controlled by the r_s values, which indicate varying velocity distributions and thus $f_{V'_s}$.

The corresponding velocity PDFs for the $S_2 - M_2$ signals are presented in Figure 79. A varying r_s does induce changes in $f_{V'_s}$. For each r_s value, $f_{V'_s}$ is symmetric about 0, i.e. no

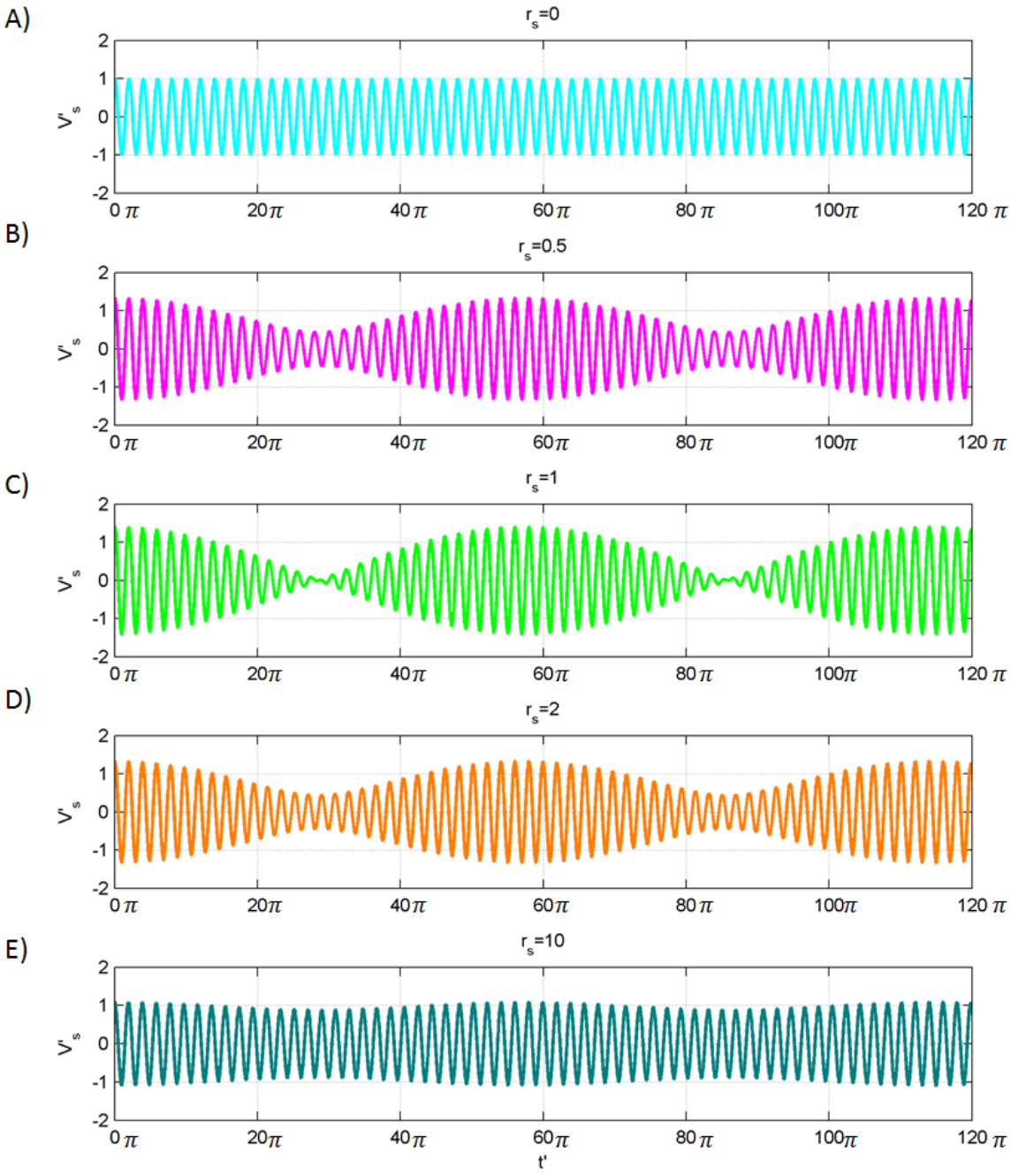

Figure 78: Non-dimensional velocity signals V_s' with varying r_s and $r = 0$. Entirety of periodic signal not shown.

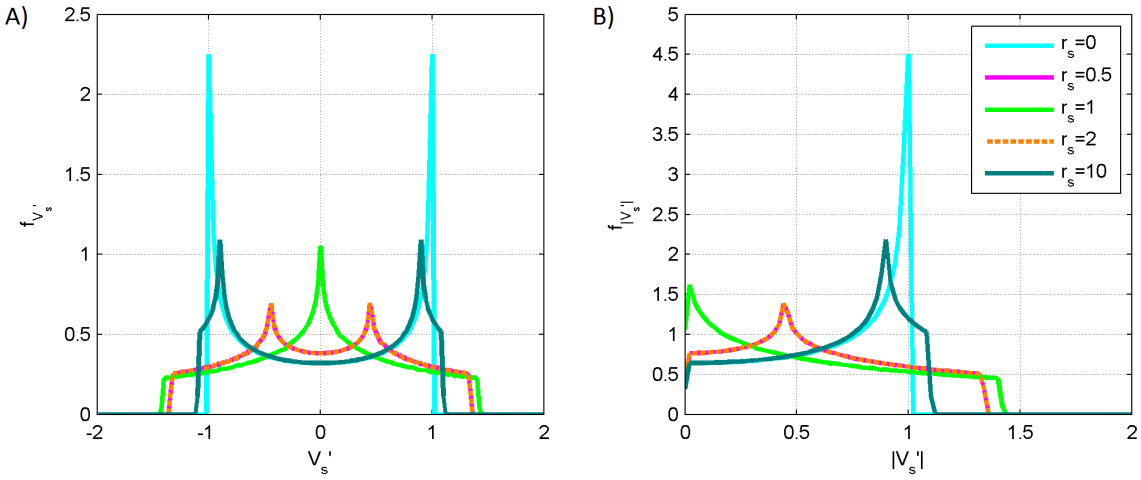

Figure 79: Non-dimensional velocity probability distribution functions $f_{V_s'}$ and $f_{|V_s'|}$ for velocity signals with varying r_s.

skewness. Yet there are drastic differences in shape, most notably: the number of peaks; the location of peaks; the amplitude of peaks; and the range of velocity values. $r_s = 0$ is the same as Signal S_A with a slightly smaller amplitude since M_4 was not included.

As r_s increases to 0.5 in Figure 79A-B, the shape changes. Peaks migrate closer to zero and are smaller but the overall distribution extends to a larger range of velocity magnitudes. The extension of range indicates the increased velocity amplitudes introduced by the constructive addition of the S_2 and M_2. The peak migration towards zero is due to destructive addition of the S_2 and M_2; which is responsible for the amplitude modulation or envelope. In terms of amplitude, destructive addition is largest when $r_s = 1$; the signals completely cancel each other out. This is seen in Figure 78C; the envelope modulation is strongest. Because the envelope severely reduces V_s' peak/trough amplitudes, the $f_{V_s'}$ peaks migrate towards zero. However for $r_s = 2$ it again has two peaks and its shape matches that of $r_s = 0.5$. This is because for $r_s > 1$, destructive addition now becomes constructive, but now in the opposite direction. As shown in Figure 78D-E the modulation becomes weaker and in Figure 79 the $f_{V_s'}$ peaks migrate outward for $r_s = 10$. Ultimately when $r_s \to \infty$, $f_{V_s'}$ will mimic the distribution of $r_s = 0$.

The kinetic energy ($P_S' f_{P_s'}$) and technical energy ($E_f P_S' f_{P_s'}$) distribution plots for varying r_s are presented in Figure 80. The distribution plots on the right hand side (B,D,F) are

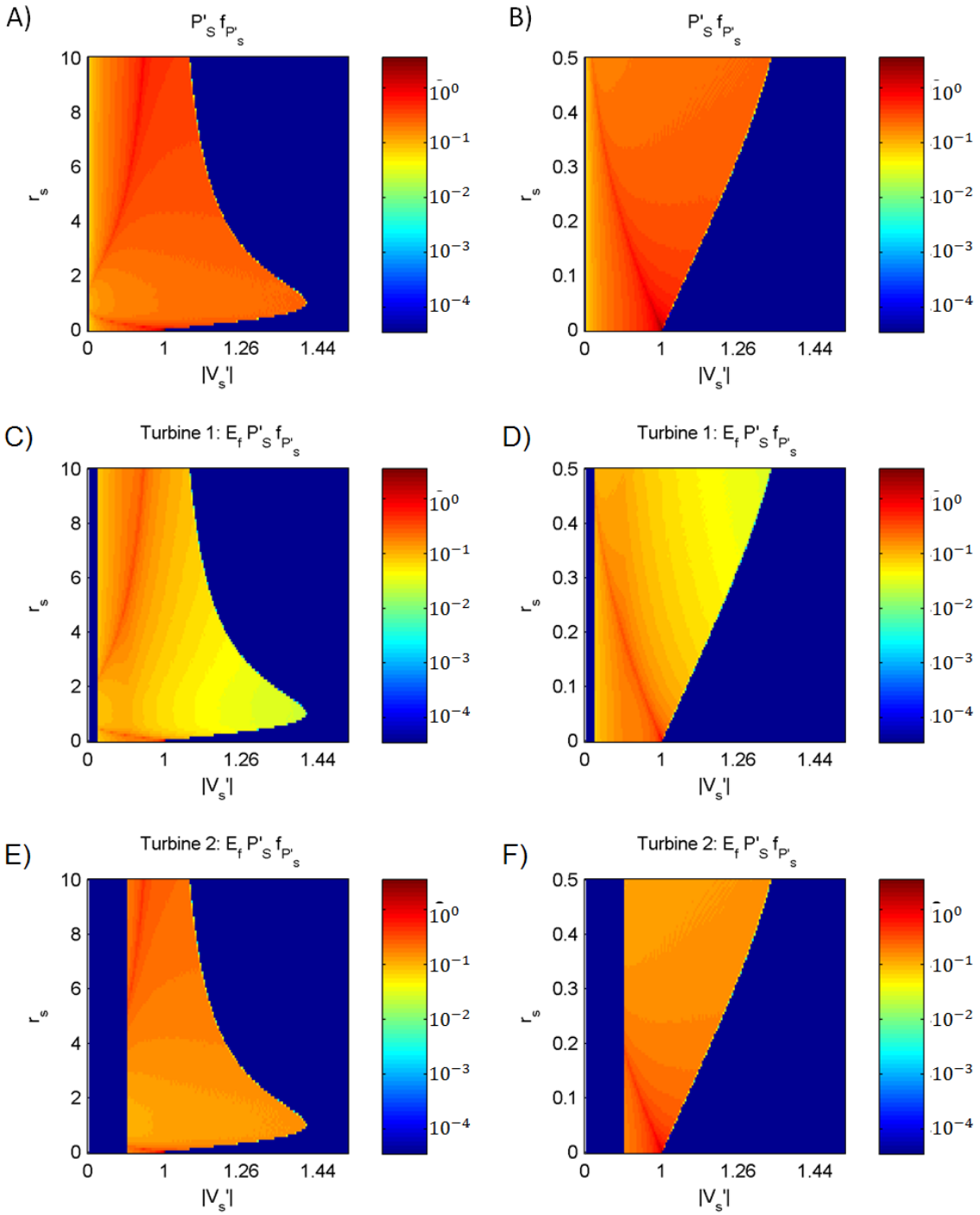

Figure 80: *A-B*: Non-dimensional energy distribution functions $P_s' f_{P_s'}$ for varying r_s. *C-D*: Non-dimensional technical energy distribution functions $E_f P_s' f_{P_s'}$ for Turbine 1 and varying r_s. *E-F*: Non-dimensional technical energy distribution functions $E_f P_s' f_{P_s'}$ for Turbine 2 and varying r_s. Left plots are calculations with higher resolution in r_s for $r_s \leq 0.5$.

calculated for a smaller range of r_s to better resolve the distribution for those values. For the kinetic energy, Figures 80A-B, as r_s becomes larger from 0, the peak migrates from a V_S' of 1 towards smaller velocities until zero at $r_s = 1$ and then asymptotically approaches 1 again as r_s increase as discussed for Figure 79. As the peak approaches zero, the energy is distributed more evenly throughout the velocity distribution and over a larger range of velocities. After r_s=1 the energy becomes more concentrated in the higher velocities as the range shrinks.

The efficiency curves from the two turbines are applied to the energy distribution curves in Figures 80C-F. Turbine 1, which captures the moderate velocities, reduces the concentration of energy past the peak as r_s grows. Distributions on either side of the peak are more symmetric. The opposite is true for Turbine 2, capturing the upper velocity distributions severely reduces energy before the peak and for some r_s values completely eliminates the peak concentration of energy ($0.2 < r_s < 5$).

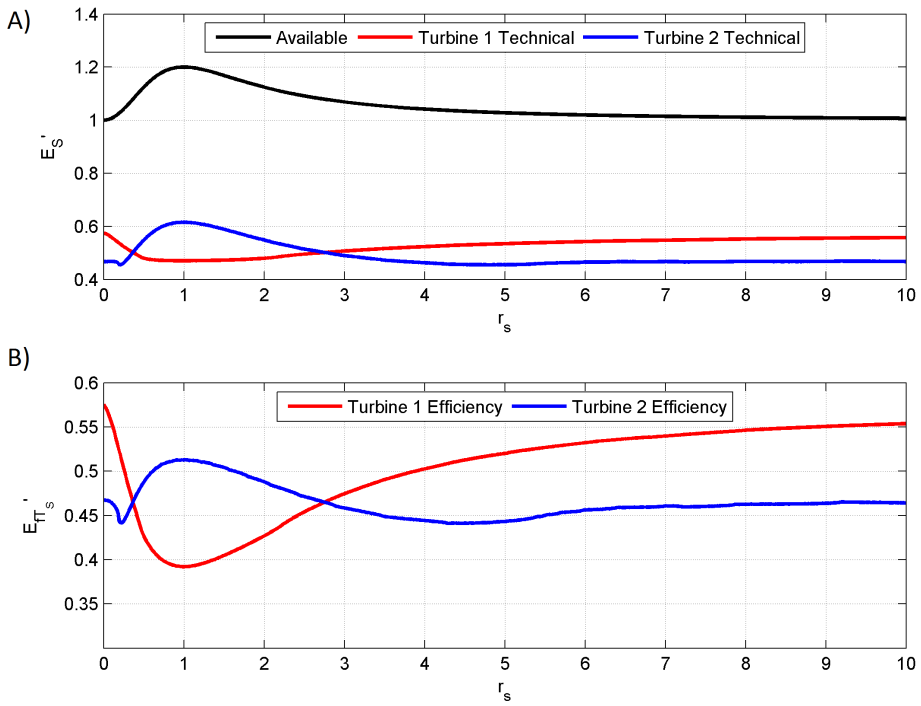

Figure 81: *A*) Available and technical kinetic energy densities for varying r_s. *B*) Total turbine efficiencies for varying r_s.

The resultant effect of application of turbine efficiencies is presented in Figures 81A-B where the technical energy E'_S and total turbine efficiencies E'_{fT_S} are plotted for varying r_s. As r_s approaches 1 the modulation is largest, the cubed larger velocities increase the available energy by 20% (Figure 81A). Turbine 2 performs best in this range near $r_s = 1$ because it has high efficiency for high velocities. The small dip for Turbine 2 for very small r_s represents the threshold where the higher velocities, overcome the reduced rate of occurrence. Turbine 1 performs poorly for r_s near 1 since its power is capped at a lower rated power. The higher incidence of low velocities is not enough to compensate for this loss. As the velocity range shrinks, for very small and very large values of r_s, Turbine 1 performs better than Turbine 2 because it operates over a larger proportion of the velocity distribution (Figure 81B). The performance of Turbine 2 increases for larger values of r_s as well because energy is concentrated in the upper range of velocities.

Constituent calculations for velocity signals across the localized domain of the numerical model for Simulation A1 show that for no point is the amplitude of S_2 greater than half of M_2, thus the following analysis will utilize signals with $r_s \leq 0.5$. Within this range, available energy increases as r_s increases, and turbine performance varies greatly. It depends on whether the increased energy from the modulation is enough to overcome the decreased rate of occurrence.

6.2.3 Analysis of Combined S_2, M_2, and M_4

To evaluate the combined effect of S_2 and distortion, three Signals A_s, B_s, and C_s are created using Equations (66) and (67) and are shown in Figure 82. The signals are designed to reconstruct the original distorted Signals A, B, and C, but with S_2 included. For each signal $r = 0.25$, $r_s = 0.30$, $\phi_s = 0$, and $\phi = 0°, 90°$ for Signals B and C respectively.

On a semi-lunar timescale, all signals appear to have an envelope modulation of the same phase and amplitude. Yet Signal C_s has increased peak and decreased trough amplitudes as compared to A_s and B_s throughout the entirety of the signal. Signal differences are more apparent on the semi-diurnal timescale. For a neap period, where the combined M_2 and

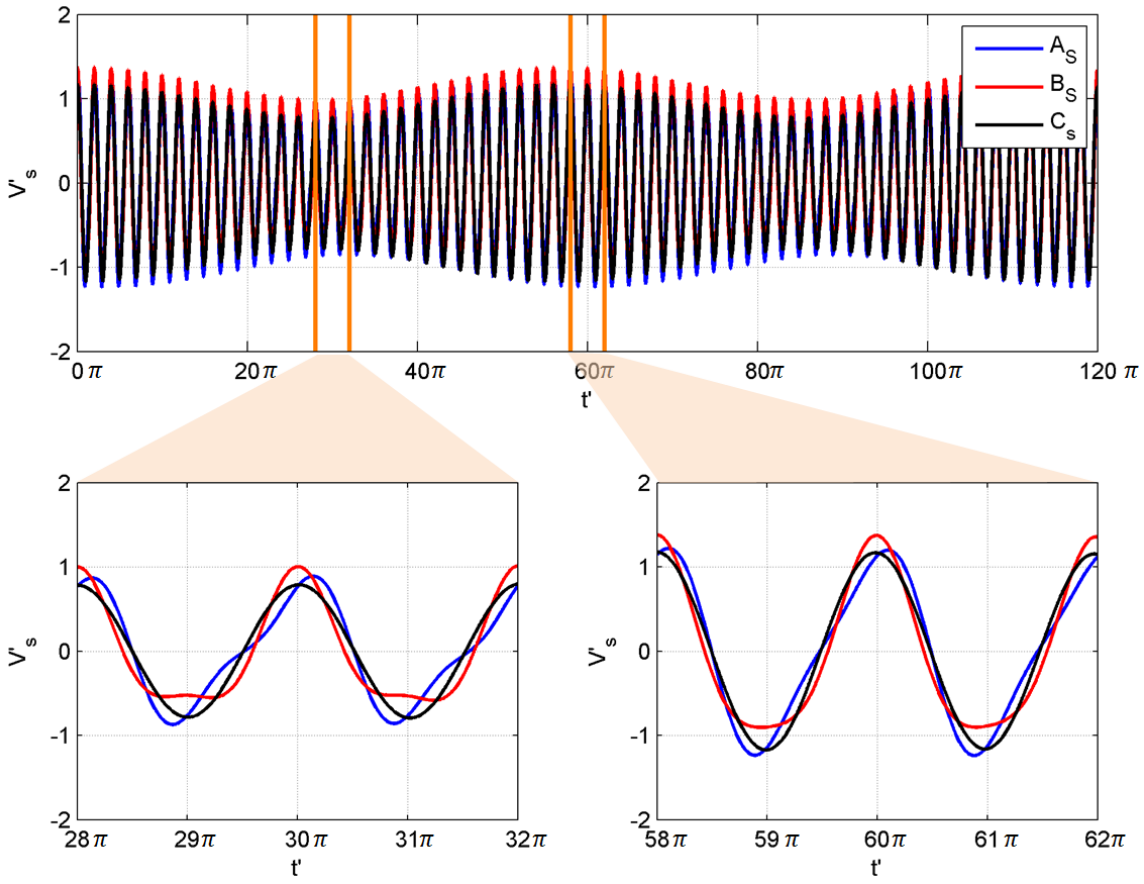

Figure 82: Non-dimensional velocity signals. All signals constructed with $r_s = 0.2$. V'_{A_s} is constructed with $r = 0$. V'_{B_s} is constructed with $r = 0.25$ and $\phi = 0°$. V'_{C_s} is constructed with $r = 0.25$ and $\phi = 90°$.

S_2 amplitude is its smallest relative to the M_4, the shape distortion is greatly pronounced. The $M4$ is so large it induces a bump or reduction in velocity magnitude in the trough. For spring periods, where the M_4 is smallest relative to M_2 and M_4 signals, shape distortion is minimized. However the distortion pertaining to peak and trough amplitude remains relatively the same on tidal timescales.

The differences in velocity distributions $f_{V'_s}$ are seen in Figure 83. As in Figure 67 Signals A_s and B_s have similar shapes and peak locations. However, the increase in probability for low velocities for Signals B_s is clearly amplified. This is the combined effect of the distortion and destructive envelope modulation. Signal C_s does share commonalities with PDF of Signal C, the extent of the flood PDF is larger than the ebb. Also, the $f_{V'_s}$ flood peak has a smaller magnitude than the ebb due to its increased 'peakiness' and shorter

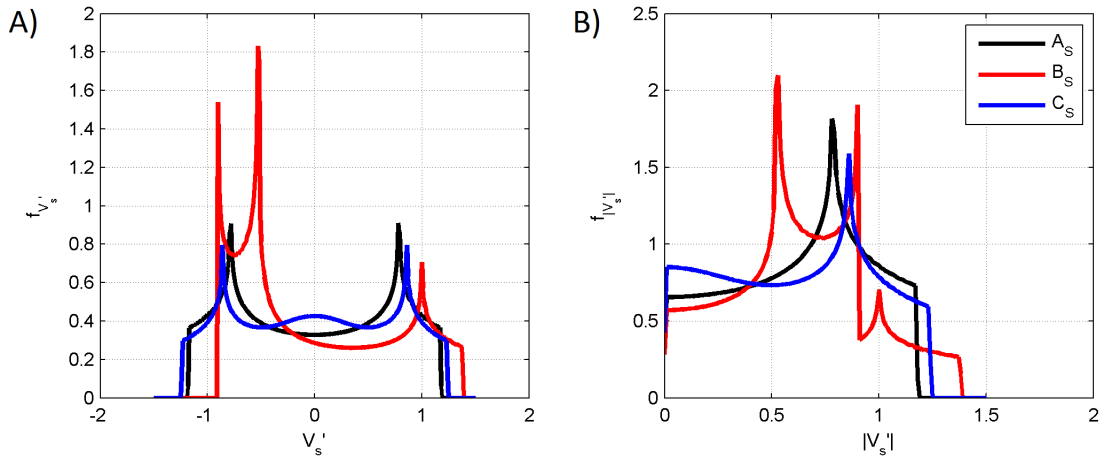

Figure 83: Non-dimensional velocity probability distribution functions $f_{V_s'}$ (A) and $f_{|V_s'|}$ (B) for velocity signals A_s, B_s, C_s.

duration. The most marked difference between Signals C and C_s is the dual peaks for the ebb PDFs. The dual peaks are a result of the small 'bump' seen in the troughs in Figure 82. The bump reduces the velocity magnitude in the trough for a longer period than the two resultant troughs. Thus, a larger peak in the PDF is found for slightly smaller velocity than the largest ebb magnitude. However, as in Signal C, both ebb $f_{V_s'}$ peaks are large than the flood due to their larger duration.

As in Figure 69, the contributed energy distribution, $P_s' f_{P_s'}$, is calculated and presented in Figure 84. Despite the addition of S_2, many properties seen in Figure 69 are retained in Figure 84. For Signal B_s, consideration of the power amplitude in addition to the probability, reduces the amplitude disparity between the peaks of highest probability. In addition, for all signals, the significance of lower velocities is reduced.

However, a significant difference between Figure 69 and 84 is the distributions after the peak with the largest velocity. In Figure 69, the last peaks mark the range of the distribution. Yet in Figure 84 there is a plateau of energy contribution past the peak. The significance of this area is emphasized due to the consideration of power amplitude as compared to Figure 83. Thus, while in Figure 69, the moderate velocities were deemed significant only in Signal B, with inclusion of the S_2, the energy contribution of the moderate velocities is important for all signals.

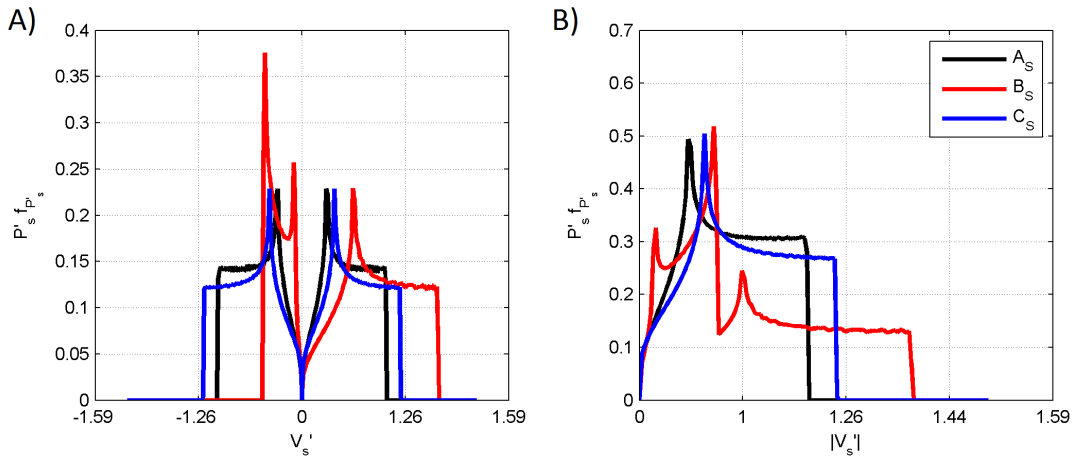

Figure 84: Non-dimensional energy distribution $P'_s f_{P'_s}$ as a function of V'_s (A) and $|V'_s|$ (B) for velocity Signals A_s, B_s, C_s.

The emergence of the tertiary peak for highly skewed signals is clear in Figure 84B. Unlike Figure 73, the same analysis sans S_2, the bowed shape of the last peak as skewness increases is not continuous. The shape is continued, but at a lower level of contribution. This is due to the bump induced by the decreased ratio to M_4 at neap tides. Also markedly different from Figure 73 is the contribution of energy after the last peaks. This is particularly significant for signals with large asymmetry. For a given V'_s in this range, $(V'_s > 1)$, $P'_s f_{P'_s}$ is markedly higher for values with larger asymmetry than skewness. As asymmetry increases, the extent of this area of high energy contribution is extended further, ultimately providing more total energy.

Table 12: Energy production of velocity signals with semi-lunar and semi-diurnal variation

	Signal A	Signal B	Signal C
r	0	0.25	0.25
r_s	0	0.25	0.25
ϕ[°]	-	0	90
ϕ_s[°]	0	0	0
Skewness	0	0.48	0
Asymmetry	0	0	0.48
$E_s{}'$	1	1.06	1.07
Turbine 1 E'_{sT}	0.58	0.49	0.53
Turbine 2 E'_{sT}	0.47	0.47	0.52
Turbine 1 E'_{fTs}	0.58	0.46	0.49
Turbine 2 E'_{fTs}	0.47	0.44	0.48

The ramifications of this effect of asymmetry on the energy distribution is clear in the energy exceedence curves in Figure 85. In Figure 85, Signal C_s has a slight overall increase in total energy compared to Signal B_s despite having the same r and r_s amplitudes. For each signal the total energy E'_s is 1.0, 1.06, and 1.07 respectively and is presented in Table 12. The shape of the energy exceedence curves for Signals A_s and C_s are similar to those of A and C in Figure 70 however the dfference between Signals B and B_s is more significant as the drastic drop in Signal B is muted in signal B_s. In Figure 70, after bypassing the first peak, the energy captured dropped from 95% to 65% in Signal B for cut in speeds of 0.6 to 0.75, well below the energy for Signals A and C. For Signal B_s the drop is only a few percent at a cut in speed of near 0.5, which is comparable to the energy of Signal A_s and only slightly lower than Signal C_s. The extension of the exceedence curve for higher velocities is also found in Signal B_s as in B, however for Signal B_s the slope is not as steep due to the plateau after the last peak. This is in fact true for Signals A_s and C_s as well. These features will have an impact when considering cut in-speeds and the technical energy.

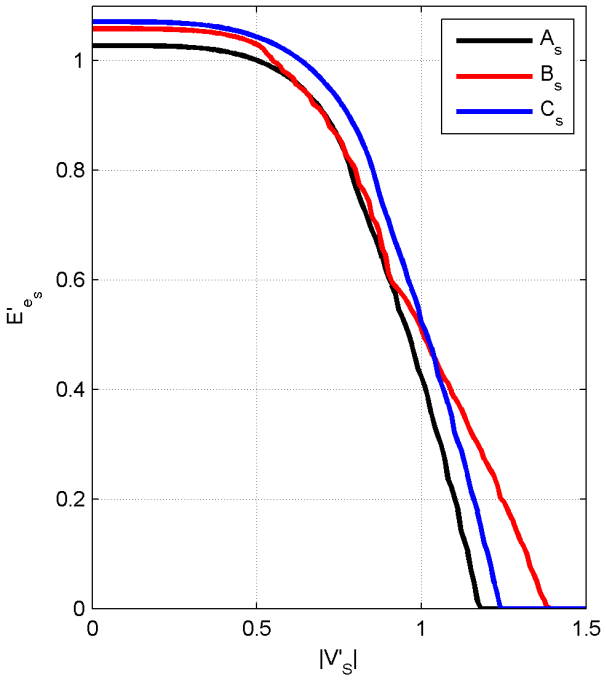

Figure 85: Non-dimensional exceedence energy curves E_{es} for A_s, B_s, C_s

To assess the effect of S_2 and distortion on the technical energy, the same efficiency curves of Turbine 1 and 2 as presented in Figure 71 are applied to the energy distributions in Figure 86. The total technical energy E'_{sT} is calculated and presented in Table 12 for each turbine.

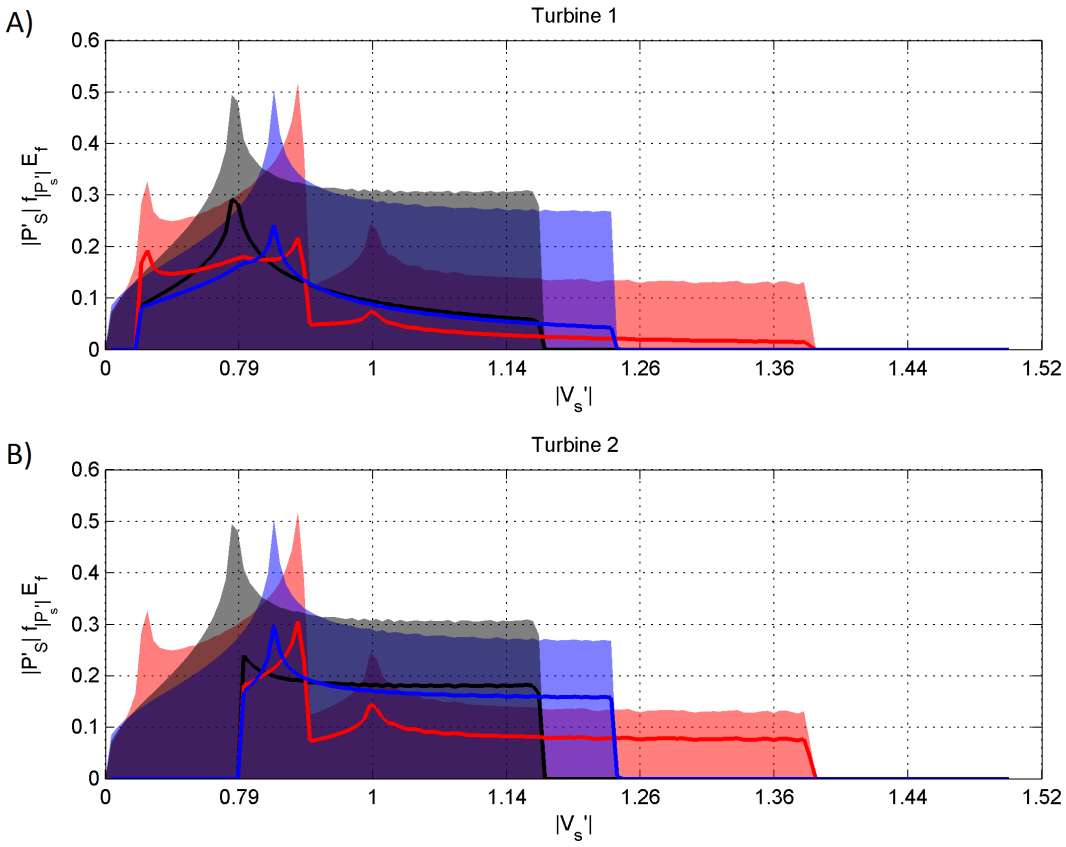

Figure 86: Non-dimensional energy distribution, $P'_s f_{P'_s}$ with (thick lines) and without (shaded area) turbine efficiencies. *A)*: Turbine 1. *B)*: Turbine 2

Turbine 1 has less total turbine efficiency for signal C_S compared to Signal C and similar efficiency between Signal B_S and B. Turbine 2 increases efficiency for both Signals B_S and C_S as compared to Signals B and C without S_2. All of these effects are due to the concentration of energy past the peaks. Turbine 1 loses efficiency for Signal C_S because more energy is concentrated past the peaks in higher velocity ranges where it has low efficiency (Figure 86A). The efficiency for B_S remains similar since the energy at moderate velocities is still retained. Turbine 2 increases efficiency for all signals since more energy is

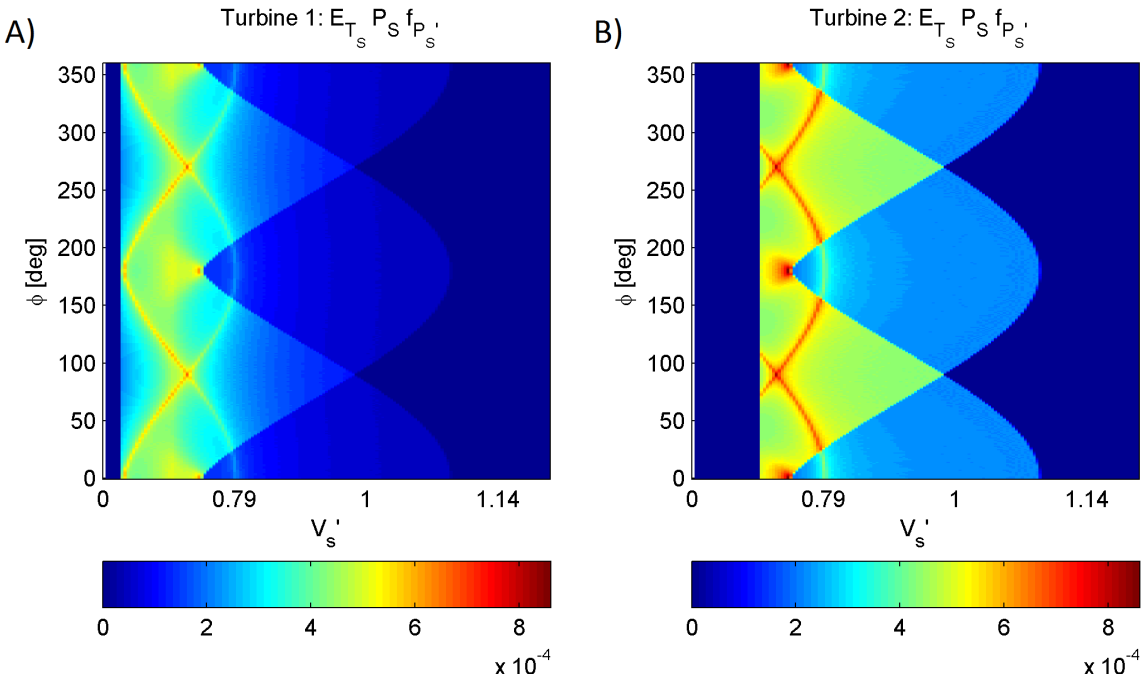

Figure 87: Non-dimensional energy distributions with turbine efficiencies, $E_f P_s' f_{P_s'}$. *(A)*: Turbine 1. *(B)*: Turbine 2

available past the peaks where it has higher efficiency (Figure 86B). The elongated tails of the distributions counteract the loss of energy in the more moderate velocities.

Because Turbine 2 performance increases, the drop in efficiency between Turbine 2 and 1 is not as severe as in the analysis sans S_2. For the highly skewed Signal B_s, the drop in total turbine efficiency between Turbine 1 and 2 is still larger than the asymmetric Signal C_S however only by a small degree. This is further emphasized in Figure 87 where $E_f P_s' f_{P_s'}$ is calculated for various ϕ and degrees of skewness and asymmetry. The large energy contribution of the large velocities for both skewed and asymmetric signals for Turbine 2 is emphasized in Figure 87B. The loss of energy in the smaller, more moderate velocities that is captured by Turbine 1 in Figure 87A does not appear as significant as it is in Figures 74A-B. The S_2 induces modulation, this modulation increases the velocities enough during spring tide to increase overall performance of a turbine tuned for higher velocities. Thus, for a S_2 contribution due to $r_s < 0.5$ it is important to capture moderate velocities but their effects are not as strong. As the r_s value decreases, the modulation decreases, and the contribution of the moderate velocities will grow.

6.2.4 Summary of Generalized Effects of Semi-Lunar Variation

The analysis of the synthetic M_4, M_2, and S_2 signals for the effect of the S_2 constituent on tidal distortion, theoretical, and technical energy was presented in this section. The combined effect of the S_2 and M_2 constituents is a semi-diurnal signal with a modulated amplitude envelope, thereby altering the velocity distributions. As the relative amplitude of the M_2 and S_2 constituents near one, the peak probability shifts closer to zero. However increased maximum velocity magnitudes due to modulation allow turbines tuned for higher velocities to have increased performance.

Distributions of distorted signals with high asymmetry and skewness remain similar to those sans S_2 however peaks no longer are at the maximum velocity range and the dual peaks

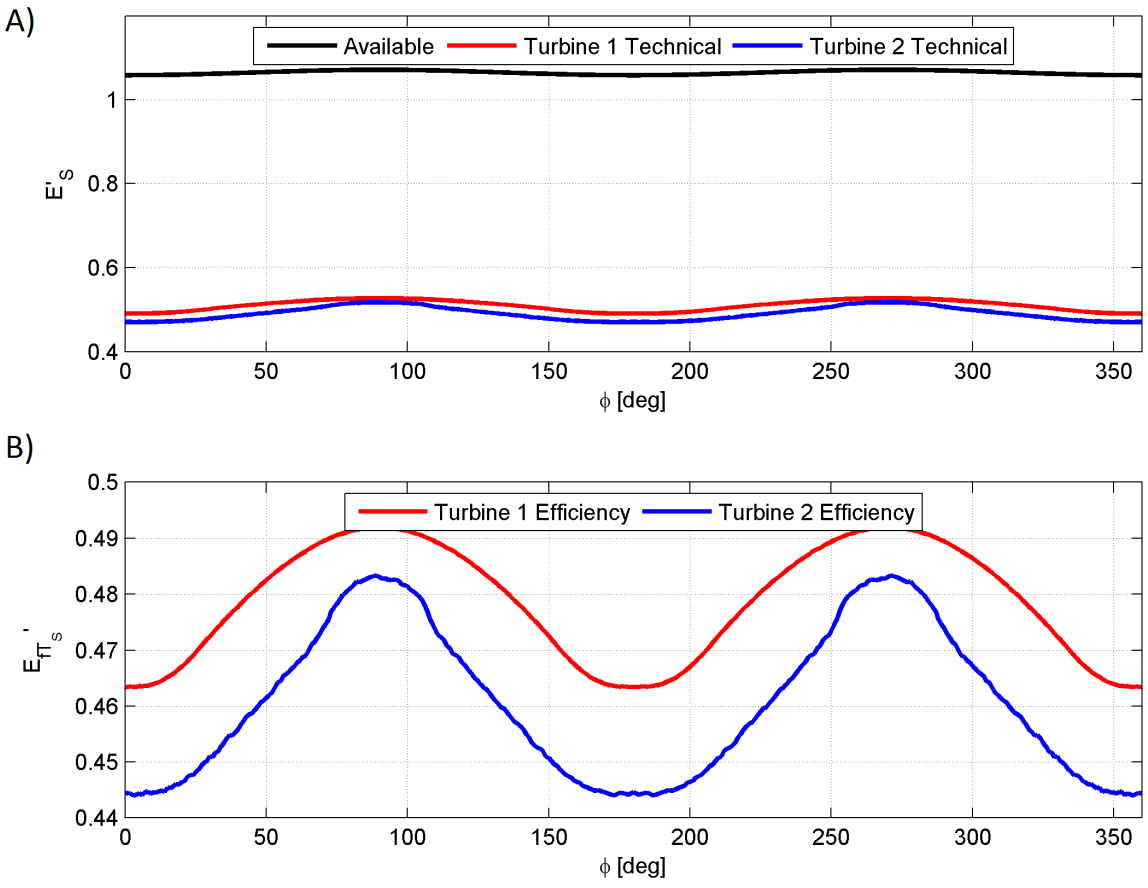

Figure 88: *A*) Available and technical kinetic energy densities for varying ϕ. *B*) Total turbine efficiencies for varying ϕ.

of the purely skewed value were closer together with a tertiary peak due to the increased distortion at neap tide. The addition of S_2 with an $r_s < 0.5$ produces similar effects on technical energy as shown in Figure 88. Capture efficiency decreases for skewed signals, particularly those which are tuned for higher velocities. However, this effect is drastically muted as compared to the M_2 and M_4 analysis. Ultimately the effects of the S_2 with an $r_s < 1$ is that it reduces the effects of distortion discussed in Section 6.1. As r_s decreases, the effect of S_2 also decreases, and the importance of distortion and skewness is more apparent. Constituent analysis on points surrounding Rose Dhu show r_s and r values of 0.11 and 0.25 respectively, thus some effects of distortion will be reduced but not as strong as the analysis shown in this section.

6.3 Rose Dhu Island Theoretical Resource Assessment

After exploring the relationship between resource assessment and tidal distortion for a simplified case, the analysis is extended to the Rose Dhu Island with spatially variable flow and a multitude of constituents. In this section, the theoretical resource assessment is discussed. First, the maximum average extractable power is calculated using the method of Garrett and Cummins (2005) on Transect A as well as the total yearly theoretical energy. The analysis is repeated for all model simulations to illustrate the effect of distortion. Next, using points of interest determined in Chapter V, yearly available power and energy densities are calculated for the localized domain. The section then concludes with the final theoretical resource assessment for the island.

6.3.1 Transect Theoretical Power

To determine the maximum average extractable tidal stream power into the domain, P_{GC}, the method of Garrett and Cummins (2005) is used on Transect A. Detailed information can be found in the Chapter II literature review. However to facilitate reading, the equations are presented again below as

$$P_{GC} = \gamma \rho g a Q_{max} \tag{9}$$

and to account for additional constituents (a_1, a_2,...) a multiplying factor is employed

$$1 + \frac{9}{16}(r_1^2 + r_2^2 + ...) \tag{10}$$

where

$$r_1 = \frac{a_1}{a}, \quad r_2 = \frac{a_2}{a}, \ ... \tag{11}$$

and a is maximum predicted water level amplitude, Q_{max} is the maximum corresponding volume flux, and typically γ=0.22.

To determine P_{GC}, Q_{max}, a, and a_n must be calculated through constituent analysis. To accomplish this, constituents of the volume flux, Q and water levels, η are calculated using the MATLAB program TTIDE created by Pawlowicz et al. (2002) and used to construct a year-long timeseries of both Q and η with a 15 minute timestep. Q_{max} and a are found as the maximum value for each respectively. As in Section 4.12, the water level is taken from the midpoint of the transect in MTL and Q is calculated using Equation (37). a_n is determined through the η constituent amplitudes. Results of the constituent calculations for all model simulations can be seen in Appendix A. The maximum amplitude for all simulations is the M_2 constituent; therefore it is the basis for a and Q_{max}.

Table 13: Maximum average power for the local domain, Transect A, using the method of Garrett and Cummins (2005) along with statistical distortion values of volume flux.

Simulation		Resource Calculations			Q Statistical Calculations	
		Q_{max} [m^3/s]	a [m]	P_{GC} [MW]	A_Q Asymmetry	S_Q Skewness
Increasing Marsh Elevation ↓	A1	2431.93	1.014	8.798	0.67	-0.13
	B1	1919.44	1.147	7.818	0.73	-0.34
Decreasing Marsh Friction ↓	A3	2382.02	1.023	8.680	0.68	-0.12
	A2	2598.40	0.989	9.221	0.67	-0.18
Increasing Domain Friction ↓	C2	2278.95	0.918	7.506	0.58	-0.13
	E1	1972.99	0.858	6.065	0.50	-0.08

Table 13 provides P_{GC} along with distortion values as calculated in Chapter IV. For an increase in marsh elevation, there is a drastic decrease in Q_{max} volume flux between simulations A1 and B1 of 27%. However, for P_{GC}, the decrease is only 13%. This is due to the inclusion of potential energy in P_{GC} calculations. Despite having almost a third less

volume flux, the decrease in power is not as large since there is an associated increase in water level amplitude a with the increase in marsh elevation and positive η skewness.

The P_{GC} calculations for an increase in marsh friction, A2 to A3, have a similar results. For 9% decrease in maximum volume flux between A2 and A3, there is only a 6% decrease in P_{GC}. Again, the decrease in volume flux is compensated by the increase in water level amplitude. This is due to the reduction in lateral flooding within the marsh and increased surface height in the main channels as described in Chapter IV. Increased domain friction has simpler behavior, decreasing both volume flux and water level amplitude. Thus the resultant P_{GC} drops accordingly since energy is removed by friction.

To further quantify the available kinetic power and energy to the system, the yearly theoretical kinetic energy for Transect A, E_{year}, is calculated. To calculate E_{year}, the kinetic energy flux, Q_{KE} is integrated over a year through

$$E_{year} = \int_0^{1year} \int_0^{D_A} \int_{-h}^{\eta} \frac{1}{2} \rho u_a |{u_a}^2 + {u_n}^2| do\ dD\ dt \tag{73}$$

where the integrand is Q_{KE},calculated for simulation output analogous to Equation (38), D is the cross channel coordinate, D_A is the cross channel length of Transect A, o is the vertical coordinate, η is the water level elevation, h is the depth, u_a is the axial velocity and u_n is the cross channel velocity. The water levels and velocities are predicted for a year using constituent calculations to find a yearly timeseries of Q_{KE}. E_{year} and skewness and asymmetry calculations of Q_{KE} for each simulation is presented in Table 14.

Table 14: Yearly kinetic energy for the local domain, Transect A, through integration of kinetic energy flux along with statistical distortion values of kinetic energy flux.

Simulation		Resource Calculations	Q_{KE} Statistical Calculations	
		E_{year} [GWhr]	$A_{Q_{KE}}$ Asymmetry	$S_{Q_{KE}}$ Skewness
Increasing Marsh Elevation ↓	A1	4.95	0.76	-0.64
	B1	2.63	0.88	-1.32
Decreasing Marsh Friction ↓	A3	4.65	0.78	-0.64
	A2	6.07	0.71	-0.76
Increasing Domain Friction ↓	C2	3.88	0.64	-0.60
	E1	2.46	0.57	-0.42

Table 14 shows the same patterns between model simulations and E_{year} as P_{GC} but are more drastic, particularly for increasing marsh elevation and friction. This is because the E_{year} calculation is not tempered by the changes in surface height amplitudes. In terms of skewness and asymmetry for Q_{KE}, it shows the same relationships as Q found in Table 13 and Chapter IV. This is as expected since Q_{KE} is a function of Q and the axial velocity squared.

To further observe the effects of distortion on Q_{KE}, Q, and the resultant energy, histograms analogous to those presented in Sections 6.1-2 are presented for the volume flux. Ultimately, for the estuarine scale analysis, Q is analogous to V. Figure 89 shows the histogram of volume flux, similar to $f_{V'}$ in Figure 67. Each value on the y-axis represents the number of hours each year Transect A is flowing at the respective volume flux Q. These plots are important because they describe the general features of the velocity distributions in response to estuarine variables; this is important for understanding the localized theoretical and technical resource assessment.

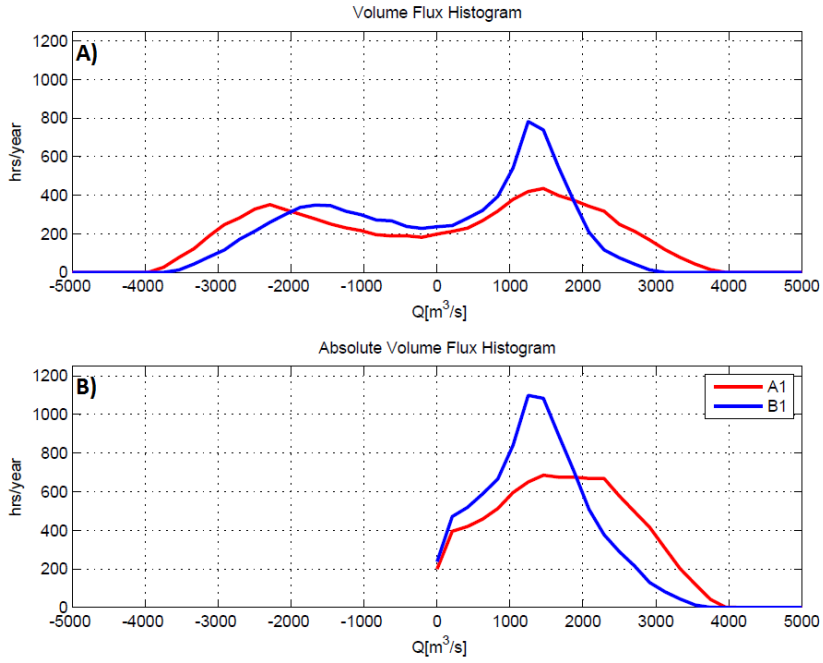

Figure 89: Histogram for yearly volume flux Q for Transect A for simulations with varying marsh elevation. A1 $\rightarrow$B1 represents increasing marsh elevation. *A):* Histogram of yearly volume flux. *B):* Histogram of yearly absolute volume flux.

Figure 89 shows an increase in hours for low velocities for Simulation B1 as expected due to its increase in asymmetry. The flood side ($Q \geq 0$) has a peakier lobe centered about a smaller Q magnitude than the ebb. This indicates smaller peak flood volume fluxes, but longer duration. The ebb side, has a shorter duration, but further extent (higher volume flux magnitudes). All of this suggests negative S_Q as indicated in Table 13. For Simulation A1, since skewness decreases in magnitude, the extent of the flood and ebb lobes are more similar, suggesting more equivalence in magnitude. However, the peaks, like B1, differ in centering and magnitude; the flood is centered about a smaller magnitude but has a larger peak or duration. The increase in marsh elevation increases skewness, which in turn concentrates more kinetic energy in the moderate velocities of the distribution. Thus for domains with increased marsh elevation, a turbine with higher efficiencies for moderate velocities will be more efficient.

Histograms for simulations with varying enhanced marsh friction are shown in Figure 90. For lower velocities, both simulations with increased marsh friction show higher hours

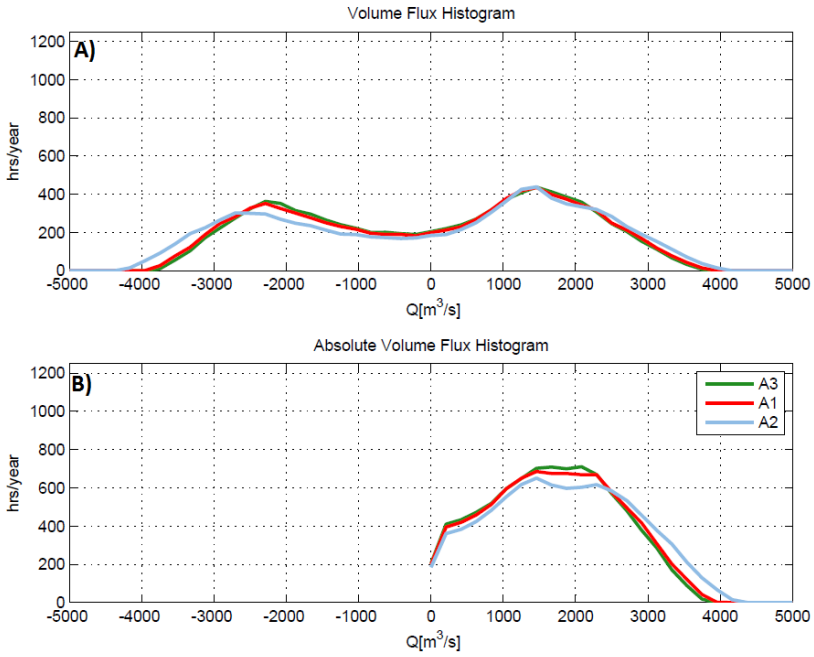

Figure 90: Histogram for yearly volume flux Q for Transect A simulations with varying enhanced marsh friction. A2 $\rightarrow$A1 $\rightarrow$A3 represents increasing marsh friction. *A):* Histogram of yearly volume flux. *B):* Histogram of yearly absolute volume flux.

as expected with an increase in asymmetry. For increasing marsh friction, skewness becomes less negative. This is apparent in Figure 90A as the flood and ebb lobes become more symmetric and its peaks become more narrow. However, unlike Figure 89B, the width of the least skewed lobe is not widest. This is a result of associated decrease in estuarine energy with increased friction. The simulation with the lowest friction may have the highest skewness, but has a greater maximum volume flux for both phases. As marsh friction increases and skewness decreases, the moderate velocities will not be as much as a significant contribution and their capture not as important. Thus as marsh friction increases, a turbine focused on the upper distribution of velocities will be more efficient.

For decreased domain friction, lobe width for both sides increases. As domain friction decreases, the peaks become wider and almost have dual peaks, which is in accordance with an increase in skewness as shown in Table 13. For the lower velocities, as the friction increases so does the hours. This is not in accordance with the decrease in asymmetry in Table 13. It is assumed this occurs because domain friction significantly reduces the velocity

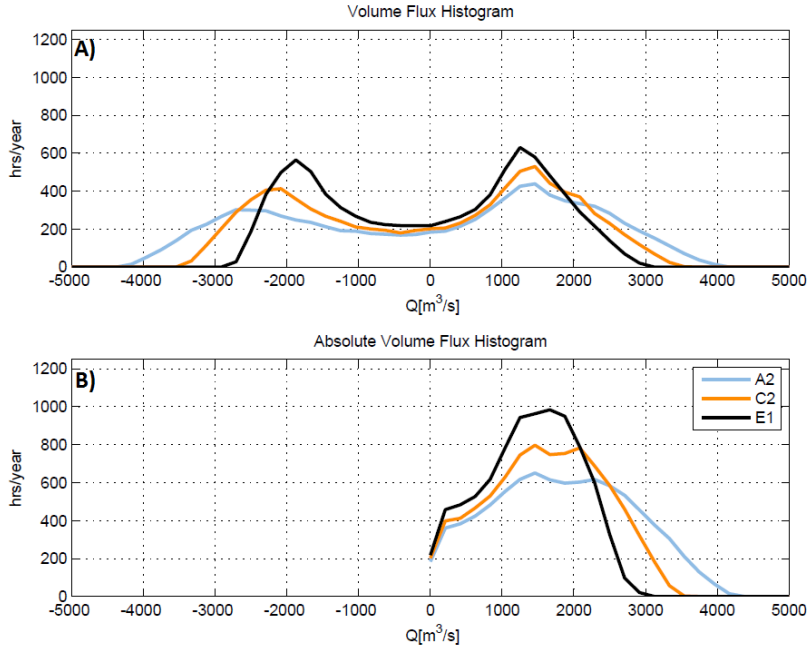

Figure 91: Histogram for yearly volume flux Q for Transect A simulations with varying domain friction. E1 $\rightarrow$C2 $\rightarrow$A2 represents increasing domain friction. *A):* Histogram of yearly volume flux. *B):* Histogram of yearly absolute volume flux.

range forcing higher representation across the entire histogram. Ultimately, increased domain friction reduces velocity magnitudes and shortens the velocity range. Considering each distribution independently however, as domain friction increases, more energy is focused in the higher velocities within its distribution. As the estuarine hydrodynamics are more dominated by overall friction and skewness decreases, the moderate velocities (of the given velocity distribution) will not be as much as a significant contribution and their capture not as important.

6.3.2 Power Density Calculations

To observe the local distribution of kinetic energy, the depth averaged kinetic energy density is calculated across the localized domain and plotted in Figure 92. Points under consideration are those in Simulation A1 that are always wet in the simulation. In the model each point has ten equally sized bins that stretch vertically with the water column.

For each bin, north/south (v_n) and west/east(v_e) velocity time series are used to compute a new complex time series ($v_e + iv_n$) that is then input into *T-TIDE* for constituents. A new time series is then constructed for an entire year for every bin. As in Equation (56), the velocity magnitude for each timestep is then taken and used to compute the kinetic power density as a function of time t, easting e, northing n and depth o

$$P_\rho(e, n, o, t) = \frac{1}{2}\rho g|\mathbf{v}|^3 \tag{74}$$

where $|\mathbf{v}| = |v_e + iv_n|$ or the velocity magnitude. For each point, the depth averaged power is then computed and numerically integrated for the entire year to find the depth averaged kinetic energy density, $E_\rho(e, n)$, as

$$E_\rho = \int_0^{1year} \bar{P}_\rho(e, n, o)dt \tag{75}$$

where $\bar{P}_\rho(e, n, o)$ is the depth averaged kinetic power density.

It is important to note the values in Figure 92 do not represent the total energy per m^2 of horizontal area across the water surface, but a vertical face with a normal vector in the direction of the velocity. Thus, given a turbine cross sectional area, $E_\rho(e, n)$ can be

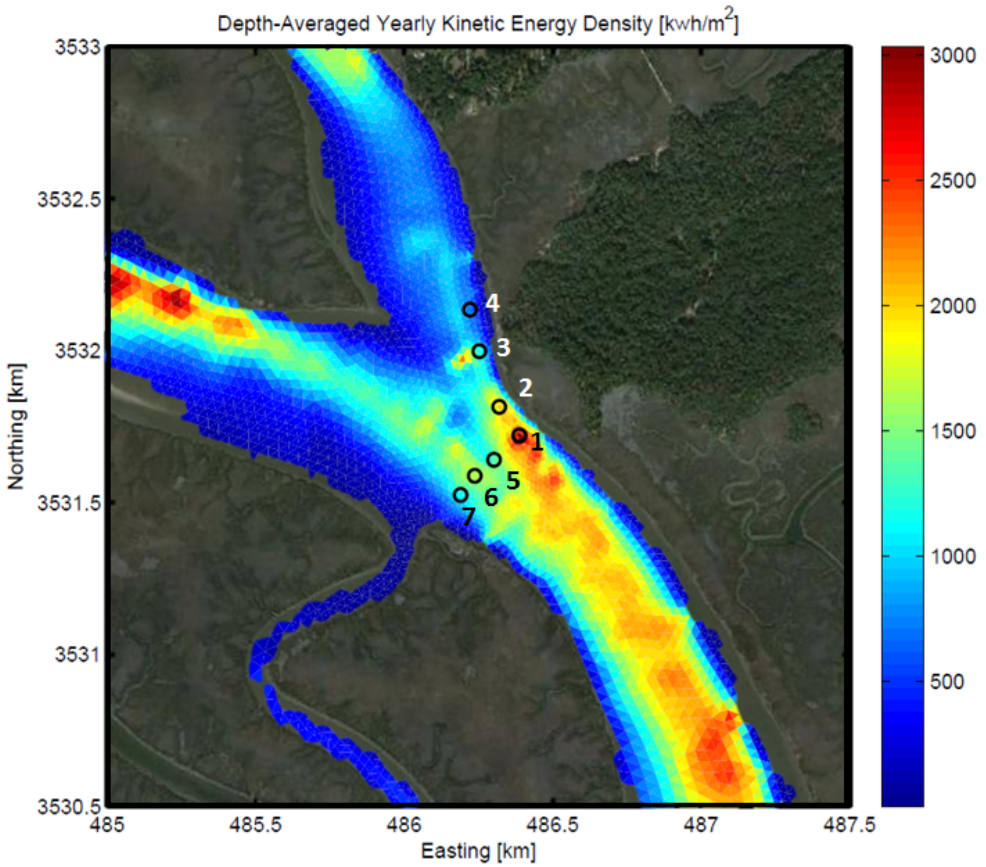

Figure 92: Yearly energy density for localized domain utilizing depth averaged currents from Simulation A1. Values in kWhr/m^2.

multiplied by that value to estimate the yearly theoretical kinetic energy. However, this does not consider effects of extraction or turbine efficiencies required for the technical resource assessment. Ultimately Figure 92 is used as a tool to identify hydrokinetic hotspots and points of further interest.

For further analysis, two sets of points are selected and are labeled in Figure 92. Set 1, includes four points (1,2,3,4) along the southwest bank of Rose Dhu; points most practical for a turbine installation due to their proximity to the island. Set 2 includes points (1,5,6,7) that span the cross section of the main channel. These points are chosen to explore the cross channel variation of power and energy. Large scale analysis typically assumes uniform currents across the channel, but as Figure 92 shows, this is not valid for the unique sinuous marsh channel geometry. Coordinates of the points as well as yearly $\bar{P}_\rho$ and E_ρ are presented in Table 15.

Table 15: Available energy estimates for points near Rose Dhu Island. Labels refer to points in Figure 92.

Name	Easting [m]	Northing [m]	Velocity Magnitude Skewness	Velocity Magnitude Asymmetry	Yearly Energy Density [kWhr/m²]	Average Power Density [kW/m²]
Set 1						
1	486387.59	3531721.00	-0.200	0.416	3034.2	0.346
2	486319.88	3531815.00	-0.186	0.378	2004.1	0.229
3	486252.94	3531998.20	-0.294	0.156	1194.5	0.136
4	486221.38	3532135.00	-0.345	0.018	693.8	0.079
Set 2						
1	486387.59	3531721.00	-0.200	0.416	3034.2	0.346
5	486302.50	3531640.80	-0.146	0.548	1343.0	0.153
6	486237.50	3531588.00	-0.223	0.417	1619.1	0.185
7	486189.94	3531525.00	-0.215	0.391	1122.5	0.128

Yearly power density timeseries for all points in both sets are presented in Figure 93. For both sets, Point 1, located in the hotspot has the highest power density reaching almost 2 kW/m^2 during peak spring tides and an average power density of 0.346 kW/m^2. For Set 1 there is a drastic decrease in power and energy density along the Rose Dhu bank northward. Toward the north, there is a decrease of 34, 61, and 77 percent power density relative to Point 1. This variation is due to the change in channel curvature around the island. The fastest currents are pushed by centrifugal acceleration to the outside bends. Points 1 and 2 lie in the outside of flow curvature for both ebb and flood. But points 3 and 4 lie on the outside soley during ebb. This ebb dominance is clear from the skewness calculations presented in Table 15. Despite being in close proximity, and all along the bank of the small island, the power and energy estimates greatly vary.

The same can be said for points across the channel in Set 2. Moving westward there is a decrease of 56, 47, and 63 percent power density relative to Point 1 despite being within the same channel cross section. This variability is in part due to the centrifugal acceleration for the bending channel as well as the confluence of the two streams. Interestingly, Point 5, has the lowest power and energy densities of the set despite being closest to the hot spot and outside bend due to its position in the shear layer of the confluence. Point 6 has the second highest due to its location at the outside bend of the flow in and from channel C. Point 7 is lower due to its location along the inside bend. Both cases emphasize the impact of spatially varying currents in sinuous marsh systems, and the necessity of spatially resolved observations and measurements for resource assessments.

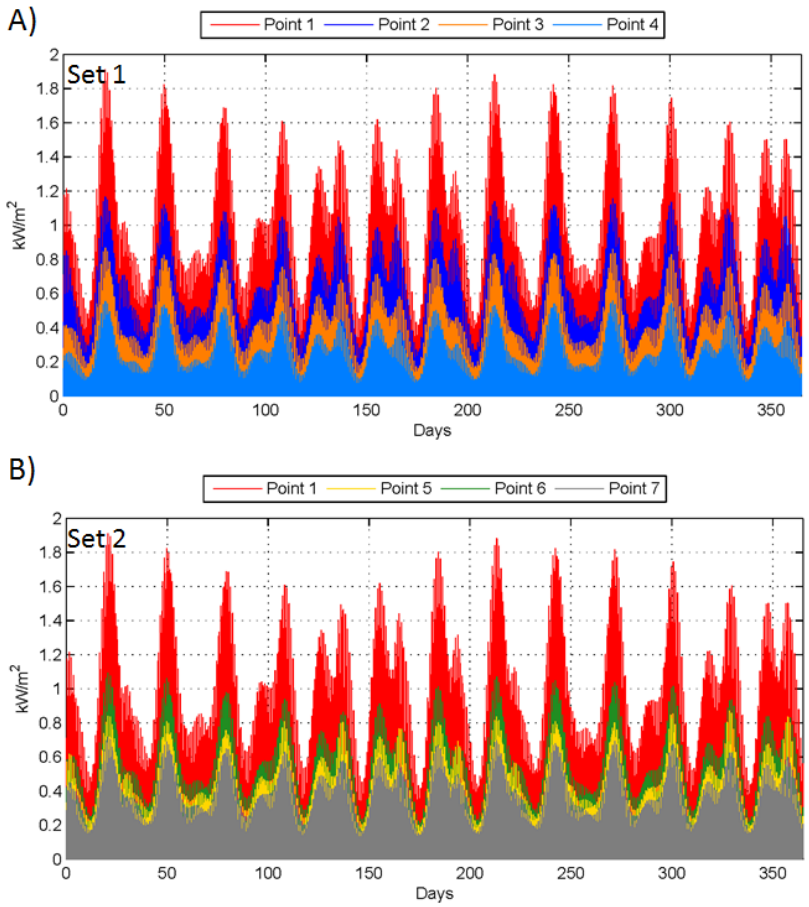

Figure 93: Power Density timeseries for points near Rose Dhu Island in Sets 1 (A) and 2 (B). Labels refer to points in Figure 92 and Table 15.

For further analysis, histograms ($h_{\bar{P}_\rho}$) of the depth averaged power density as well as energy density distribution plots $\bar{P}_\rho h_{\bar{P}_\rho}$ are plotted in Figures 94 and 95. $\bar{P}_\rho h_{\bar{P}_\rho}$ is power multiplied by occurance time each year, giving yearly energy. Corresponding depth averaged velocities are presented in red axis in m/s. Additional plots are also presented with the x-axis for the histograms normalized so the maximum observed power density is 1 to better observe differences in shape regardless of magnitude.

Set 1 has the greatest differences in shape. Traveling northward, more energy is concentrated in the lower velocities, providing a more peaked shape with a long tail. As skewness increases, as shown in Table 15, there is more energy concentrated in the lower velocities as in Figures 84 and 89. This also may be due to the drastic decrease in asymmetry as well also shown in Figure 84. Points 1 and 2 have the most similar shapes as expected

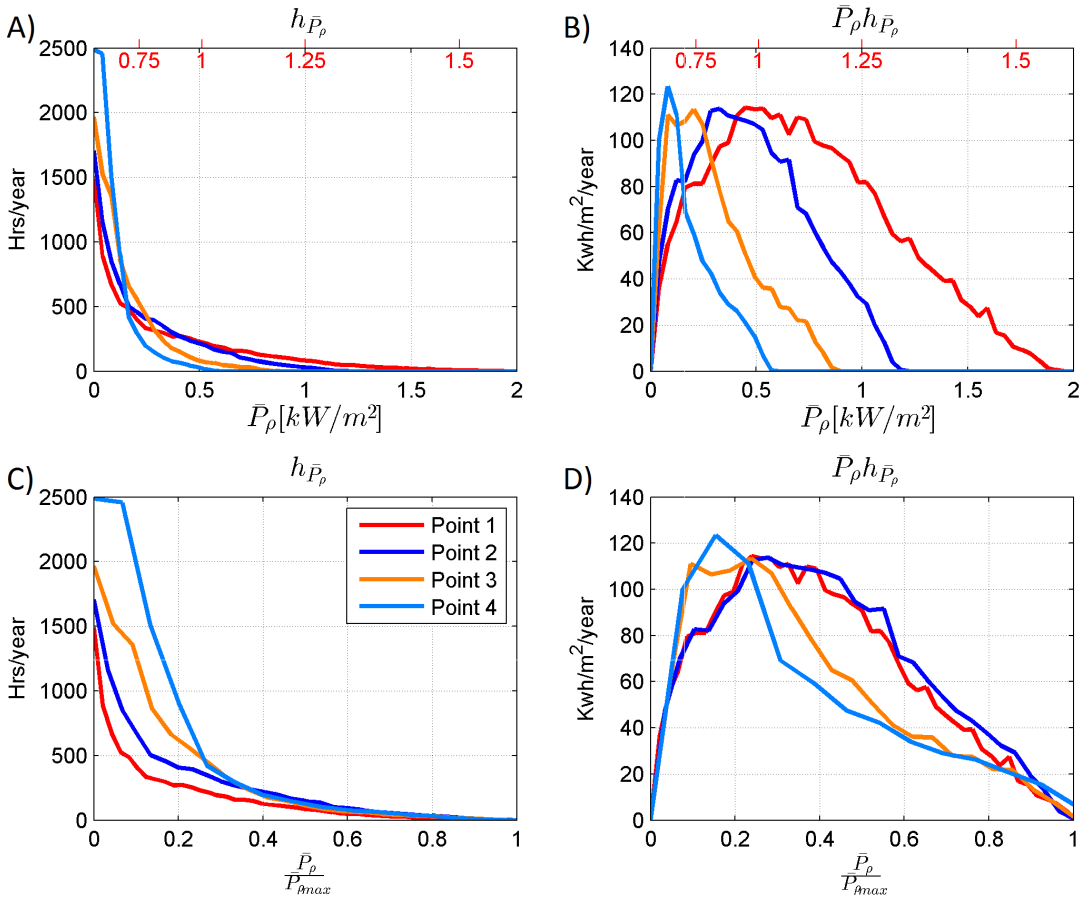

Figure 94: Power (A, C) and Energy density (B, D) histograms for points in Set 1. Corresponding depth averaged velocities are presented in red axis in m/s. In the bottom row the x-axis is normalized by the maximum extent of each curve. Labels refer to points in Figure 92 and Table 15.

since their distortion statistics are most similar. Both shapes are reminiscent of the volume flux histogram for Transect A in Figure 89 which is as expected due to their proximity and inclusion in the transect.

For the same reasons, all the points in Set 2 have a similar shape closely resembling the volume flux of Transect A in Figure 89. In fact the points all share similar statistical parameters to Transect A as presented in Table 14 for a skewness of -0.13 and asymmetry of 0.67. However the two points along the inside bank, Points 6 and 7, have an unique feature, a spike in energy for lower velocities. This inside spike is reminiscent of increasing skewness as shown in Figure 84. The values in Table 15 show a slight increase in skewness for these points.

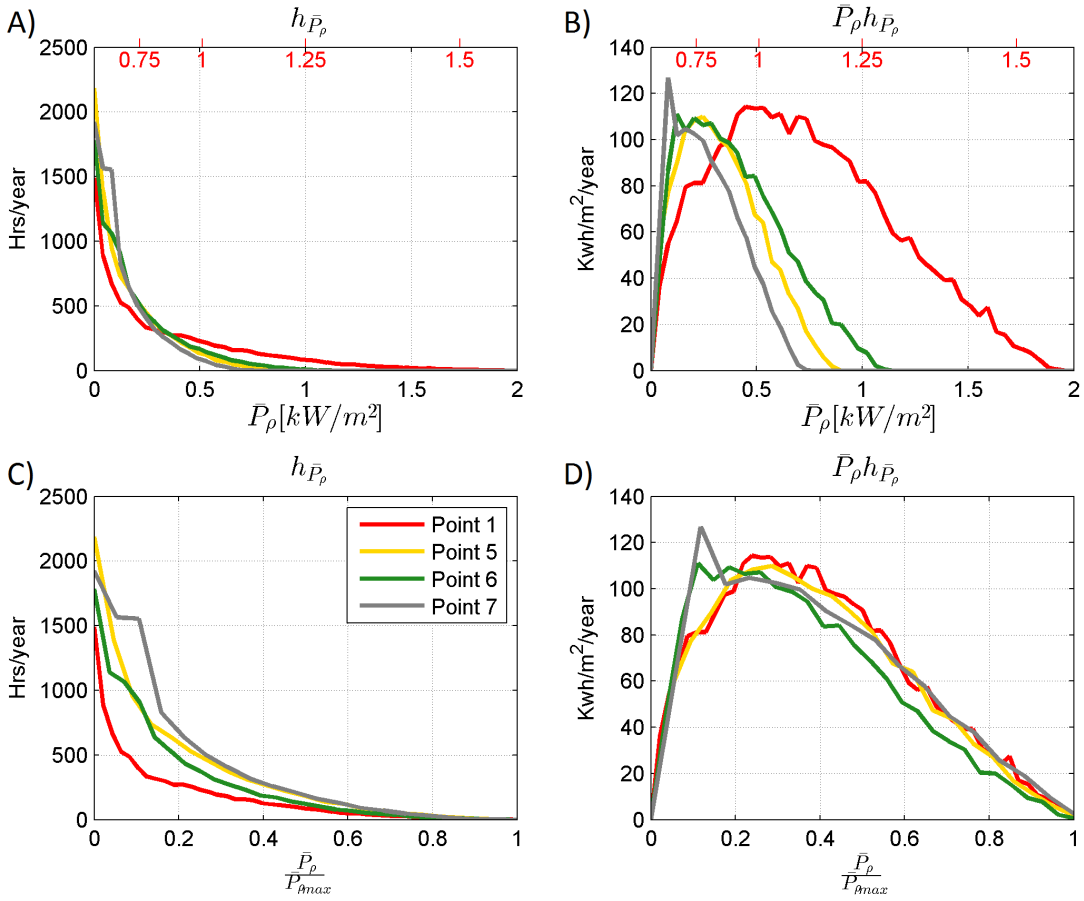

Figure 95: Power (A, C) and Energy density (B,D) histograms for points in Set 2. In the bottom row the x-axis is normalized by the maximum extent of each curve. Labels refer to points in Figure 92 and Table 15.

To provide an estimate of the theoretical power and yearly energy available to the island without turbine efficiencies, a turbine area of 10 m^2 is applied to the yearly energy density for the hotspot at Point 1. The model grid point, which extends 20m across the channel is assumed wide enough so the energy density can be assumed constant for all turbines. With these considerations the available energy at the hotspot, Point 1, is 30.3 MWh with an average power of 3.46 kW. Although this amount is small for utility scale applications, it is enough to power at least two average Georgian households, which is adequate for the Eco-Village's needs (EIA, 2009).

Even at 100% extraction efficiency, the extracted power is small (0.6 %) compared to the maximum theoretical extractable power (8.8 MW) calculated through the method of

Garrett and Cummins (2005) in Section 6.3.1. Thus, it is assumed extraction will induces little hydrodynamic disruption. An average power of 3.46 kW is small, especially when turbine cut-in speeds are considered, power provision will be intermittent and energy storage will be crucial to provide a consistent source of power to the island. Considering turbine operation parameters, the technical assessment provides a more realistic estimate of the power and storage needs.

6.4 In-Situ Rotor Testing and Efficiency Curve Development

In order to conduct a more accurate technical resource assessment, a rotor prototype was tested at hydrokinetic hotspots predicted by the numerical model and measurements. In-situ efficiency curves are desired in lieu of laboratory testing and measurements since site-specific conditions such as turbulence and wave motion are present. The rotor, sans electrical conversion, was tested through a mechanical disk brake system developed developed by Dr. Thorsten Stoesser and Tom Harries at Cardiff University. In-situ testing methodology as well as resultant measurements and efficiency curves are presented below.

6.4.1 Turbine Testing Fundamentals

A tidal turbine consists of two major design components: 1) the rotor and 2) the Power Take Off (PTO) system. The rotor is the most easily identifiable part of the turbine; it consists of the blades that capture and transmit the kinetic energy of the flow into mechanical energy of a rotating shaft. The PTO system includes the generator, which converts the mechanical energy of the rotating shaft (typically through electromagnetic induction) into electrical energy; a gearbox, which increases the rotation speed for the generator; as well as control units, which optimizes the rotation of the rotor for maximum electricity production.

The design of the rotor and PTO are somewhat interdependent. The PTO induces opposing torque on the rotor, affecting its rotation speed and thus performance. Depending on the ambient flow speed, this can be detrimental or beneficial. If the rotor spins too slowly with too much torque, water will flow through the open space and have no effect on the blades; if the rotor spins too fast with too little torque, the blades act as if a wall and

completely block the flow. Thus, for a given flow speed and rotor design, the extractable power is dependent on the rotation speed; the most efficient not necessarily the natural rotation speed induced by the flow. This relationship is quantified by

$$P_T = \omega\tau \tag{76}$$

where P_T is the captured power of the hydrokinetic energy by the turbine in watts, ω is the rotation speed of the turbine/shaft in radians/s, and τ is the opposing torque of the PTO and frictional losses onto the turbine. Note, this relationship does not consider any electrical efficiencies, only captured mechanical power.

To evaluate the efficiency of a given turbine configuration, typically a performance coefficient, C_P, is used and is calculated as

$$C_p = \frac{P_T}{P_A} \tag{77}$$

where P_A is the available hydrokinetic power of the ambient flow and is calculated as

$$P_A = \frac{1}{2}\rho A|U_\infty|^3 \tag{78}$$

where ρ is the density of the water, A is the cross-sectional area of the rotor, and U_∞ is the velocity magnitude of the undisturbed flow upstream of the turbine. For our test, the cross-sectional rotor dimensions were 0.7m by 0.7m giving an A of 0.49 m^2 and ρ was measured as 1013 kg/m^3 using coincident temperature and salinity measurements and the linear equation of state.

Typically in laboratory tests, different turbine configurations (combinations of ω and τ_o) for a constant U_∞ and thus P_A tested. P_T is measured, C_P is calculated and plotted against rotational speed. Rather than ω however, it is industry standard to use a non-dimensional form, the tip speed ratio (TSR) given as

$$\lambda = \left|\frac{\omega r}{U_\infty}\right| \tag{79}$$

where r is the length of the radial arm of the turbine and for this case equal to 0.35m. Examples of the Power Curves $C_P(U_\infty, \lambda)$ shown in Figure 96 are an industry tool. The

peak C_P for each U_∞ identifies the optimum operating τ_o and ω. This knowledge can be used to program PTOs to apply the correct τ_o for a given incoming U_∞ to achieve optimum power. Taking the peak from each curve or incoming velocity U_∞, another industry tool known as an Efficiency Curve, $E_f(U_\infty)$, can be created as shown in Figure 96 and used in Chapter 6.1.3 and Figure 71. This can be used to estimate the maximum possible captured mechanical power or efficiency for a given site assuming the turbine is optimally tuned. Thus, these curves are typically used in technical resource assessments.

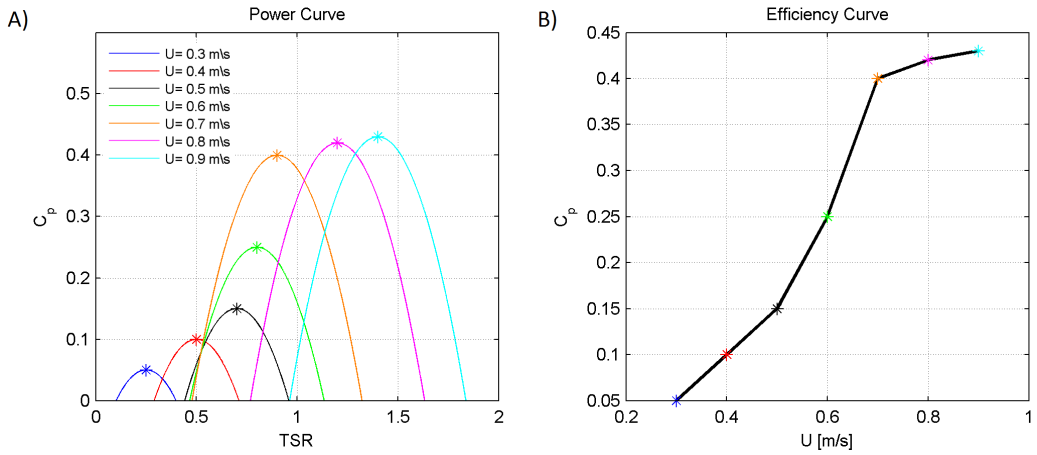

Figure 96: Example Power Curves (A) and resultant Efficiency Curve (B) for a synthetic Turbine. Color dots in Efficiency Curves refer to C_P maxima in Power Curve.

Scaled laboratory experiments of the rotor with a mechanical PTO (no electrical conversion) have been conducted by Cardiff University to find the optimum rotation speeds of the particular rotor design at various ambient flows. However, laboratory flumes do not necessarily simulate the turbulent characteristics generated in a real tidal estuary. Therefore, in-situ prototype testing is also vital for an accurate power curve and estimate of extractable power. The testing itself is similar to the laboratory experiments, however now the rotor is evaluated under the real flow conditions, unsteady and turbulent. By observing rotor performance throughout multiple tidal cycles at the demonstration site, experiencing a range of real flow speeds with the associated turbulence, this testing provides even more accurate power curves that can be utilized for technical power calculations and numerical modeling of extraction.

The laboratory tests performed at the University of Cardiff were replicated using the scaled prototype at hotspots surrounding Rose Dhu Island during a spring tidal cycle. As the tide evolved, various rotation speeds and torques were be tested to develop a power curve for a given ambient flow. It is assumed the time scale of these tests are short enough to assume the flow is stationary. Ultimately the power curve development was to be repeated throughout the tidal cycle for various flow speeds. The methodology for power curve testing is described in the following section.

6.4.2 Turbine Data Collection + Processing

Once the rotor was deployed as described in Chapter II, a mechanical PTO manufactured by Cardiff University was assembled about the shaft as pictured in Figure 97. The system

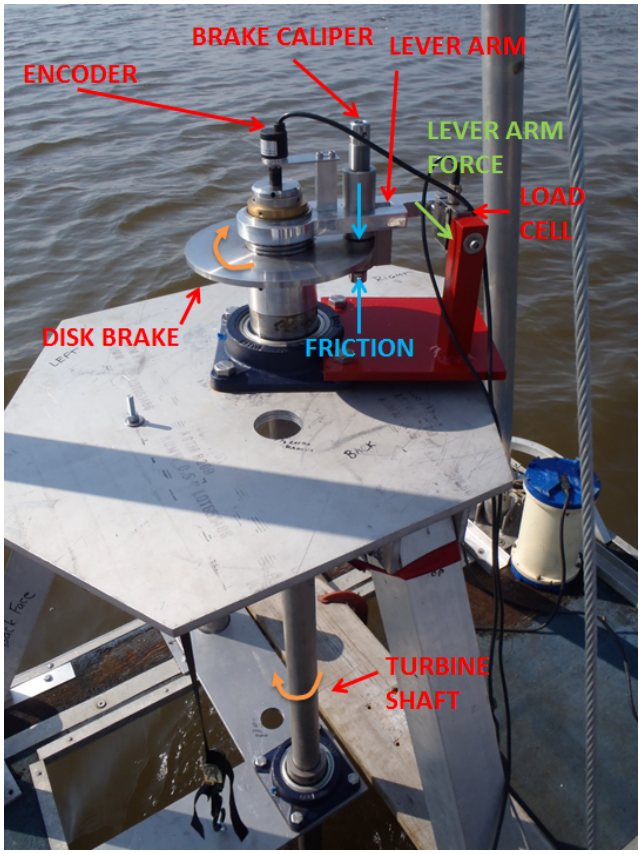

Figure 97: Components of mechanical PTO during field testing. Red arrows and text indicate component labels. Orange arrows indicate direction of rotation and torque. Blue and green arrows indicate forces.

comprises of a disk brake securely locked to the shaft so it rotates as a rigid body. Opposing torque is applied through a brake caliper which pinches the disk brake, applying friction to oppose rotational motion of the disk brake, shaft, and ultimately the rotor. The friction application is used to slow the rotational speed of the rotor ω which is measured using an in-line shaft quadrature encoder with 2000 pulses per revolution resulting in the rotated angle being measured every 0.18^o.

The torque itself is measured indirectly by a 50-N range load cell which measures nominal force. Torque is transferred to the load cell by the brake caliper and a load arm 10 cm long. The brake caliper is firmly attached to the load arm. When friction is applied to the disk brake, an opposing friction is applied to the brake caliper and load arm assembly. This force is transferred to and measured by the load cell. The equivalent torque is calculated by multiplying the length of the load arm by the measured force. These calculations are performed automatically by the PC program *Carbine* which also syncs and records the encoder measurements. The data is streamed in real time to the Carbine program through a USB connection and LabJack data logger at a frequency of 100 Hz.

It is important to note that the torque measured in this method is the total torque resisted by the PTO, τ. Thus this torque consists of both the torque induced purely by the friction losses, τ_l and the imposed opposing torque τ_o as quantified by

$$\tau = \tau_o + \tau_l \tag{80}$$

For the power calculations the opposing torque of the PTO is most relevant. To quantify τ_l, prior to each series of tests, the brake caliper is released from the disk, essentially setting $\tau_o = 0$. These τ_l values, also referred to as freewheel torques, are then used for the subsequent tests to find τ_o. Because τ_l is a function of the rotational speed, this requires the hydrodynamic conditions to be similar during the free wheel test and subsequent tests. For a laboratory test this requirement can be satisfied relatively easily. However in the estuary the hydrodynamic variability is much greater and this condition is generally not met. Upon analysis of the collected data, the variability of the incoming flow made it difficult to obtain a representative freewheel condition. Therefore, all the analysis use the measured torque to

approximate the output torque, neglecting the losses.

Each test series consisted of a freewheel test and subsequent tests where various opposing torques were applied. Individual tests were all 90 seconds in duration. More test cases were performed on day three within the same length of time to see if increased freewheel tests improved accuracy. Tests were carried out by Tom Harries. Further details of the mechanical PTO and *Carbine* program can be read in Harries (2014).

For each test, the 90 second time series of measured torque and angle are split into smaller timeseries demarcated by individual rotor revolutions. For each individual revolution, an average torque is calculated, $\bar{\tau}$. The length of the time of each resolution is determined by the number of samples multiplied by the sampling rate, and the average rotational speed, $\bar{\omega}$ is calculated by dividing 2π radians by the revolution time. For each test, only complete revolutions are considered so the averages are not biased. The averaged data, $\bar{\tau}$ and $\bar{\omega}$ are input into Equation (76) to provide the average captured power per revolution $\bar{P_T}$.

Efficiency values are calculated through syncing the PTO data along the current velocity data measured by the ADCP on the bow of the boat. Almost two rotor diameters in front of and above the rotor, it is assumed the measured values are representative of the undisturbed flow approaching the turbine. The current component measurements are averaged values from the first three bins of the ADCP measurements, an area 0.75m in length and encompassing the rotor depth in the water column centered at 1.18m below the water surface. The measured velocities are of the relative motion of the ADCP, i.e. the boat and the rotor, to the water, not the actual current. However, since the boat was doubly anchored it is assumed this motion is minimal. The representative velocity magnitude U_∞ is comprised of current velocity components processed in boat coordinates and thus relative to the rotor assuming a rigid and vertical connection: starboard ($u_s^{\mathbb{B}}$) and forward ($u_f^{\mathbb{B}}$) and is given by

$$U_\infty = \sqrt{{u_s^{\mathbb{B}}}^2 + {u_f^{\mathbb{B}}}^2} \tag{81}$$

To ensure correct syncing between the ADCP and PTO data, a cross correlation analysis is performed between U_∞ and $\bar{\tau}_l$ timeseries. The cross correlation indicates a difference of

5 seconds between the two timestamps, increasing 1 second every day. Timestamps are accordingly corrected for this. Because the sampling rate of the ADCP is on the order of the rotation rate of the rotor, the ADCP U_∞ data is linearly interpolated to match the sampling rate of the PTO. To find a representative velocity of the incoming freestream flow for each cycle, interpolated velocity measurements coincident with the revolution cycle are averaged to provide $\bar{U}_\infty$. $\bar{U}_\infty$ is then used in Equations (76)-(79) to provide revolution averaged $\bar{P}_A$, $\bar{C_P}$, and $\bar{\lambda}$. In addition, the turbine rotated on the order of 50 rpm so each 90 second test provides approximately 75 revolutions and data points.

6.4.3 Turbine Testing Results

Combining all sessions, revolution data points are sorted into bins according to their corresponding freestream velocity $\bar{U}_\infty$. Captured power is plotted against the rotational speed in both the dimensional and non-dimensional form in Figure 98. The data shows a large degree of scatter, common even in controlled laboratory tests (Harries, 2014). This is most likely due to the non-stationary incoming current, wave forces, neglect of τ_l, and increased turbulence as compared to a laboratory setting.

To improve clarity of the data, a quadratic curve of the form

$$\bar{P_T} = a\bar{\omega}^2 + b\bar{\omega} + c \tag{82}$$

is fit to each dimensional and non-dimensional bin data set through the method of non-linear least squares. A quadratic curve is chosen due to its simplicity as well as industry custom. To reasonably fit the data, the curve fit is bound to a concave downward shape ($a < 0$) as well as a negative intercept ($c \leq 0$) to avoid non-zero efficiencies at zero rotation. Values of a, b, and c are calculated for each bin and presented in Table 16 along with 95% confidence intervals for the fit and shown in Figure 98.

The dimensional power curves do show an increase in power with current velocity as expected as well as an increase in dimensional rotational speed; this suggests the results are physically reasonable. Overall the C_P values are low, not reaching above 0.35; however this is reasonable considering the maximum possible value is the Betz limit at 0.59. Unfortunately

this high efficiency is found for the lowest speeds, thus not necessarily producing a great deal of power.

Surprisingly, the C_P plots show a decrease in efficiency as current speeds increase. One would assume an increase in Reynolds number would reduce the opposing viscous drag and increase the lift on the blades and further overcome the frictional losses in the system. However, while the blades are pitched and designed to obtain optimum lift, the radial spokes are not optimized to decrease manufacturing cost. The rotor perhaps is less efficient at high speeds due to an increase in drag on the flat faced rotor spokes with increased mean flow velocities. Although not desired, this is plausible and suggests the rotor captures power most efficiently for lower or moderate speeds. It was anticipated the rotor would have a

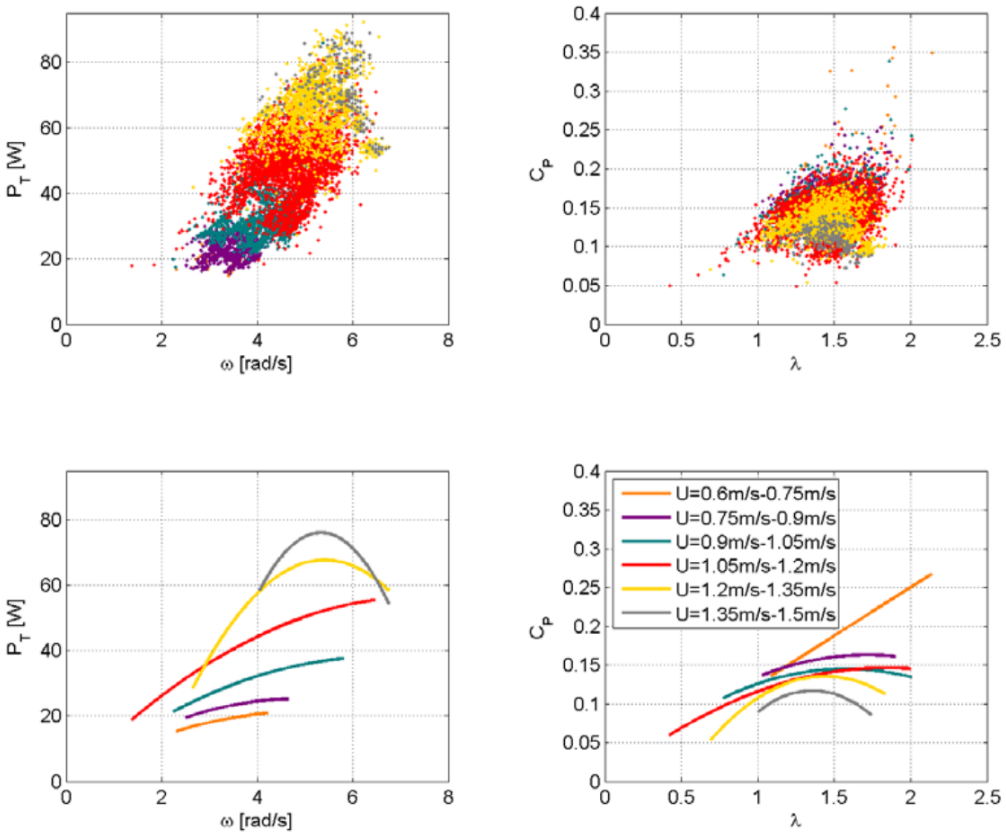

Figure 98: Results of rotor in-situ testing. *A-D:* Dimensional and non-dimensional power versus rotation speed plots from revolution averaged data from all tests except Day 1: Test A. *C-D:* Fitted quadratic curves according to Equation 82 with parameters presented in Table 16

relatively high cut-in speed and require swift currents, thus a spring tide was targeted for testing. As a result the lower current speeds have less data points.

Ultimately for the technical resource assessment, the rotor results are not utilized for a final efficiency curve. There is a great deal of spread and uncertainty in the data and the curve itself is incomplete. However, the rotor testing did provide an informative first attempt and a baseline procedure to improve upon. Most notably, a better methodology to obtain τ_l will be carried out as well as testing during more moderate/low speeds. For subsequent tests a different methodology will most likely be utilized to try to more accurately resolve torque in time.

A degree of the spread is also due to the variability of the performance of the turbine in response to variable current conditions such as waves and turbulence. Despite the loss in precision, the field testing did show the performance of the turbine under real conditions and may portray more realistic performance coefficients than that of those in the laboratory. The rotor was more efficient at lower free stream velocities due to reduced optimization associated with minimizing manufacturing costs. This is a real consideration for a permanent installation, especially when multiple full scale turbines are to be manufactured.

Table 16: Quadratic fit parameters for dimensional power curves

P_t, ω			
U_∞ [m/s]	a ± 95% CI [Ws^2rad^{-2}]	b ± 95% CI [$Wsrad^{-1}$]	c ± 95% CI [W]
0.60 - 0.75	-0.867 ± 0.63	8.607 ± 2.20	0 (bounded)
0.75 - 0.90	-1.084 ± 0.15	10.47 ± 0.56	0 (bounded)
0.90 – 1.05	-0.860 ± 0.13	11.48 ± 0.58	0 (bounded)
1.05 – 1.20	-1.004 ± 0.12	15.09 ± 0.58	0 (bounded)
1.20 – 1.35	-5.153 ± 1.65	55.73± 8.58	-82.94 ± 22.2
1.35 – 1. 50	-10.74 ± 2.49	114.5 ± 27.3	-229.0 ± 74.7
C_P, λ			
U_∞ [m/s]	a ± 95% CI	b ± 95% CI	c ± 95% CI
0.60 - 0.75	0 (bounded)	0.125 ± 0.006	0 (bounded)
0.75 - 0.90	-0.055 ± 0.006	0.190 ± 0.008	0 (bounded)
0.90 – 1.05	-0.058 ± 0.004	0.184± 0.007	0 (bounded)
1.05 – 1.20	-0.043 ± 0.003	0.159 ± 0.005	0 (bounded)
1.20 – 1.35	-0.147 ± 0.025	0.422 ± 0.071	-0.1686 ± 0.050
1.35 – 1. 50	-0.214 ± 0.061	0.583± 0.172	-0.278 ± 90.120

6.5 Technical Resource Assessment

For the technical resource assessment the two efficiency curves (E_f) from Section 6.1.3, Turbine 1 and Turbine 2, are utilized to represent turbines with enhanced efficiencies for low and high speeds respectively. To dimensionalize the curves, the multiplying factor of $A_{M_2}\sqrt{1+r^2+{r_s}^2}$ is determined as 1.06. A_{M_2}, r and r_s are calculated from the constituent calculations of the depth averaged current magnitude for Point 1 as 1.03, 0.22, and 0.11 m/s respectively. Because the multiplying factor is only 1.06, $V \approxeq V'$ and the curves from Figure 71 are used as if dimensional for simplicity in referencing cut in speeds. To reiterate, Turbine 1 has a cut in speed of 0.5 m/s and a rated speed of 1.0 m/s. Turbine 2 has a cut-in speed of 0.8 m/s and a rated speed of 1.5 m/s. Both turbines have a constant C_P within the operational range of 0.59.

Table 17: Technical energy estimates for points near Rose Dhu Island. Labels refer to points in Figure 92 and Table 15. Turbines refer to efficiency curves in Figure 71.

Name	Velocity Magnitude Skewness	Velocity Magnitude Asymmetry	Turbine 1 Yearly Energy [kWhr]	Turbine 2 Yearly Energy [kWhr]	Turbine 1 Percent of Available Yearly Energy Captured	Turbine 2 Percent of Available Yearly Energy Captured
Set 1						
1	-0.200	0.416	16189	11760	0.53	0.39
2	-0.186	0.378	10792	5039	0.54	0.25
3	-0.294	0.156	5631	1127	0.47	0.09
4	-0.345	0.018	2321	35	0.33	< 0.01
Set 2						
1	-0.200	0.416	16189	11760	0.53	0.39
5	-0.146	0.548	6800	1447	0.51	0.11
6	-0.223	0.417	8356	2811	0.52	0.17
7	-0.215	0.391	5118	547	0.46	0.05

The efficiency curves are remapped as a function of power density similar to Section 6.1.3 and applied to the energy histogram calculated for the two sets of points located in the energy density map in Figure 92. The application of the efficiency curves are analogous to Equation (62) in Section 6.1.3 and is formulated as

$$\bar{\bar{P}}_{\rho t} = \int_0^{\bar{P}_{\rho max}} E_f \bar{P}_\rho h_{\bar{P}_\rho} d\bar{P}_\rho \tag{83}$$

where $\bar{\bar{P}}_{\rho t}$ is the average technical power density. This multiplied by a year and the total cross sectional area of the turbines (10 m^2) provides the technical energy for the resource assessment, presented in Table 17.

The energy histograms for Set 1 shown in Figure 99 clearly show a discrepancy between the two turbines, particularly for the more northward Points 3 and 4. The high cut-in speeds for Turbine 2 negate a large amount of energy for these points as shown from the drop of approximately 20-30% drop in captured energy between the two turbines for these points. This is expected since the majority of the energy is concentrated in low velocities for these two points and are highly skewed. There is a slight drop for Point 2 of 5% which is also skewed. However efficiency rises for Point 1 by 10%. This is due to the higher efficiencies in the long tail of high velocities. Turbine 1 has higher efficiencies for all points except Point 1 due to the overall large velocity magnitudes and the less skewed distribution.

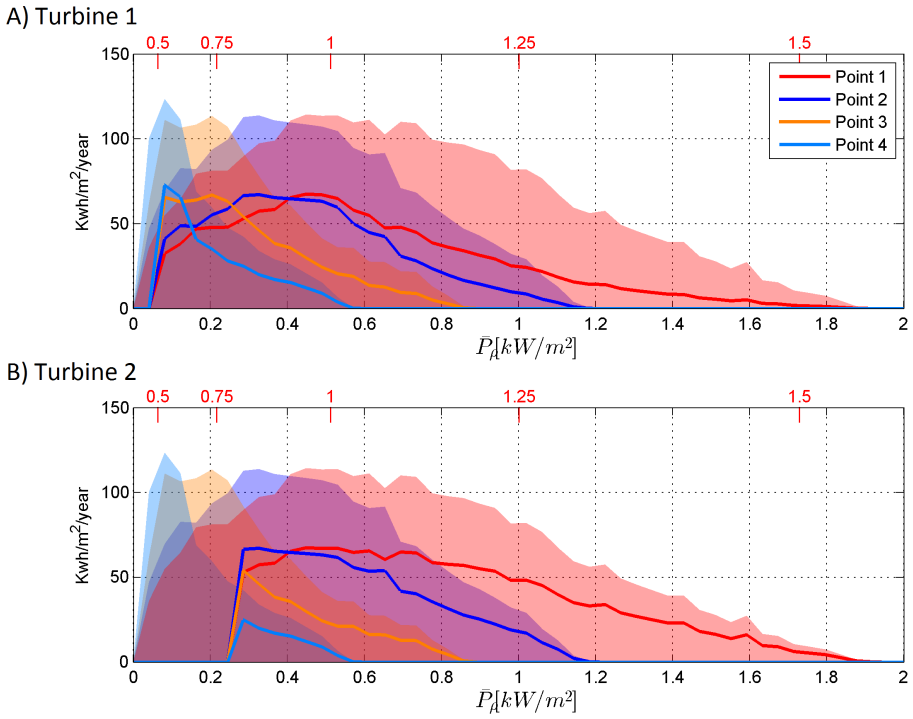

Figure 99: Energy density histograms for points in Set 1. Shaded area represents available energy; lines represent energy captured by turbine. Red numbers indicate corresponding depth averaged velocities for x-axis. Points refer to locations in Figure 92 and Table 15.

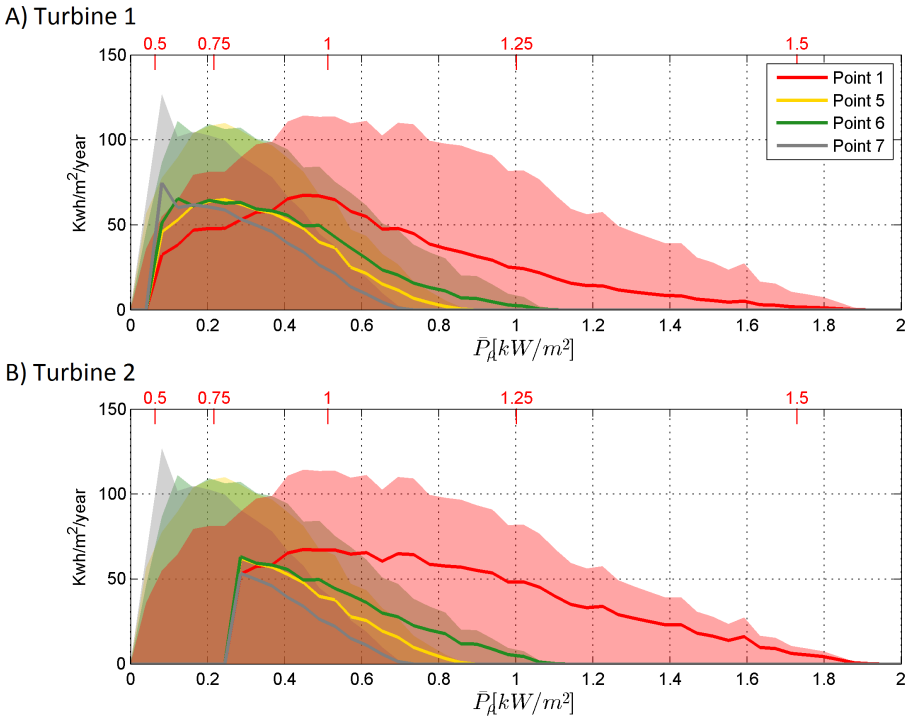

Figure 100: Energy density histograms for points in Set 2. Shaded area represents available energy; lines represent energy captured by turbine. Red numbers indicate corresponding depth averaged velocities for x-axis. Points refer to locations in Figure 92 and Table 15.

It is clear Points 3 and 4 are not desirable for energy extraction due to their low velocities. However, even if velocities were comparable to those of Points 1 and 2, due to its energy distribution, larger skewness and smaller asymmetry, more of the energy would be concentrated at low velocities and Turbine 1 would be more advantageous. It is no surprise Turbine 1 out performs Turbine 2 for all the points, it encompasses a larger range of the velocity distribution. The increased efficiencies at the higher velocities, included in the tails with little energy production do little to compensate for the loss at the lower velocities due to their high rate of occurrence. This is clear from the dramatic drops in efficiencies for Points 3 and 4.

Similar results are seen for Set 2. However the discrepancy between points and turbine performances are more interesting since they are all along the same cross section. For Turbine 2, the capturing efficiencies differ drastically. However for Turbine 1, efficiencies are relatively similar but energy values differ greatly. Again, this highlights the importance

of resolving the spatial variability in currents for these sinuous marsh channels.

Point 1 is clearly the most practical and advantageous point to install the turbines from a yearly energy perspective. For turbine selection, in reality most likely cut-in speeds are above 0.5 m/s. Although the tested rotor spun at at least 0.35 m/s, larger scaled versions will require higher speeds. Thus for a conservative technical estimate Turbine 2 is used. Using Turbine 2, the yearly energy captured is 15.6 MWh and the average power is 1.78 kW. Applying a further mechanical to electrical efficiency of 70% the resultant yearly power is 10.9 MWh and average power 1.25 kW. The yearly power is a small amount; however suitable for the rustic campsite. The power is intermittent and therefore requires energy storage to supply sustained draws.

6.6 Resource Assessment Conclusions

In this chapter the relationship between tidal distortion and energy resource assessments are explored. First synthetic cases are analyzed. It is found for a principle constituent and its first harmonic, the M_2 and M_4, distortion greatly changes as does the distribution of velocities and energy as the relative phase varies. While the theoretical energy remains consistent, the technical energy can greatly vary. For skewed signals, it is more important to capture the lower or moderate velocities. Upon inclusion of the S_2 constituent, which in part with the M_2 is responsible for Spring and Neap tide variation, the velocity distributions are greatly altered. While the theoretical energy remained similar between distorted signals with the S_2 included, the technical energy varied by a smaller degree and muted the effects of the combined M_2 and M_4.

For the theoretical resource assessment, both the incoming power to the domain and available power of localized points are analyzed. For the incoming power, different output from varying model simulations are analyzed to observe effects of increasing domain friction, marsh friction, and marsh elevation. It is observed that an increase in skewness, whether by increased marsh elevation or a decrease in marsh friction induced volume flux distributions

towards lower values. An increase in friction severely reduces the spread of the distribution, moving the concentration towards lower velocities despite the increase in asymmetry. Using the method of Garret and Cummins, it is hypothesized that the maximum average extractable power is 8.8 MW and the yearly integrated kinetic energy flux was 4.95 GWhr.

Power and energy calculations are performed for all points across the domain. It is observed that the distribution of yearly energy across the domain are highly variable. Time series and energy distributions are calculated for 7 points across the domain; three along the Rose Dhu bank, three across transect A, and a shared point at a predetermined hotspot. Velocity and energy distributions varied greatly between points due to vast differences in velocity magnitudes and distortion. Most surprisingly was the variation across Transect A. Centrifugal acceleration and confluence mixing induced such variation across the channel. For the hotspot it was conservatively estimated that there is theoretically 30.4 MWh available to capture yearly with an average power of 3.46 kW for a turbine with a cross sectional area of $10m^2$.

To provide efficiency curves for a technical resource assessment, a rotor prototype was tested at the hotspot near Rose Dhu Island. The power data is highly scattered and provided low kinetic to mechanical power conversion efficiencies topping out at 35% for low speeds. Ultimately the results are not used for the technical resource assessment. Despite the loss in precision, the field testing did show the performance of the turbine under real conditions and may portray more realistic performance coefficients than that of those in the laboratory. The rotor perhaps is more efficient at low speeds due to an assumed decrease in turbulence with decreased mean flow velocities.

For the technical resource assessment, synthetic turbine efficiencies are applied to the 7 points analyzed for the theoretical assessment. Because of the spatially varying velocity magnitudes, energy captured efficiencies varied greatly across the domain for turbines with high cut in speeds. For a turbine with a cut-in and rated speed of 0.8 m/s, an area of $10m^2$, and 1.5 m/s respectively and a combined mechanical efficiency and electrical efficiency of 70%, it is assessed that the hotspot near Rose Dhu could provide a yearly energy of 10.9 MWh and average power of 1.25kW. While the yearly energy is suitable for the needs of the

Girl Scouts, due to the intermittent power they will likely need a power storage system.

CHAPTER VII

CONCLUSIONS

The high cost of fossil fuel consumption and the need for clean renewable energy is more apparent today than ever in the US. A potential solution, hydrokinetic tidal power, is a novel and emergent technology undergoing continuous advancement with the majority of the progress focused on large utility scale projects. Using numerical ocean modeling, it has been estimated there is upwards of 50 GW of available tidal power along the US coast (Haas, 2011; Defne et al., 2012a). Other than fiscal and political considerations, this resource is vastly underutilized because much of the coastal US, despite having substantial tidal currents, do not have the deep, wide environments required by the current turbine technology. Thus these shallow estuaries, bays and sinuous tidal rivers with moderate velocities are a vast untapped resource for the United States.

A challenge facing tidal power development of shallow, small scale environments, is the prediction of the complex hydrodynamics. Although the celestial tidal forcing is relatively consistent, the resultant current flows are difficult to analytically predict and model. In open water, such modeling and prediction is fairly straightforward. However, for the sinuous tidal rivers networks, some with extensive tidal marshes, the hydrodynamic prediction and assessment can be more complex with many more nonlinear interactions and spatial variation. In addition, marshes not only make for complicated tidal hydrodynamics but also are environmentally sensitive, requiring more scrutiny during the permit process. As a result, little study has been focused on tidal energy applications in US tidal marsh environments, despite having extensive energy potential.

The presented study further established the precedent for small scale hydrokinetic energy projects in estuaries with tidal marsh environments through an energy extraction assessment at Rose Dhu Island, Georgia through the use of field measurements and a numerical model.

7.1 Dissertation Results

The hydrokinetic tidal energy assessment of Rose Dhu Island included the following activities: 1) Field measurement collection 2) Characterization of the large-scale hydrodynamics of the estuary as pertains to available kinetic energy; 3) Location of hydrokinetic energy hotspots near the island and identification of the hydrodynamic processes responsible for their formation; and culminating in 4) Yearly available and technical energy assessments. Conclusions from each study are summarized below.

1) Field Measurement Collection

Numerous boat-based field campaigns were executed in the immediate vicinity of Rose Dhu Island from 2010-2014. The campaigns are categorized into three types delineated by their objectives: spatial reconnaissance; hydrodynamic analysis; and prototype testing. The spatial reconnaissance campaign in October 2010, was the first field campaign aimed at identifying if and where areas of high hydrokinetic energy exist. Once areas of interest were identified from the first campaigns, hydrodynamic analysis campaigns, held in November-December 2011 and the latter portion of June 2014, consisted of transect measurements of water surface heights, current velocities, and channel volume fluxes to characterize local and estuarine hydrodynamics. These measurements were also utilized to calibrate the numerical model simulations by Bomminayuni et al. (2012). Measurements and model output were then used to identify areas of persistent hydrokinetic energy and a turbine rotor prototype was tested at these locations to obtain mechanical turbine efficiency curves in June 2014.

2) Estuarine Hydrodynamics

Data from various numerical simulations of the Ogeechee Estuary are evaluated against field measurements. Wetland estuarine commonly have a high degree of non-linear distortion which govern the relative durations and strengths of the tidal stages and thus the overall hydrodynamics and incoming hydrokinetic energy. This type of distortion is known to

be caused primarily by intertidal tidal storage and bottom friction. Parameters relating to these processes are varied between simulations to observe their implications on tidal distortion and improve model accuracy. Field measurements congruence is measured by a skill score and relative distortion is quantified by the statistical parameters asymmetry and skewness. Results are presented below.

- Skill scores assessing the congruence between model and measurements for distortion and amplitude are calculated and compared for tidal phases. Simulation A1, with the more resolute LIDAR elevation, typical domain friction coefficient, and 10x enhanced marsh friction, is chosen because it consistently had reasonable distortion skill scores for all phases. Distortion accuracy is given precedence since it could not be corrected by a simple scaling factor and governs not only the strength but duration of strong volume fluxes and currents.

- The distortion of the Ogeechee estuary is primarily governed by intertidal storage. The full estuary system has positive volume flux asymmetry with peak ebb and flood volume fluxes near high tide. However, the degree of ebb dominance illustrated by the surface height asymmetry and the volume skewness calculations across the estuary varies considerably, making the degree of ebb dominance a more localized effect.

- Increased channel friction in the Ogeechee Estuary affects tidal distortion; the flow is less ebb dominant with increased friction. Instead of shortening the rising tide, it extends the duration of the falling tide making the volume flux skewness less negative.

- Increased wetland friction reduces the influence of wetland intertidal storage on tidal distortion. The model suggests an increase in wetland friction does little to dampen wave propagation at high tide but rather impedes the lateral flooding of wetlands, reducing ebb dominance.

3) Localized Hydrodynamics

In this chapter the localized hydrodynamics are analyzed to isolate areas of persistently high current velocities suitable for tidal energy extraction. The outer bend of Transect A

near the island has persistently high current velocities for both flood and ebb tide. To identify the physical processes behind this hotspot location the kinematics and dynamics surrounding the spot are studied through the use of measurements from specific transects across the channel. Results are presented below.

- For flood tide, the concentration of strong axial velocity is a result of the topographic bump in Transect A. The bump induces an acceleration of flow throughout the water column above it due to sub-critical flow behavior. Axial momentum is further restricted to this area due to the two clockwise, co-rotating secondary circulation cells associated with flow in a curved channel. There are dual co-rotating cells rather than one cell because the bump not only serves as a physical boundary but also locally accelerates axial flow, advects cross channel momentum away at the surface, and splits the cells. Ultimately, the sub-critical flow and secondary circulation grows and weakens with the tide and overall axial velocity. However, the secondary circulation takes longer to dissipate and continues to distort axial momentum distributions well after peak flood tide.

- For the ebb tide, the cross channel momentum distribution is governed primarily by the centrifugal acceleration terms of the confluent streams which is an order of magnitude larger than the centrifugal acceleration associated with the channel curvature in flood tide. Upstream of the hotspot, flows from two confluent streams are funneled and redirected into a singular channel. Redirection of each inflow requires opposite curvature and thus opposing centrifugal acceleration. The resultant circulation is two counter-rotating secondary circulation cells, with surface flow directed towards the interface of the two confluent streams, forming peaked water surface near the center of the channel. Circulation along the seabed is guided by the bathymetry: the bump on the right hand side of the transect splits the counter clockwise cell on the right hand side of the channel into two co-rotating counter clockwise cells. As in flood tide, the strength of these cells and associated pressure gradients grow and weaken with the tidal stage. Axial momentum is consistently concentrated depth uniformly slightly to

the right and above of the bump due to the secondary circulation. The concentration is restrained to the middle of the channel due to the opposing cross channel velocities from the other incoming channel flow. The cross channel momentum is relatively consistent as compared to the axial throughout ebb tide. The axial momentum is highly volatile and turbulent as expected for confluent channels with discordant beds.

- Some terms for the dynamic analysis could not be resolved, most notably the advection of cross channel momentum in the axial direction as well as turbulence terms. The axial advection term is suspected important for areas with great variability in the streamwise direction. This includes the localized topographic bump, or hotspot. It is hypothesized this term is responsible for advecting cross channel momentum downstream from the hotspot, interrupting secondary circulation and splitting circulation cells.

- The consistent mechanisms behind hotspot formation that can be resolved include subcritical flow over a topographic bump, secondary circulation due to flow curvature, both by channel curvature and flow confluence, and concentration of axial momentum along circulation cell vertical interfaces and boundaries. It is important to note the topographic bump is a function of sediment transport and may be variable over longer timescales (>weeks).

4) Resource Assessments

The previous activities analyzed the tidal hydrodynamics surrounding Rose Dhu Island; model results were compared against measurements and the tidal distortion was characterized. These results are used to perform theoretical and technical tidal current energy resource assessments and to explore the effects of tidal distortion. To accomplish this, the generalized effects of tidal distortion on theoretical and technical hydrokinetic energy are explored through the analysis of simplified synthetic signals. The yearly theoretical resource estimates of Rose Dhu are performed and the effects of localized and estuarine distortion explored. Turbine efficiency curves are developed in part from an in situ turbine rotor testing at identified localized hotspots. These curves are utilized to complete the technical

resource assessment for Rose Dhu and explore the effects of tidal distortion. Important findings are surmised in the following.

- For a principle constituent and its first harmonic, the M_2 and M_4, distortion greatly changes as does the distribution of velocities and energy as the relative phase varies. While the theoretical energy remains consistent, the technical energy can greatly vary. For skewed signals, it is more important to capture the lower or moderate velocities. Upon inclusion of the S_2 constituent, which in part with the M_2 is responsible for Spring and Neap tide variation, the velocity distributions are greatly altered. While the theoretical energy remained similar between distorted signals with the S_2 included, the technical energy varied by a smaller degree and muted the effects of the combined M_2 and M_4.

- For the theoretical resource assessment, both the incoming power to the domain and available power of localized points are analyzed. For the incoming power, different output from varying model simulations are analyzed to observe effects of increasing domain friction, marsh friction, and marsh elevation. It is observed that an increase in skewness, whether by increased marsh elevation or a decrease in marsh friction induced volume flux distributions towards lower values. An increase in friction severely reduces the spread of the distribution, moving the concentration towards lower velocities despite the increase in asymmetry. Using the method of Garret and Cummins, it is hypothesized that the maximum extractable average power is 8.78 MW and the yearly integrated kinetic energy flux was 4.95 GWhr.

- Power and energy calculations are performed for all points across the domain. The distribution of yearly energy across the domain is highly variable. Centrifugal acceleration and confluence mixing induced such variation across the channel. For the hotspot it is estimated that there is theoretically 30.3 MWh available to capture yearly with an average power of 3.46 kW for a turbine with an area of 10 m^2.

- To provide efficiency curves for a technical resource assessment, a rotor prototype was tested at the hotspot near Rose Dhu Island. The power data is highly scattered and

provided low kinetic to mechanical power conversion efficiencies topping out at 35% for low speeds. Ultimately the results are not used for the technical resource assessment. Despite the loss in precision, the field testing did show the performance of the turbine under real conditions and may portray more realistic performance coefficients than that of those in the laboratory. The rotor perhaps is more efficient at low speeds due to an assumed decrease in turbulence with decreased mean flow velocities.

- For the technical resource assessment, synthetic turbine efficiencies are applied to points analyzed for the theoretical assessment. Because of the spatially varying velocity magnitudes, energy captured efficiencies varied greatly across the domain for turbines with high cut in speeds. For a turbine with a cut-in and rated speed of 0.8 m/s and 1.5 m/s respectively, a cross sectional area of 10 m^2 and a combined mechanical efficiency and electrical efficiency of 70%, it is assessed that the hotspot near Rose Dhu could provide a yearly energy of 10.9 MWh and average power of 1.25 kW. While the yearly energy is suitable for the needs of the Girl Scouts, due to the intermittent power they will most likely need a power storage system.

7.2 Scientific Merit

The presented study provides unique contributions to not only the field of hydrokinetic tidal energy research, but also measuring and modeling wetland hydrodynamics. Contributions with novel scientific merit include:

- A hydrokinetic tidal energy resource assessment for a domain in a wetland estuary;
- A novel method for processing boat based ADCP data under wave conditions utilizing a coupled dual GPS system to infer instrument orientation and motion;
- A unique structural system to perform boat based in-situ hydrokinetic turbine rotor prototype testing at various locations;
- A novel method to describe tidal distortion, using statistical parameters, skewness and asymmetry, typically used in ocean wave analysis;

- A sensitivity analysis for the FVCOM model concerning wetland elevation and friction parameters and the resultant effects on simulated tidal distortion;
- An analysis of the general effects of tidal distortion on theoretical and technical tidal energy assessments.

7.3 Future Considerations

The presented study established evidence for the benefit of further exploration and development of tidal energy applications for Rose Dhu Island and wetland estuaries. The following areas of research are suggested.

- Deploy a bottom mounted ADCP at the hotspot to obtain accurate tidal constituents. These constituents can be used alone to provide highly accurate yearly power predictions as well as used to calibrate the numerical model. In addition the ADCP measurement data can be used to help resolve the occurrence and frequency of turbulent fluctuations and help differentiate transient and quasi-steady features in the kinematic and dynamic measurement analysis.
- Further refine the numerical FVCOM simulation of Rose Dhu Island to improve congruence with measurements. It is hypothesized that more accurately resolving the channel bathymetry and wetlands in the upper reaches of the estuary will improve model congruence with the measurements, especially the nascent stages of flood tide.
- Upon model refinement, output momentum terms to obtain a complete momentum balance to identify key physical processes in hotspot generation. Output can be used to identify causes in model/measurement discrepancies as well as supplement dynamic transect measurements with additional resolution in the streamwise direction.
- Characterize disturbed hydrodynamics and resultant energy through numerical modeling of turbine installations and energy extraction. Extraction modeling would highlight any changes in the estuarine and localized hydrodynamics, particularly estuarine

distortion and the localized effect on the secondary circulation cells and channel confluence/bifurcation. Other important environmental considerations include sediment transport, estuarine flushing times and net flux, and the duration and extent of wetland submersion.

- Further develop a vertical axis turbine for an island installation as well as in-situ testing methodology. It is suggested increasing encoder resolution and freewheeling test frequency will reduce data scatter and provide clearer efficiency curves.

- Develop operational schemes for the Eco-Village on the island to suit the needs of the Girl Scouts. The variation of power draws by the inhabitants must be predicted and compared to the technical power provided. Because of the variable theoretical power, both on the semi-diurnal and semi-lunar timescale, supplemental energy or energy storage systems must be considered to provide continuous power when needed.

- In addition to the technical and theoretical resource completed in this study, all of the future considerations mentioned herein will help obtain permitting for the construction and operation of a pilot turbine system for the island. The combined activities are required for a practical resource assessment which includes environmental, economic, navigational, and construction considerations.

7.4 General Remarks

Through field measurements and an existing numerical model, it is determined that Rose Dhu Island can provide sufficient hydrokinetic tidal energy, at least in part, to suit the needs of the Girl Scouts rustic Eco-Village. A hotspot located adjacent to the island has 3.46 kW average power and 30.3 MWh yearly energy available for a turbine with a cross sectional area of 10 m^2 capture. The enhanced current magnitudes of the encompassing channel are due to the distortion effects of wetland intertidal storage. The localized hotspot is formed by the convergence of axial momentum by secondary circulation in the cross channel direction as well as an elevated bump in topography that may or not be variable on

long timescales (> weeks). These combined effects provide enhanced currents with reduced skewness. Resultant velocity distributions can be more efficiently captured with turbines tuned for upper velocity range cut-in speeds.

APPENDIX A

SIMULATION CONSTITUENT CALCULATIONS

Transect A: Simulation A1: Water Levels					
Constituent	Period ω_n [hrs^{-1}]	Amplitude a_n [m]	Amplitude Error [m]	Phase ϕ_n [°]	Phase Error [°]
MM	661.309	0.044	0.009	15.835	11.120
MSF	354.367	0.030	0.009	19.014	15.998
ALP1	29.073	0.000	0.001	85.591	181.457
2Q1	28.006	0.001	0.001	250.434	56.063
Q1	26.868	0.002	0.001	247.534	37.187
O1	25.819	0.080	0.001	222.715	0.972
NO1	24.833	0.004	0.001	263.323	14.823
K1	23.934	0.098	0.001	212.559	0.789
J1	23.098	0.003	0.001	17.451	25.963
OO1	22.306	0.002	0.001	110.857	42.958
UPS1	21.578	0.001	0.001	341.235	65.896
EPS1	13.127	0.008	0.006	140.833	49.977
MU2	12.872	0.018	0.006	133.736	19.609
N2	12.658	0.133	0.006	23.709	2.883
M2	12.421	0.815	0.007	27.527	0.453
L2	12.192	0.029	0.006	338.090	12.219
S2	12.000	0.084	0.006	51.561	3.959
ETA2	11.755	0.009	0.007	46.677	45.514
MO3	8.386	0.014	0.003	16.538	9.246
M3	8.280	0.005	0.002	293.203	25.240
MK3	8.177	0.015	0.002	9.286	8.924
SK3	7.993	0.002	0.002	88.465	62.100
MN4	6.269	0.017	0.006	222.471	19.245
M4	6.210	0.062	0.006	198.903	5.691
SN4	6.160	0.015	0.007	262.861	21.702
MS4	6.103	0.009	0.006	259.529	36.393
S4	6.000	0.002	0.005	356.546	188.442
2MK5	4.931	0.008	0.003	275.261	26.806
2SK5	4.797	0.001	0.002	89.850	226.831
2MN6	4.166	0.019	0.006	120.699	18.005
M6	4.140	0.034	0.005	126.099	8.793
2MS6	4.092	0.012	0.006	155.240	23.284
2SM6	4.046	0.002	0.004	226.915	145.962
3MK7	3.530	0.005	0.002	137.178	21.567
M8	3.105	0.011	0.002	328.683	8.759
Percent Variance Captured: 99.9%					

Transect A: Simulation B1: Water Levels					
Constituent	Period ω_n [hrs^{-1}]	Amplitude a_n [m]	Amplitude Error [m]	Phase ϕ_n [°]	Phase Error [°]
MM	661.309	0.031	0.006	17.863	12.506
MSF	354.367	0.022	0.007	15.245	21.871
ALP1	29.073	0.001	0.001	7.171	141.664
2Q1	28.006	0.001	0.001	179.212	90.574
Q1	26.868	0.004	0.002	246.820	22.843
O1	25.819	0.076	0.002	220.001	1.379
NO1	24.833	0.006	0.001	225.938	14.221
K1	23.934	0.094	0.002	209.962	1.104
J1	23.098	0.002	0.002	333.055	43.281
OO1	22.306	0.004	0.002	94.427	25.430
UPS1	21.578	0.002	0.002	310.191	65.416
EPS1	13.127	0.010	0.007	124.973	41.057
MU2	12.872	0.020	0.007	117.394	20.098
N2	12.658	0.141	0.007	19.041	2.521
M2	12.421	0.824	0.006	21.240	0.485
L2	12.192	0.031	0.007	321.152	12.872
S2	12.000	0.090	0.007	47.844	4.694
ETA2	11.755	0.010	0.008	33.052	41.847
MO3	8.386	0.018	0.004	358.523	11.489
M3	8.280	0.008	0.003	253.134	22.589
MK3	8.177	0.020	0.004	356.119	9.638
SK3	7.993	0.004	0.003	58.442	45.328
MN4	6.269	0.026	0.007	204.146	13.667
M4	6.210	0.069	0.007	186.722	5.282
SN4	6.160	0.015	0.006	230.869	24.371
MS4	6.103	0.016	0.007	241.482	23.634
S4	6.000	0.003	0.006	325.118	124.005
2MK5	4.931	0.005	0.003	213.840	41.675
2SK5	4.797	0.001	0.003	14.290	141.800
2MN6	4.166	0.013	0.003	91.373	14.523
M6	4.140	0.019	0.003	106.278	8.713
2MS6	4.092	0.010	0.003	124.084	17.339
2SM6	4.046	0.002	0.003	184.823	98.016
3MK7	3.530	0.003	0.001	70.641	23.607
M8	3.105	0.009	0.002	289.123	9.389
Percent Variance Captured: 99.9%					

Transect A: Simulation A3: Water Levels					
Constituent	Period ω_n [hrs^{-1}]	Amplitude a_n [m]	Amplitude Error [m]	Phase ϕ_n [°]	Phase Error [°]
MM	661.309	0.043	0.009	16.734	11.714
MSF	354.367	0.029	0.009	19.284	16.720
ALP1	29.073	0.000	0.001	84.750	186.262
2Q1	28.006	0.001	0.001	248.582	60.901
Q1	26.868	0.003	0.001	259.928	33.950
O1	25.819	0.086	0.002	226.187	0.906
NO1	24.833	0.005	0.001	268.862	15.570
K1	23.934	0.106	0.002	215.211	0.771
J1	23.098	0.003	0.001	17.506	26.433
OO1	22.306	0.002	0.002	118.941	36.444
UPS1	21.578	0.001	0.002	343.338	62.005
EPS1	13.127	0.010	0.007	142.857	43.246
MU2	12.872	0.023	0.007	140.554	16.535
N2	12.658	0.144	0.006	25.021	2.813
M2	12.421	0.908	0.007	28.041	0.435
L2	12.192	0.037	0.006	343.816	10.353
S2	12.000	0.090	0.007	52.789	4.555
ETA2	11.755	0.010	0.008	47.963	43.824
MO3	8.386	0.021	0.003	30.880	9.588
M3	8.280	0.007	0.003	302.582	24.826
MK3	8.177	0.024	0.004	24.640	7.447
SK3	7.993	0.003	0.003	98.141	65.226
MN4	6.269	0.030	0.008	228.121	15.136
M4	6.210	0.102	0.009	212.556	5.114
SN4	6.160	0.021	0.009	272.413	20.925
MS4	6.103	0.016	0.009	262.751	33.669
S4	6.000	0.003	0.006	355.329	160.858
2MK5	4.931	0.010	0.005	264.233	33.821
2SK5	4.797	0.001	0.004	81.199	220.630
2MN6	4.166	0.022	0.005	122.101	13.088
M6	4.140	0.038	0.005	129.413	7.765
2MS6	4.092	0.015	0.005	155.763	19.802
2SM6	4.046	0.002	0.004	222.447	113.452
3MK7	3.530	0.005	0.002	161.671	24.543
M8	3.105	0.011	0.002	358.882	10.955
Percent Variance Captured: 99.8%					

Transect A: Simulation A2: Water Levels					
Constituent	Period ω_n [hrs^{-1}]	Amplitude a_n [m]	Amplitude Error [m]	Phase ϕ_n [°]	Phase Error [°]
MM	661.309	0.048	0.009	15.897	12.620
MSF	354.367	0.033	0.009	19.080	17.630
ALP1	29.073	0.000	0.001	79.223	199.856
2Q1	28.006	0.001	0.001	245.023	63.989
Q1	26.868	0.003	0.001	254.063	30.583
O1	25.819	0.084	0.002	226.949	0.995
NO1	24.833	0.005	0.001	261.363	13.154
K1	23.934	0.101	0.002	217.126	0.772
J1	23.098	0.003	0.002	13.516	28.700
OO1	22.306	0.003	0.001	116.145	38.994
UPS1	21.578	0.001	0.002	342.728	56.684
EPS1	13.127	0.009	0.006	145.674	42.312
MU2	12.872	0.021	0.006	139.219	15.078
N2	12.658	0.127	0.006	30.478	2.753
M2	12.421	0.787	0.006	31.824	0.434
L2	12.192	0.035	0.007	342.287	10.902
S2	12.000	0.079	0.007	58.808	4.363
ETA2	11.755	0.009	0.007	52.293	47.704
MO3	8.386	0.021	0.003	29.678	8.175
M3	8.280	0.007	0.003	302.856	22.726
MK3	8.177	0.023	0.003	23.287	7.880
SK3	7.993	0.003	0.003	100.712	60.740
MN4	6.269	0.027	0.008	231.351	17.147
M4	6.210	0.091	0.009	211.807	5.236
SN4	6.160	0.020	0.008	270.821	26.202
MS4	6.103	0.014	0.008	268.370	34.447
S4	6.000	0.002	0.006	1.413	177.767
2MK5	4.931	0.010	0.005	255.667	33.236
2SK5	4.797	0.001	0.004	80.991	214.250
2MN6	4.166	0.020	0.006	116.979	15.724
M6	4.140	0.035	0.005	121.781	8.991
2MS6	4.092	0.013	0.005	151.533	25.230
2SM6	4.046	0.002	0.004	224.818	152.995
3MK7	3.530	0.004	0.001	165.589	22.879
M8	3.105	0.012	0.002	4.692	10.900
Percent Variance Captured: 99.8%					

Transect A: Simulation C2: Water Levels					
Constituent	Period ω_n [hrs^{-1}]	Amplitude a_n [m]	Amplitude Error [m]	Phase ϕ_n [°]	Phase Error [°]
MM	661.309	0.049	0.010	16.026	10.589
MSF	354.367	0.033	0.009	19.862	16.762
ALP1	29.073	0.000	0.001	89.663	203.618
2Q1	28.006	0.001	0.001	251.653	54.189
Q1	26.868	0.003	0.001	265.288	27.415
O1	25.819	0.080	0.001	231.511	1.026
NO1	24.833	0.005	0.001	270.707	12.066
K1	23.934	0.096	0.001	221.613	0.852
J1	23.098	0.003	0.001	18.037	23.334
OO1	22.306	0.003	0.001	128.195	34.498
UPS1	21.578	0.001	0.001	352.545	69.450
EPS1	13.127	0.008	0.005	153.521	46.059
MU2	12.872	0.022	0.006	147.690	15.735
N2	12.658	0.114	0.006	35.123	2.647
M2	12.421	0.730	0.005	35.686	0.487
L2	12.192	0.035	0.005	350.471	9.148
S2	12.000	0.070	0.006	63.221	4.493
ETA2	11.755	0.008	0.007	58.618	48.679
MO3	8.386	0.019	0.003	44.692	10.131
M3	8.280	0.007	0.003	319.582	26.054
MK3	8.177	0.020	0.003	40.089	9.546
SK3	7.993	0.003	0.003	119.866	73.789
MN4	6.269	0.023	0.007	254.333	17.184
M4	6.210	0.075	0.007	232.764	5.422
SN4	6.160	0.018	0.007	290.708	23.124
MS4	6.103	0.012	0.007	292.424	39.144
S4	6.000	0.002	0.005	19.685	171.107
2MK5	4.931	0.011	0.005	282.969	31.163
2SK5	4.797	0.001	0.004	107.888	237.653
2MN6	4.166	0.021	0.007	133.985	19.439
M6	4.140	0.040	0.007	136.508	10.075
2MS6	4.092	0.013	0.007	169.619	33.159
2SM6	4.046	0.002	0.005	250.418	156.071
3MK7	3.530	0.005	0.002	172.498	27.250
M8	3.105	0.010	0.002	20.911	12.117
Percent Variance Captured: 99.7%					

Transect A: Simulation E1: Water Levels					
Constituent	Period ω_n [hrs^{-1}]	Amplitude a_n [m]	Amplitude Error [m]	Phase ϕ_n [°]	Phase Error [°]
MM	661.309	0.049	0.010	16.345	10.432
MSF	354.367	0.033	0.011	20.544	14.458
ALP1	29.073	0.000	0.001	109.263	206.190
2Q1	28.006	0.002	0.001	259.214	51.315
Q1	26.868	0.003	0.001	274.677	28.962
O1	25.819	0.076	0.001	235.097	1.100
NO1	24.833	0.005	0.001	280.379	12.153
K1	23.934	0.090	0.001	225.114	0.774
J1	23.098	0.003	0.001	24.530	23.107
OO1	22.306	0.002	0.001	138.327	30.761
UPS1	21.578	0.001	0.001	0.659	66.816
EPS1	13.127	0.008	0.005	159.751	34.342
MU2	12.872	0.021	0.005	154.474	14.341
N2	12.658	0.103	0.005	38.493	3.049
M2	12.421	0.682	0.005	38.898	0.408
L2	12.192	0.034	0.005	357.313	8.589
S2	12.000	0.063	0.005	66.248	4.691
ETA2	11.755	0.008	0.006	63.926	46.904
MO3	8.386	0.015	0.003	55.241	9.660
M3	8.280	0.006	0.003	334.114	30.221
MK3	8.177	0.016	0.003	52.738	9.237
SK3	7.993	0.002	0.002	139.657	81.722
MN4	6.269	0.020	0.006	274.498	18.224
M4	6.210	0.062	0.006	252.121	5.567
SN4	6.160	0.015	0.007	309.457	23.268
MS4	6.103	0.010	0.006	312.744	35.125
S4	6.000	0.002	0.005	37.005	157.070
2MK5	4.931	0.011	0.005	306.959	25.786
2SK5	4.797	0.001	0.004	135.484	227.323
2MN6	4.166	0.019	0.007	149.360	22.611
M6	4.140	0.040	0.007	150.055	10.374
2MS6	4.092	0.012	0.007	186.097	33.101
2SM6	4.046	0.002	0.005	272.080	155.793
3MK7	3.530	0.005	0.002	181.723	31.382
M8	3.105	0.009	0.002	42.060	12.162
Percent Variance Captured: 99.7%					

Transect A: Simulation A1: Volume Fluxes					
	Period ω_n [hrs^{-1}]	Amplitude Q_n [m^3/s]	Amplitude Error [m^3/s]	Phase ϕ_n [°]	Phase Error [°]
Phase Error [°]	661.309	13.416	2.851	240.304	10.981
MSF	354.367	12.429	2.365	263.123	12.503
ALP1	29.073	1.211	3.318	37.062	150.225
2Q1	28.006	5.383	3.772	194.950	37.611
Q1	26.868	6.397	4.144	127.525	35.812
O1	25.819	195.188	3.696	146.117	1.310
NO1	24.833	11.386	2.906	189.638	16.241
K1	23.934	233.128	3.893	140.621	0.996
J1	23.098	9.874	3.836	316.001	20.179
OO1	22.306	3.702	3.758	20.215	61.328
UPS1	21.578	3.617	4.163	290.888	64.614
EPS1	13.127	22.277	20.203	85.339	55.621
MU2	12.872	57.070	21.844	53.394	21.409
N2	12.658	420.322	21.227	333.697	2.870
M2	12.421	2380.308	24.895	336.392	0.562
L2	12.192	91.453	22.572	259.216	14.527
S2	12.000	275.141	21.425	3.956	5.211
ETA2	11.755	25.569	25.421	356.658	53.935
MO3	8.386	101.914	13.971	261.612	8.132
M3	8.280	22.973	13.853	192.090	40.338
MK3	8.177	124.007	14.206	243.888	6.611
SK3	7.993	8.262	12.940	333.810	96.202
MN4	6.269	160.077	37.522	48.546	13.166
M4	6.210	647.073	29.570	61.215	3.347
SN4	6.160	80.128	34.054	152.117	25.997
MS4	6.103	90.004	35.494	71.533	21.970
S4	6.000	2.591	21.182	126.529	241.507
2MK5	4.931	24.053	11.908	312.986	28.727
2SK5	4.797	0.305	7.706	205.521	244.588
2MN6	4.166	99.372	36.474	95.744	22.744
M6	4.140	236.940	37.624	113.715	10.322
2MS6	4.092	59.044	42.496	128.984	30.609
2SM6	4.046	3.540	20.498	216.398	259.513
3MK7	3.530	38.913	10.345	95.870	16.829
M8	3.105	89.629	11.090	254.042	8.418
Percent Variance Captured: 99.6%					

Transect A: Simulation B1: Volume Fluxes					
Constituent	Period ω_n [hrs^{-1}]	Amplitude Q_n [m^3/s]	Amplitude Error [m^3/s]	Phase ϕ_n [°]	Phase Error [°]
MM	661.309	8.629	3.590	230.317	25.811
MSF	354.367	9.432	3.460	255.437	25.450
ALP1	29.073	1.280	3.029	257.490	144.788
2Q1	28.006	4.305	3.287	19.452	47.417
Q1	26.868	15.171	3.750	138.677	15.570
O1	25.819	154.441	3.956	133.624	1.442
NO1	24.833	18.934	3.522	106.015	9.071
K1	23.934	184.963	3.991	130.358	1.208
J1	23.098	5.751	3.877	173.543	39.196
OO1	22.306	12.084	4.004	350.534	22.054
UPS1	21.578	4.978	4.498	216.927	53.261
EPS1	13.127	23.546	18.633	32.163	52.871
MU2	12.872	82.052	21.242	20.633	13.526
N2	12.658	371.388	22.282	317.139	2.738
M2	12.421	1919.443	23.162	315.181	0.642
L2	12.192	114.606	20.478	223.595	11.232
S2	12.000	259.532	21.824	347.448	5.345
ETA2	11.755	23.069	26.210	306.673	63.290
MO3	8.386	134.124	18.619	227.298	7.438
M3	8.280	40.438	18.229	111.160	25.674
MK3	8.177	151.185	19.799	219.451	6.900
SK3	7.993	22.091	19.238	274.811	47.270
MN4	6.269	173.477	28.434	37.859	9.895
M4	6.210	496.330	30.462	36.880	2.825
SN4	6.160	62.292	27.797	73.776	25.676
MS4	6.103	107.336	33.811	69.940	16.934
S4	6.000	8.810	24.030	156.968	142.662
2MK5	4.931	70.258	33.260	287.201	30.776
2SK5	4.797	4.295	22.231	163.769	236.020
2MN6	4.166	116.125	37.497	83.236	19.047
M6	4.140	248.583	42.387	88.507	9.872
2MS6	4.092	75.210	34.661	116.731	30.157
2SM6	4.046	9.085	27.009	200.847	164.189
3MK7	3.530	38.141	12.137	13.957	22.569
M8	3.105	108.430	14.011	178.650	7.341
Percent Variance Captured: 99.3%					

Transect A: Simulation A3: Volume Fluxes					
Constituent	Period ω_n [hrs^{-1}]	Amplitude Q_n [m^3/s]	Amplitude Error [m^3/s]	Phase ϕ_n [°]	Phase Error [°]
MM	661.309	13.680	2.530	238.567	10.621
MSF	354.367	13.116	2.763	263.259	12.902
ALP1	29.073	1.080	2.869	37.163	191.135
2Q1	28.006	5.547	3.700	196.280	43.856
Q1	26.868	6.579	3.490	130.018	41.037
O1	25.819	195.514	4.148	146.401	0.978
NO1	24.833	11.668	3.573	187.955	17.370
K1	23.934	233.588	3.743	140.861	1.057
J1	23.098	9.847	3.891	316.562	23.251
OO1	22.306	4.216	3.460	18.776	59.579
UPS1	21.578	3.717	3.822	282.943	64.499
EPS1	13.127	22.253	23.277	84.567	69.644
MU2	12.872	57.495	20.329	52.282	20.554
N2	12.658	420.536	20.213	332.836	3.304
M2	12.421	2382.028	20.502	335.404	0.547
L2	12.192	91.618	22.663	258.213	13.965
S2	12.000	275.572	20.766	2.959	4.480
ETA2	11.755	25.749	22.903	355.781	59.148
MO3	8.386	100.238	13.414	258.578	8.110
M3	8.280	21.833	14.208	189.972	34.433
MK3	8.177	122.654	15.141	240.801	6.338
SK3	7.993	7.797	13.115	328.442	89.510
MN4	6.269	161.734	31.476	44.984	11.470
M4	6.210	639.339	30.536	57.977	3.030
SN4	6.160	75.199	33.613	148.245	25.169
MS4	6.103	92.299	33.641	68.534	23.256
S4	6.000	3.094	23.755	124.635	213.711
2MK5	4.931	28.961	11.321	309.670	22.532
2SK5	4.797	0.810	7.719	174.446	233.295
2MN6	4.166	101.778	34.147	94.542	22.825
M6	4.140	243.000	33.043	112.292	8.360
2MS6	4.092	59.885	37.990	127.445	37.622
2SM6	4.046	3.527	27.187	214.213	228.987
3MK7	3.530	36.519	10.307	92.122	16.413
M8	3.105	89.703	13.675	245.921	7.503
Percent Variance Captured: 99.7%					

Transect A: Simulation A2: Volume Fluxes					
Constituent	Period ω_n [hrs^{-1}]	Amplitude Q_n [m^3/s]	Amplitude Error [m^3/s]	Phase ϕ_n [°]	Phase Error [°]
MM	661.309	25.521	5.562	217.500	13.851
MSF	354.367	19.675	5.275	231.929	15.876
ALP1	29.073	1.181	3.171	75.021	175.423
2Q1	28.006	6.396	4.035	206.642	35.867
Q1	26.868	7.259	4.488	117.815	33.013
O1	25.819	204.868	4.380	141.017	1.208
NO1	24.833	10.129	3.768	192.530	21.259
K1	23.934	247.914	4.336	136.429	1.009
J1	23.098	11.168	4.851	323.292	22.477
OO1	22.306	3.572	4.237	7.790	73.537
UPS1	21.578	3.215	4.340	293.505	102.252
EPS1	13.127	24.924	22.771	88.504	49.450
MU2	12.872	56.708	28.315	52.731	23.775
N2	12.658	459.940	25.973	333.951	3.145
M2	12.421	2598.409	25.568	337.421	0.534
L2	12.192	91.793	21.491	259.151	16.263
S2	12.000	300.190	23.475	4.470	4.119
ETA2	11.755	29.977	26.263	358.641	48.995
MO3	8.386	111.925	19.346	264.087	10.124
M3	8.280	28.891	16.744	205.525	39.513
MK3	8.177	138.869	17.864	245.973	7.402
SK3	7.993	9.107	14.651	356.692	109.751
MN4	6.269	177.467	39.651	55.486	13.865
M4	6.210	750.874	38.520	68.093	3.194
SN4	6.160	98.998	44.077	161.943	24.814
MS4	6.103	97.016	40.775	76.589	28.950
S4	6.000	1.596	24.838	177.003	269.555
2MK5	4.931	11.395	11.966	287.073	74.724
2SK5	4.797	0.684	10.454	293.201	256.456
2MN6	4.166	105.901	32.597	97.090	18.083
M6	4.140	246.749	33.076	117.654	7.905
2MS6	4.092	64.860	34.126	127.658	29.063
2SM6	4.046	3.036	22.358	188.568	232.038
3MK7	3.530	31.132	10.684	95.375	18.628
M8	3.105	108.815	16.785	260.900	9.743
Percent Variance Captured: 99.5%					

Transect A: Simulation C1: Volume Fluxes					
Constituent	Period ω_n [hrs^{-1}]	Amplitude Q_n [m^3/s]	Amplitude Error [m^3/s]	Phase ϕ_n [°]	Phase Error [°]
MM	661.309	12.837	2.488	238.298	10.778
MSF	354.367	11.450	2.321	264.308	10.893
ALP1	29.073	0.958	2.621	38.604	199.417
2Q1	28.006	5.021	3.862	195.433	43.924
Q1	26.868	5.866	3.504	142.911	37.535
O1	25.819	177.759	3.835	151.071	1.036
NO1	24.833	11.889	3.584	192.097	17.002
K1	23.934	212.256	3.681	145.487	0.948
J1	23.098	9.562	3.456	315.293	19.487
OO1	22.306	3.859	3.442	33.284	55.260
UPS1	21.578	3.363	3.392	293.019	64.596
EPS1	13.127	21.432	18.675	91.000	58.001
MU2	12.872	58.354	19.872	63.330	20.165
N2	12.658	370.777	21.038	338.824	3.156
M2	12.421	2142.955	17.800	339.809	0.514
L2	12.192	94.230	17.022	268.083	10.582
S2	12.000	240.529	19.443	9.349	5.194
ETA2	11.755	23.645	21.354	0.627	52.048
MO3	8.386	92.051	13.723	274.600	8.867
M3	8.280	22.329	11.961	206.039	28.863
MK3	8.177	106.111	12.501	256.604	7.706
SK3	7.993	7.255	10.180	348.369	100.815
MN4	6.269	117.020	28.108	55.262	13.558
M4	6.210	491.097	29.299	68.871	3.344
SN4	6.160	62.581	27.966	162.463	25.495
MS4	6.103	65.504	32.527	77.093	26.795
S4	6.000	1.567	19.658	115.198	247.775
2MK5	4.931	27.217	8.482	310.434	16.776
2SK5	4.797	0.337	5.546	170.816	249.939
2MN6	4.166	93.717	37.701	103.382	23.544
M6	4.140	220.311	32.481	117.058	9.298
2MS6	4.092	56.057	36.184	137.154	38.100
2SM6	4.046	4.719	23.917	234.867	239.810
3MK7	3.530	33.974	10.009	104.033	15.627
M8	3.105	68.107	10.212	260.295	7.705
Percent Variance Captured: 99.7%					

Transect A: Simulation E1: Volume Fluxes					
Constituent	Period ω_n [hrs^{-1}]	Amplitude Q_n [m^3/s]	Amplitude Error [m^3/s]	Phase ϕ_n [°]	Phase Error [°]
MM	661.309	13.337	3.062	236.022	12.841
MSF	354.367	10.816	2.883	251.354	16.120
ALP1	29.073	0.914	2.307	47.033	160.553
2Q1	28.006	4.789	3.058	199.049	41.120
Q1	26.868	4.970	3.006	137.186	34.936
O1	25.819	167.866	3.070	154.682	1.109
NO1	24.833	10.090	3.160	196.452	15.840
K1	23.934	200.487	3.393	149.549	0.811
J1	23.098	9.131	3.404	319.972	19.859
OO1	22.306	3.109	3.208	34.176	64.211
UPS1	21.578	2.887	3.401	304.923	67.274
EPS1	13.127	20.216	17.909	98.518	54.945
MU2	12.872	59.615	17.952	73.103	19.234
N2	12.658	337.040	16.169	346.580	2.960
M2	12.421	1972.986	16.617	346.157	0.597
L2	12.192	96.668	18.257	276.712	11.596
S2	12.000	216.852	17.947	17.777	5.285
ETA2	11.755	22.640	18.945	9.751	55.816
MO3	8.386	90.327	14.313	291.652	9.056
M3	8.280	24.356	12.623	225.262	28.415
MK3	8.177	99.717	13.610	274.155	8.032
SK3	7.993	7.403	12.329	15.583	113.046
MN4	6.269	87.722	24.759	70.258	15.577
M4	6.210	403.259	28.108	84.171	3.669
SN4	6.160	56.807	24.710	180.854	24.510
MS4	6.103	47.448	25.227	87.927	26.947
S4	6.000	0.925	17.564	50.690	270.619
2MK5	4.931	23.992	6.291	312.998	13.568
2SK5	4.797	0.354	3.835	139.536	256.009
2MN6	4.166	86.285	35.580	117.071	22.677
M6	4.140	204.407	41.943	127.169	10.036
2MS6	4.092	52.240	34.511	152.813	44.020
2SM6	4.046	5.150	28.262	255.320	184.947
3MK7	3.530	33.827	13.905	120.010	20.047
M8	3.105	54.820	10.954	293.165	11.246
Percent Variance Captured: 99.7%					

REFERENCES

Adcock, T. A. and Draper, S. (2014). Power extraction from tidal channels–multiple tidal constituents, compound tides and overtides. *Renewable Energy*, 63:797–806.

Adcock, T. A., Draper, S., Houlsby, G. T., Borthwick, A. G., and Serhadlıoğlu, S. (2013). The available power from tidal stream turbines in the pentland firth. *Proceedings of the Royal Society A: Mathematical, Physical and Engineering Science*, 469(2157):20130072.

Ahmadian, R. and Falconer, R. A. (2012). Assessment of array shape of tidal stream turbines on hydro-environmental impacts and power output. *Renewable Energy*, 44:318–327.

Airy, G. (1842). Tides and waves: Encyclopedia metropolitana, 5: 24l-396. coleridge editor.

Alaee, M. J., Ivey, G., and Pattiaratchi, C. (2004). Secondary circulation induced by flow curvature and coriolis effects around headlands and islands. *Ocean Dynamics*, 54(1):27–38.

Ashmore, P., Ferguson, R., Prestegaard, K., Ashworth, P., and Paola, C. (1992). Secondary flow in anabranch confluences of a braided, gravel-bed stream. *Earth Surface Processes and Landforms*, 17(3):299–311.

Atwater, J. F. and Lawrence, G. A. (2010). Power potential of a split tidal channel. *Renewable energy*, 35(2):329–332.

Barwis, J. H. (1977). Sedimentology of some south carolina tidal-creek point bars, and a comparison with their fluvial counterparts.

Basdurak, N. and Valle-Levinson, A. (2013). Tidal variability of lateral advection in a coastal plain estuary. *Continental Shelf Research*, 6162(0):85 – 97.

Batchelor, G. K. (1967). *An introduction to fluid dynamics*. Cambridge university press.

Best, J. L. (1987). Flow dynamics at river channel confluences: implications for sediment transport and bed morphology.

Betz, A. (1920). Das maximum der theoretisch möglichen ausnützung des windes durch windmotoren. *Zeitschrift für das gesamte Turbinenwesen*, 26:307–309.

Biron, P. M., Ramamurthy, A. S., and Han, S. (2004). Three-dimensional numerical modeling of mixing at river confluences. *Journal of Hydraulic Engineering*, 130(3):243–253.

Blanchfield, J., Garrett, C., Wild, P., and Rowe, A. (2008). The extractable power from a channel linking a bay to the open ocean. *Proceedings of the Institution of Mechanical Engineers, Part A: Journal of Power and Energy*, 222(3):289–297.

Blanckaert, K. and De Vriend, H. (2004). Secondary flow in sharp open-channel bends. *Journal of Fluid Mechanics*, 498:353–380.

Blanckaert, K. and de Vriend, H. J. (2003). Nonlinear modeling of mean flow redistribution in curved open channels. *Water Resources Research*, 39(12).

Blanckaert, K. and Graf, W. H. (2004). Momentum transport in sharp open-channel bends. *Journal of Hydraulic Engineering*, 130(3):186–198.

Blanton, J. O., Lin, G., and Elston, S. A. (2002). Tidal current asymmetry in shallow estuaries and tidal creeks. *Continental Shelf Research*.

Blunden, L. and Bahaj, A. (2006). Initial evaluation of tidal stream energy resources at portland bill, uk. *Renewable Energy*, 31(2):121–132.

Boden, T., Marland, G., and Andres, R. (2010). Global, regional, and national fossil-fuel carbon dioxide emissions. *Carbon Dioxide Information Analysis Center, Oak Ridge National Laboratory,U.S. Department of Energy*.

Bomminayuni, S., Bruder, B., Stoesser, T., and Haas, K. (2012). Assessment of hydrokinetic energy near rose dhu island, georgia. *Journal of Renewable and Sustainable Energy*, 4(6):063107–063107.

Boon, J. D. and Byrne, R. J. (1981). On basin hyposmetry and the morphodynamic response of coastal inlet systems. *Marine Geology*, 40(1):27–48.

Boussinesq, J. (1868). Memoire sur l'influence des frottements dans les mouvements reguliers des fluides. *J. Math. Pures Appl*, 13(377-424):21.

Bradbrook, K., Lane, S., and Richards, K. (2000). Numerical simulation of three-dimensional, time-averaged flow structure at river channel confluences. *Water Resources Research*, 36(9):2731–2746.

Bricker, J. D., Inagaki, S., and Monismith, S. G. (2005). Bed drag coefficient variability under wind waves in a tidal estuary. *Journal of Hydraulic Engineering*, 131(6):497–508.

Brock, J. C. and Purkis, S. J. (2009). The emerging role of lidar remote sensing in coastal research and resource management. *Journal of Coastal Research*, pages 1–5.

Brooks, D. A. (2011). The hydrokinetic power resource in a tidal estuary: The kennebec river of the central maine coast. *Renewable Energy*, 36(5):1492–1501.

Bulle, H. (1926). *Untersuchungen über die Geschiebeableitung bei der Spaltung von Wasserläufen: Modellversuche aus dem Flussbaulaboratorium der Technischen Hochschule zu Karlsruhe*. VDI-Verlag.

Buschman, F. A., van der Vegt, M., Hoitink, A. J. F., and Hoekstra, P. (2013). Water and suspended sediment division at a stratified tidal junction. *Journal of Geophysical Research: Oceans*, 118(3):1459–1472.

Carballo, R., Iglesias, G., and Castro, A. (2009). Numerical model evaluation of tidal stream energy resources in the ría de muros (nw spain). *Renewable Energy*, 34(6):1517–1524.

Cartwright, D. (1999). *Tides: A Scientific History*. Cambridge University Press.

Chant, R. J. (2002). Secondary circulation in a region of flow curvature: Relationship with tidal forcing and river discharge. *Journal of Geophysical Research*, 107(C9):3131.

Chant, R. J. and Wilson, R. E. (1997). Secondary circulation in a highly stratified estuary. *Journal of Geophysical Research: Oceans (1978–2012)*, 102(C10):23207–23215.

Chen, C., Beardsley, R. C., and Cowles, G. (2006). An unstructured grid, finite-volume coastal ocean model: Fvcom user manual. *SMAST/UMASSD*.

Chen, C., Liu, H., and Beardsley, R. C. (2003). An unstructured grid, finite-volume, three-dimensional, primitive equations ocean model: application to coastal ocean and estuaries. *Journal of atmospheric and oceanic technology*, 20(1):159–186.

Chen, W.-B., Liu, W.-C., and Hsu, M.-H. (2013). Modeling assessment of tidal current energy at kinmen island, taiwan. *Renewable Energy*, 50:1073–1082.

Christensen, B., Gislason, K., and Fredsoe, J. (1999). Secondary turbulent flow in an infinite bend. 1st rcem symp. *Genova, Italy*, 1:543–553.

Constantinescu, G., Miyawaki, S., Rhoads, B., and Sukhodolov, A. (2012). Numerical analysis of the effect of momentum ratio on the dynamics and sediment-entrainment capacity of coherent flow structures at a stream confluence. *Journal of Geophysical Research: Earth Surface (2003–2012)*, 117(F4).

Constantinescu, G., Miyawaki, S., Rhoads, B., Sukhodolov, A., and Kirkil, G. (2011). Structure of turbulent flow at a river confluence with momentum and velocity ratios close to 1: Insight provided by an eddy-resolving numerical simulation. *Water Resources Research*, 47(5).

D'Alpaos, A., Lanzoni, S., Marani, M., and Rinaldo, A. (2007). Landscape evolution in tidal embayments: modeling the interplay of erosion, sedimentation, and vegetation dynamics. *Journal of Geophysical Research: Earth Surface (2003–2012)*, 112(F1).

Dame, R., Alber, M., Allen, D., Mallin, M., Montague, C., Lewitus, A., Chalmers, A., Gardner, R., Gilman, C., Kjerfve, B., et al. (2000). Estuaries of the south atlantic coast of north america: their geographical signatures. *Estuaries*, 23(6):793–819.

Dargahi, B. (2004). Three-dimensional flow modelling and sediment transport in the river klarlven. *Earth Surface Processes and Landforms*, 29(7):821–852.

Darwin, S. G. H. and Adams, J. C. (1883). *Report of a committee for the harmonic analysis of tidal observations*. Spottiswoode and Company.

De Serres, B., Roy, A. G., Biron, P. M., and Best, J. L. (1999). Three-dimensional structure of flow at a confluence of river channels with discordant beds. *Geomorphology*, 26(4):313–335.

De Vriend, H. J. (1977). A mathematical model of steady flow in curved shallow channels. *Journal of Hydraulic Research*, 15(1):37–54.

Dean, R. and Dalrymple, R. (1984). *Water wave mechanics for engineers and scientists.* Prentice Hall Inc.

Defne, Z., Haas, K. A., and Fritz, H. M. (2011). Numerical modeling of tidal currents and the effects of power extraction on estuarine hydrodynamics along the georgia coast, {USA}. *Renewable Energy*, 36(12):3461 – 3471.

Defne, Z., Haas, K. A., Fritz, H. M., Jiang, L., French, S. P., Shi, X., Smith, B. T., Neary, V. S., and Stewart, K. M. (2012a). National geodatabase of tidal stream power resource in usa. *Renewable and Sustainable Energy Reviews*, 16(5):3326–3338.

Defne, Z., Haas, K. a., Fritz, H. M., Jiang, L., French, S. P., Shi, X., Smith, B. T., Neary, V. S., and Stewart, K. M. (2012b). National geodatabase of tidal stream power resource in USA. *Renewable and Sustainable Energy Reviews*, 16(5):3326–3338.

Dietrich, W. (1987). Mechanics of flow and sediment transport in river bends. *River channels: Environment and process*, 134:179–227.

DOE (2013a). Marine & Hydrokinetic Technology Database. *US Department of Energy Energy Efficiency & Renewable Energy http://www1.eere.energy.gov/water/hydrokinetic*.

DOE (2013b). US Energy Sector Vulnerabilities to Climate Change and Extreme Weather. *US Department of Energy*.

Doodson, A. T. (1921). The harmonic development of the tide-generating potential. *Proceedings of the Royal Society of London. Series A*, 100(704):305–329.

Draper, S., Borthwick, A., and Houlsby, G. (2013). Energy potential of a tidal fence deployed near a coastal headland. *Philosophical Transactions of the Royal Society A: Mathematical, Physical and Engineering Sciences*, 371(1985):20120176.

Draper, S., Houlsby, G., Oldfield, M., and Borthwick, A. (2010). Modelling tidal energy extraction in a depth-averaged coastal domain. *IET renewable power generation*, 4(6):545–554.

Dronkers, J. (1964). *Tidal computations in rivers and coastal waters*. North-Holland.

Dronkers, J. (1986a). Tidal asymmetry and estuarine morphology. *Netherlands Journal of Sea Research*, 20(23):117 – 131.

Dronkers, J. (1986b). Tidal asymmetry and estuarine morphology. *Netherlands Journal of Sea Research*, 20(2):117–131.

Dronkers, J. (1996). The influence of buoyancy on transverse circulation and on estuarine dynamics. *Buoyancy Effects on Coastal and Estuarine Dynamics*, pages 341–356.

EIA (2009). Residential Energy Consumption Survey. *US Energy Information Administration*.

EIA (2012). Annual Energy Review 2011. *US Energy Information Administration*.

Elgar, S. and Guza, R. (1985). Observations of bispectra of shoaling surface gravity waves. *Journal of Fluid Mechanics*, 161(1):425–448.

Engelund, F. (1974). Flow and bed topography in channel bends. *Journal of the Hydraulics Division*, 100(11):1631–1648.

Fagherazzi, S., Kirwan, M. L., Mudd, S. M., Guntenspergen, G. R., Temmerman, S., D'Alpaos, A., Koppel, J., Rybczyk, J. M., Reyes, E., Craft, C., et al. (2012). Numerical models of salt marsh evolution: ecological, geomorphic, and climatic factors. *Reviews of Geophysics*, 50(1).

FERC (2012). Order Issuing Pilot Project License (Minor Project) Ocean Renewable Power Company Maine, LLC, Project No. 12711-005. *US Federal Energy Regulatory Commission*.

Friedrichs, C. T. and Aubrey, D. G. (1988). Non-linear tidal distortion in shallow well-mixed estuaries: a synthesis. *Estuarine, Coastal and Shelf Science*, 27(5):521–545.

Friedrichs, C. T. and Aubrey, D. G. (1994). Tidal propagation in strongly convergent channels. *Journal of Geophysical Research: Oceans (1978–2012)*, 99(C2):3321–3336.

Friedrichs, C. T. and Perry, J. E. (2001). Tidal salt marsh morphodynamics: a synthesis. *Journal of Coastal Research*, pages 7–37.

Garrett, C. and Cummins, P. (2004). Generating power from tidal currents. *Journal of waterway, port, coastal, and ocean engineering*, 130(3):114–118.

Garrett, C. and Cummins, P. (2005). The power potential of tidal currents in channels. *Proceedings of the Royal Society A: Mathematical, Physical and Engineering Science*, 461(2060):2563–2572.

Garrett, C. and Cummins, P. (2007). The efficiency of a turbine in a tidal channel. *Journal of fluid mechanics*, 588:243.

Ginsberg, S. S., Aliotta, S., and Lizasoain, G. O. (2009). Morphodynamics and seismostratigraphy of a deep hole at tidal channel confluence. *Geomorphology*, 104(3):253–261.

Ginsberg, S. S. and Perillo, G. M. (1999). Deep-scour holes at tidal channel junctions, bahia blanca estuary, argentina. *Marine Geology*, 160(1):171–182.

Gunawan, B., Neary, V. S., and Colby, J. (2014). Tidal energy site resource assessment in the east river tidal strait, near roosevelt island, new york, new york. *Renewable Energy*, 71:509–517.

Haas, K. A. (2011). Assessment of energy production potential from tidal streams in the united states. Technical report, Georgia Tech Research Corporation.

Haidvogel, D. B., Arango, H., Budgell, W., Cornuelle, B., Curchitser, E., Di Lorenzo, E., Fennel, K., Geyer, W., Hermann, A., Lanerolle, L., et al. (2008). Ocean forecasting in terrain-following coordinates: Formulation and skill assessment of the regional ocean modeling system. *Journal of Computational Physics*, 227(7):3595–3624.

Hardy, R., Lane, S., and Yu, D. (2011). Flow structures at an idealized bifurcation: a numerical experiment. *Earth Surface Processes and Landforms*, 36(15):2083–2096.

Harries, T. (2014). *Physical testing and numerical modelling of a novel vertical-axis tidal stream turbine*. PhD thesis, Cardiff University.

Hartmann, D. (2014). Atm 552 s class notes.

Hench, J. L. and Luettich Jr, R. A. (2003). Transient tidal circulation and momentum balances at a shallow inlet. *Journal of Physical Oceanography*, 33(4):913–932.

Hladik, C. and Alber, M. (2012). Accuracy assessment and correction of a lidar-derived salt marsh digital elevation model. *Remote Sensing of Environment*, 121:224–235.

Huang, H., Chen, C., Blanton, J. O., and Andrade, F. A. (2008). A numerical study of tidal asymmetry in okatee creek, south carolina. *Estuarine, Coastal and Shelf Science*, 78(1):190–202.

Iglesias, G., Sánchez, M., Carballo, R., and Fernández, H. (2012). The tse index–a new tool for selecting tidal stream sites in depth-limited regions. *Renewable Energy*, 48:350–357.

Iyer, A., Couch, S., Harrison, G., and Wallace, A. (2013). Variability and phasing of tidal current energy around the united kingdom. *Renewable Energy*, 51:343–357.

Joukowsky, N. (1920). Windmill of the nej type. *Transactions of the Central Institute for Aerohydrodynamics of Moscow*, pages 405–409.

Kalkwijk, J. P. T. and Booij, R. (1986). Adaptation of secondary flow in nearly-horizontal flow. *Journal of Hydraulic Research*, 24(1):19–37.

Karsten, R., McMillan, J., Lickley, M., and Haynes, R. (2008). Assessment of tidal current energy in the minas passage, bay of fundy. *Proceedings of the Institution of Mechanical Engineers, Part A: Journal of Power and Energy*, 222(5):493–507.

Karsten, R., Swan, A., and Culina, J. (2013). Assessment of arrays of in-stream tidal turbines in the bay of fundy. *Philosophical Transactions of the Royal Society A: Mathematical, Physical and Engineering Sciences*, 371(1985):20120189.

Kennedy, B. A. (1984). On playfair's law of accordant junctions. *Earth Surface Processes and Landforms*, 9(2):153–173.

Kim, K.-P., Ahmed, M. R., and Lee, Y.-H. (2012). Efficiency improvement of a tidal current turbine utilizing a larger area of channel. *Renewable Energy*, 48:557–564.

Kjerfve, B., Shao, C.-C., and Stapor Jr, F. W. (1979). Formation of deep scour holes at the junction of tidal creeks: an hypothesis. *Marine Geology*, 33(1):M9–M14.

Kleinhans, M. G., Ferguson, R. I., Lane, S. N., and Hardy, R. J. (2013). Splitting rivers at their seams: bifurcations and avulsion. *Earth Surface Processes and Landforms*, 38(1):47–61.

Lacy, J. R. and Monismith, S. G. (2001). Secondary currents in a curved, stratified, estuarine channel. *Journal of Geophysical Research: Oceans (1978–2012)*, 106(C12):31283–31302.

Lamb, Horace, S. (1932). *Hydrodynamics*. Cambridge mathematical library. Cambridge University Press.

Lanchester, F. (1915). A contribution to the theory of propulsion and the screw propeller. *Journal of the American Society for Naval Engineers*, 27(2):509–510.

Lanerolle, L. W., Paternostro, C. L., Dusek, G., McLaughlin, L. R., and Skaling, S. (2012). An assessment of the renewable hydrokinetic energy potential in cook inlet, alaska. In *Oceans, 2012*, pages 1–9. IEEE.

Laplace, P.-S. (1775). Recherches sur plusieurs points du systeme du monde. *Mem. Acad. R. Sci. Paris*, 88:75–182.

Lawrence, D., Allen, J. R. L., and Havelock, G. (2004). Salt marsh morphodynamics: an investigation of tidal flows and marsh channel equilibrium. *Journal of Coastal Research*, pages 301–316.

Le Provost, C. (1991). Generation of over-tides and compound tides (review).

Leite Ribeiro, M., Blanckaert, K., Roy, A., and Schleiss, A. (2012). Flow and sediment dynamics in channel confluences. *Journal of Geophysical Research: Earth Surface (2003–2012)*, 117(F1).

Lerczak, J. A. and Rockwell Geyer, W. (2004). Modeling the lateral circulation in straight, stratified estuaries*. *Journal of Physical Oceanography*, 34(6):1410–1428.

Lim, Y. S. and Koh, S. L. (2010). Analytical assessments on the potential of harnessing tidal currents for electricity generation in malaysia. *Renewable Energy*, 35(5):1024–1032.

McLelland, S. J., Ashworth, P., and Best, J. L. (1996). The origin and downstream development of coherent flow structures at channel junctions.

Mellor, G. L. and Yamada, T. (1982). Development of a turbulence closure model for geophysical fluid problems. *Reviews of Geophysics*, 20(4):851–875.

Miori, S., Hardy, R. J., and Lane, S. (2012). Topographic forcing of flow partition and flow structures at river bifurcations. *Earth Surface Processes and Landforms*, 37(6):666–679.

Murphy, A. H. (1988). Skill scores based on the mean square error and their relationships to the correlation coefficient. *Monthly weather review*, 116(12):2417–2424.

Neary, V. S. and Odgaard, A. J. (1993). Three-dimensional flow structure at open-channel diversions. *Journal of hydraulic engineering*, 119(11):1223–1230.

Neill, S. P., Hashemi, M. R., and Lewis, M. J. (2014). The role of tidal asymmetry in characterizing the tidal energy resource of orkney. *Renewable Energy*, 68:337–350.

Nepf, H. (1999). Drag, turbulence, and diffusion in flow through emergent vegetation. *Water resources research*, 35(2):479–489.

Newton, I. (1687). *Philosophiae naturalis principia mathematica*, volume 1. The Royal Society.

NOAA (2013). US Climate Extremes Index. *National Oceanic and Atmospheric Administration National Climatic Data Center. www.http://www.ncdc.noaa.gov/extremes/cei/.*

ORPC (2012). *Ocean Renewable Power Company, www.orpc.co.*

Pacheco, A., Ferreira, Ó., Carballo, R., and Iglesias, G. (2014). Evaluation of the production of tidal stream energy in an inlet channel by coupling field data and numerical modelling. *Energy.*

Parker, B. B. (1991). The relative importance of the various nonlinear mechanisms in a wide range of tidal interactions (review). *Tidal hydrodynamics*, pages 237–269.

Pawlowicz, R., Beardsley, B., and Lentz, S. (2002). Classical tidal harmonic analysis including error estimates in matlab using t_tide. *Computers & Geosciences*, 28(8):929–937.

Pierini, J. O., Perillo, G. M., Carbone, M. E., and Marini, F. M. (2005). Residual flow structure at a scour-hole in bahia blanca estuary, argentina. *Journal of coastal research*, pages 784–796.

Plew, D. R. and Stevens, C. L. (2013). Numerical modelling of the effect of turbines on currents in a tidal channel–tory channel, new zealand. *Renewable Energy*, 57:269–282.

Polagye, B. and Bedard, R. (2006). Tidal in-stream energy resource assessment for southeast alaska. *Electric Power Research Institute.*

Polagye, B. and Thomson, J. (2013a). Implications of tidal phasing for power generation at a tidal energy site. In *Proceedings of the 1st Marine Energy Technology Symposium METS13.*

Polagye, B. and Thomson, J. (2013b). Tidal energy resource characterization: methodology and field study in admiralty inlet, puget sound, wa (usa). *Proceedings of the Institution of Mechanical Engineers, Part A: Journal of Power and Energy*, page 0957650912470081.

Polagye, B. L. and Malte, P. C. (2011). Far-field dynamics of tidal energy extraction in channel networks. *Renewable energy*, 36(1):222–234.

Proudman, J. (1953). Dynamical oceanography.

Ramos, V., Carballo, R., Sanchez, M., Veigas, M., and Iglesias, G. (2014). Tidal stream energy impacts on estuarine circulation. *Energy Conversion and Management*, 80:137–149.

Rhoads, B. L. and Kenworthy, S. T. (1998). Time-averaged flow structure in the central region of a stream confluence. *Earth Surface Processes and Landforms*, 23(2):171–191.

Rhoads, B. L. and Sukhodolov, A. N. (2001). Field investigation of three-dimensional flow structure at stream confluences: 1. thermal mixing and time-averaged velocities. *Water Resources Research*, 37(9):2393–2410.

Rhoads, B. L. and Sukhodolov, A. N. (2008). Lateral momentum flux and the spatial evolution of flow within a confluence mixing interface. *Water resources research*, 44(8).

Riley, J. D. and Rhoads, B. L. (2012). Flow structure and channel morphology at a natural confluent meander bend. *Geomorphology*, 163:84–98.

Roberts, M. V. T. (2004). *Flow dynamics at open channel confluent-meander bends*. PhD thesis, University of Leeds.

Rozovskii, I. (1957). Flow of water in bend of open channel academy of sciences of ukrainian ssr. *Kiev (translated from Russian by the Israel Program for Scientific Translations, Jerusalem, 1961)*.

Seim, H., Blanton, J., and Elston, S. (2006). Tidal circulation and energy dissipation in a shallow, sinuous estuary. *Ocean Dynamics*, 56(3-4):360–375.

Seim, H. E., Blanton, J. O., and Gross, T. (2002). Direct stress measurements in a shallow, sinuous estuary. *Continental Shelf Research*, 22(11):1565–1578.

Seim, H. E. and Gregg, M. C. (1997). The importance of aspiration and channel curvature in producing strong vertical mixing over a sill. *Journal of Geophysical Research*, 102(C2):3451–3472.

Serhadlıoğlu, S., Adcock, T. A., Houlsby, G. T., Draper, S., and Borthwick, A. G. (2013). Tidal stream energy resource assessment of the anglesey skerries. *International Journal of Marine Energy*, 3:e98–e111.

Smagorinsky, J. (1963). General circulation experiments with the primitive equations: I. the basic experiment*. *Monthly weather review*, 91(3):99–164.

Speer, P. and Aubrey, D. (1985). A study of non-linear tidal propagation in shallow inlet/estuarine systems part ii: Theory. *Estuarine, Coastal and Shelf Science*, 21(2):207 – 224.

State of Maine DOC (2012). Submerged Lands Lease Application No.1684. *State of Main Department of Conservation*.

Stevens, C., Smith, M., Grant, B., Stewart, C., and Divett, T. (2012). Tidal energy resource complexity in a large strait: The karori rip, cook strait. *Continental Shelf Research*, 33:100–109.

Sutherland, G., Foreman, M., and Garrett, C. (2007). Tidal current energy assessment for johnstone strait, vancouver island. *Proceedings of the Institution of Mechanical Engineers, Part A: Journal of Power and Energy*, 221(2):147–157.

Tang, H., Qu, K., Chen, G., Kraatz, S., Aboobaker, N., and Jiang, C. (2014). Potential sites for tidal power generation: A thorough search at coast of new jersey, usa. *Renewable and Sustainable Energy Reviews*, 39:412–425.

Teledyne RD Instruments (1996). Principles of operation a practical primer. *Available from RDInstruments. com*.

Teledyne RD Instruments (February 2007). Winriver ii user's guide.

Teledyne RD Instruments (January 2010). ADCP coordinate transformation.

Temmerman, S., Bouma, T. J., Govers, G., Wang, Z. B., De Vries, M. B., and Herman, P. M. J. (2005). Impact of vegetation on flow routing and sedimentation patterns: Three-dimensional modeling for a tidal marsh. *Journal of Geophysical Research: Earth Surface*, 110(F4):n/a–n/a.

Temmerman, S., Govers, G., Meire, P., and Wartel, S. (2003). Modelling long-term tidal marsh growth under changing tidal conditions and suspended sediment concentrations, scheldt estuary, belgium. *Marine Geology*, 193(1):151–169.

The National Research Council (2013). *An Evaluation of the U.S. Department of Energy's Marine and Hydrokinetic Resource Assessments*. The National Academies Press.

Thomas, R. E., Parsons, D. R., Sandbach, S. D., Keevil, G. M., Marra, W. A., Hardy, R. J., Best, J. L., Lane, S. N., and Ross, J. A. (2011). An experimental study of discharge partitioning and flow structure at symmetrical bifurcations. *Earth Surface Processes and Landforms*, 36(15):2069–2082.

Thomson, J. (1876). On the origin of windings of rivers in alluvial plains, with remarks on the flow of water round bends in pipes. *Proceedings of the Royal Society of London*, 25(171-178):5–8.

Thomson, S. W. (1868). Report of committee for the purpose of promoting the extension, improvement, and harmonic analysis of tidal observations. *Brit. Assoc. Advancement Sci., Rept*, pages 489–505.

Timko, P. G., Arbic, B. K., Richman, J. G., Scott, R. B., Metzger, E. J., and Wallcraft, A. J. (2012). Skill tests of three-dimensional tidal currents in a global ocean model: A look at the north atlantic. *Journal of Geophysical Research: Oceans (1978–2012)*, 117(C8).

van der Mark, C. F. and Mosselman, E. (2013). Effects of helical flow in one-dimensional modelling of sediment distribution at river bifurcations. *Earth Surface Processes and Landforms*, 38(5):502–511.

Vandenbruwaene, W., Meire, P., and Temmerman, S. (2012). Formation and evolution of a tidal channel network within a constructed tidal marsh. *Geomorphology*, 151152(0):114 – 125.

Vennell, R. (2010). Tuning turbines in a tidal channel. *Journal of fluid mechanics*, 663:253–267.

Vennell, R. (2012a). The energetics of large tidal turbine arrays. *Renewable Energy*, 48:210–219.

Vennell, R. (2012b). Realizing the potential of tidal currents and the efficiency of turbine farms in a channel. *Renewable Energy*, 47:95–102.

Vennell, R. (2013). Exceeding the betz limit with tidal turbines. *Renewable Energy*, 55:277–285.

Vennell, R. and Old, C. (2007). High-resolution observations of the intensity of secondary circulation along a curved tidal channel. *Journal of Geophysical Research: Oceans (1978–2012)*, 112(C11).

VerdantPower (2007). *www.verdantpower.com*.

Von Storch, H. and Zwiers, F. W. (2001). *Statistical analysis in climate research*. Cambridge university press.

Warner, J., Schoellhamer, D., Burau, J., and Schladow, G. (2002). Effects of tidal current phase at the junction of two straits. *Continental shelf research*, 22(11):1629–1642.

Weisberg, R. H. and Zheng, L. (2008). Hurricane storm surge simulations comparing three-dimensional with two-dimensional formulations based on an ivan-like storm over the tampa bay, florida region. *Journal of Geophysical Research: Oceans (1978–2012)*, 113(C12).

Yang, Z., Wang, T., and Copping, A. E. (2013). Modeling tidal stream energy extraction and its effects on transport processes in a tidal channel and bay system using a three-dimensional coastal ocean model. *Renewable Energy*, 50:605–613.

Zhang, J.-S., Wang, J., Tao, A.-F., Zheng, J.-H., and Li, H. (2013). New concept for assessment of tidal current energy in jiangsu coast, china. *Advances in Mechanical Engineering*, 2013.

Zheng, L., Chen, C., and Liu, H. (2003). A modeling study of the satilla river estuary, georgia. i: Flooding-drying process and water exchange over the salt marsh-estuary-shelf complex. *Estuaries*, 26(3):651–669.